UNIVERSITÀ DEGLI STUDI DI PADOVA

DIPARTIMENTO DI FISICA E ASTRONOMIA G. GALILEI

DOTTORATO DI RICERCA IN ASTRONOMIA
CICLO XXVI

PHOTOMETRIC ANALYSIS OF ASTEROIDS AND COMETS FROM SPACE OBSERVATIONS

Direttore della Scuola: prof. GIAMPAOLO PIOTTO

Supervisori: dott.ssa MONICA LAZZARIN
dott.ssa SARA MAGRIN

Dottoranda: FIORANGELA LA FORGIA

31 Gennaio 2014

Contents

List of Figures

List of Tables

Riassunto

La missione Rosetta dell'Agenzia Spaziale Europea, durante il suo viaggio verso la cometa 67P/Churyumov-Gerasimenko, attualmente in corso, ha effettuato una tappa intermedia il 10 luglio 2010, passando a meno di 3 200 km dall'asteroide 21 Lutetia osservando questo corpo minore da vari punti di vista inaccessibili da Terra. Meno di quattro mesi dopo, il 4 novembre 2010, la missione EPOXI, estensione della precedente Deep Impact della NASA, ci ha offerto un'altra straordinaria occasione, avvicinandosi a meno di 700 km dal nucleo della piccola cometa super-attiva 103P/Hartley 2 alcuni giorni dopo il suo passaggio al perielio.

Questi passaggi ravvicinati hanno costituito un'enorme opportunità per l'avanzamento delle conoscenze sulla formazione e sulla storia del nostro Sistema Solare. Gli asteroidi e le comete sono infatti gli unici resti ancora esistenti dei planetesimi primordiali che si svilupparono nella nebulosa solare originaria. Essi sono quindi fondamentali per lo studio delle condizioni iniziali e dei processi che si verificarono durante le fasi iniziali di formazione del Sistema Solare.

Lo scopo principale di questa tesi è pertanto quello di apportare un avanzamento nella scienza dei piccoli corpi del Sistema Solare, in particolare le comete, attraverso l'analisi fotometrica di immagini ad alta risoluzione ottenute mediante le due missioni spaziali Rosetta ed EPOXI.

L'analisi delle immagini di Lutetia, ottenute mediante OSIRIS (Optical Spectroscopic and Infrared Remote Imaging System), il telescopio ottico a bordo della sonda Rosetta, è stata focalizzata principalmente sullo studio delle proprietà fisiche della superficie asteroidale.
Attraverso l'indagine sulla curva di fase integrale e la sua modellazione mediante il modello fotometrico di Hapke, è stato possibile stimare che le particelle di regolite che costituiscono la superficie di Lutetia sono altamente riflettenti, molto piccole, compatte ed opache, e formano uno strato sostanzialmente liscio, a bassa porosità, che ricopre il nucleo molto denso di Lutetia ($3.4 \pm 0.3 \cdot 10^3$ kg m^{-3}, Pätzold et al., 2011).

Gli spettri osservati, sostanzialmente piatti e privi di caratteristici assorbimenti, combinati con l'elevata densità di Lutetia, suggeriscono una classificazione spettrale tassonomica che lo identifica come un asteroide di tipo X con una composizione dominata da enstatite condrite.
La pendenza spettrale presenta una significativa variazione all'aumentare dell'angolo di fase evidenziando un pronunciato arrossamento. Questo fenomeno, che necessita ancora oggi una spiegazione esaustiva, potrebbe essere responsabile dell'ampia variazione nella pendenza spettrale di Lutetia osservata da Terra.
Tramite l'analisi dei colori sulla superficie di Lutetia, sono state osservate evidenze di variegazione superficiale, in particolare nella regione denominata Baetica Region, considerata geologicamente interessante. In questa regione, si misura una variegazione di circa il 10%, che probabilmente indica la presenza di grani di dimensioni maggiori, vista la colorazione più blu sulle pareti del cratere, il che potrebbe essere riconducibile alla presenza di materiale più fresco. Mentre le regioni ai piedi del cratere sembrano essere arrossate, ad indicare materiale più fino, trattandosi probabilmente di depositi di detriti causati da frane.
In vista di una futura estensione del presente lavoro alla fotometria risolta, sono stati implementati una serie di strumenti di analisi complementari che fanno uso del modello di forma di Lutetia per poter effettuare studi locali dettagliati oltre che globali sulla superficie.

L'analisi delle immagini della cometa 103P/Hartley 2, osservata mediante la camera multi-banda MRI (Medium Resolution Imager) a bordo della sonda EPOXI, è stata incentrata invece sulla fotometria dell'atmosfera cometaria, in particolare sullo studio delle strutture di gas e polvere presenti nella chioma, e sui meccanismi di emissione del gas.
Lo studio dei colori, effettuato mediante osservazioni nel continuo a banda stretta, hanno permesso di notare che la polvere nella chioma della Hartley 2 è leggermente arrossata in direzione della coda. Questo fenomeno potrebbe essere spiegato considerando che i ghiacci e le particelle di polvere sono emessi generalmente in direzione solare e che, mentre i ghiacchi sublimano sotto l'influsso del calore del sole, i materiali refrattari vengono invece spinti dalla pressione di radiazione e formano una coda di sola polvere che quindi è leggermente più rossa.
È stato poi affrontato lo studio delle strutture visibili nell'emissione del gas OH, nel periodo che si estende dal giorno del perielio ai 10 giorni successivi. L'OH ha una distribuzione prevalentemente antisolare in quasi tutte le osservazioni, a parte quelle acquisite durante il massimo avvicinamento (Closest Approach, CA) alla cometa. In queste ultime infatti, è evidente un getto di

gas in direzione solare proveniente dalla zona centrale del nucleo cometario, che si estende entro un raggio di 35 km dal nucleo. Questa struttura, molto vicina al nucleo, costituisce un'indicazione della presenza di un meccanismo di emissione secondario. É stato suggerito possa trattarsi di emissione diretta (prompt emission, PE) di molecole di OH eccitate, proveniente direttamente dalla fotodissociazione dell'acqua.
L'analisi delle strutture di CN nelle regioni vicine al nucleo hanno rivelato invece una struttura curva, anch'essa entro 35 km dal nucleo, che è stata interpretata come indicazione del fatto che il gas CN viene emesso nella chioma non direttamente dal nucleo, ma piuttosto da grani e particelle che sono influenzate dalla rotazione del nucleo, la quale sarebbe pertanto responsabile della forma incurvata, piuttosto che radiale, delle strutture.
Le osservazioni in OH sono state ulteriormente utilizzare per lo studio del tasso di produzione di acqua nella chioma della cometa Hartley 2. L'OH è infatti un diretto prodotto della dissociazione dell'acqua. É stato utilizzato un modello di chioma corrispondente a quello vettoriale oltre la zona di collisione, ma esteso all'interno della sfera di collisione, fino alle regioni prossime al nucleo. É stato trovato un tasso di produzione d'acqua di $1.17 \cdot 10^{28}$ mol s^{-1} ($\log Q = 28.07$), compatibile con le misure effettuate da altri autori (vedi Knight et al., 2013).
Il tasso di produzione d'acqua risulta comunque variabile in funzione del tempo, mostrando una periodicità compatibile con la rotazione del nucleo, che ha un periodo di circa 18 ore. Nelle immagini ad alta risoluzione, acquisite durante il CA sembra esserci un picco di produzione superiore alla media osservata.
Il meccanismo di emissione di OH dovuto alla PE è stato pertanto proposto come possibile responsabile e ne è stata effettuata una valutazione della quantità teorica osservabile attraverso il filtro a banda stretta dell'OH della camera MRI. Risulta che, ad una distanza di 50 km dal nucleo, la PE avrebbe un'intensità pari al 26% dell'emissione dovuta a fluorescenza. Probabilmente tale valore teorico sovrastima la percentuale di emissione diretta. Considerando invece che la PE abbia un'efficienza pari al 10% della fluorescenza, le osservazioni vengono ben riprodotte dal modello cometario utilizzato, anche nelle vicinanze del nucleo.

Tutte le analisi svolte in questa tesi avranno una diretta applicazione nell'imminente incontro di Rosetta con la cometa 67P/Churyumov-Gerasimenko che avverrà ad agosto 2014 e durerà fino a dicembre 2015. Rosetta si avvicinerà infatti alla cometa, rilascerà un modulo di atterraggio sulla sua superficie e seguirà la cometa lungo la sua orbita fino al suo prossimo passaggio al perielio. Ci si aspetta che questo incontro rivoluzioni la scienza

cometaria, portando risposte alla maggior parte dei misteri ancora irrisolti. Le analisi compiute sull'asteroide 21 Lutetia e sulla cometa 103P/Harltey 2 saranno pertanto combinate insieme per la riduzione e l'analisi dei dati, l'implementazione di procedure e l'interpretazione dei risultati, in occasione dell'arrivo di Rosetta sulla cometa, con lo scopo ultimo di ottenere una migliore comprensione delle comete in tutti i loro aspetti.

Abstract

The European space mission Rosetta, during its still ongoing journey to the comet 67P/Churyumov-Gerasimenko, on 10 July 2010 made an intermediate stop flying close to the asteroid 21 Lutetia at a distance of less than 3 200 km and observed it from a varying observing point, otherwise inaccessible from Earth. Less than four months later, on 4 November 2010, the EPOXI mission, extension of the NASA Deep Impact mission, offered another unexpected opportunity approaching the small hyperactive Jupiter family comet 103P/Hartley 2 a few days after its perihelion passage at a distance of less than 700 km from its nucleus.

Those encounters provided an extremely important possibility for the advance in understanding our Solar System formation and history. Asteroids and comets are indeed the unique left samples of the primordial planetesimals that accreted in the original solar nebula. They are therefore key bodies for understanding the conditions and the processes occurred during the Solar System initial formation phases.

The principal aim of this thesis is therefore to provide an advance in the small bodies science, particularly comets, through the photometric analysis of high-resolution observations obtained by the two mentioned space missions.

Investigations of asteroid 21 Lutetia, observed on 10 July 2010 through the OSIRIS imaging system (Optical Spectroscopic and Infrared Remote Imaging System) onboard the Rosetta spacecraft, have been focused mainly on its surface physical properties.
The integral phase curve analysis and Hapke's modeling showed that the regolith particles constituting Lutetia's surface are highly reflecting, very small, compact and opaque, and form a low-porosity and overall smooth layer over the high-density nucleus of Lutetia.
The quite flat and featureless spectra observed suggest, together with the high density, that Lutetia is an X-type asteroid for the spectral taxonomy and that it has possibly an enstatite chondrite composition.
Moreover the spectral slope is found to vary significantly with phase angle

showing a pronounced reddening. This evidence, still to be completely explained, may be one possible explanation of the continuously changing spectral slope of Lutetia spectrum observed from Earth.
We found strong evidences of color variegation over the surface of Lutetia, and in particular on a geologically interesting surface area, called Baetica Region. The variegation of this region, found to be about 10%, suggests the presence of bluer particles on the crater walls, indicative of bigger grains, possibly revealing fresh material, and of redder particles at the bottom of the slant, where debris deposits are potentially present.
In view of a future extension of the work to the resolved photometric analysis, a series of complementary processing tools which make use of the high-resolution shape model have been implemented.

The photometric analysis of comet 103P/Hartley 2, visited by EPOXI spacecraft on 4 November 2010, and pictured through MRI (Medium Resolution Imager) multi-band imaging system, has been focused instead on the cometary atmosphere and its dust and gas features and emission processes. The study of the colors and reddening of the dust, through narrowband continuum observations, shows that dust in Hartley 2 coma is slightly redder in the tailward direction than in the sunward direction. This is tentatively explained considering that ices and refractories are both emitted in the sunward direction, but, while ices sublimate, refractories are pushed away by the Sun's radiation pressure and form a slightly redder tail.
A detailed study of OH emission structures in the period spanning from the day of perihelion up to 10 days afterward, has been performed. It shows an overall radial antisunward OH distribution in all observations apart the closest approach (CA) images, where a radial sunward jet coming from the central waist of the nucleus is evident in the very innermost regions of the coma, within 35 km from the nucleus. This OH feature, very close to the nucleus, provided an indication of a possible secondary emission mechanisms. The prompt emission (PE) of excited OH molecules coming from photodissociation of water has been proposed.
CN structure analysis in the near-nucleus region shows instead a rounded structure, within 35 km from the nucleus, which is interpreted as an indication that CN is emitted in the coma by grains or particles that are affected by the nucleus rotation.
OH observations have been further investigated in order to derive the water production rate in the coma of Hartley 2. A coma model has been adopted, correspondent to vectorial model but extending inside the coma down to the nucleus. A water production rate of $1.17{\cdot}10^{28}$ mol s^{-1} ($\log Q = 28.07$) has been evaluated, consistent with other authors measurements (see Knight et

al., 2013).
However the water production rate is found to be varying as function of time with a periodicity that suggests a correlation with the nucleus rotation, which has a period of about 18 hours. However a strong peak in the production rate is observed, correspondent to CA nucleus-resolved observations.
The prompt emission mechanism for OH brightness has been invoked as possible responsible and an evaluation of the theoretical observable OH PE flux through MRI-OH narrowband filter has been performed, yielding an intensity of about 26% of the fluorescence emission at about 50 km from the nucleus. However, this is probably an overestimate of the prompt emission, considering indeed a value of about 10%, observations are well reproduced by the cometary model used, even in the innermost coma.

All the studies performed in this thesis will have a direct application to the upcoming encounter of Rosetta with the comet 67P/Churyumov-Gerasimenko occurring on August 2014, and lasting more than a year, until December 2015. Rosetta will approach the comet, deliver a lander on its surface and escort the comet along its orbit up to its next perihelion passage. This encounter is expected to revolutionize the cometary science, giving answer to most of the up-to-date still unexplained comets mysteries. The investigations performed on asteroid Lutetia and comet Hartley 2 will be therefore combined together for data reduction, analysis, procedures implementation and results interpretation, with the final aim to obtain a better understanding of comets in all their aspects.

Introduction

The European space mission Rosetta, on its journey to the comet 67P/Churyumov-Gerasimenko, made an intermediate stop on 10 July 2010 flying close to asteroid 21 Lutetia at a distance of less than 3 200 km and observed it from varying observing geometries, otherwise inaccessible from Earth. Less than four months later, on 4 November 2010, the EPOXI mission, extension of the NASA Deep Impact mission, after the success of comet Tempel 1 rendezvous, offered another unexpected opportunity approaching the small hyperactive Jupiter family comet 103P/Hartley 2 a few days after its perihelion passage.

Those encounters provided an extremely interesting possibility for the planetary sciences in general and for the advance in understanding our Solar System, its formation and history, in particular.

Lutetia's fly-by allowed to investigate in detail the surface of this very primitive small body of the Solar System in order to eventually understand the mechanisms that are responsible for asteroids composition, variegation, surface properties, and that rule their evolution. Hartley 2's approach, on the other hand, offered the possibility to analyze a cometary nucleus in the peak of its activity, and eventually better comprehend the processes that govern the onset and development of cometary outgassing, that shape the coma structures and rule its composition.

Asteroids and comets are the unique left samples of the primordial planetesimals that accreted in the original solar nebula. They are therefore key bodies for understanding the dynamical, chemical and physical processes occurred during the initial phases of the formation of the Solar System.

Asteroids, although apparently quite simple solid bodies, are subject to collisions, orbital evolution, and many physical processes. They need deep investigation, together with a statistical study in order to provide enough information to help building a complete scenario of the Solar System history. Comets, on the other hand, are very complex space objects, subject to outgassing and periodic activity which constantly changes their orbit, mass, relative composition etc. However they are both the most well-preserved

bodies and they still enclose many information about our formation and evolution. The full understanding of comets requires the overall understanding of each of their physical components (nucleus, coma, tail) and of all the interconnections and exchanges existing among them. The coma composition depends on the nucleus composition and its activity is also governed by the nucleus properties. Understanding the complexity of a comet's world is still a huge challenge for the planetary science despite many space missions have been recently dedicated to those primitive bodies.

Aim of this thesis

In this scientific framework, the principal aim of this thesis is to give an advance in the science of small bodies, and particularly comets, through the analysis of close up observations obtained by Rosetta and EPOXI space missions.

The main technique adopted is the photometric analysis of high-resolution spacecraft images. Asteroid Lutetia's analysis is focused on the study of the resolved nucleus, the surface properties and the shape modeling application. Comet Hartley 2's investigation has been instead focused on the coma activity, on the study of the visible gaseous structures, the water production rates and the processes involved in the gas emissions in a cometary atmosphere. These two studies are very different but complementary in the complex analysis of the whole cometary nature, which requires a deep understanding of both nucleus and coma at the same time and of the interconnections among them.

All the studies performed in this thesis have the additional purpose to achieve experience and competences for the upcoming rendezvous of Rosetta with the comet 67P/Churyumov-Gerasimenko occurring on August 2014, an lasting until December 2015. This encounter is expected to revolutionize the cometary science. Rosetta will indeed approach the comet, deliver a lander on its surface and escort the comet on its orbit up to the perihelion passage. It will hopefully reveal most of the comets mysteries that are still unexplained, but a huge investment of time, resources, and software tools will be necessary to interpret the observations.
The experience acquired in the investigation performed on both asteroid Lutetia and comet Hartley 2 will be therefore very useful for data reduction and analysis, procedures implementation and results interpretation on the occasion of comet 67P encounter.

Overview

In Chapter 1 we discuss the importance of studying asteroids and comets, their similarities and differences. Then we focus separately on asteroids and comets separately, describing their physical, dynamical, photometric and spectral properties as derived from up to date observations, discoveries, and interpretations.

In Chapter 2 we highlight most of the advantages of space missions as respect to ground-based observations, we summarize briefly the history of the past missions to small bodies of the Solar System. We then describe the main scientific objectives, operation timelines and instrumental payloads of the Rosetta and EPOXI space missions.

In Chapter 3 we discuss and explain the details of the major theory of light scattering by a particulate medium: Hapke's bidirectional reflectance model that will be used for Lutetia photometric analysis in Chapter 4. The model parameters are illustrated and their physical interpretation is presented. A brief review of the other light scattering theories is also outlined.

In Chapter 4 we focus on the performed photometric analysis of 21-Lutetia, we briefly describe the instrument, OSIRIS camera onboard Rosetta, and the data considered. We then run over the photometric calibration issues and methods, and we describe the scientific analysis performed: integral phase curve study and Hapke's modeling, spectrophotometry and color variegation investigations over the surface and phase reddening calculations. We conclude the chapter with the shape model processing and we present some application for photometric utility.

In Chapter 5 we illustrate the gas emission process occurring in cometary atmospheres, starting from the coma gas distribution models, the photochemistry of the main parent molecule, water, and introducing then the fluorescence emission mechanism. A final presentation of a secondary emission mechanism known as prompt emission is also provided.

In Chapter 6 we introduce the data analysis performed on 103P/Hartley 2 comet. A short instrument and data description is given, followed by a description of a few data processing methods applied. Then the scientific analysis of the coma dust is presented including the analysis of dust colors and reddening, and then the coma gas analysis which includes gas fluxes, structures and column density in the near-nucleus region. We conclude the chapter with the water production rate calculation and with the proposal of OH prompt emission as possible contributor to OH observed flux.

The conclusions and the future perspectives of this PhD thesis work are then presented.

Chapter 1

Asteroids and Comets in the Solar System

1.1 Why studying Asteroids and Comets?

It is widely acknowledged that asteroids and comets represent the most primitive and preserved bodies of the Solar System. Indeed, they did not experienced the physical processes at very high temperature and pressure, such as differentiation, erosion and metamorphism, that transformed instead the planets and the satellites during the original formation process occurred about 4.6 billion years ago.

Many are still the open problems about the birth and evolution of the Solar System, including the nature of the accretion process in the protoplanetary disk, the physical and chemical conditions that existed at that time, such as temperature, pressure and composition, the relationship between the original interstellar composition and the accretion disk composition, the variation of the disk properties with heliocentric distance, its evolution with time, and many others.

In this very complex scenario, what we call today asteroids and comets have actually played a very important role as seeds for the developing planetesimals. Afterward they have been subject to collisions, resonances, orbit changes, space weathering, cosmic rays and others. However they are still made up of the same chemical material from which they formed when our planetary system was gaining shape.

Being thus the only left samples of the primordial planetesimals that accreted in the original solar nebula, make these bodies very special and unique. Their study has then the great potential to get back from the today's

appearance of the Solar System to the physical, chemical and dynamical conditions that existed when it formed and to trace a complete scenario of our evolution, answering to many open question.

Asteroids and comets have been widely observed and studied for decades for this reason and many space missions have been dedicated to them, improving significantly our understanding of the basic physical, chemical and geological processes that shape and influence those bodies. Nevertheless, many are still the poorly understood aspects of their nature and evolution. Understanding the complex properties of these bodies and their primary transformation mechanisms is essential to interpret the information that they are able to provide us, in view of the full comprehension of the Solar System as we see it today.

For example, the mechanisms that rule the evolution of asteroids and that govern the composition differences, the events that drive the cometary activity, the factors that shape the gas and dust in the coma, the actual mineralogical composition of cometary nuclei, the chemical processes that take place in the inner coma, among many others, are only some of the important issues that are still waiting for an exhaustive explanation.

Asteroids and comets have been and are still involved in frequent collisional and fragmentation processes. This gives us another very important reason to investigate them, primarily asteroids. It is therefore crucial to understand how these physical processes happen and which are their effects on different types of materials and their consequences for the Solar System history.

A fraction of the asteroidal population had in the past, and could still have, collisional interactions with the Earth. Discovering still unknown objects and monitoring them is then indispensable if we want to be at least warned, if not prepared, to face them in case they would actually hit our planet.

It is also possible, and believed by many, that through these impacts, probably by comets, liquid water was brought into Earth. Some other theories believe even that they may have brought also small organic molecules such as amino-acids, that developed later into life, so that our planet acted only as the cradle of the life. This hypothesis is supported by some observational evidences but further and deeper studies are necessary to actually confirm or rule out this theory and probably even change completely the perspective of our origin and evolution.

Last but not least reason to investigate asteroids and comets is that they give us the unique opportunity to use them as a real cosmic physics laboratory, allowing the study of extreme physical conditions. For example the optics of reflection, diffraction, and scattering of light by the solid surfaces of asteroids, the dynamical phenomena in a celestial mechanics laboratory, the emissivity phenomena of gas in the coma ambient of the comets, the interactions of the cometary material with the solar radiation and solar wind, the generation of instabilities and waves, are only some of the many interesting phenomena to be investigated, that cannot be produced under laboratory conditions.

1.2 Similarities and Differences

The accretion disk from which the Solar System formed, was made of various materials: rocks, ices, dust and gas. Some of those dust and rocks eventually collided and started to grow in dimensions, collecting material from their neighborhood and cleaning gradually their orbit, until they formed the planetesimals and then the cores of the present planets.

Not all of the original rocky and icy bodies contributed to the planets formation, a number of objects were left behind for different reasons: in the vicinity there wasn't any planetesimal big enough to clean its orbit; they were too far away from the Sun that the gravitational force was not strong enough to collect material; the dust density was not high enough to allow a planetesimal formation and so on.

These leftovers of the formation process are the current asteroids and comets. Thus they all share the evolutionary origin and history but they are also deeply different in many aspects.

Asteroids formed much closer to the Sun, where it was too warm for ices to remain solid, while comets formed further from the Sun where ices could not melt.

Comets are made up of volatiles chemical compounds that vaporize when heated by the Sun, such as water, carbon dioxide, carbon monoxide, methane and so on, beyond dust and rocky materials. Asteroids instead are made of dust, rocks and metals, and they present much more variety of composition and mineralogy. Thanks to their composition comets have a distinctive behavior: when they pass close to the Sun, at the perihelion, their volatiles are heated up and vaporize dragging out also the dust. Thus they grow a huge coma all around the body, then the solar wind and radiation pressure push it away forming a long antisolar tail.

Another difference is in their orbital patterns. Comets tend to have very extended, elliptical orbits with high inclinations. Sometimes they reach distances greater than 50 000 AU from the Sun. Asteroids have much shorter, circular and regular planar orbits.

Their abundance is also different: there are more than one million known asteroids, of which 625 106 had enough information to be given numbered designations (as for Sept 2013). There are instead only 4 894 known comets (as of July 2013) (http://www.johnstonsarchive.net/astro/sslist.html). This is probably only a selection effect due to the higher distance of these last ones. Indeed it is believed that at the very edges of the Solar System, the Oort Cloud contains several trillion individual objects larger than approximately 1 km.

However, there are some objects which show intermediate properties between asteroids and comets, for example there are objects which do not show any evidence of coma or tail but which have very elliptical and highly inclined orbits. These are called Damocloids. There are instead comets on very regular and circular orbits which show evidence of coma and tail. Some of them are known as Main Belt Comets (Bertini, 2011) and are dynamically indistinguishable from asteroids.

Thus, even though there are many differences, the distinction can be sometime very fuzzy. There is probably no clear separation between these two classes of objects. They are more probably part of the same group of celestial bodies with gradually changing properties.
Moreover, after a large number of revolutions around the Sun, the cometary activity may die out completely, leaving finally a residual solid nucleus, which may possibly lead to an asteroid (Weissman et al., 2002). Some asteroids could be therefore died comets.

1.3 Asteroids

The first discovered asteroid, 1 Ceres, was seen by Giuseppe Piazzi on 1 January 1801 from Palermo, in Sicily, and was originally considered a new planet, the missing planet in the region between Mars and Jupiter, as expected by Titius-Bode law.

In the following six years three other asteroids were discovered: 2 Pallas, 3 Juno and 4 Vesta. After eight more years of fruitless searches, no more asteroids were found and the astronomers abandoned the researches. The fifth asteroid was discovered more than 38 years later and from that day many more new asteroids are discovered each year.

As for Sept 2013 there are more than one million known asteroids, of which 625 106 have been orbitally studied and numbered.

1.3.1 Physical properties

The sizes of asteroids ranges between some hundreds of kilometers down to a few meters, even thought below 10 meters they are formally considered meteoroids.

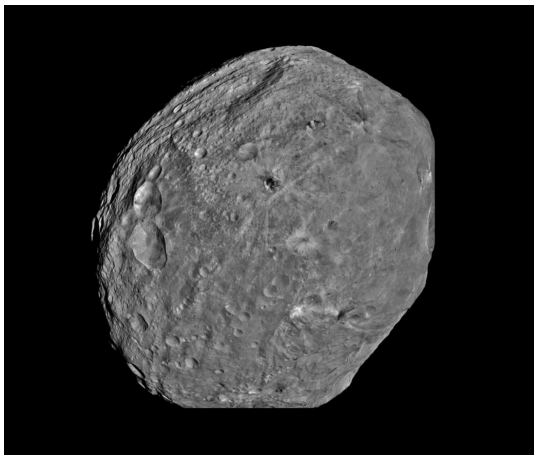

Figure 1.1: Asteroid 4 Vesta as imaged by Dawn spacecraft.

The biggest asteroid, 1 Ceres, recently redefined a dwarf planet, is 950 km across. It is massive enough to have a fully ellipsoidal shape and being in hydrostatic equilibrium. Its oblate shape suggests also its internal differentiation (Thomas et al., 2005) with a rocky core and an icy mantle. It is also believed to contain an ocean of liquid water under its surface (McCord

and Sotin, 2005). In 2015 the spacecraft Dawn, presently departed from Vesta, is going to unveil the mysteries of this large asteroid, orbiting it for more than six months.

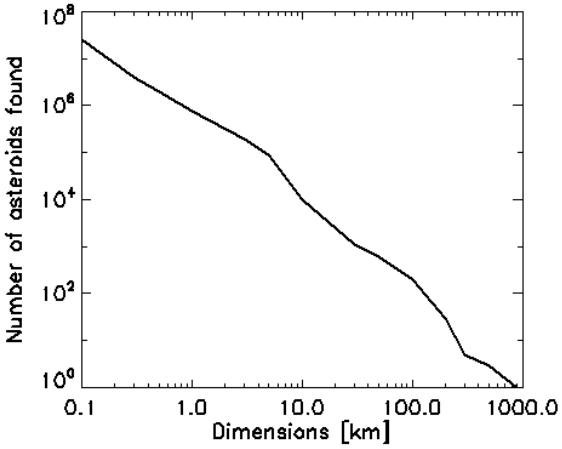

Figure 1.2: Distribution of asteroids dimensions.

The other largest asteroids are 2 Pallas and 4 Vesta, both about 500 km across. Vesta, being more massive, is also nearly spherical and differentiated, while Pallas has a more irregular shape. Vesta is considered the largest protoplanet of the kind that formed the terrestrial planets, or the smallest terrestrial planet (Keil, 2002). Vesta has been closely observed by Dawn spacecraft for more than a year, and reveled its irregular surface filled by craters (Fig. 1.1).

However, the vast majority of asteroids are much smaller, not enough massive to be differentiated and irregularly shaped, being either surviving planetesimals or fragments of larger bodies. The number of asteroids decreases markedly with size, following generally a power law (Fig. 1.2), with two bumps at 5 and 100 km, where more asteroids are found than expected from a logarithmic distribution. The shape and the surface of these objects is usually irregular and covered by impact craters of varying sizes and depths.

Numerous asteroids have been found to have a companion. 243 Ida was the first binary asteroid to be identified by the Galileo spacecraft in 1993. As of January 2014 (http://www.johnstonsarchive.net/astro/sslist.html), a total of 241 objects with companions are known, of which 10 triple system. Several theories have been posited to explain the formation of binary asteroid systems. Either they formed by disruption of a single asteroid after an

impact, or they formed during the formation of the Solar System by mutual capture or three-body interaction, or even they formed from a tidal splitting of a common parent, after a close encounter with a planet.

The total mass of all asteroids of the Solar System is estimated to be less than the 5% of the mass of our Moon.

The totality of the asteroids show a spin rotation with periods typically between a few hours and one day. Measurements of the rotation rates of large asteroids showed that no asteroid with a diameter larger than 100 meters has a rotation period smaller than 2.2 hours. However, a solid object should be able to rotate much more rapidly. This suggests that most asteroids bigger than 100 meters are rubble piles formed through accumulation of debris of collisions and fragmentation. In this case, in fact, if they would rotate faster, the inertia at the surface would be greater than the gravitational force and any loose material on the surface would be flung out.

Most have simple rotations around a fixed axis, while others, like 4179 Toutatis for example, have a complex tumbling rotation, probably due to a strongly irregular shape, arising presumably from a history of violent collisions. It is believed that violent collisions are common for asteroids, and that many asteroids have experienced complex rotations in their past, like Toutatis, as a consequence of such collisions, but that internal friction has caused them to dampen into simple rotation in relatively brief amounts of time.

The spin axis orientation depends then on the origin of the asteroids but also on their collisional history in the Solar System.

The age of the asteroids may be estimated from the crater distribution in sizes and number over the surface which reveals the exposition of the body to the space ambient and to probable collisions with other asteroidal bodies and fragments.

1.3.2 Dynamical properties

The main dynamical driver of asteroids and comets is obviously the Sun's gravity, but they are affected also by other dynamical powers: giant planets gravitation effects, mean motion and secular resonances, Sun's radiation pressure, Yarkovsky and YORP effects, Poynting-Robertson effect, gas drag, collisions and fragmentation. These mechanisms drive today the orbital evolution of asteroids and are probably responsible for both the past and the present dynamical situation.

The orbital resonance is a particular circumstance in which two orbiting bodies, gravitationally attracting each other, have their orbital periods related

by a ratio of two small integers. The resulting effect is that the gravitational influence gains a periodicity and may cause a modification of the orbit of the bodies, making them more stable or totally unstable. For example the orbits of Pluto and the Plutinos are stable, despite crossing that of the much larger planet Neptune, because their orbital periods are in a ratio of 2/3, meaning that they are in resonance 2:3. While among the rings of Saturn, the Cassini division is a gap between two rings that has been cleared by a 2:1 resonance with the moon Mimas, which caused the orbits to be very unstable in this region. The secular resonance is a similar phenomenon in which the precession periods are involved, rather than the orbital periods.

The solar radiation pressure is a pressure exerted upon any surface exposed to Sun's electromagnetic radiation. Since photons carry momentum and momentum is conserved, when a photon is absorbed by a body, it feels a force and thus a pressure. The force from radiation pressure has the same dependence on the heliocentric distance as the gravity, but it is in the opposite direction. The balance between the two forces strongly depends on the body's properties, such as its size. From fundamental constants and astronomical quantities such as the luminosity and the mass of the Sun, it results that particles smaller than 0.1 μm will be immediately expelled from the Solar System, while larger particles will orbit the Sun.

Yarkovsky and YORP forces act on a rotating body in space and are caused by the thermal inertia of the body and by the anisotropic emission of thermal photons. Usually the surface hemisphere illuminated by the Sun is warmer than the dusk hemisphere and emits more thermal radiation. This repeats periodically during the orbit of the body (seasonal effect) and at the same way it repeats periodically with the rotation of the body around its axis (diurnal effect), causing a cumulative force in a direction depending on the orientation of the rotational axis as respect to the orbital motion. The YORP effect is a second-order effect of the Yarkovsky mechanism. Both effects have significant dynamical influence only on small asteroids and meteoroids.

The Poynting-Robertson effect is a process by which solar radiation causes small dust grains in the Solar System to spiral slowly into the Sun. The drag is due essentially to the component of the Sun's radiation pressure tangential to the grain motion.

The gas-drag is a drag caused by the dispersed gas residual in the solar nebula which pushes the small dust particles in the direction of the gas motion.

Collisions are though to influence also the dynamics of asteroids in the sense that they may cause the bodies to fragment into smaller objects and thus to be more influenced by the Yarkovsky, Poynting-Robertson and gas-

drag effects. Moreover collisions cause rotational state to change thus creating for example tumbling asteroids.

Thanks to all those mechanisms, asteroids are spread all over the Solar System and present a great variety of orbits and behaviors. Many are the numerical simulations which aim at the explanation of the present distribution of asteroids in the Solar System but it is a non straightforward problem due to the many processes involved.

Based on their orbital characteristics, asteroids are divided into groups and families. Groups are collections of relatively weakly bound bodies with similar orbital behavior, whereas families are tighter and most probably are remnants of a catastrophic breakup of a unique large parent asteroid. The name of a group or family comes usually from the first, and generally largest, discovered member.

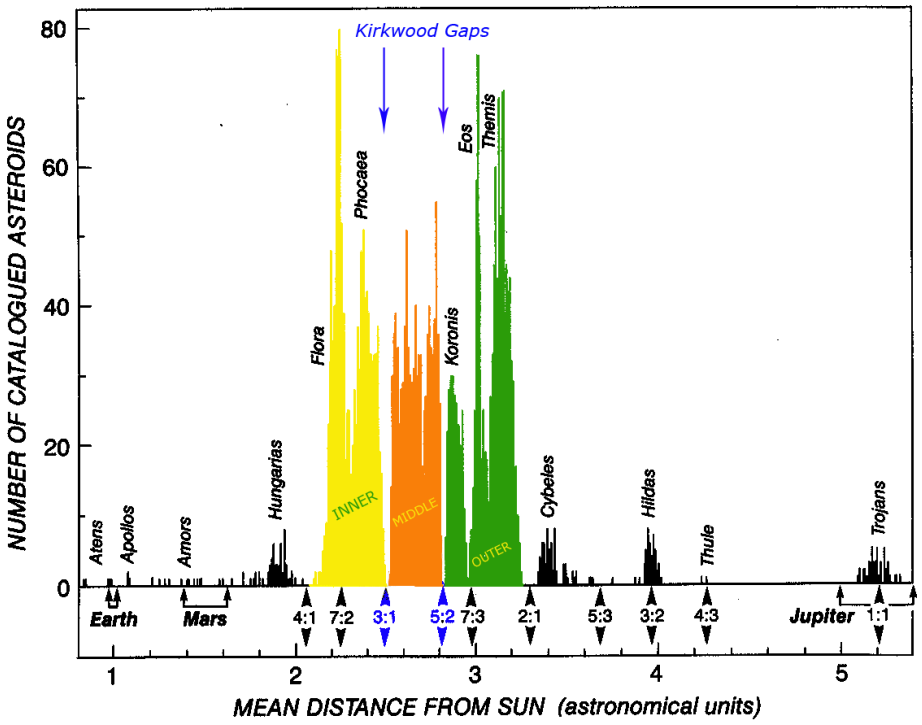

Figure 1.3: Main Belt structure and other asteroids families and groups.

Fig. 1.3 shows the distribution of known asteroids as function of their mean distance from Sun in astronomical units. It is clear that a strong concentration of asteroids occurs in the region between Mars and Jupiter

orbits. This is called the Main (Asteroid) Belt and is the primary asteroidal population reservoir. However many other groups and families exist.

Near Earth Asteroids

Asteroids of the inner Solar System, with perihelion, q, smaller than Mars' ($q = a(1 - e) < 1.3$ AU) are called altogether Near Earth Asteroids (NEAs), and with Near Earth Comets (NECs) constitute the Near Earth Objects (NEOs) class. They are divided into four groups: Apollos, Atens, Amors and Inner Earth Objects (IEOs). Apollos and Atens are Earth crossers while Amors approach the Earth but never intersect its orbit. Apollos have semimajor axis, a, greater than 1 AU while Atens have $a < 1$ AU. IEOs are asteroids with an orbit completely inside the Earth's one, showing an aphelion smaller than Earth's perihelion. As of June 2013, almost ten thousand near-Earth asteroids are known, ranging in size from 1 up to 32 kilometers.

Mars Crossers

These are bodies whose perihelions are included between Mars perihelion and aphelion and that cross Mars orbit. The population of Mars crossers is roughly four times the NEO population and is constantly resupplied.

Main Belt Asteroids

As it is clear from Fig. 1.3, asteroids are located mainly between the orbits of Mars and Jupiter, and more precisely between 2.1 and 3.28 AU: the Main Asteroid Belt. The borders of this region are defined by the 4:1 and 2:1 mean motion resonances with Jupiter.

The Main Belt is further divided into three large regions, Inner Main Belt, Middle Main Belt and Outer Main Belt by the Kirkwood gaps, regions almost totally lacking in asteroids, due to the mean motion resonances 3:1 and 5:2 with Jupiter which lie respectively at 2.50 and 2.82 AU. Additionally Main Belt Asteroids are dynamically divided into a large number of groups, sub-groups and families.

The original hypothesis on the origin of this thick belt suggested that a planetesimals formed in that region but suffered a series of perturbations and collisions which broke it down leaving behind plenty of rocky remnants. This hypothesis was soon abandoned and today it is believed that the small planetesimals lying in this region during the period of Solar System formation, were highly perturbed by Jupiter, rapidly formed due to the run-away process. Stressed and speed up by Jupiter they had faster and destructive collisions

and never succeeded in accrete and form a planet (Petit et al., 2001).

Trojans Asteroids

Some planets have companion asteroids lying along their own orbits, 60° ahead and behind them, in their L4 and L5 Lagrangian points. As L4 and L5 Lagrangian points are stable equilibrium solutions of three body problem, Trojans are usually stable objects and their orbits do not evolve significantly.

Jupiter's companions were called the Greeks and Trojans respectively but for simplicity they are now called altogether Jupiter's Trojans.

In 1990 the first Mars Trojan was found: 5261 Eureka. Presently, this group contains seven confirmed members.

In 2001 the first Neptune Trojan was also found. Nine Neptune's Trojans are currently known and they are expected to outnumber the Jupiter's Trojans by an order of magnitude.

In 2010 it was discovered the 300-meter wide asteroid 2010-TK7, being associated with the Earth L4 Lagrangian point, leading Earth's orbit. It is the first and sole confirmed Earth's Trojan.

At present, searches for Trojans of other planets are in progress.

Centaurs Asteroids

These are bodies orbiting between Jupiter and Neptune (5.4 AU $<$ a $<$ 30 AU). Their orbits are chaotic, rapidly evolving and their behavior has characteristics of both asteroids and comets. Centaurs are probably objects perturbed from the Scattered-Disk (see next paragraph). As they make repeated close encounters to the outer planets they can further evolve into Jupiter-crossers and even enter in the inner Solar System.

Trans Neptunian Objects

As of January 2014, more than 1 250 objects have been detected beyond Neptune orbit (a $>$ 30 AU). They are defined altogether as Trans-Neptunian Objects (TNOs) and are arranged in three main regions: Kuiper Belt, Scattered Disk and Oort Cloud.

Kuiper Belt objects have nearly circular and low inclination orbits, extending from $\sim$36 to $\sim$48 AU. The Cubewanos, named after 1992 QB1, the first of this type, discovered by David Jewitt at the University of Hawaii (Jewitt and Luu, 1993), are the Classical Kuiper Belt objects, not affected by any particular resonance. Some of the Kuiper Belt bodies are instead captured in mean motion resonance with Neptune and are called Resonant Kuiper Belt objects. Among them famous are the Plutinos, asteroids in

mean motion resonance 2:3 with Neptune, exactly as Pluto, the largest of these bodies. Two distinct classical Kuiper Belt populations are identified: the *hot* and *cold* classical populations. The hot population refers to objects with $i > 4°$ while the cold population refers to objects with $i < 4°$.

From 48 to 50 AU there is a sharp gap, while objects with larger orbits are spread in the Scattered-Disk. They have very elliptical ($0.34 < e < 0.94$) and very large orbits ($50 < a < 675$ AU), and are probably objects that encountered Neptune and were scattered into long-period, far orbits.

A spherical cloud of objects is thought to extend much further, from 10 000 to 50 000 AU from the Sun. The Oort cloud probably contains millions of comet nuclei; it is only loosely bound to the Solar System and is easily affected by the gravitational pull by passing stars and by the Milky Way Galaxy potential. The outer extent of the Oort Cloud defines the gravitational boundary of our Solar System.

1.3.3 Photometric properties

In the visible and near-infrared spectral range, the asteroids brightness is due mainly to reflection and scattering of the solar light by the surface of the bodies. The observed flux depends thus on the chemical and physical characteristics of the surface and on the illumination and observation conditions.

The chemical and mineralogical composition of the surface plays an important role in establishing the fraction of light reflected or scattered. Different compounds have indeed different reflectivity properties: for example organics are dark since they absorb most of the light and the scattered fraction is small, while silicates reflect more and therefore are brighter, much brighter are then ices and volatiles.

The flatness or irregularity of the surface, its porosity or compactness, its solid or particulate nature may contribute to the determination of the total amount of light scattered and on the way it is diffused. The dimension of the regolith grains constituting the surface is also important.

The illumination and observations conditions are described usually by the *phase angle*, α: the angle between the light source and the observer as seen from the target surface. The phase angle is indeed the angle that determines the fraction of the body which is both illuminated and visible. This is the reason why we call phases of the Moon the different conditions of the Moon's visibility, due to the orbit of the Moon around the Earth, according to the changing relative positions of the Earth, Moon, and Sun. The condition of simultaneously zero incident, emission and phase angles, meaning that the

Sun's direction is coincident with the observer's direction, is called *opposition* and the reflecting properties in this situation may vary significantly respect to other geometric situations (see Sec. 3.1.4).

The physical quantity that describes the overall reflectivity properties of an object is called *geometric albedo*, A_p. It is defined as the ratio of its observed brightness at zero phase angle to that of a flat, fully reflecting, diffusively scattering (Lambertian) disk with the same cross-section. A Lambertian surface reflects totally the incident light, not only in the specular direction, but in all the directions in the hemisphere, following Lambert's cosine law distribution (see Fig. 1.4).

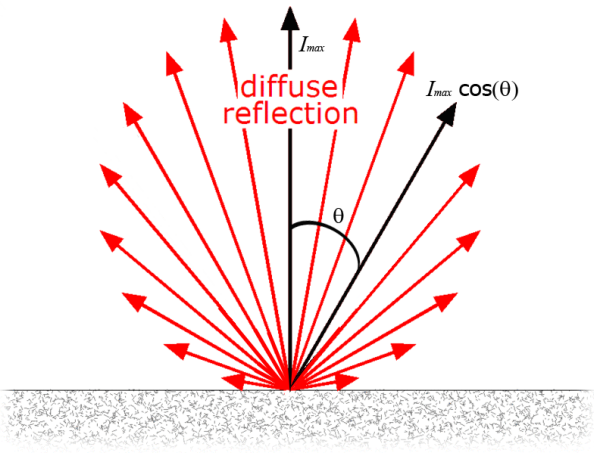

Figure 1.4: Lambertian surface diffuse reflection.

Asteroids are usually neither totally reflecting, nor Lambertian, thus the geometric albedo is usually smaller than 1. There is only one case of an airless body, the Saturn's moon Enceladus, which shows an albedo of 1.4.

The geometric albedo has also been used as contributor factor for the classification of asteroids in different classes of composition since, as said before, it strongly depends on the compounds constituting the surface and their capacity to reflect the light.

The *Bond albedo* is instead defined as the fraction of the power incident on an astronomical body that is scattered back out into space in the total electromagnetic range. Thus it accounts for all of the light scattered from a body at all wavelengths and all phase angles. The Bond albedo, A_B, is related to the geometric albedo by the expression:

$$A_B = A_p \cdot q \tag{1.1}$$

where q is called phase integral and it is given by:

$$q = 2 \int_0^{\pi} \frac{I(\alpha)}{I_{\alpha=0}} \sin \alpha d\alpha \tag{1.2}$$

where $I(\alpha)$ is the total brightness of the body in all wavelengths at the phase angle α and $I_{\alpha=0}$ is obviously its total brightness at zero phase angle. Measuring the Bond albedo is very problematic since it assumes full wavelength and phase angle coverage, which is impossible to obtain from Earth and extremely difficult even from space. Therefore it is often estimated on the basis of the measures available. Bond albedo is, by definition, always lower than 1.

The brightness of asteroids shows generally a periodic variability, due to their rotation. Because asteroids are usually not spherical, as they rotate, the incident solar light intersects different cross sections and, at the same time, different geometric sections becomes visible to any observer depending on its relative position. Thus the total observed flux can vary significantly. The function that describes how the brightness changes as function of time is called *light curve* and it is of big importance in determining the rotational period of an asteroid, an estimate of its shape and sometimes even an idea of the position and orientation of the rotational axis.

If the photometric observations are available in numerous filters, the surface colors can be evaluated simply as ratios of brightness in different filters. Colors allow to infer low-resolution spectral behavior and therefore assess the presence of some selected mineral species bands. Colors can moreover be indicative of surface variegation and thus of differences in the nature of the materials present in different regions. It may indicate differences in mineralogical compositions and/or differences in the grains sizes.

Another important photometric tool is the *integral phase curve*. It is the total brightness of the entire object, as function of the phase angle. Interpretation of this curve asks for a detailed analysis of the scattering process that occurs on the surface of asteroids. The most important effect visible in the phase curve of asteroids is the *opposition effect* (see Sec. 3.1.4). The brightness of the body increases rapidly when the phase angle approaches zero. The full explanation of this process is still in dispute but a realistic theory involves mutual shadowing effect among particles and multiple coherent scattering of the normal incident light in the opposite direction. An atmosphere destroys the opposition effect, thus the planets phase curves do not show this effect.
The integral phase curve contains important information on the structural and physical properties of the asteroid surface. The most used models to

interpret the phase curve will be described in Chapter 3 with a particular attention to Hapke's model that will be used in Chapter 4 for the analysis of the photometric properties of asteroid 21 Lutetia through Rosetta resolved observations.

1.3.4 Spectral properties

Visible and near-infrared reflectance spectroscopy has been widely used to determine asteroids surface composition.

Chemical and mineralogical composition can be investigated by the interpretation of observable properties and features of the reflectance spectrum.

Diagnostic features of particular mineral species that come from electronic and vibrational transitions are detectable in the ultraviolet to infrared wavelength region. Hence it is possible to determine the presence and, in some cases, the abundance of minerals and compounds in the surface materials.

Most important mineral species present in asteroid spectra are silicates (olivine, pyroxene), iron-nickel metals, spinel, feldspar, hydrated phyllosilicates and organic compounds. Most asteroids are composed of a mixture of these minerals.

Origin of absorption bands in minerals spectra

The absorption bands detected in the visible and near-infrared spectra of asteroids originate usually from electronic transitions of minerals and mixtures composing the material on the surface of asteroids. The bands are due to the absorption of the solar radiation illuminating the surface which causes the external electrons of metal cations of the minerals to be excited and jump on higher energy levels.

The observed spectral features are broad bands, not narrow lines as those formed in the stellar atmospheres, but the positions, profiles, intensities and widths are often sufficiently diagnostic to enable individual minerals to be identified and sometimes to allow an estimate of the relative abundances.

Electronic transitions occur to the external electrons of cations of the transition metals, in particular of the first series (Ti, V, Cr, Mn, Fe, Co, Ni and Cu) which have the external 3d orbitals incompletely filled. These metals are indeed some order of magnitude more abundant than the other transition series, and iron is by far the predominant transition element, followed by titanium. The primary silicate minerals containing Fe and Ti are olivine and pyroxene.

Minerals are usually present as crystals whose constituent atoms, molecules, or ions are arranged in an ordered pattern extending in all three spatial dimensions with usually macroscopic visible geometrical shape, consisting of flat faces with specific, characteristic orientations.

The defining property of a crystal is its inherent symmetry and the *coordination number* of the central atom, i.e. the number of its nearest neighbors.

Three types of electronic transitions are responsible for the absorption bands (Pieters and Englert, 1993):

- Crystal Field (CF):

  d-d or f-f electron orbital transitions within individual cations; explained by the Crystal Field Theory;

- InterValence Charge Transfer (IVCT):

  metal to metal transitions between adjacent cations in a crystal structure; explained by the Ligand Field Theory;

- Oxigen to Metal Charge Transfer (OMCT):

  transitions between nearest-neighbor atoms; explained by the Molecular Orbital Theory;

Crystal Field transitions depend on the symmetry properties of the transition metal 3d orbitals. The five 3d orbitals have identical energies in a gaseous free ion, however this degeneracy is removed when the cation is surrounded by ligands in a crystal structure, and then the relative energies of the five 3d orbitals depend on the symmetry of the ligand environment and on the coordination number. The energy separation is called *crystal field splitting* and is indicated as Δ_O. Beside the coordination number, other factors influencing Δ_O are the type of ligands, the type of cation, the cation-oxygen interatomic distance, the pressure and the temperature. A variation in Δ_O causes obviously a change in the frequency of the absorbed photon and consequently a redshift or blueshift of the absorption band.

Inter Valence Charge Transfer transitions occur when the electron in a 3d orbital is transferred between close cations and consequently there is a transient change of valence. They are usually of intensity from one to three orders of magnitude higher than CF transitions and have larger bandwidths. Two different situations occur, depending on whether the same element (in different oxidation states) or two different elements are involved in the electron transfer.

Oxygen to Metal Charge Transfer transitions are usually induced by high-energy ultraviolet light. However absorption edges may extend in the visible and influence the optical spectrum. These transitions have usually intensities from 10^3 up to 10^4 times higher than CF transitions.

Each transition is almost unique in wavelength position, intensity and width, so that the detailed study of transitions occurring in all the cations of minerals involved in the asteroids composition, and of the probability of those transitions to happen, provides a very powerful tool to discern the presence of those minerals from the observational spectra.

Spectral Taxonomy

The analysis of reflectance spectra shows a great variety of typologies, reflecting the great diversity of possible compositions of minerals, which have been used to classify asteroids. The principal aim is to identify groups of asteroids that share similar surface composition and thermal histories. This taxonomy is completely independent of the dynamical properties.

The most widely used taxonomy was introduced by Tholen (1989). He used a combined spectrum-albedo criterion to identify fourteen classes of asteroids. Eleven classes (A, B, C, D, F, G, Q, R, S, T and V) could be distinguished by spectra. Other three classes (E, M and P) had degenerate spectra and could only be separated using albedos (Fig. 1.5). When albedo information was not available, the E, M and P-type were grouped into a generic X-type.

class A: A-asteroids exhibit a strong decrease in reflectance shortward of 0.7 μm, related to metal compounds, and a strong broad absorption feature centered near 1 μm with no significant 2 μm absorption (characteristic of pyroxene). Composition is dominated by olivine.

class S: S-types are the second most abundant asteroids in the Solar System. They have spectra with moderate to steep reddish slopes shortward of 0.7 μm and weak to moderate absorption features near 1 and 2 μm. This indicates the presence of some mixture of olivine, pyroxene and Fe-Ni metal.

class Q: The spectrum is strongly reddened shortward of 0.7 μm and has a strong 1 μm absorption feature characteristic of a mixture of olivine and pyroxene. Q-types are found primarily among NEO (DeMeo et al., 2013).

class V: Typical V-type asteroid Vesta shows a spectrum characterized

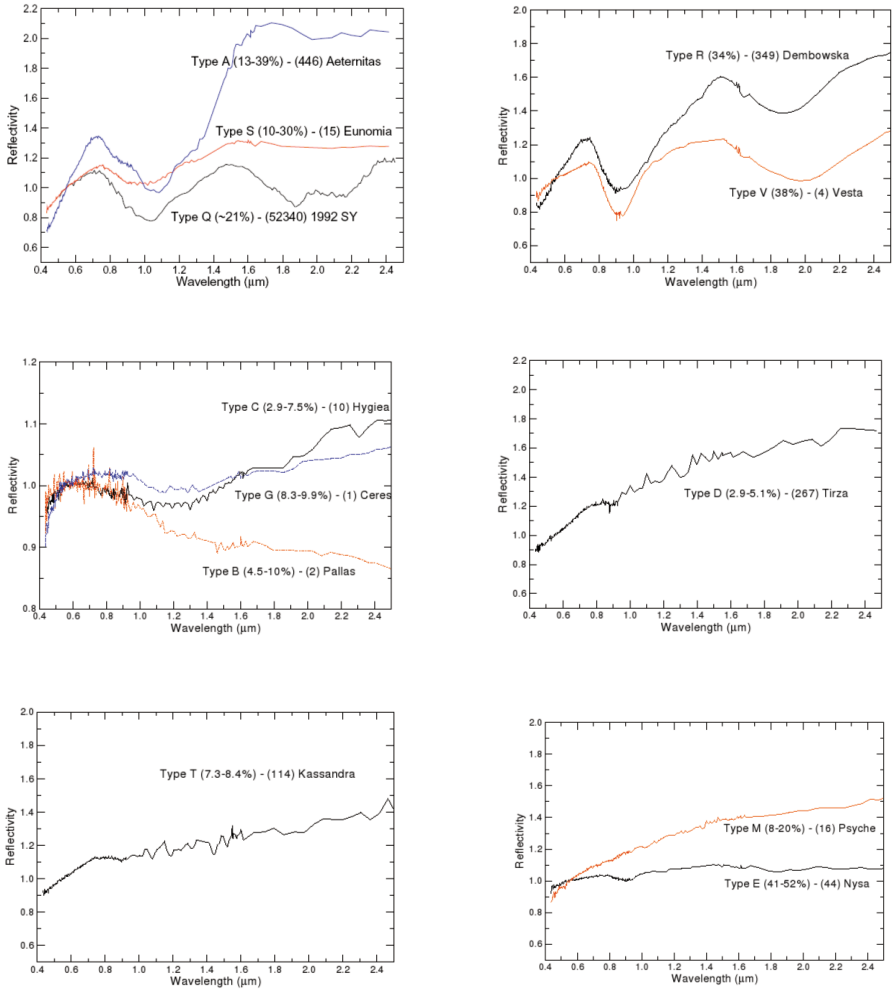

Figure 1.5: Typical spectra of different classes of asteroid types (Magrin, 2006) based on Tholen taxonomy (1989).

by two strong symmetric absorption features centered near 1 and 2 μm, with a weaker feature near 1.2-1.3 μm.

class R: R-types reflectance spectra exhibits strong 1 and 2 μm absorption features similar to those of V-types. The features are broadened toward longer wavelength while the 2 μm feature is narrower and centered at shorter wavelength.

class C (B,F,G,P): The C-class asteroids have nearly featureless spectra longward of 0.4 μm, but have different UV absorption intensity. Within this set, several subclasses have been distinguished, namely C, B, F, G and P. The P-class has no UV absorption feature and a reddish spectrum, the F-class has a weak one, the B- and C-classes have a slightly stronger one, and the G-class has the strongest UV absorption edge of the C-group. Other important features observed in C-class spectra are the absorption at 3 μm and 0.7 μm, significant of hydration. The C-types are usually thought to represent dark and primitive objects.

class D: The spectra of the D-asteroids are generally featureless with neutral to slightly red spectra shortward of 0.55 μm, and very red spectra longward of 0.55 μm. More than 60% of known Trojans are D-types.

class T: T-asteroids have low albedos (< 0.10) with spectra that are slightly red shortward of 0.85 μm. They are probably made by highly altered (either thermally or aqueously) carbonaceous material and also by physical mixture of S and C-type material.

class M: The M-type asteroids have reddened and weakly featured spectral reflectance curves, similar in shape to those of the E and P-asteroids, but have albedos intermediate between the E and P-classes. These asteroids are generally thought to be exposed metallic cores of differentiated parent bodies which suffered catastrophic disruption.

class E: As M and P types, E-asteroids exhibit featureless or very weakly featured flat to slightly reddish spectra but they have high albedo (average $\simeq 0.44$), which distinguishes them from the M and P. E-types are probably made by very iron-poor or iron-free silicate (e.g. enstatite, forsterite or feldspar). Three different subgroups of E-type asteroids are identified by their spectral properties (Fornasier et al., 2008). Some asteroids in particular, show an absorption band centered at 0.49 μm (Fornasier and Lazzarin, 2001)

considered distinctive for EII subtype. Steins, first asteroids visited by Rosetta, is a small Main Belt E-type asteroid.

Bus and Binzel (2002a, 2002b) introduced a new asteroid classification based on the robust Tholen system. They defined three major groups (the S-, C-, and X-complexes) in agreement with Tholen's definition of the S-, C-, and X-type asteroids. A total of 26 classes were defined, based on the presence or absence of specific spectral features. One of the originality is that asteroids with intermediate spectral characteristics are assigned multi-letter designations.

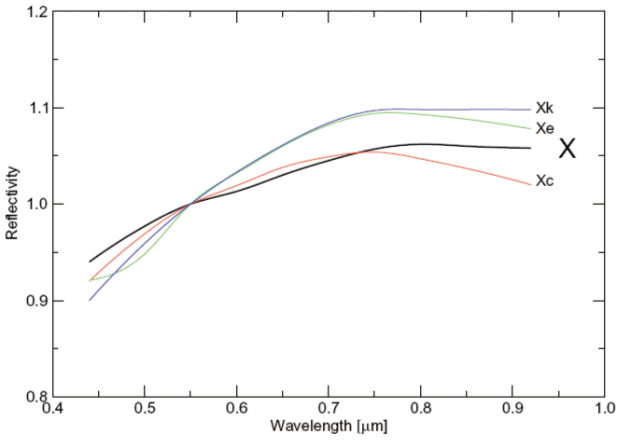

Figure 1.6: X-complex typical spectra as for Bus and Binzel classification (Magrin, 2006).

In particular X-complex refers to generally featureless spectrum, with slight to moderately reddish slope, a weak UV absorption feature, shortward of 0.55 μm, and an occasional shallow absorption feature longward of 0.85 μm and includes Xc, Xe and Xk subgroups. Xc-types show a slightly reddish spectrum with a subtle convex curvature over the middle and red portions of the spectrum. Xe-types show a slightly to moderately red overall slope with a series of weak absorption shortward of 0.55 μm. They have a concave-up curvature, most visible in the spectrum of 64 Angelina, where the band center is located at about 0.49 μm. Xk-types have moderately red slope, shortward of about 0.75 μm, and generally flat longward of 0.75 μm, the change in slope occurring very gradually. They are similar in spectral shape to Xc, but redder in overall slope.

With the advent of near-infrared instrumentation, an increasing number of asteroids had available spectra covering the entire range 0.45-2.45 μm. Hence, DeMeo et al. (2009) extended the Bus and Binzel taxonomy into the near-infrared, ending up with 24 classes constructed using the principal component analysis. Fig. 1.7 displays the average spectrum for each of the 24 class in this taxonomy.

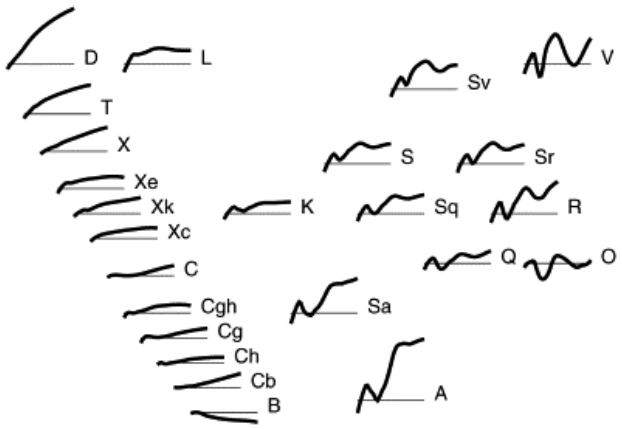

Figure 1.7: Average spectra of the 24 classes of DeMeo et al. (2009) extension of asteroids taxonomy to near-infrared.

Effects of physical parameters on spectra

Spectra of asteroids are thus mainly indicative of the chemical and mineralogical composition. However there are many physical parameters that also influence the spectra (Pieters and Englert, 1993).

The regolith particles size affects the overall brightness of the asteroid, that is the albedo, as seen in Sec. 1.3.3, but it also influences the intensities of absorption features in the spectra of minerals.
For transparent or weakly absorbing materials, a decrease in particle size increases the number of reflecting boundaries inside the material, causing a decrease in absorption and an increase of the scattered fraction of light.
Differently, in very strongly absorbing opaque materials, where the specular reflection is predominant as respect to diffuse reflection, a decrease in the particle size tends to decrease the total amount of reflected light, allowing the light to penetrate more in the material and being absorbed.
In a distribution of particle sizes, the small particles dominate because they

tend to coat larger particles.
Particle size will not affect, however, the positions of the absorption features.

The porosity also affects the spectral brightness and in particular the band contrast since the scattering process strongly depends on the incoming wavelength.

The viewing geometry is another parameter influencing the appearance of the observed spectrum. In particular the phase angle is known to influence the slope of the spectrum causing an increased steepness with the increase of phase angle. The spectral slope of the ordinary chondrites spectra shows also a significant increase with increasing phase angle (Sanchez et al., 2012). This effect is known as *phase reddening* (see Sec. 4.5) and its explanation is not yet satisfactory. Moreover, the analysis of visible and near-infrared spectra of NEA observed at different phase angles revealed also an increase of band depths with increasing phase angles (Sanchez et al., 2012) which is retrieved also in laboratory experiments on meteorites.

Another effect influencing the spectrum is the *space weathering*. It is the result of a continuous exposition of the surface of asteroids to the space ambient, i.e. to solar irradiation, cosmic rays, collisions, micrometeorites impacts and so on.
This exposition is found to cause a series of effects on spectra, such as changes in albedo, band depths and spectral slope.
Although the general trend seems to be the increase of the spectral slope, the reddening rates decreases, passing from the S-complex to the X-complex to C-complex, and there are evidences of slope-exposure anticorrelation among some C-complex families (Lazzarin et al., 2006).

On the other side, some mechanisms have been suggested to be responsible for the freshening of the surfaces which would change significantly the spectral appearance. These mechanisms are tidal effects from close planetary encounters, YORP spinup, asteroid collisions, electrostatic levitation of grains from passing through Earth's magnetosphere, etc. Earth's tidal forces due to close Earth encounters are thought to be the dominant mechanisms for surface refreshing (Nesvorný et al., 2005). Mars encounters are likely to play also an important role in refreshing (DeMeo et al., 2013).

1.4 Comets

There are evidences that numerous comets had been seen in the antiquity for millennia. For example a comet noted in Chinese records in the year 69 B.C. has been recognized to be the 109P/Swift-Tuttle (Yau et al., 1994), which most recently passed perihelion in 1992. However, it is only in the last 400 years that comets have been generally accepted as astronomical, as opposed to atmospheric, phenomena (e.g. Bailey et al., 1990; Yeomans, 1991).

Nevertheless, the real nature of these "phenomena" has been unclear until the beginning of 18th century when Edmond Halley understood that comets are solid bodies that belong to the Solar System.
He used the Newtonian mechanics to show that the comets which appeared in 1531, 1607 and 1682 were the same returning comet with a period of about 75.5 years.
Furthermore he noticed a time delay in the perihelion passages, and interpreted it as the consequence of the cometary orbit perturbation caused by the planets Jupiter and Saturn.
Hubble predicted that the same comet would have returned in 1758-9. It actually returned and had its next perihelion on 13 March 1759, but Halley, unfortunately, did not live enough to witness the validation of his theory. Thereafter the comet was named after him and, three perihelions afterward, it became the primary target of the first successful space mission dedicated to a comet, the European Giotto mission (see Sec. 2.2).

In recent times more and more fainter comets are being discovered due to vast improvement in the observational techniques and also thanks to several systematic search programs. The newly discovered comets are around 12 to 15 per year. As of July 2013, there are 4 894 comets known, of which 294 are numbered and have a well defined orbit.
(http://www.johnstonsarchive.net/astro/sslist.html)

1.4.1 Physical properties

The very spectacular exhibition of a comet is actually produced by a very small *nucleus* made up of rocky and icy materials. When such a nucleus passes close to the Sun, it is heated up, the volatile materials sublimate and begin to outgas. This causes the formation of a very extended spherical atmosphere, called *coma*. As the solar radiation and the solar wind interact with the coma, they pushes away the materials in the coma giving rises to the *tail*. When the coma and the tail are present, the comet is said "active".

Cometary nuclei are very small objects of the Solar System and when

they are far from perihelion, the Sun is not capable to heat up the volatiles and make them outgas, thus the coma and tail are not present and the brightness of the comet is due only to the sunlight reflected from the nucleus, exactly as it is for the asteroids.

When the nucleus come close to the Sun the coma and tail are sustained by the solar irradiation, they are much larger than the small nucleus itself and their brightness far dominates the nucleus reflectance.

The nucleus

In 1950 Whipple suggested that the cometary nuclei were made of icy conglomerates or "dirty snowballs", as opposed to the preceding model which considered comets nuclei as swarm of small solid particles not gravitationally bounded, called "sandbanks"(Levin, 1943; Lyttleton, 1948).

The Whipple's model was confirmed long afterward by the Giotto spacecraft in 1986 when it visited the comet Halley and obtained detailed pictures of its nucleus (see Sec. 2.2).

Comet nuclei range from a few hundred meters to tens of kilometers across and are composed of loose collections of ice, dust, and small rocky particles. The ices are primarily solid water, methane, ammonia and carbon dioxide. The dust and rocky materials are though to be made of two major components: silicate refractory dust particles and carbonaceous materials.

It is believed that cometary nuclei are homogeneous and not differentiated apart form the very external layer of the oldest comets which, after several perihelion passages, may have been depleted in volatiles and be more similar to a solid crust than to the interior of the nucleus.

Cometary nuclei, as well as asteroids, appear to be very weakly bounded, with high porosity and low density. This is usually called a *rubble pile* object, as opposed to a "monolith", meaning that it consists not of a single rocky body but rather of numerous pieces of rocks. They have low density and high porosity due to the large cavities between the various chunks. Comets are thus considered rubble piles of icy planetesimals which have been collisionally processed.

This idea is supported by various arguments. The estimate of the nuclear density strongly suggests that nuclei contain substantial macroscopic voids. It results indeed that comets, like asteroids, are "under-dense" compared with their constituent materials. It is defined *grain density*, ρ_g, the mass of an object divided by the volume that is occupied by solid grains. It is named instead *bulk density*, ρ_b, the total mass of the object divided by its total volume, including voids. The *porosity*, p, of an object is thus defined

as:

$$p = \frac{1 - \rho_b}{\rho_g} \tag{1.3}$$

Generally, only the bulk density can be measured from independent estimates of the volume and the mass. The volume is obtained from the direct imaging, assuming a typical albedo, while the mass estimate is obtained from the modeling of rocket effect (see Sec. 1.4.2) and the measure of non-gravitational forces acting on the comet. The bulk density of cometary nuclei results to be in the range $0.5 - 1.2$ g cm^{-3} (Weissman et al., 2004), which, compared to the typical density of water, 1 g cm^{-3} and of silicate or carbonaceous material, abut $2 - 3$ g cm^{-3}, shows clearly that there are macro voids inside the comets. It is more complicated to estimate, instead, the porosity, since it requires the knowledge of the grain density. Assuming Greenberg's (1998) grain density for cometary materials, it results that a comet with bulk density of about 0.6 g cm^{-3} would have a porosity of about 64%.

However, the strongest observational evidence for cometary nuclei as rubble piles comes from observations of disrupted or split comets. Comet LINEAR, D/1999 S4, for example, was observed to disrupt completely as it passed through perihelion in July 2000 (Weaver et al., 2001). There was evidence that the fragments continued to split over time, suggesting that the splitting events do not always lead to total disruption of the nucleus.
For example, comet 73P/Schwassmann-Wachmann 3 has been observed to shed fragments on at least two perihelion passages, yet it still returns every 5.4 years. In fact, the majority of fragmentation events involve one or more small fragments breaking off the main nucleus, and the latter surviving the event. The fragmentation during the perihelion passages is due to the tidal force of the Sun, which has been used by Öpik (1966) to estimate the nuclei strengths, resulting in the range $10^4 - 10^6$ dynes cm^{-2}.

There are also other fragmentation and splitting events not correlated with perihelion passages, nor with passages close to a giant planet. There is at present no final explanation of these random splitting events. One proposed mechanism by Samarasinha (1999) is the gas pressure release from volatile pockets. Weissman et al. (2003) proposed the rotational spin-up due to asymmetric outgassing forces as a likely cause, which is supported by the fast rotation of many comet nuclei. The derived rotation periods range indeed from 5.2 to 29.8 hours (Weissman et al., 2004).

Regardless of the mechanism and of the cause, it seems clear that nuclei are fragile objects and this supports the theory that comets are rubble piles.

It was believed that the overall surface of the nucleus was responsible for

the outgassing and the formation of the coma. However, from the Halley encounter it has been detected that not all the nucleus surface is actually responsible for the outgassing. There are only some regions, called *active regions*, distinguishable on the surface, which account for the formation of the coma and tail releasing dust and gas. What makes a region active or inactive is still to be well understood, for example, if there is any compositional, or topographic characterizing feature, and it constitutes one of the still unanswered fundamental questions on comets.

The presence of inactive regions on the surface of comets have been tentatively explained by the theory of the refractory mantle. It is believed that during the perihelion passages, the volatile materials on the surface sublimate leaving the bigger refractory particles on the surface. These are probably lift off by the outgassing but then they fall back onto the surface in a random way, composing a sort of rocky mantle which covers the volatiles underneath preventing them to sublimate possibly in some regions. This theory may explain also the decrease of the activity of the comet in successive perihelion passages and the asymmetry of its brightness before and after perihelion. It may also explain the total dead of a comet which may end with an inert nucleus leftover.

The coma

When the comet comes close to the Sun, this warms the nucleus and the evaporation of the volatiles starts, thus the coma develops around the nucleus.

The coma is made up essentially of two constituents: the gas component and the solid (dusty and icy grains) component.

The source of the gas component is primarily the direct sublimation of ices on the nucleus, not only from the surface, but also from subsurface layers (Prialnik et al., 2004). However it seems that a considerable fraction of the gas is also emitted from the sublimation of icy grains that are also present in the coma.

The direct products of the sublimation of ices, usually water ice, carbon dioxide, methane, ammonia, and other complex molecules, are called *parent molecules*. From these parent molecules, through photodissociation, photoionization and many other chemical reactions occurring in the coma, other simpler molecules are released, which are called *daughter molecules*, usually neutral radicals such as CO, CN, C_2, OH, CH, NH_2 etc. Ultimately radical ions are produced such as CO^+, CH^+, CO_2^+, OH^+, and, at very large distances from the nucleus of 10^6-10^7 km, the neutral coma is finally broken down into its atomic constituents, such as O, H, C, N, Na, Si, Ca etc.

It is custom to divide the coma into three main regions: the *inner coma*, which is the parent molecules production zone, with a typical diameter of 10^4 km; the *visible coma*, that is the expansion zone of the species produced, about 10^5 km; and the *atomic coma*, where the photoionization and charge exchange with the solar wind occur, and ranges from 10^5 to 10^7 km.

The dominant volatile component is water ice, while the other volatiles, such as CO, CO_2, HCN, N_2, etc., are mixed with the water ice or incorporated in it, either in the form of clathrate-hydrates, or as trapped gases within the (amorphous) ice matrix. Having been formed at low temperatures and pressures, cometary ice is indeed believed to be amorphous (Mekler and Podolak, 1994).

Different ices sublimate at different heliocentric distances. Usually CO_2 is the first to sublimate at large distances. As the comet comes closer to the Sun, the water ice starts to sublimate and becomes the driver for the other ices due to its high abundance in the nucleus. Water dominates up to ∼90% of the volatile species that outflow from the cometary nucleus within ∼3-4 AU from the Sun (Combi et al., 2004), apart some exception such as comet Hartley 2 observed by EPOXI mission (see Sec. 2.4) whose activity seems to be driven mainly by CO_2 (A'Hearn et al., 2011).

Hence the photochemistry of water, and of the other ices, including the photodestruction rates, the branching ratios, and the velocity states of the dissociation products are of great importance in the interpretation of the gas coma structure and a deep knowledge of this processes is essential for the understanding of the physics of comets.

These processes are usually also depending on the solar radiation field which triggers them, in particular they are affected by the time variability of the extreme and far UV fluxes from the Sun which causes changes in the dissociation and ionization rates of water and its daughter products.

The solid component of the coma is made up of icy grains and dust material, often mixed together to form a very complex swarm of particles. Both icy and dust grains come from the nucleus and are thought to be raised by the sublimation of the gas which lifts up the light grains from the surface and subsurface. The dust was though to be only some form of silicate, but in situ measurements revealed that other major components of the grains are the CHON particles, made up of Carbon, Hydrogen, Oxygen and Nitrogen.

The coma is not gravitationally bound to the nucleus, thus it is a transient phenomenon rapidly changing as function of the comet's orbit and distance from the Sun. However, since sublimation from the nucleus surface is constantly replenishing the outflowing gas and dust, the coma appears stable and unchanging.

Initially the dust is coupled with the gas and it is totally driven by its outflow. The gas expands and cools down almost adiabatically and, at scales of ∼100 km the dust becomes collisionally decoupled from the gas. Here the gas flows with a speed of ∼700 m s^{-1} and has a cool temperature of less than 30 K (Combi et al., 2004).

Our knowledge of the composition and structure of comets has come primarily from studies of the coma since its brightness is far dominant when the comet is active and it is otherwise very difficult to study comets nuclei when they are not active and thus very far from the Sun. However, what is eventually important is to understand the nature of the cometary nucleus. This requires therefore the interpretation of the complex physical and chemical processes that occur in the coma, in particular in the inner coma, and of the interrelation existing between the coma and the nucleus. This, in turn, strongly requires complex physical and chemical models of the coma, beyond detailed resolved observations and in-situ analysis.

Reproducing the distribution and the production of parent molecules from the observations of the daughter molecules for example requires detailed physical models of the gas dynamics and chemical models of the reactions occurring in the very near-nucleus region. The chemistry and the physics are indeed intimately coupled in this environment and detailed models should include both.

The first simple analytical model of the molecules distribution in the coma was published by Haser (1957) in a now classic formulation that is still widely used today; photodaughters distributions in the coma was later modeled using the vectorial model of Festou (1981). These models will be described more in detail in Chapter 5 together with the description of the photochemistry of water and of the fluorescence mechanisms in the coma that will be used in Chapter 6 for the photometric analysis of Hartley 2 coma observations.

The tail

The comet's tail usually visible in the sky as yellow-colored is the *dust tail*, which is made visible through the scattering of the solar radiation by dust particles. The dust tail extends up to about 10^7 km and is generated by the radiation pressure of the Sun which pushes the dust particles in the direction away from the Sun. Since they lag behind as they stream away from the Sun, they take a typical curved path.

The solar radiation also breaks up the parent and daughter molecules, released by the nucleus in the coma, and ionizes them. The ionized gas is

swept outwards by a stream of charged particles present in the solar wind. This gives rise to an *ion* or *plasma tail* which extends in the antisolar direction up to about 10^7 to 10^8 km.
The plasma tail is mainly made up of ions like H_2O^+, CO^+, CO_2^+ , N_2^+. The emission due to CO^+ is dominant and since it lies in the blue spectral region, the ion tail appears blue. Differently from the dust tail, the ion tail is instead straight, not being influenced by solar radiation pressure.

Many comets generally show a short tail in the solar direction which is called the *anti-tail*. The anti-tail really does not point towards the Sun but its apparent direction depends on the geometry of the Sun-comet-Earth system. It can be seen clearly only when the orbit of the comet cuts the orbital plane of the Earth.

A narrow, straight and long tail superposed over the dust tail composed of sodium atoms has been also observed in bright comets as Hale-Bopp (Cremonese et al., 1997) and Hyakutake. The straight *sodium tail* could arise from the dissociation of some molecules containing sodium which is then dragged out due to radiation pressure.

1.4.2 Dynamical properties

When inactive, comets behave dynamically exactly as asteroids, in the sense that they are influenced by the same processes which govern the asteroids dynamics such as the resonances, Sun's radiation pressure, Yarkovsky and YORP effects, Poynting-Robertson effect, gas-drag, collisions and fragmentation processes (see Sec.1.3.2).
However, comets are affected by many other processes when they are active, in particular at the perihelion. The most important effect is the so-called *rocket-effect*, due to the gas release in the anti-solar direction, which accelerates the comet in the direction of the orbital motion. Another effect is due to the mass depletion at each perihelion, which may change the gravitational behavior of the body.

Comets have a very wide dynamical distribution in orbital periods, eccentricities and inclinations in the Solar System. Unlike asteroids, they are believed to have formed in the outer Solar System, beyond the condensation zone of the volatiles, called snow-line (Hayashi, 1981), where the temperature was below 170 K.

They reside presently in two main cold reservoirs: the *Kuiper Belt* disk-like structure beyond Neptune at $\sim$ 36-48 AU from the Sun (Morbidelli, 2008), and the isotropic, quasi-spherical *Oort cloud*, at 10 000-50 000 AU (Wiegert and Tremaine,1999).

It is believed that gravitational interactions with the giant planets injects comets from the Kuiper Belt in the inner Solar System into elongated orbits (Levison and Duncan, 1997). Furthermore tidal effects from the mass distribution of the Galaxy, sporadic passing stars, and giant molecular clouds (Wiegert and Tremaine, 1999) act on the Oort cloud comets in the same way and modify their perihelion causing them to jump into the inner Solar System. These perturbations do not modify usually the inclination, thus the comets coming from the Oort cloud remain distinguishable by their high inclination orbits.

The Kuiper Belt is believed to be an original remnant of the Solar System formation process which left non-aggregated material in a disk-like structure. It appears to have an outer edge at ∼50 AU from the Sun. 1992 QB1 was the first object observed beyond the orbit of Neptune and the precursor of this totally new class of objects called trans-neptunian objects (see Sec. 1.3.2).

The Oort Cloud formation appears more complex and less clear than the Kuiper Belt formation. It is possible that giant planets perturbations pumped up the orbital energy and then the semimajor axis, of some original planetesimals, but their perihelion distance would have remained nearly constant. However if the presence of stars and other matter in the solar neighborhood provided a stabilizing mechanism, comets perihelion would also be raised up still remaining gravitationally bounded to the Solar System. Since trajectories of the stars are randomly oriented in space, stellar perturbations would have caused comets to attain a nearly isotropic velocity distribution (Dones et al., 2004), such as the Oort Cloud.
Thus from this scenario it results that even if Oort Cloud comets are presently further away from the Sun, they actually formed in the regions of giant planets, hence closer to the Sun as respect to Kuiper Belt objects, which probably formed in the same place where they are presently.

The population of comets in the Oort Cloud is estimated to be about $5 - 10 \cdot 10^{11}$ objects larger than 2.3 km, based on observations of long-period comets injected in the inner Solar System (Dones et al., 2004). Recent studies suggest that a further inner Oort cloud exist, in the gap between the Kuiper Belt outer edge and the Oort Cloud inner edge. Recent simulations suggest that its population may be comparable to that of the outer Oort cloud (Dones et al., 2004), but more realistic simulations are needed. The Oort Cloud remains one of the most poorly explored regions of the Solar System.

Recently discovered Main Belt Comets (MBCs) form a distinct class, orbiting in more circular orbits within the Main Asteroid Belt (Bertini, 2011). 133P/Elst-Pizarro is the first discovered and the best characterized member

of MBCs, being the proto-type of this new class.

Dynamical classification

Comets have been historically classified according to their orbital periods (See Fig. 1.8, Levison, 1996).
A general distinction exists between *short-period* and *long-period* comets. The division is defined by a boundary of 200-years orbital period. This has a main historical reason since orbit determinations have been reliable for about 200 years, thus it is possible to link any comet with period shorter than 200 years with previous apparitions.

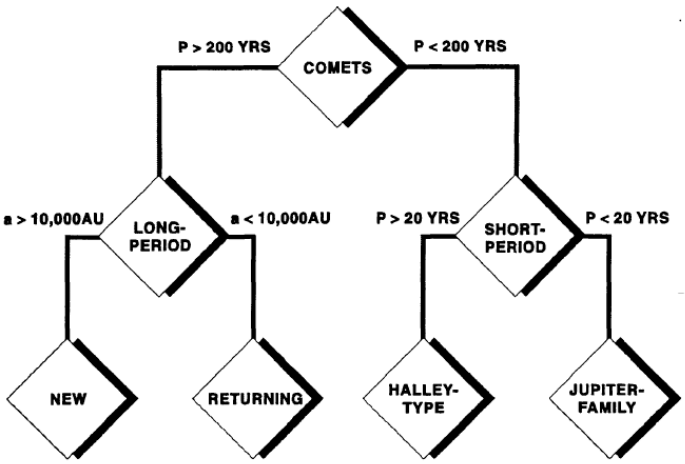

Figure 1.8: Historic comets classification (Levison, 1996).

Short-period comets are further divided into two groups. Comets with orbital periods shorter than 20 years and low inclinations (up to 30°) are called *Jupiter-family comets*. Indeed these comets have a strong concentration of semi-major axis between 3 and 4 AU and tend to have the aphelion close to the orbit of Jupiter. Since they have small encounter velocities with it, they are dynamically dominated by the planet. The observed Jupiter-family comets have a very flat inclination distribution and are on prograde orbits. Those with orbital periods between 20 and 200 years and inclinations extending from 0° to more than 90°, are called *Halley-type comets*. They have mean inclination of 41° and several of them are on retrograde orbits.
As of 2013, only 72 Halley-type comets have been observed, compared to 470 identified Jupiter-family comets.

Long-period comets have periods ranging from 200 years to thousands or even millions of years and have highly eccentric orbits. The orbits of long-period comets take them far beyond the outer planets at aphelia, and the plane of their orbits do not lie near the ecliptic. Long-period comets such as comet West (C/1975 V1) and C/1999 F1 can have apoapsis distances of nearly 70 000 AU with orbital periods estimated around 6 million years.
Long-period comets have been also further divided into two major groups, based on the value of their semi-major axis. It is considered unlikely that a comet that has semi-major axis greater than about 10 000 at the first passage in the inner Solar System would have the same semi-major axis at successive passages (Levison, 1996). Hence, a long-period comet with $a \gtrsim 10\,000$ is considered a *dynamically new* comet. Comets with $a \ll 10\,000$ are most likely objects that have been through the planetary system before and are called *returning* comets. Probably they were also initially new but have evolved to smaller semi-major axis during previous passages through the planetary system.

Single-apparition or non-periodic comets are similar to long-period comets because they also have parabolic or slightly hyperbolic trajectories when near perihelion in the inner Solar System.

However, the arbitrary boundaries present in the standard classification drove Levison (1996) to propose a new classification (see Fig. 1.9) based mainly on *Tisserand's parameter*.
Tisserand's parameter (or Tisserand's invariant) is a combination of orbital elements used in a restricted three-body problem. For a small body with semi-major axis a, eccentricity e, and inclination i, relative to the orbit of a perturbing larger body, mainly Jupiter, with semi-major axis a_J, the Tisserand parameter is defined as follows:

$$T_J = \frac{a_J}{a} + 2\left[(1-e^2)\frac{a}{a_J}\right]^{1/2}\cos(i) \tag{1.4}$$

It is an approximation of the Jacobi constant, hence it is quasi-conserved in the three body problem.

The new classification states that comets with $T_J > 2$ are defined *ecliptic* sine they have small inclinations, and comets with $T_J < 2$ are designated as *nearly isotropic* comets, reflecting their inclination distribution.

Ecliptic comets are then divided into three groups: comets with $2 < T_J < 3$ are called *Jupiter-crossing* or *Jupiter family* comets and are dynamically dominated by the planet. Comets with $T_J > 3$ are instead designed as *Encke-type* if $a < a_J$ (the orbit is interior to Jupiter) and *Chiron-type* if

$a > a_J$ (the orbit is exterior to Jupiter).

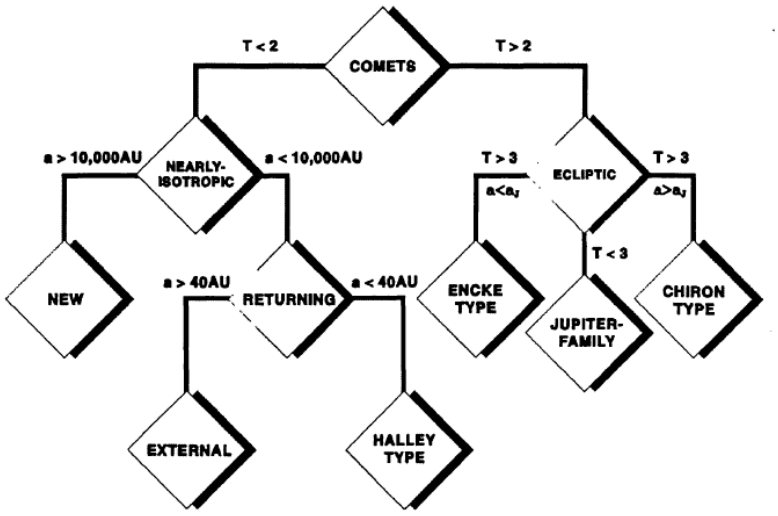

Figure 1.9: New comets classification based on the Tisserand's parameter (Levison, 1996).

The nearly-isotropic objects are also subdivided in two groups: *new* and *returning* comets. The new comets are designed, as before, based on their semi-major axis being $a \gtrsim 10\,000$ AU, while the returning group is further divided in two subgroups: the *external* comets and the *Halley-type* comets. Those which have a semi-major axis small enough to be trapped in a mean motion resonance with a giant planet are designed as *Halley-type* comets while those that have semi-major axis larger than this are named *external* comets. The proposed boundary between the two groups is the semi-major axis of Pluto: 40 AU.

This new classification, based on more objective parameters, is presently the most used one.

The Kuiper Belt or more properly its associated Scattered Disk is considered to be the supplier of the so-called Jupiter family comets. The Oort Cloud is instead considered the reservoir of the Halley type and long-period comets (Wiegert and Tremaine, 1999, and references therein).

1.4.3 Photometric properties

Two main processes are responsible for the comets brightness in the visible observing range. The nucleus surface and the dust particles in the coma partially reflect and scatter the continuum light coming from the Sun, while the gas present in the coma is excited by absorbing sunlight and is de-excited by re-emitting photons at well-defined wavelengths, producing strong emission bands.

When the comet is active and close to the Sun, the coma dust and gas brightness is far prevailing the nucleus reflectance while when it is far away from the Sun, the coma does not exist and the total brightness is due only to the nucleus reflectance, as it is for asteroids.

To perform photometric analysis of active comets is very challenging since it is necessary to disentangle the different components of the luminosity in order to interpret them. Hence to measure the dust flux it is needed an accurate removal of the gas emission, and, on the other hand, to measure the gas emission is necessary to subtract the continuum flux from the dust. Therefore a careful calibration of both the continuum and the emissions is required.

A useful quantity to describe the continuum flux of the dust coma was introduced by A'Hearn et al. (1984). The quantity, called $A_B(\alpha)f\rho$, is the product of the Bond albedo, at a particular phase angle α, the filling factor f, and the projected aperture radius ρ, as seen on the sky plane. The filling factor is defined as the total cross section of grains within the field of view $N(\rho)\sigma$, divided by the area of the field of view $\pi\rho^2$, where σ is the cross section of a single grain (A'Hearn et al., 1984). The product A_Bf is determined directly from observations and the two factors can not be disentangled. $A_B(\alpha)f\rho$ is independent of the aperture size if the dust follows a canonical $1/\rho$ spatial profile for outflowing dust and is independent of the wavelength if the dust has no color as respect to the Sun. It is often used to derive the production rate of the dust in the cometary atmosphere.
The dust, however, may exhibit some color variation with time and/or spatial distribution, as respect to solar radiation, suggesting differences in grain sizes or even in composition.

The gas emissions are very strong usually when the comet is close to the Sun and active. Daughter molecules are responsible for emission bands in the visible range, while in the radio and IR range, parent molecule emissions becomes observable. With the help of a set of narrow-band filters, selected especially for comets (Farnham et al., 2000), it is possible to study the daughter molecules abundances and thus derive, using appropriate models,

the production rates of the parent molecules. Gas flux has usually a flatter radial profile as respect to dust, because it expands more rapidly than do dust particles. The conversion of an observed flux into molecular abundance require the awareness of the physical process responsible for the light emission, typically fluorescence, and the knowledge of its principal parameters. Coma production models needs also to be applied, in particular Haser or vectorial models (see Sec. 5.1), or the more advanced Monte-Carlo simulations, in order to retrieve information on the parent molecule emitted by the nucleus.

The comparison between gas and dust abundances and distributions is also an important tool to understand the relative composition of molecules in the coma and in the nucleus.

Resolved photometry allows to analyze detailed features in the coma. Indeed many comets exhibit well-defined structures both in dust and gas coma (Schleicher and Farnham, 2004). Some types of features observed include jets (collimated radial stream of gas and dust), fans (broader and more diffuse jet-like structures), spirals and arcs (outflowing material that form total or partial segments of spirals) and coma asymmetries (some regions appear brighter than others). The presence of those features indicates that the surfaces of the nuclei are not uniformly active but emit material anisotropically. The quantitative study of these features is essential to understand the processes responsible for their production, the strengths of different source regions, the amount of material released and so on.

The observed time variation of the coma brightness reflects mainly variation in the activity of the comet unlike the light curve of asteroids that was correlated with the nucleus rotation and with the shape of the asteroid. In a way the variation of the brightness of the coma is also related with the rotation of the cometary nucleus but in the sense that the activity of the comets varies as the active regions are exposed to the sunlight or are in the dusk hemisphere due to the rotation of the nucleus. Thus the brightness variation can be used also to infer the number, position, and relative strengths of individual active regions on the surface of the nucleus.

1.4.4 Spectral properties

As the photometric observations, also the spectra of comets are characterized by two components, the continuum and the emissions. The continuum component is due to the reflection and scattering of the solar light by the dust particles in the coma, while the emission bands are produced by the gas excited by the sunlight in the coma.

The molecules, ions and atoms in the coma are excited by the absorption

of the solar radiation and produce, mainly for fluorescence (see Sec. 5.4), a series of emission bands in different wavelength ranges.

The emission lines from the constituent atoms such as H, O, C, N and S produced by the dissociation of the molecular species in the coma lie in the ultraviolet region of the spectrum together with bands from CS and CO the first parent molecule directly detected spectroscopically (Feldman and Brune, 1976).

In the optical region a series of emission bands of mainly daughter molecules appear roughly in a sequence as the comet approaches the Sun. The molecular bands first to appear are those of CN at $r \sim 3$ AU followed by the emissions from C_3 and NH_2 ($r \sim 2$ AU). Thereafter at $r \sim 1.5$ AU the emission from C_2 (Swan bands), CH, OH and NH appear in the spectrum. At $r < 1.5$ AU, emissions from ions CO^+, OH^+, N_2^+ and CH^+ appear. A strong forbidden doublets from [OI] is usually visible in the optical range. Emissions from Na, if present, appear around 0.8 AU. The relative intensity of emission bands and continuum varies from comet to comet.

In the visible, the Sun-grazing comet Keya-Seki C/1965 S1 showed also emission bands from metals K, Ca^+, Ca, Fe, V, Cr, Mn, Ni, Cu (Preston, 1967), probably from vaporization of refractory grains.

Neutrals:	H, C, O, S, Na, K, Ca, V, Cr, Mn, Fe, Co, Ni, Cu
	C_2, CH, CN, CO, CS, OH, NH, S_2, SO, H_2, C_3, NH_2
	H_2O, HCN, H_2S, CO_2, HNC, OCS, SO_2, CS_2, H_2CO
	NH_3, HNCO, H_2CS, CH_4, C_2H_2, C_2H_6, HCOOH
	HC_3N, CH_3CN, CH_3OH, CH_3CHO, NH_2CHO, $HCOOCH_3$
	$HOCH_2CH_2OH$, NH_2CH_2COOH
Ions:	C^+, CO^+, CH^+, CN^+, H_2O^+, HCO^+, H_3O^+, CO_2^+
Dust:	Silicate, CHON

Table 1.1: Some of the observed species in comets.

The infrared region of the spectrum is characterized by vibrational-rotational transitions of many molecules. Several bands of CN, many weak features of NH_2 and the Phillips bands of C_2 are present. A very high resolution spectrum would allow to resolve also the rotational structure of the bands.
The first and direct detection of H_2O in comet Halley came from the high resolution observation of the vibrational band at 2.7 μm with the Kuiper

Airborne Observatory.
In the 3 μm region strong emissions from hydrocarbons are present: methane (CH_4), acetylene (C_2H_2) and ethane (C_2H_6) bands can often be observed. However most of the observed features in this range are attributed to methanol (CH_3OH).
The CO_2 molecule can only be observed in the infrared region. It has indeed a very strong feature at 4.25 μm, but it cannot be observed from the ground because of strong absorption band from terrestrial CO_2. It has been detected for the first time in comet Halley and later on in many comets. CO molecule has also a strong emission band in the infrared range at 4.7 μm, clearly detected in Comet Hyakutake (C/1996 B2).
Polycyclic Aromatic Hydrocarbon molecules (PAHs) are commonly seen from interstellar medium near 3.28, 7.6 and 11.9 μm. Some of these features have been seen also in comet 9P/Tempel 1 from the observations carried out with Spitzer Space Observatory. Glycine (NH_2CH_2COOH), an amino acid has been detected for the first time in the dust particles of comet 81P/Wild 2.
The infrared observations in the region 1 - 30 μm of many comets have shown the presence of two strong broad emission features around 10 and 20 μm generally attributed to silicate materials.

Many large molecules have also been detected in cometary spectra through the millimeter and radio observations, such as HCN, H_2CO, H_2S, SO_2, HCOOH, H_2CS, HNC.

A summary of some of the atomic, ionized and molecular species observed in different wavelength ranges in cometary spectra is given in Tab. 1.1.

Chapter 2

Space missions to Comets and Asteroids

2.1 Ground-based observations versus space explorations

Ground based observations have provided a huge amount of data and a very big improvement in understanding asteroids and comets science. These observations are usually possible even with short notice, so they are very useful to study and monitor short-term variation events. They allow to investigate a big sample of objects, making possible statistical analysis, comparison and taxonomy studies.

However ground-based observations have strict limits on the maximum spatial and spectral resolution reachable, and on the viewing geometry. Even the best modern ground-based telescopes and the Earth-orbiting Hubble Space Telescope in fact, can resolve a small amount of details on the surfaces of just the largest asteroids, and most of them remain anyway indistinct points.

Much more information can be obtained from resolved images and high spatial resolution spectra. Close up observations allow to study the shape, size and structure of asteroids and cometary nuclei. It becomes possible to distinguish the details on the surface, to recognize craters and identify active regions and jets origin features. It allows to investigate different areas on the resolved disk and their photometric properties and analyze colors and albedo variations to identify different types of terrains and compositional heterogeneity. Going close to a comet allows to study and investigate the very innermost coma, which in invisible from Earth, and its composition and

chemical abundances, and to examine the interconnections between coma structures and nucleus features to understand the mechanisms that drive the cometary activity and its evolution. Space exploration may provide a much wider range of geometry configurations, allowing the study of the object from different viewing positions and varying illuminating conditions. Moreover comets are visible from Earth only when they become active, while a space exploration allows the study of the comet when it is still inactive and may even follow the onset of its activity while it comes close to the Sun, as it is expected from Rosetta mission (see Sec. 2.3).

These are the main reasons why the principal space agencies commissioned big amount of effort in space missions devoted to asteroids and comets. Those missions provided a great improvement in understanding those objects, giving answer to many fundamental questions, but they also reveled various unexpected aspects of these intriguing space bodies, giving rise to new questions and opening different issues.

2.2 History of Small Bodies Space Missions

The first close-up images of asteroid-like objects were taken in 1971 when the Mariner 9 probe imaged Phobos and Deimos, the two small moons of Mars, which are considered captured asteroids (see for example Pajola et al., 2013). These images revealed irregular shapes and small sizes.

However, the first true asteroid closely observed by a spacecraft was the S-type asteroid 951 Gaspra followed by 243 Ida and its moon Dactyl, both imaged by the Galileo probe during its journey to Jupiter, respectively in 1991 and 1993. Ida was the first asteroid found to possess a satellite of only 1.4 km diameter. Data returned from the flyby allowed to understand that S-type asteroids are the plausible source for the ordinary chondrite meteorites, the most common type found on Earth's surface.

The NEAR Shoemaker (Near Earth Asteroids Rendezvous) was the first asteroid-dedicated probe. In 1997 it passed by 253 Mathilde, the first C-type visited asteroid, but its final target was 433 Eros, the first discovered NEA, an S-type asteroid belonging to the Amor group (see Sec. 1.3.2). The spacecraft flew by Eros in 1998 and later in 2000 entered into orbit around it and one year later it made a slow controlled descent to its surface using maneuvering jets. Sixteen days later the last signal from NEAR was received before it definitely shut down.

In 1999 the technological-based mission Deep Space 1 briefly visited 9969 Braille, a 2-km sized Mars crosser asteroid, but a malfunction caused the

spacecraft to pass at more than 26 km from the surface and resulted in indistinct images. Fortunately this did not happen again for the second planned flyby with comet 19P/Borrelly which was a great success and returned extremely detailed images of the comet's surface.

The Stardust mission in 2002 used the asteroid 5535 Annefrank to practice the flyby technique that it would have used to its primary target: the comet 81P/Wild 2, visited two years later.

In September 2005, the Japanese Hayabusa probe landed on its target, the asteroid 25143 Itokawa, after a series of malfunctioning, and was able to gather minute particles from the surface during its 30-minutes stay on the asteroid. Hayabusa's samples capsule containing the captured particles reentered in Earth's atmosphere on 13 June 2010.

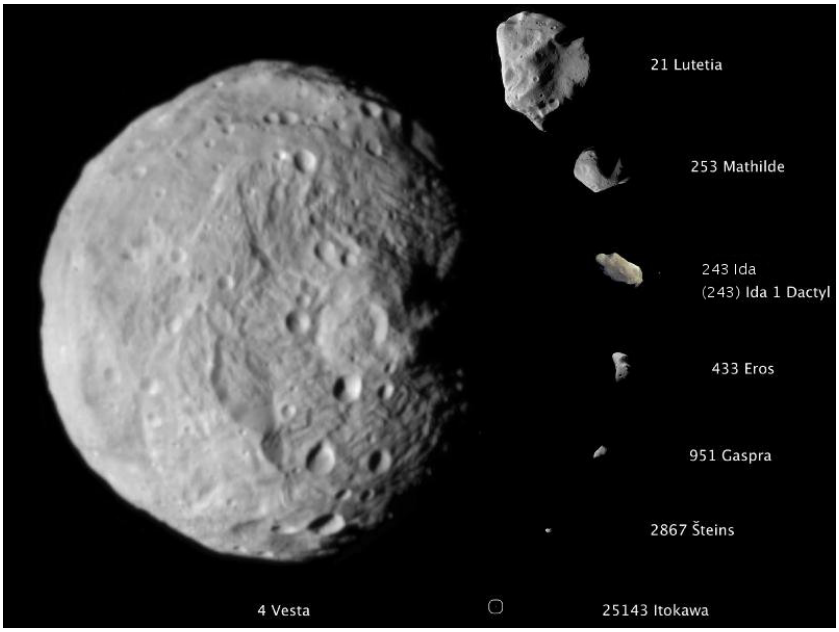

Figure 2.1: The collection of asteroids visited by spacecrafts pictured in scale.

The subsequent asteroid encounters were performed by the European spacecraft Rosetta (see Sec. 2.3) which visited the small E-type asteroid 2867 Steins on 5 September 2008 and the big Main Belt asteroid 21 Lutetia on 10 July 2010.

From July 2011 to September 2012 the NASA Dawn Mission, orbited the asteroid 4 Vesta, the biggest after the dwarf planet 1 Ceres, which is planned to be visited by the same spacecraft in 2015. 4 Vesta is by far the

largest asteroid visited up to date as clearly visible in Fig. 2.1 which shows a collection of some of the asteroids currently visited by spacecrafts, pictured in scale. As shown in the figure, the sample of asteroids encountered is very small but it is even smaller the sample of comets approached.

Since 1682, when Halley's identified and predicted its return, every 76 years, comet 1P/Halley's apparition in Earth's skies was strongly awaited, but it was exceptionally desired in 1986, when a populous spacecrafts's "armada" was designed and launched to approach it.
This comet was the subject of the most numerous and extensive space investigation occurred in such a short time period. During March 1986 six spacecrafts from various space agencies flew close to the comet when it was next to the closest approach to the Sun (Fig. 2.2). The Russian spacecrafts Vega 1 and 2 passed at distances of about 8 000 km from the nucleus, the Japanese spacecrafts Suisei and Sakigake were further away at about $1.5 \cdot 10^5$ km and $7 \cdot 10^6$ km respectively, and the American ICE (International Cometary Explorer) spacecraft passed at a distance of about 0.2 AU later in March 1986.

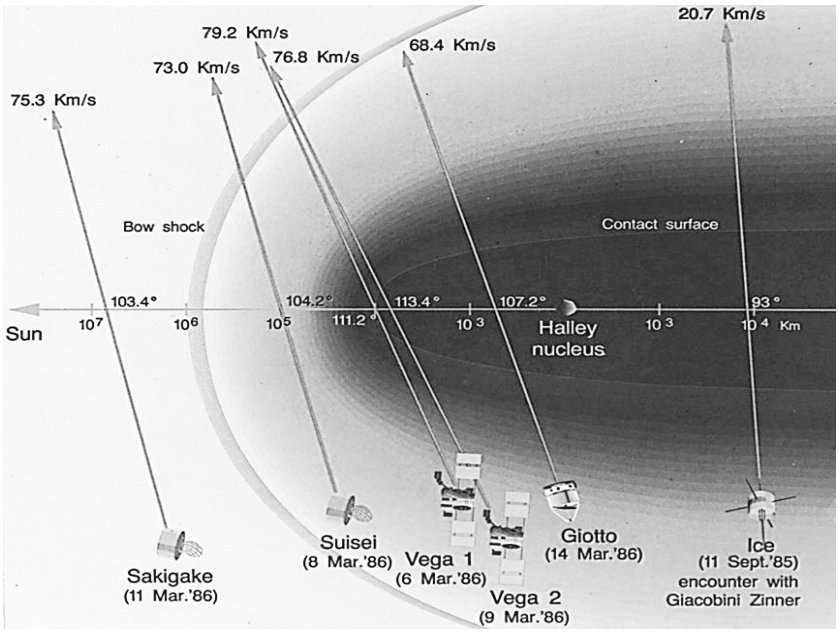

Figure 2.2: Halley's "armada" in 1986.

The closest one was the European Space Agency's spacecraft Giotto,

which passed at a distance of less than 600 km from the nucleus and obtained the most amazing and close up images of a cometary nucleus ever taken until then (Fig. 2.3), revealing, for the very first time, the real nature of a comet. The comet Halley, moves in a retrograde motion with respect to the planets, therefore the relative encounter velocity was very high, about 68 km/sec. A total of 2 000 images were transmitted to Earth from the onboard camera, the Halley Multicolor Camera, built with a big Italian contribute from Padova University.
Thanks to Giotto's images Whipple's model of "dirty snowballs" was finally accepted even though the "dirt" was found to be more important than the "snow". However, it was not seen, as expected, a spherical object, similar to a snowball, rather an elongated object, irregularly shaped, 15×10 km across, with a very dark surface and a very porous and low density structure. Luminous jets were identified to come out from the surface at a velocity of 3 tons per second but not all the nucleus was observed to be emitting, rather a small fraction of about 10% of the surface was considered "active". From later analysis it resulted that 80% of the volume emitted by the comet was composed of water but other volatiles as CO, CO_2, CH_4 and NH_3 were also found (Woods et al., 1986).

Figure 2.3: 1P/Halley's nucleus revealed in the closest image obtained by Giotto spacecraft in March 1986.

On 2 April 1986 the Giotto spacecraft was hibernated and 4 years later, in February 1990 the wake-up signal was sent to Giotto and in one week the full control of the spacecraft was established. It performed a gravity assist with the Earth and was later hibernated again for other 2 years. It was awaken again and, on 10 July 1992, realized another successful fly-by with

comet 26P/Grigg-Skjellerup passing within 200 km from its nucleus. Despite the Halley Multicolor Camera was destroyed during the 1986 encounter, the fly-by allowed numerous experiments for the study of flux of neutrals, ions, electrons and dust, magnetic field and waves, in the inner coma ambient.

The next encounter to a comet occurred when the spacecraft Deep Space 1, launched on 24 October 1998, more than eight years after the conclusion of Giotto mission, pictured the comet 19P/Borrelly on 22 September 2001 from a distance of 3 500 km.

Fragments of cometary material from comet 81P/Wild 2 were successfully brought back to Earth by the Stardust mission, the first big American comet-dedicated mission, launched on 1999, which encountered the comet Wild 2 on January 2004. Two years later, at 10:10 UT more than 2 000 particles of cometary dust of 50 μm on average, reentered the Earth's atmosphere and crashed in the Utah desert inside the Stardust capsule. This was the first time that laboratory studies were carried out on real cometary dust particles.

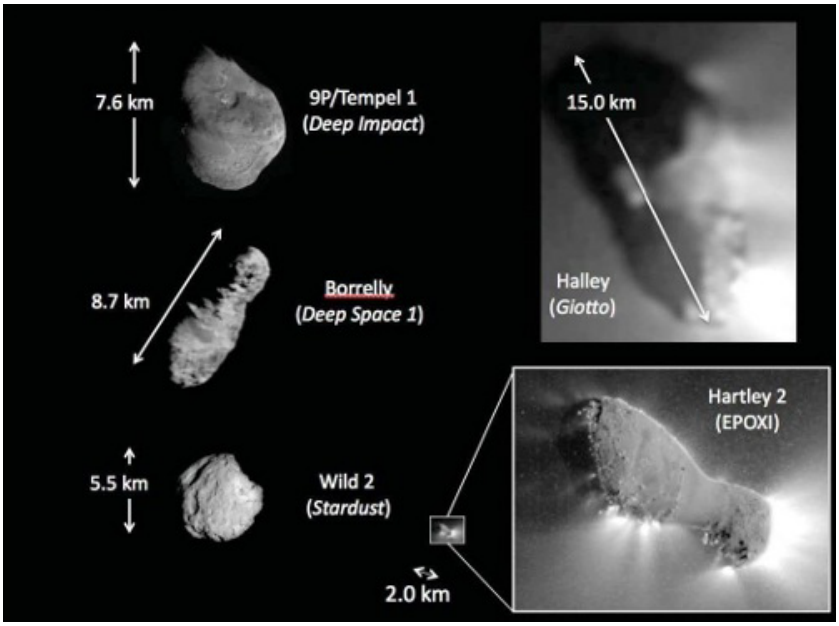

Figure 2.4: Collection of the cometary nuclei approached by spacecrafts pictured in scale.

The Deep Impact mission, launched on January 2005, after solely 174 days of journey, reached the small comet 9P/Tempel 1, 8×5 km across, and released a copper projectile of 370 kg which impacted on the surface of

the nucleus resulting in a crater of 100 meters. As a result, the vaporized ejecta from the deeper layers came out. This material was subject to a thorough investigation, in addition to studying the crater itself. This gave the opportunity for the first time to study the material in the deeper layers of the nucleus of a comet, providing numerous high-value scientific results (A'Hearn et al., 2005).

Two years later, NASA communicated the extension of Deep Impact mission and authorized the use of the spacecraft for a second journey to another comet. After three other Earth gravity assists, on 4 November 2010 the extended mission called EPOXI (see Sec. 2.4) flew past the surface of the very small comet 103P/Hartley 2 obtaining incredible images of its nucleus and dust and gas jets. It revealed, for the first time, that the surrounding ambient of a comet is anything but an isotropic stable environment, but rather a very dense place full of rocky materials, boulders, grains, dust and jets expanding from the nucleus in a very complex physic process which has to be better understood.

The next comet's encounter will be soon in August 2014 when Rosetta will approach the comet 67P/Churyumov-Gerasimenko up to 10 km distance and will deliver a lander on its surface, analyzing samples of its nucleus and will escort the comet along its orbit around the Sun in order to attend the very beginning of the activity and its development as the heliocentric distance decreases.

Fig. 2.4 shows a collection of images of the various comets encountered so far by any space mission. As it is clear, cometary nuclei are very small and an always increasing resolution is necessary to obtain valuable data and be able to analyze the deep structure of these very interesting objects.

For both asteroids and comets, the present state of visited bodies constitute still a very minimal sample of the numerous populations existing, which needs to be soon enlarged to many others if an overall view of the physics of these bodies is searched.

2.3 The Rosetta mission

The International Rosetta Mission, approved in November 1993 by ESA's Science Programme Committee, is a Planetary Cornerstone Mission in ESA's long-term space science programme Horizon 2000 and was successfully launched on 2 March 2004.

The mission is named after the famous Rosetta Stone, a 762-kilogram stone of black volcanic basalt, kept in the British Museum in London, which was the key to unravel the civilization of ancient Egypt. On the stone there were three types of carved inscriptions: hieroglyphics, i.e the written language of very ancient Egypt, Demotic, i.e. the evolved Egyptian language and Greek, which was readily understood. By comparing the inscriptions on the stone, historians were able for the first time to decipher the mysterious carved figures and piece together the history of a culture remained unknown for centuries.

Rosetta's lander is named Philae, after an island in the Nile, where an obelisk was found that was used to translate the Rosetta stone.

Just as the Rosetta stone and Philae's obelisk provided the keys to unveil an ancient civilization, ESA's Rosetta spacecraft and its lander are supposed to unlock many of the mysteries of the oldest building blocks of our Solar System: asteroids and comets.

2.3.1 Scientific objectives

Rosetta's main objective is to rendezvous with the Jupiter family comet 67P/Churyumov-Gerasimenko in August 2014 and to perform a series of controlled orbits around it at varying distances allowing observations of both the comet's nucleus and coma and a detailed characterization of the landing site for Philae. The Philae lander will be deployed and will make the first controlled landing on a comet ever. Rosetta will continue orbiting around the comet when it will proceed towards the Sun and will reach its perihelion, thus monitoring the onset and development of cometary activity while the Sun's rays warm it.

Rosetta will carry out a global characterization of the comet and a detailed study of the physical evolution of cometary activity and of dynamic properties, surface morphology and chemical composition of this primitive body.

During the cruise phase Rosetta has observed asteroid 2867 Steins in September 2008, and asteroid 21 Lutetia in July 2010. Secondary objective of the mission was indeed the study of asteroids, as primitive as comets and

much more diverse in composition. It performed two very successful flybys and obtained huge amount of high-quality scientific data, high-resolution analysis of the surfaces, craters, densities, mineralogical composition, and so on (see for example Keller et al., 2010 and Sierks et al., 2011).

2.3.2 Mission timeline

Fig. 2.5 represents Rosetta trajectory in the Solar System while Tab. 2.1 summarizes the fundamental events of the mission.

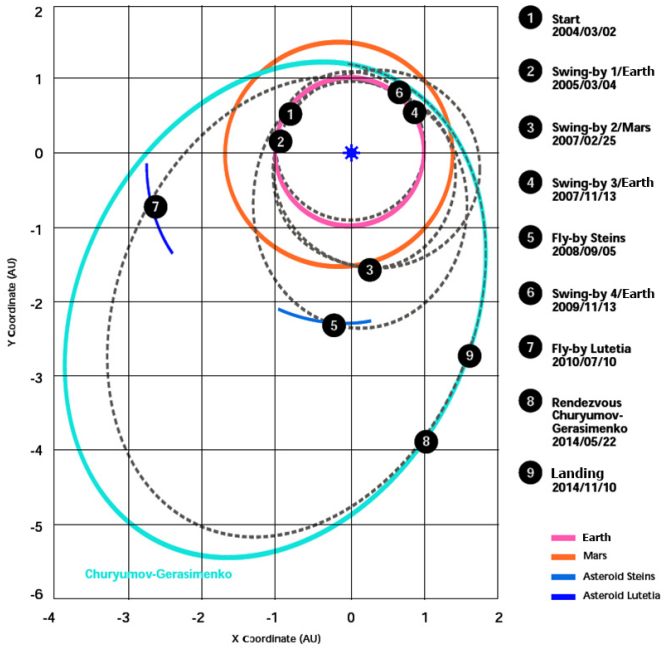

Figure 2.5: Rosetta trajectory (dashed line) in the Solar System.

To reach the comet at a distance of 5.25 AU from the Sun, Rosetta bounced around the inner Solar System, circling the Sun almost four times. During this complex route, Rosetta entered the asteroid belt twice and stole energy of motion from the planets, in a swing-by of Mars and three swing-bys of the Earth.

To limit consumption and cost during the long journey of the spacecraft, Rosetta has been into hibernation for more than 2.5 years and has been successfully awakened on 20 January 2014.

Date	Operation	Dist. to object
2 March 2004	Launch	-
4 March 2005	First Earth swing-by	1 900 km
25 February 2007	Mars swing-by	250 km
13 November 2007	Second Earth swing-by	5 301 km
5 September 2008	2867 Steins fly-by	800 km
13 November 2009	Third Earth-Moon swing-by	2 481 km
10 July 2010	21 Lutetia fly-by	3 170 km
23 January 2011	Comet rendezvous maneuver 1	-
8 June 2011	Start of hibernation	-
20 January 2014	Spacecraft wake up	-
May 2014	Comet rendezvous maneuver 2	-
August 2014	Insertion into orbits	∼30-300 km
	and flybys around comet	∼10-20 km
November 2014	Lander delivery	∼30 km
Nov 2014-Jul 2015	Escort Phase	10-400 km
August 2015	Perihelion passage	-
31 December 2015	End of nominal mission	-

Table 2.1: Rosetta Mission timeline.

Launch and initial parking orbit. Rosetta's ten-year expedition began on 2 March 2004 when it was successfully launched by an Ariane-5 G+ rocket from Kourou, French Guiana. After burn-out of the lower stage, the spacecraft and upper stage remained in Earth's parking orbit (4 000 × 200 km) for about two hours. Ariane's upper stage then ignited to boost Rosetta into its interplanetary trajectory, before separating from the spacecraft.

First Earth swing-by. In order to gain enough orbital energy to reach its final target four gravity assists were required. Rosetta returned to its home planet a year after the launch, on 4 March 2005 at a distance of 1 900 km. During Earth flybys operations have been mainly focused on orbit determination, payload check-out and calibrations, however some scientific observations have also been performed.

Mars swing-by. Rosetta flew past Mars on 25 February 2007 at a distance of about 250 km, obtaining some science observations of Mars, revealing for example interesting morning and evening clouds on Mars's atmosphere. Observations of Mars allowed also to perform interesting investigation on its moon Phobos (Pajola et al., 2012). During the swing-by, Rosetta survived

a 37-minutes eclipse which the spacecraft was not specifically designed to handle. A communications black-out was also caused by the occultation. The operation required a significant effort, but was entirely successful.

Second and third Earth swing-by. Rosetta returned to 5 301 km from Earth on 13 November 2007 for its second swing-by of our planet and on 13 November 2009 to an altitude of 2 481 km for the third and last time to receive the conclusive boost required to reach its final target, passing the Moon at a distance of about 233 000 km.

Asteroids flybys. Rosetta surveyed the asteroid 2867 Steins on 5 September 2008 from a distance of 803 km, and flew at 3 170 km from the asteroid 21 Lutetia on 10 July 2010. Rosetta obtained a wealth of data (see Fig. 2.6a) and 2.6b) and science results (see Keller et al., 2010; Sierks et al., 2011) as it flew by these rocks composed of primitive material

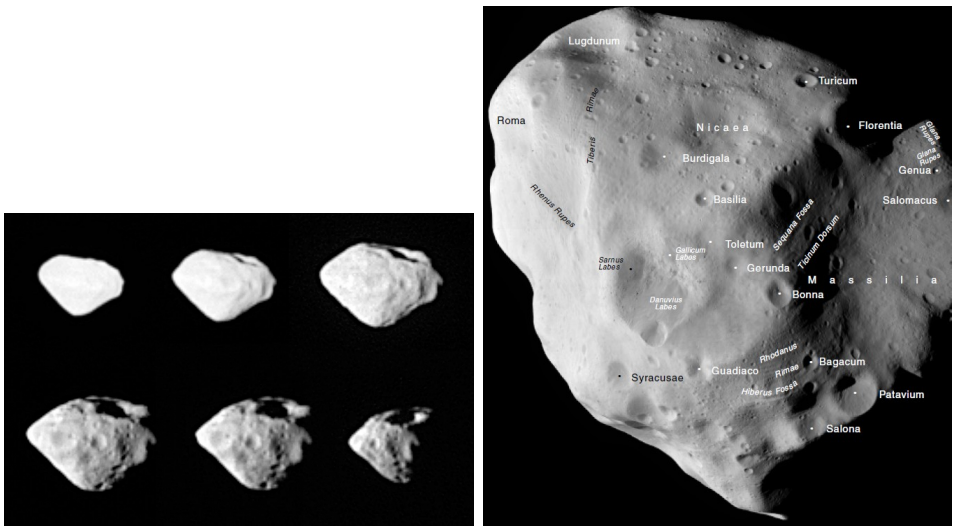

Figure 2.6: 2867 Steins and 21 Lutetia asteroids as observed by Rosetta-OSIRIS.

Deep-space hibernation. The long mission duration has required the introduction of an extended hibernation period. It helped to limit consumption of power and fuel, and minimize operating costs. During hibernation the spacecraft have been spinning once per minute facing the Sun, so that the

solar panels received as much sunlight as possible. The spacecraft has gone into hibernation on June 2011 and has been successfully awakened on 20 July 2014. Almost all electrical systems have been switched off, except for the thermal subsystem, on-board computer, radio receivers, command decoders and power supply. During hibernation Rosetta recorded its maximum distance from the Sun, about 800 million km, and from the Earth, about 1 000 million km.

Comet rendezvous. In August 2014, Rosetta's will match comet 67P/Churyumov-Gerasimenko's orbit. It will edge closer to the black, dormant nucleus until it is only a few kilometers away. The spacecraft will arrive at less than 100 kilometers from the nucleus, where it will analyze the comet's spin-axis orientation, angular velocity, major landmarks and other basic characteristics. The spacecraft will perform a series of orbits around the nucleus at varying distances, from about 30 to 300 km. The orbiter will map the overall surface of the nucleus in great detail to select the potential landing site for Philae.

Lander delivery. Once a suitable landing site is chosen, the lander will be released from an orbit at about 30 km of distance from the nucleus. Once it is anchored to the nucleus, the lander will send back high-resolution images and in situ measurements of the comet's ices and organic crust. The data will be relayed to the orbiter, which will store them for transmission back to Earth at the next period of contact with a ground station.

Comet escorting. The orbiter itself will continue orbiting the comet, observing what happens as the icy nucleus approaches the Sun, reaches its next perihelion on August 2015 and then travels away from it. A series of close fly-bys are foreseen in this phase at about 10-20 km.

End of the mission. The mission will end in December 2015 when Rosetta will once again pass close to Earth's orbit, more than 4 000 days after the launch.

2.3.3 Spacecraft

Rosetta is a 2 900-kilograms large aluminum box with dimensions 2.8 × 2.1 × 2.0 meters with two wings covered of solar panels (Fig. 2.7). The scientific instruments (165 kilograms) are mounted on the top of the box in the Payload Support Module, while the subsystems are on the base in the Bus Support Module.

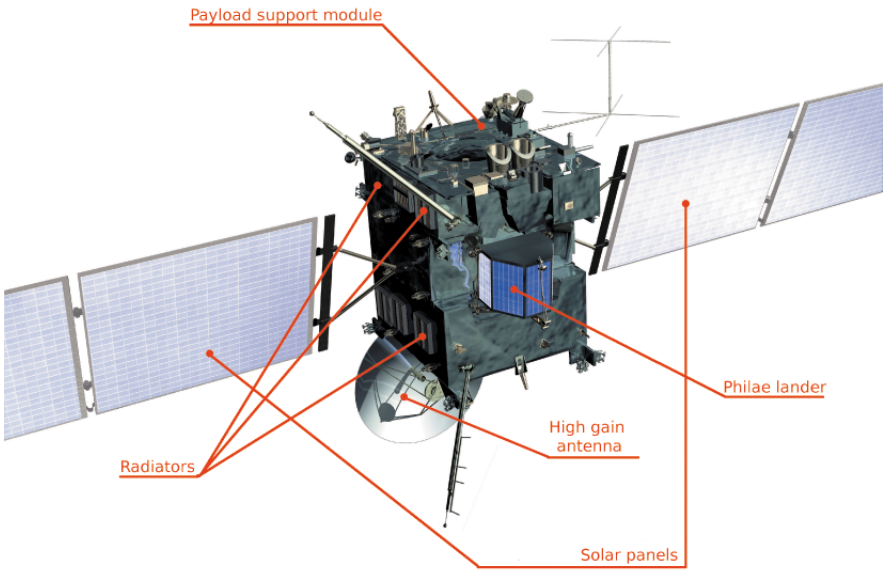

Figure 2.7: Rosetta Spacecraft.

On one side of the orbiter, there is the 2.2-meter diameter communications high-gain antenna. The lander is attached to the opposite face.

The two 32 meters-long solar panel wings extend from the other sides. Each wing comprises five panels, and can be rotated through +/-180 degrees to catch the maximum amount of sunlight. Rosetta will be the first space mission to journey beyond the Main Asteroid Belt and rely solely on solar cells for power generation, rather than the traditional radio-isotope thermal generators.

Near the Sun, overheating has to be prevented by using radiators to dissipate surplus heat into space. In the outer Solar System instead, the hardware and scientific instruments must be kept warm, especially in hibernation, to ensure their survival. This is achieved by black paint, multilayer insulation, and electric heaters located at strategic points.

The main propulsion system is in the heart of the orbiter. Over half the launch weight of the entire spacecraft is taken up by propellant. Attitude is maintained by four reaction wheels as well as using two star trackers, Sun sensors, navigation cameras, and three lasers.

During Rosetta's interplanetary expedition, reliable communications

between the spacecraft and the ground are essential. All of the scientific data collected by the instruments on board the spacecraft are sent to Earth via a radio link. The operations center, in turn, remotely controls the spacecraft and its scientific instruments via the same radio link.
Radio communications between Rosetta and the ground use a newly developed ESA's deep-space antenna situated in New Norcia in Western Australia. This 35-meter diameter parabolic antenna concentrates the energy of the radio signal in a narrow beam, allowing it to reach distances of more than 1 000 million kilometers from Earth. Signals are transmitted and received in two radio frequency bands: S-band (2 GHz) and X-band (8 GHz). The radio signals will take up to 50 minutes to reach the spacecraft. Another 35-meter parabolic antenna, situated in Cerebros in Spain, began to operate in 2005 providing further coverage for Rosetta.

However, the rotation of the Earth causes that real-time communications are not always possible. In addition, there are several periods of communications black-out when the spacecraft passes behind the Sun. To overcome these breaks in communications Rosetta is equipped with attitude and orbit control systems and a solid-state memory of 25 Gbits which stores the scientific data until the next period of transmission.

The 100-kilogram box-shaped Philae lander is carried on the side of the orbiter. It consists of a baseplate, an instrument platform, and a polygonal structure, all made of carbon fiber. Some of the instruments and subsystems are covered with solar cells.

Once the orbiter is aligned correctly, the lander is commanded to self-eject from the main spacecraft and unfold its three legs. On landing, the legs damp out most of the kinetic energy to reduce the chance of bouncing, and can rotate, lift or tilt to return the lander to an upright position. Immediately after touchdown, a harpoon is fired to anchor the lander to the ground and prevent it escaping from the comet's extremely weak gravity. The minimum target lifetime of the lander is one week, but surface operations may continue for many months. An antenna will transmit data from the surface to Earth via the orbiter.

2.3.4 Instrument payload

In order to investigate the comet nucleus and the gas and dust ejected from the nucleus as the comet approaches the Sun, Rosetta carries a suite of eleven instruments on-board the orbiter. The lander, Philae, is equipped with further ten instruments to perform surface measurements.

The orbiter instruments combine remote sensing techniques, such as

cameras and radio science measurements, with direct sensing systems such as dust and particle analyzers.

ALICE, an Ultraviolet Imaging Spectrometer, will characterize the composition of the nucleus and coma. It will perform observations of spectral features in the extreme and far ultraviolet spectral regions from 70 to 205 nm. It will make measurements of noble gas abundances in the coma and major ion abundances in the tail. It will determine the production rates, variability, and spatial structure of H_2O, CO, and CO_2 gas in the coma through their far-UV features. It already performed far-UV observations during the previous mission phases (see for example A'Hearn et al., 2010)

CONSERT (*Comet Nucleus Sounding Experiment by Radio wave Transmission*) will perform tomography of the comet nucleus. A radio signal passes from the orbiting component of the instrument to the component on the lander and is then immediately transmitted back to its source. The varying propagation delay as the radio waves pass through different parts of the cometary nucleus will be used to determine the dielectric properties of the nuclear material.

COSIMA (*Cometary Secondary Ion Mass Analyzer*) is a secondary ion mass spectrometer equipped with a dust collector, a primary ion gun, and an optical microscope. Dust from the near comet environment is collected on a target which is then moved under the microscope where the positions of any dust particles are determined. The cometary dust particles are then bombarded with pulses of indium ions from the primary ion gun. The resulting secondary ions are extracted into the mass spectrometer.

GIADA (*Grain Impact Analyzer and Dust Accumulator*) will measure the scalar velocity, size and momentum of dust particles in the coma using an optical grain detection system and a mechanical grain impact sensor. Five microbalances will measure the amount of dust collected as the spacecraft orbits the comet.

MIDAS (*Micro-Imaging Dust Analysis System*) is intended for the micro-textural and statistical analysis of cometary dust particles. The instrument is based on the technique of atomic force microscopy. It will obtain a spatial resolution of dust particles down to 4 nm.

MIRO (*Microwave Instrument for the Rosetta Orbiter*) is composed of a

millimeter wave mixer receiver and a submillimeter heterodyne receiver. The submillimeter wave receiver provides both broad band continuum and high resolution spectroscopic data, whereas the millimeter wave receiver provides continuum data only. It will measure the near surface temperature of the comet, allowing estimate of the thermal and electrical properties of the surface. Results have been obtained already for the asteroids targets (see for example Gulkis et al., 2012)

OSIRIS (*Optical, Spectroscopic, and Infrared Remote Imaging System*) is a dual camera imaging system operating in the visible, near infrared and near ultraviolet wavelength ranges, from 245 up to 990 nm. OSIRIS consists of two independent camera systems sharing common electronics. The narrow angle camera (NAC), is designed to produce high spatial resolution images of the nucleus and the wide angle camera (WAC), with a wide field of view and high straylight rejection to image the dust and gas in the coma. Each camera is equipped with filter wheels to allow selection of imaging wavelengths for various purposes. It already hardly operated during the previous mission phases and obtained extraordinary results on Mars, Earth and asteroids observations (see for example Keller et al., 2010; Sierks et al., 2011; Magrin et al., 2012; Pajola et al., 2012).

ROSINA (*Rosetta Orbiter Spectrometer for Ion and Neutral Analysis*) consists of two mass spectrometers. In addition, two pressure gauges provide density and velocity data for the cometary gas.

RPC (*Rosetta Plasma Consortium*) is a set of five instruments sharing a common electrical and data interface with the Rosetta orbiter. The RPC instruments are designed to make complementary measurements of the plasma environment around the comet. The RPC instruments are an Ion Composition Analyzer (ICA) to measure the 3D velocity distribution and mass distribution of positive ions; an Ion and Electron Sensor (IES) to simultaneously measure the flux of electrons and ions in the plasma; a Langmuir Probe (LAP) to measure the density, temperature and flow velocity of the plasma; a Fluxgate Magnetometer (MAG) to measure the magnetic field in the region where the solar wind plasma interacts with the comet; and a Mutual Impedance Probe (MIP) to derive the electron gas density, temperature, and drift velocity in the inner coma.

RSI (*Radio Science Investigation*) makes use of the communication system that the Rosetta spacecraft uses to communicate with the ground stations

on Earth. Either one-way or two-way radio links can be used for the investigations. These analysis will yield information on the motion of the spacecraft, the perturbing forces acting on it and the propagation medium.

VIRTIS (*Visible and Infrared Thermal Imaging Spectrometer*) is an imaging spectrometer that combines three data channels in one instrument. Two of the data channels are designed to perform spectral mapping. The third channel is devoted to spectroscopy. It has an overall coverage ranging from 0.22 μm up to 5 μm. VIRTIS instrument has also provided already scientific results for the visited asteroids (see for example Tosi et al., 2010; Coradini et al., 2011; Tosi et al., 2012)

The Lander instruments are designed to measure the elemental, molecular, mineralogical, and isotopic composition of the comet's surface and subsurface material and to measure characteristics such as near-surface strength, density, texture, porosity, ice phases and thermal properties. Texture measurements will include microscopic studies of individual grains. The sampling device will drill more than 20 cm into the surface, collect samples and deposit them in different ovens or deliver them for microscope inspection. The lander instruments are:

APXS: Alpha-p-X-ray spectrometer

CIVA: Panoramic and microscopic imaging system

CONSERT: Radio sounding, nucleus tomography

COSAC: Evolved gas analyzer - elemental and molecular

MODULUS Ptolemy: Evolved gas analyzer - isotopic composition

MUPUS: Measurements of surface and subsurface properties

ROLIS: Imaging system

ROMAP: Magnetometer and plasma monitor

SD2: Sampling, Drilling and Distribution Subsystem

SESAME: Surface electrical, acoustic and dust impact monitoring

2.4 The EPOXI mission

The EPOXI mission is the extension of the NASA Deep Impact (DI) mission launched on 12 January 2005, which was part of NASA's Discovery Program of low-cost spacecrafts. Deep Impact successfully visited the comet 9P/Tempel 1 on 4 July 2005 after only 174 days of space travel releasing an impactor onto the surface in order to explore its interior (A'Hearn et al., 2005).

On 3 July 2007 the NASA communicated the extension of the mission and, using the fuel left, defined new objectives and reoriented the Deep Impact vehicle towards a new target. The new mission, led by University of Maryland, assumed the name EPOXI and combined two distinct science programs: the Deep Impact eXtended Investigation (DIXI), and the Extrasolar Planet Observation and Characterization (EPOCh).

The EPOCh program's aim was to observe multiple transits of known giant planets orbiting around other stars, to characterize those planets and analyze their flux to learn about clouds and atmospheres. Main objective was also to find unknown planets, down to Earth-size, from a direct search for transits and from perturbations to the giant planets transits, and to search for rings and moons associated with the giant planets.

The DIXI program's aim was instead to perform a second fly-by with a cometary nucleus. The selected target was the hyperactive Jupiter-family comet 103P/Hartley 2. As Rosetta, also the DIXI mission had the objective to understand the structure, composition, and formation history of cometary nuclei to learn more about the origin of the Solar System, to understand how features of a cometary nucleus are related to structures of the coma and to analyze diversity between different cometary nuclei and heterogeneity within the same nucleus.

2.4.1 Mission Timeline

Fig. 2.8 shows the EPOXI trajectory in the Solar System and Tab. 2.2 summarizes the main events in the mission timeline.

On 26 September 2007 a signal from Earth woke up the DI spacecraft which had been into hibernation for the previous 24 months, and EPOXI cruise phase began.

The initial plan was to fly by comet 85P/Boethin on 5 December 2008 getting within 700 km from its surface. However during the cruise phase the comet was not correctly located due to the its faintness and its orbit could not be calculated with sufficient precision to permit a flyby. Therefore the team decided to change target and send EPOXI to comet 103P/Hartley 2, which

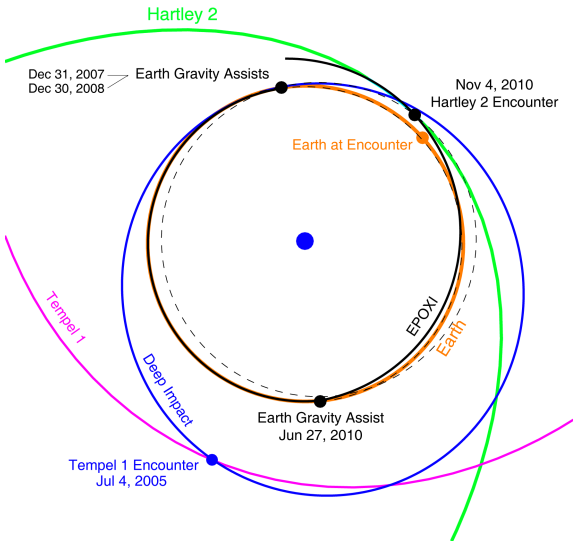

Figure 2.8: EPOXI trajectory (black line) in the Solar System .

would have required an extra two years. NASA approved the additional funding required and retargeted the spacecraft.

Mission controllers at the Jet Propulsion Laboratory began redirecting EPOXI on November 1, 2007. They commanded the spacecraft to perform a three-minute rocket burn that changed the spacecraft's velocity. EPOXI's new trajectory envisioned a series of Earth's gravity assists to gain velocity to reach the new target.
EPOXI performed the first Earth swing-by on 31 December 2007, when 15 567.63 km separated it from eastern Asia. Because of the close approach, several observers were able to image the spacecraft.

From January to August 2008 EPOXI's telescopes studied the stars with several known extrasolar planets in the attempt to find other extrasolar planets and characterize them, in the framework of the EPOCh's program. The larger of the spacecraft's two telescopes attempted to find the planets using the transit method. A total of 198 434 images were exposed and the physical properties of giant planets were studied and a deep search for rings, moons and planets as small as three Earth masses, were performed. It also looked at Earth as though it were an extrasolar planet to provide data that could characterize Earth-type planets for future missions, and it imaged the Earth over 24 hours to capture the Moon passing in front on 29 May 2008.

The spacecraft flew by Earth for the second gravity assist on 29 December

Date	Operation	Dist. to object
12 January 2005	Launch of DI spacecraft	-
4 July 2005	Fly-by of Tempel 1	500 km
3 July 2007	Extended mission approved	-
26 September 2007	Spacecraft wake up	-
31 December 2007	First Earth swing-by	15 567 km
January-August 2008	EPOCh program observations	-
30 December 2008	Second Earth swing-by	43 450 km
29 June 2009	Distant Earth flyby	
28 December 2009	Distant Earth flyby	
27 June 2010	Third Earth swing-by	36 900 km
5 September 2010	Start observations of Hartley 2	-
4 November 2010	Closest Approach to Hartley 2	694 km
8 August 2013	Communication lost	-
20 September 2013	End of mission	-

Table 2.2: EPOXI Mission timeline.

2008 when it reached a closest distance of 43 450 km. It made then two further distant flybys of Earth on 29 June and 28 December 2009. In June 2009 EPOXI's spectrometer scanned the Moon and discovered traces of water or hydroxyl (Sunshine et al., 2009), confirming a Moon Mineralogy Mapper observation. The last Earth's gravity assist occurred on 27 June 2010 which gave the last thrust for the final cruise to the comet.

Observations of 103P/Hartley 2 began on 5 September and ended on 25 November 2010. The closest approach to Hartley 2 occurred on 4 November 2010 at a distance of 694 kilometers from this small comet's nucleus with a speed of 12.3 km/s. Early results of the observations show that the comet is powered by dry ice, not water vapor as was previously thought. Another big discovery of EPOXI was that the ambient coma was full of rocky and icy grains, of sizes up to a few tents of centimeters (A'Hearn et al., 2011)

The images show a coma of large particles surrounding the nucleus at a spacecraft comet ranges $\Delta < 10^4$ km with size distribution ranging $1 - 30$ cm assuming an icy composition and $12 - 400$ cm instead, for dark, organic material (Kelley et al., 2012). These discrete grains were not detected around any other spacecraft target, and undoubtedly affect the coma and perhaps even the nucleus in many ways.

Spectral observations of the ambient coma (Fig. 2.9, Feaga et al., 2012) show that H_2O is enhanced from the central waist even though it is spread all around the nucleus, while CO_2 and icy grains seem to be coming out

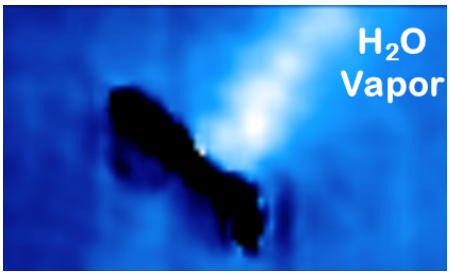

H_20 vapor in Hartley2.

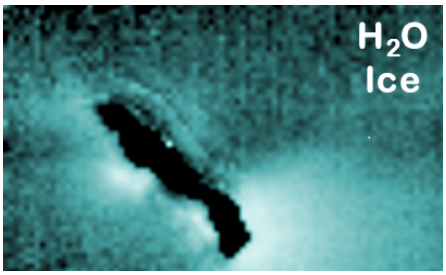

H_20 ice in Hartley2.

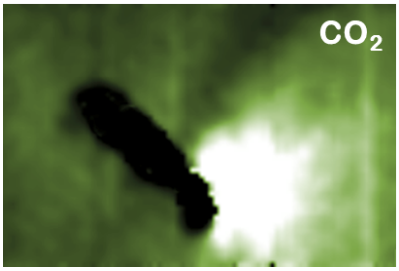

CO_2 ice in Hartley2.

Figure 2.9: H_20 vapor (a), H_20 ice (b) and CO_2 (c) in ambient coma of comet Hartley 2 Figure from Feaga et al., 2012.

mainly from the two lobes (Feaga et al., 2012; Protopata et al., 2012). This may suggest that H_2O comes only from the waist directly at the surface of the nucleus and from icy grains all around the nucleus.

The correlation between the asymmetric distribution of CO_2 and the icy grains around the nucleus, much different than the gaseous, H_2O distribution, implies that CO_2 and H_2O have different source regions and that CO_2 rather than H_2O drags solid grains with it into the coma as it leaves the nucleus (Feaga et al. 2012).

From 20 February to 8 April 2012, EPOXI observed Comet Garradd (C/2009 P1) through a variety of filters. The comet was between 1.75 to 2.11 AU from the Sun and 1.87 to 1.30 AU from the spacecraft, while in February 2013, EPOXI observed comet ISON (C/2012 S1) a dynamically new comet in a sungrazing orbit (Farnham et al., 2013).

On 8 August 2013, communications with the spacecraft were lost and the mission team attempted to restore contacts but on 20 September 2013 NASA abandoned further attempts to contact the probe and declared the mission ended.

2.4.2 Spacecraft

The DI spacecraft (Fig. 2.10), as part of NASA's Discovery program, was a simple spacecraft, designed to be rapid and perform only the very urgent science. It consists of two main sections: the Smart Impactor that hit the comet Tempel 1, and the Flyby Spacecraft, which imaged the comet from a safe distance during the encounter.

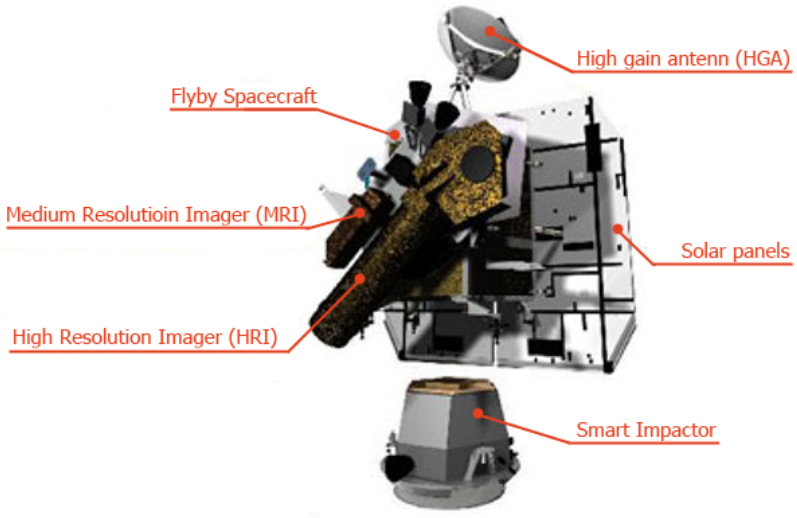

Figure 2.10: Deep Impact/EPOXI Spacecraft.

The flyby spacecraft is about 650 kg and 3.2×1.7×2.3 meters across. It includes two solar panels, of 2.5 square meters, a debris shield, an optical navigation camera, the high gain antenna and the instrument payload. It is three-axis stabilized and uses a fixed solar array and a small NiH_2 battery for its power system. The structure is aluminum and aluminum honeycomb construction. The temperature is controlled passively by blankets, surface radiators, finishes, and heaters. The propulsion system employs a simple blowdown hydrazine design that provides 190 m/s of ΔV.

The high gain antenna transmitted data back to Earth using X-band. It also communicated with the impactor with a S-band radio link after it was deployed from the flyby spacecraft.

The debris shield is a key part of the flyby spacecraft design. As the spacecraft passes through the inner coma indeed being hit by small particles could damage the control, imaging and communication systems. To minimize this possibility the spacecraft rotated before passing through the inner coma

allowing debris shield to provide complete protection to the flyby spacecraft and instrument elements.

The Smart Impactor was made primarily of copper (49%) and aluminum (24%) to minimize corruption of spectral emission lines from the nucleus. In fact, since it is not expected to find any copper on a comet, this could be easily eliminated from spectral features.

The impactor separated from the flyby spacecraft 24 hours before it impacted the surface of Tempel 1's nucleus, delivering 19 Gigajoules of kinetic energy and excavating a 100-m crater. This kinetic energy was generated by the combination of the mass of the impactor, 370 kg, and its velocity, ∼10.3 km/s. Targeting and hitting the comet in a lit area was one of the mission's greatest challenges since the impactor was traveling at 10 km/s and it hit an area less than 6 km in diameter from about 864 000 km away. To accomplish this goal, the impactor used a high-precision star tracker and auto-navigation algorithms to guide it to the target. Minor trajectory corrections and attitude control were available by using the impactor's small hydrazine propulsion system which could provide 25 m/s of ΔV for targeting. The impactor was mechanically and electrically attached to the flyby spacecraft for all but the last 24 hours of the mission, but during the 24 hours of descending phase it run on its internal battery power.

2.4.3 Instrument payload

The flyby spacecraft employed the same suite of two science instruments that the DI spacecraft used during its prime mission to guide the impactor into comet Tempel 1: the High Resolution Imager (HRI), and the Medium Resolution Imager (MRI).

The HRI has been designed for nucleus observations and consists of a 10.5 m focal length Cassegrain telescope, with a 30 cm aperture, equipped with a visible camera and a long-slit imaging spectrometer called Spectral Imaging Module (SIM) that operates on a spectral band from 1.05 to 4.8 μm, optimized for observing the comet's nucleus. It is equipped with a 9 positions filter wheel containing broadband filters with central wavelengths ranging from 350 nm to 950 nm and bandwidths going from 100 to 700 nm.

The MRI camera has been designed for coma observations and is based on a 2.1 m focal length Cassegrain telescope, with 12 cm aperture, a field of view of approximately 35 × 35 arcminutes, and a per pixel resolution of 2 arcsec (A'Hearn et al., 2005). The MRI camera, considered also a backup device, has been primarily used for navigation during the final 10-day approach. It

carries on a series of band filters which have been used during Hartley 2 approach, to analyze the gas features in the coma.

The Impactor contained an instrument, called Impactor Targeting Sensor (ITS), optically identical to the MRI, but without the filter wheel. Its dual purpose was to sense the Impactor's trajectory, which could then be adjusted up to four times, and to image the comet from close range. As the impactor neared the comet's surface, this camera took high-resolution pictures of the nucleus (as good as 0.2 meters per pixel) that were transmitted in real-time to the flyby spacecraft before the impactor was destroyed. The final image taken by the impactor was snapped only 3.7 seconds before impact.

Chapter 3

Surface Light Scattering

Among the photometric analysis performed on Lutetia, the phase curve modeling requires further considerations on the mechanisms responsible for its shape and properties: the surface light scattering.

The process of scattering of light by a surface of particulate medium, such as asteroid regoliths, is indeed a very complex mechanism. A deep knowledge of the physics involved is essential to solve the inverse scattering problem, i.e. from the observed pattern and intensity of the scattered light, obtain information on the surface responsible for the scattering.

The aim is thus to model the observable phase curve of the body as function of a series of parameters able to describe the physical properties of the surface.

The geometry of illumination and observation, illustrated in Fig. 3.1, is a crucial factor in determining the fraction of light scattered by a surface and thus the final observed flux.
The plane formed by the direction of the light source and the normal to the surface is called *incident plane* and the angle formed between the two vectors is the *incident angle*.
The plane formed by the normal to the surface and the observer's direction is called *emission plane*, and the angle between the two vectors is the *emission angle*.
It is called *phase angle* the angle between the light source and the observer as seen from the target surface. The plane containing the incident and emergent rays is called *scattering plane*.
The *azimuthal angle*, ψ, is the angle between the incidence and emission planes, measured on the surface plane.

Many theoretical, empirical and semi-empirical theories have been devel-

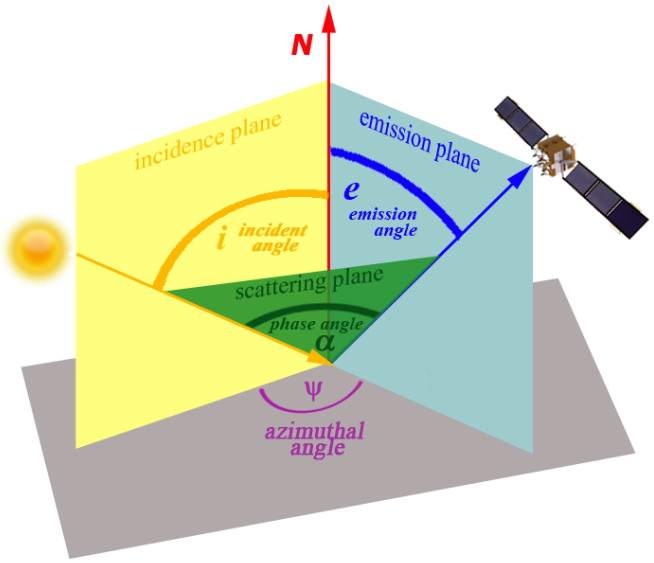

Figure 3.1: Surface scattering process geometry and definitions.

oped to model the phase curves observed from asteroids and comet nuclei (see Sec. 3.2) to obtain information on the surface physical properties. One of the still most used model up to date is Hapke's bidirectional reflectance theory (Hapke, 1981a, 1981b, 1984, 1986, 1993, 2002, 2008).

3.1 Hapke's bidirectional reflectance theory

Hapke studied in detail the phase curve of a particulate, porous surface and developed a parametric model to represent its behavior. It started from the property of a single particle to scatter the light and then considered the effects of a compact and interacting ensemble of particles.

Hapke's theory is solidly based on the solution of the radiative transport equation and uses well-justified assumptions. It assumes that the particles are larger than the wavelength, such that when the real particle sizes are smaller, the "fundamental scatterers" of the medium are considered the aggregates rather than individual particles. However, the optical wavelength range, where particles are usually smaller than the wavelength, is the best range for the application of this theory.

The most important quantity used is the *bidirectional reflectance*, r, defined as the ratio of the scattered radiance at the detector to the incident

irradiance to the surface, i.e. the fraction of light scattered by the surface in a unit emission angle, respect to the light that illuminates the surface per unit incident angle.

In Hapke's model the bidirectional reflectance is expressed as a function of the incident, emission, and phase angles making use of a series of parameters related to the physical properties of the surface. The complete parametrization yields:

$$r(i,e,\alpha) = \frac{\mathrm{w}}{4\pi}\frac{\mu_{0e}}{\mu_{0e}+\mu_e}\left\{[1+B_S(\alpha)]p(\alpha,g) + H(\mu_{0e},\mathrm{w})H(\mu_e,\mathrm{w}) - 1\right\}B_C(\alpha)S(i,e,\alpha,\bar{\theta}) \tag{3.1}$$

where w is the *single scattering albedo* (SSA) of the particles; $B_S(\alpha)$ and $B_C(\alpha)$ are the two component of the *opposition effect*; $p(\alpha, g)$ is the *single-particle phase function*; $H(x, \mathrm{w})$, with $x = \mu_e, \mu_{0e}$, is a function accounting for the multiple scattering process; $S(i, e, \alpha, \bar{\theta})$ is the correction factor accounting for the global *surface roughness* $\bar{\theta}$ and μ_{0e} and μ_e are the effective cosines of the incident and emission angles, respectively, which take into account the effects of the roughness. In the following sections each of these components will be discussed more in detail.

3.1.1 Single particle scattering

The SSA simply describes the capacity of the single particle to scatter the light.

If J is the collimated irradiance incident onto the particle, the *scattered power* and the *absorbed power* by the particle are defined as:

$$P_S = J\sigma_S \qquad P_A = J\sigma_A \tag{3.2}$$

where σ_S and σ_A are respectively the *scattering cross section* and the *absorption cross section* of the particle which depend mainly on its composition, opacity, size and shape. It is called then *extinction power* the sum of the absorbed and scattered power:

$$P_E = P_A + P_S \tag{3.3}$$

thus the *extinction cross section* is given by

$$\sigma_E = \sigma_A + \sigma_S \tag{3.4}$$

Are then defined *extinction, scattering* and *absorption efficiencies*, respectively:

$$Q_E = \frac{\sigma_E}{\sigma} \qquad Q_S = \frac{\sigma_S}{\sigma} \qquad Q_A = \frac{\sigma_A}{\sigma} \tag{3.5}$$

where $\sigma = \pi a^2$ is the *geometric cross section* of the particle, with a being the radius of the particle.

The single scattering albedo is thus defined as the ratio of the total amount of power scattered by the particle to the extinction power, which yields:

$$\mathrm{w} = \frac{P_S}{P_E} = \frac{\sigma_S}{\sigma_E} = \frac{Q_S}{Q_E} \tag{3.6}$$

Analytical approximation of the scattering efficiency Q_E can be derived, as function of the composition and the size of the particles, assuming a spherical shape. This would allow for example, for a given composition, to have a direct relation between the single scattering albedo and the diameter of the particle.

3.1.2 Single particle phase function

The single-particle phase function describes the pattern in which the single particle scatters the light into space.

For example if the particle scatters isotropically in all directions, then $p(\alpha)$ is equal to unity. Otherwise the particle phase function will have different geometrical patterns (Fig. 3.3).

It is defined *scattering angle*, δ, the angle formed between the direction of propagation of the incident light and the scattered light direction (Fig. 3.2). It is supplementary to the phase angle.

It is defined *cosine asymmetry factor* g the average value of the cosine of the scattering angle ranging from 0 to π:

$$g = \overline{\cos\delta} = -\overline{\cos\alpha} \tag{3.7}$$

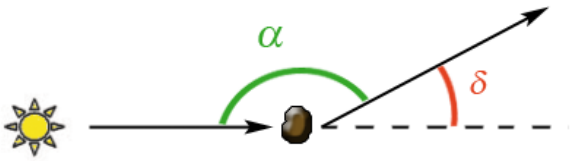

Figure 3.2: Scattering angle definition.

g is then the factor that accounts for the anisotropy of the single particle scattering. A positive value of g indicates that most of the light is scattered into the forward hemisphere (diffraction) whereas a negative value means that

the particle is predominantly back-scattering, suggesting that the particles scatter the light more similarly to the geometric optics. This could be interpreted as depending on the size and opacity of the grains: small and transparent particles would mainly forward scatter the light, while big and opaque particles would more probably back-scatter the light.

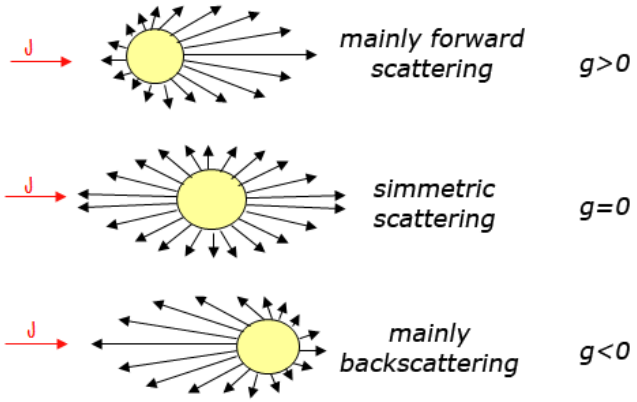

Figure 3.3: Single scattering different spatial distributions and correspondent g factors.

The exact solution of a plane electromagnetic wave scattered by a single uniform spherical particle larger than the incident wavelength has been computed, and is part of the Mie scattering theory (Mie, 1908). However perfect spherical particles are rarely found in nature. Most materials, including planetary regolith, are made of irregular particles, constituting a rough surface not uniform in either structure or composition. It is nowadays not possible, to compute the exact analytical solution of the scattering by such irregular particles. It is then necessary to rely on approximate models.

Many empirical scattering functions have been proposed to model single-particle phase functions for irregular particles. One of the most used for planetary regolith (Helfenstein et al., 1996; Li et al., 2004; Clark et al., 2002) is the Henyey and Greenstein function (1941):

$$p(\alpha) = \frac{1 - g^2}{(1 + 2g\cos\alpha + g^2)^{3/2}} \tag{3.8}$$

If $g > 0$ then $p(\alpha)$ increases monotonically, if $g < 0$ it decreases monotonically as shown in Fig. 3.4.

Other empirical models are the Legendre polynomial representation, the Allen diffraction approximation (Allen, 1946), the Lambert and Lommel-

Seeliger spheres (Schönberg, 1929) and the double Henyey-Greenstein function form (McGuire, 1993) which considers separately the forward and the back scattering lobes. They have not been considered here for the larger complexity due to the increase of parameters and also for continuity and compatibility with other works performed on other small bodies.

3.1.3 Multiple scattering component

For the solution of the scattering by particulate medium it is relevant not only the contribute of the single well-separated particles, but also the contribute due to the fact that many particles are close together.

The light reflected by single particles indeed interacts with the other close particles and is subject to multiple scattering and reflecting processes, depending on the physical properties of the material.

This effect is taken into account including the Ambartsumian-Chandrasekhar H-function which derives from the two-stream approximation solution of the radiative transfer equation, valid only for isotropic scattering particles.

In the anisotropic case other M functions are introduced, which include the weighted integrals of the particles phase function on the incident and

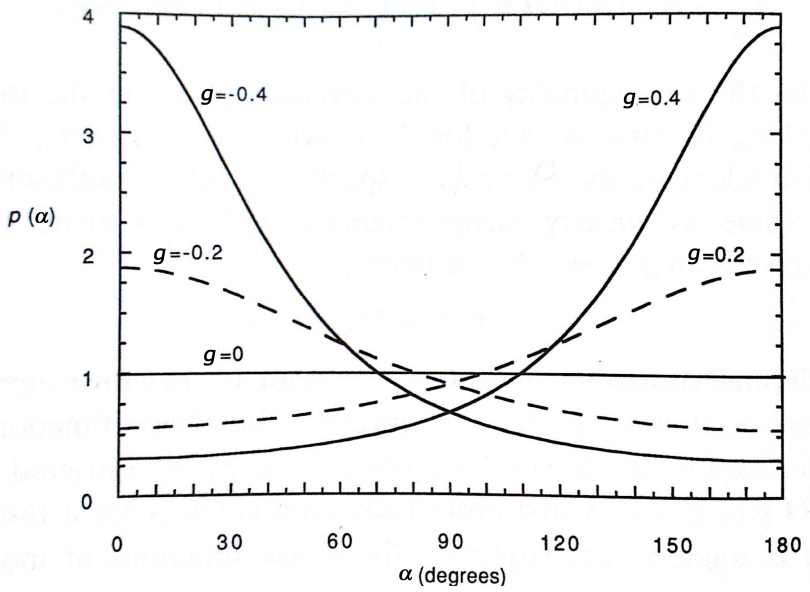

Figure 3.4: The Henyey-Greenstein function for different values of the cosine asymmetric factor g.

emission angles. Very often however, the anisotropic scattering is neglected for what concerns the multiple scattering and is instead accounted only for the single scattering.

Therefore, the improved version of the two-stream approximation of the Ambartsumian-Chandrasekhar H-function as given in Hapke (2002) is:

$$H(x, \mathrm{w}) \simeq \left[1 - \mathrm{w}x\left(r_0 + \frac{1 - 2r_0 x}{2} \ln \frac{1+x}{x}\right)\right]^{-1} \tag{3.9}$$

where r_0, called *diffusive reflectance*, is given by

$$r_0 = \frac{1 - \sqrt{1 - \mathrm{w}}}{1 + \sqrt{1 - \mathrm{w}}}. \tag{3.10}$$

and x assumes the values μ_{0e} and μ_e, the effective cosines of the incident or emission angle respectively (see Sec. 3.1.5).

3.1.4 Opposition Effect

Moving the particles close together to form a dense particulate medium affects the scattering process for the multiple scattering component but also for the exhibition of the opposition effect (OE). It is a non-linear increase in brightness as the phase angle approaches zero, occurring in all porous, particulate media.

In Fig. 3.5a for example, it is shown an hot-air balloon's shadow projected on the grass. The phase angle is about zero just over the shadow and it increases towards the boundaries. The increased brightness for small-phase angles is clearly visible as an halo around the hot-air balloon visible on the grass and it is further emphasized by the contrast with the shadow.

The first mechanism proposed to explain this evidence is the *shadow hiding opposition effect* (SHOE). Particles close together in a medium observed at high phase angle partially shadow one another. At zero phase angle, each particle hides its own shadow and thus the surface appears brighter to the observer. Fig. 3.5b shows the SHOE at decreasing resolution. As particle size increases, the particulate surface becomes more uniform, the amplitude of SHOE gradually decreases and the brightness peak occurs for narrower ranges of phase angle.

The second major mechanism proposed is the *coherent backscatter opposition effect* (CBOE) introduced to explain the very large OE observed for bright asteroids such as E-types. CBOE refers to the constructive interference

Figure 3.5: Opposition Effect (a) Hot-air balloon shadow on grass at zero phase angle. Opposition effect is clearly visible as an halo around the baloon. (b) Effect of SHOE at decreasing resolution. The phase angle equal zero at the center of each panel and increase toward the edges where shadows become visible. (http://www.atoptics.co.uk/atoptics/oppos2.htm)

between multiply scattered light waves that travel the same path through the material. The CBOE is however a second order correction of the SHOE.

The SHOE is modeled by the function (Hapke, 2002):

$$B_s(\alpha) = 1 + B_{s,0}\frac{1}{1+\frac{\tan(\alpha/2)}{h_s}} \tag{3.11}$$

where $B_{s,0}$ is the amplitude of the SHOE and h_s is the angular width; while the CBOE is modeled by the function (Hapke, 2002):

$$B_c(\alpha) = 1 + B_{c,0}\frac{1+\frac{1-e^{-\tan(\alpha/2)/h_c}}{\tan(\alpha/2)/h_c}}{2\left(1+\frac{\tan(\alpha/2)}{h_c}\right)^2} \tag{3.12}$$

where $B_{c,0}$ is the amplitude of the CBOE and h_c is the angular width.

The SHOE involves only the singly scattered light whereas the CBOE would act on both the singly scattered and multiply scattered rays.

However the similarity in the shapes of the SHOE and CBOE surges suggests that it would be extremely difficult to distinguish the two effects on the basis of the shape of the phase curve alone. A distinction could be made considering that the SHOE is a wavelength independent process whereas the

coherent back-scattering shows a wavelength dependence (Domingue et al., 2002; Li et al., 2004).

The angular width of the opposition effect may also be interpreted in terms of the porosity ρ. Assuming a grain size distribution function, Y, for example the lunar-like distribution expressed by:

$$Y = \frac{\sqrt{3}}{\ln\left(\frac{a_l}{a_s}\right)} \tag{3.13}$$

where a_l and a_s are respectively the radius of the largest and the smallest particle, the angular width of the opposition effect will be related to Y and ρ by equation (Hapke, 1993):

$$h = -\frac{3}{8} Y \ln \rho \tag{3.14}$$

This would allow an estimate of the porosity of the body if the grain size distribution is known, or assumed.

3.1.5 Macroscopic Roughness

The implicit assumption heretofore has been that the apparent surface of the particulate medium is smooth on large scales compared with the particle sizes. This is certainly not the case of asteroids surface which are covered by rims, craters, depressions, etc.

This macroscopic roughness of the surface is modeled by a series of small, locally smooth facets larger than the mean particle size and are tilted by a variety of angles (Fig. 3.6).

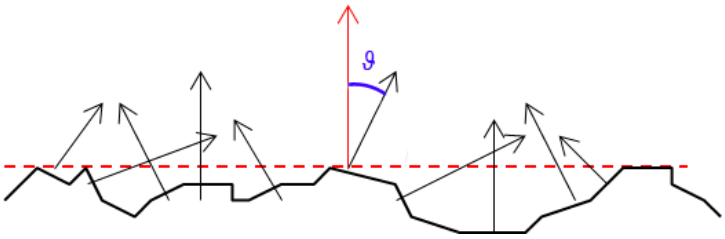

Figure 3.6: Macroscopic roughness modeling.

The normals to the facets are described by a two-dimensional slope distribution function $a(\vartheta)d\vartheta d\zeta$, where ϑ is the zenith angle between a facet normal and the vertical, and ζ is the azimuth angle of the facet normal.

The parameter which is then considered is the *mean slope angle* $\bar{\theta}$, defined by:

$$\tan\bar{\theta} = \frac{2}{\pi}\int_0^{\pi/2} a(\vartheta)\tan\vartheta d\vartheta \tag{3.15}$$

The effects of a macroscopic roughness are then taken into account evaluating the total bidirectional reflectance as the product of a shadowing function $S(i, e, \alpha)$ and the bidirectional reflectance $r(i_e, e_e, \alpha)$ of a smooth surface of area A_e tilted so as to have effective angle of incidence i_e, and angle of emergence e_e, and with the same phase angle α.

The derivation yields that the cosines of the effective incidence and emergence angle, $\mu_{0e} = \cos i_e$ and $\mu_e = \cos e_e$, in the case $e > i$ are given by:

$$\mu_{0e} \simeq \chi(\bar{\theta})\left[\cos i + \sin i\tan\bar{\theta}\frac{\cos\psi E_2(e) + \sin^2(\psi/2)E_2(i)}{2 - E_1(e) - (\psi/\pi)E_1(i)}\right] \tag{3.16}$$

$$\mu_e \simeq \chi(\bar{\theta})\left[\cos e + \sin e\tan\bar{\theta}\frac{E_2(e) - \sin^2(\psi/2)E_2(i)}{2 - E_1(e) - (\psi/\pi)E_1(i)}\right] \tag{3.17}$$

where $\chi(\bar{\theta}) =< \cos\vartheta >$, and the two E_1 and E_2 functions are given by $E_1(x) = \exp(-2/\pi\cot\bar{\theta}\cot x)$, and $E_2(x) = \exp(-1/\pi\cot^2\bar{\theta}\cot^2 x)$. The shadowing function is thus given by:

$$S(i, e, \alpha) \simeq \frac{\mu_e}{\mu_e(0)}\frac{\mu_0}{\mu_{0e}}\frac{\chi(\bar{\theta})}{1 - f(\psi) + f(\psi)\chi(\bar{\theta})[\mu_0/\mu_{0e}(0)]} \tag{3.18}$$

with $f(\psi) = \exp(-2\tan(\psi/2))$. Similar expressions are obtained in the case of $e \leq i$ (see Hapke, 1993 pp. 344-345).

3.1.6 Integral phase curve

The result all these component is Eq. (3.1) which is a three-variable function, hence it can be compared with the observed phase curve, only if this last one is resolved, i.e. if the incident and emission angles are available for each surface point. This requires the use of a detailed shape model of the object and of the information on the observation geometry. This is not always possible and very time-consuming, therefore it may be useful to obtain e model that could be compared with the disk-integrated flux of the object, as function of the sole phase angle of observation. This is obtained by integrating Eq. (3.1) over the incident and emission angles in the simultaneously visible and illuminated hemispheres, which gives the integral phase curve model. For the assumption of a perfect spherical shape, if the coherent backscattering

opposition effect is ignored and only the shadow hiding process is invoked, the integration yields (Li et al., 2004):

$$\langle r \rangle(\alpha) = \frac{A_p(\bar{\theta})}{A_p(0)} \left\{ \left[\frac{\mathrm{w}}{8} \left[\left(1 + B_s(\alpha) \right) p(\alpha) - 1 \right] + \frac{r_0}{2}(1 - r_0) \right] F(\alpha) + \frac{2}{3} r_0^2 G(\alpha) \right\} K(\alpha, \bar{\theta}) \tag{3.19}$$

where F and G factors are functions of the sole phase angle expressed by:

$$F(\alpha) = 1 - \sin\left(\frac{\alpha}{2}\right) \tan\left(\frac{\alpha}{2}\right) \ln\left[\cot\left(\frac{\alpha}{4}\right) \right] \tag{3.20}$$

$$G(\alpha) = \frac{\sin(\alpha) + (\pi - \alpha)\cos(\alpha)}{\pi} \tag{3.21}$$

$K(\alpha, \bar{\theta})$ is the roughness correction factor, analogous to S factor in Eq. 3.1, numerically calculated and tabulated by Hapke (1993, p. 354). $A_p(\bar{\theta})$ and $A_p(0)$ are the geometric albedos of a surface with roughness parameter $\bar{\theta}$, and of a perfectly smooth surface, respectively:

$$A_p(\bar{\theta}) = \frac{\mathrm{w}}{8} \left[(1 + B_{0,s}) p(0) - 1 \right] + U(\mathrm{w}, \bar{\theta}) r_0 \left(1 + \frac{r_0}{6} \right) \tag{3.22}$$

$$A_p(0) = \frac{\mathrm{w}}{8} \left[(1 + B_{0,s}) p(0) - 1 \right] + r_0 \left(1 + \frac{r_0}{6} \right) \tag{3.23}$$

where roughness correction $U(\mathrm{w}, \bar{\theta})$ in equation (3.22) has also been numerically calculated by Hapke (1993, p. 353).

3.1.7 Hapke's parameters

Eq. 3.1 and 3.19 allow to model respectively the resolved and the integrated observed flux as function of the phase angle and to eventually retrieve the relevant parameters describing the properties of the surface of the body either as averaged over the surface, or as resolved maps.

Those parameters are ultimately:

w (single scattering albedo): describes the intrinsic scattering efficiency of the regolith single particles; it depends mainly on the particles composition.

g (cosine asymmetric factor): describes the spatial pattern of the light scattered by single particles; it is positive for small and transparent particles and negative for big and opaque particles;

$B_{S,0}$ and h_S (intensity and width of the SHOE): indicate the non-linear increase of reflectance at zero phase angle due to the shadow hiding effect;

$B_{C,0}$ and h_C (intensity and width of the CBOE): indicate the non-linear increase of reflectance at zero phase angle due to the coherent backscattering effect; these are often disregarded;

$\bar{\theta}$ (roughness parameter): is the average mean slope of the facets describing the rough surface; it is usually higher for small bodies.

Hapke considers that these add-hoc defined parameters are therefore able to represent physically the surface and to give information such to solve, at least partially, the question about the nature of the material that form these bodies, and eventually to infer hypothesis on the history and the evolution that they experienced.

Howevre, modeling the curve and fit the parameters is often very challenging due to the high degeneracy of some parameters and to some divergence problems in the various fitting methods. However many small bodies phase curves have been modeled by various authors and are reported as a summary in Tab. 3.1.

Object Name	w	h_S	$B_{S,0}$	g	θ	λ[nm]	Reference
ast. 2867 Steins	0.64	0.074	0.63	-0.28	28	630	Spjuth (2009)
ast. typical type S	0.23	0.020	1.32	-0.35	(20)	540	Helfenstein+(1989)
ast. typical type C	0.037	0.025	1.03	-0.47	(20)	540	Helfenstein+(1989)
ast. 1 Ceres	0.070	(0.06)	(1.6)	(-0.40)	48	535	Li+(2006)
ast. 243 Ida	0.22	0.020	1.53	-0.33	18	560	Helfenstein+(1996)
ast. Dactyl	0.21	(0.020)	(1.53)	-0.33	23	560	Helfenstein+(1996)
ast. 951 Gaspra	0.36	0.060	1.63	-0.18	29	560	Helfenstein+(1994)
ast. 433 Eros	0.33	0.010	1.40	-0.25	28	550	Li+(2004)
ast. 253 Mathilde	0.035	0.074	3.18	-0.25	19	700	Clark+(1999)
ast. 25143 Itokawa	0.42	0.01	0.87	-0.35	26	1570	Kitazato+(2008)
com. 19P/Borrelly	0.057	0.039	1.00	-0.43	22	660	Li+(2007b)
com. 9P/Tempel 1	0.039	(0.01)	(1.00)	-0.49	16	550	Li+(2007a)
com. 81P/Wild 2	0.035	(0.01)	(1.00)	-0.53	27	700	Li+(2008)

Table 3.1: Hapke's parameters obtained for several small bodies of the Solar System (Spjuth, 2009).

3.1.8 Debated issues

Shepard and Helfenstein (2007) claim that Hapke's model does not represent a proper description of the scattering process and that Hapke's parameters do not have an actual physical meaning because of the coupling of different parameters acting on the same physical effect.

Hapke's theory considers that the scattering process of electromagnetic radiation from particulate media, such as planetary regoliths, is very complex and the exact numerical solution is usually useless because the absolute accuracy in not such high in planetary applications. He considers that scattering models based on key assumptions and simplifications are more convenient and, although approximate, describe the essential physics of the problem.

Cheng and Domingue (2000) compared accurate numerical solutions of the radiative transfer equation with Hapke's estimates, demonstrating that the Hapke's equations were accurate to within 7%.

Moreover, Hapke's is the most widely used model in solving the inverse scattering problem (e.g. Li et al., 2004, 2006, 2007a, 2007b, 2008; Helfenstein et al., 1994, 1996; Kitazato et al., 2008), therefore the intention to compare the results with those obtained by other authors for other asteroids, with the final aim to obtain a wider picture of the asteroidal population photometric properties, somehow forces to use this model.

These are the reasons why this model will be used in Chapter 4 to perform asteroid 21 Lutetia's phase curve analysis.

3.2 Other light scattering models

However, apart from Hapke, several other models have been proposed to deal with the surface light scattering problem. However, most of these models are almost completely empirical and do not attempt to describe realistically the scattering behavior of a particulate surface. For completeness, a brief description of these alternative models is presented here.

Lambert's

Lambert reflection law (Lambert, 1760) describes a highly simplified case which assumes that the brightness of a surface only depends on the incident angle, and is independent on the emission angle. In this model the surface results equally bright from every viewing direction, being perfectly diffusive. This model may adequately describe very high-albedo surfaces such as snow while bodies as asteroids and comets do not show a good fit to Lambert's reflection law. The analytic expression of Lambert's law is:

$$r_L(i, e, \alpha) = \frac{1}{\pi} A_L \mu_0 \tag{3.24}$$

where $\mu_0 = \cos i$ and A_L is the Lambert's albedo which equals one for a perfectly diffusive Lambertian surface.

Minnaert's

Minnaert's law (Minnaert, 1941) is a generalization of Lambert's law and depends on both the incident angle and the emission angle. It describes the reflectance sufficiently well only for small phase angles. The expression yields:

$$r_M(i, e, \alpha) = A_M \mu_0^k \mu^{k-1} \tag{3.25}$$

where $\mu = \cos e$, k is called *limb darkening parameter* and A_M is the Minnaert's albedo.

Lommel-Seeliger's

The Lommel-Seeliger law is a single-scattering model, suitable only for uniform particles in low-albedo surfaces where multiple scattering is negligible. It can be considered a rough simplification of Hapke's model:

$$r_{LS}(i, e, \alpha) = \frac{\mathrm{w}}{4\pi} \frac{\mu_0}{\mu_0 + \mu} \tag{3.26}$$

Lunar-Lambert's

Lunar-Lambert's law is another empirical law describing the behavior of the reflectance. It is a weighted sum of the Lommel-Seeliger law and Lambert's law:

$$r_{LL}(i, e, \alpha) = A_{LL} \left[(1 - L(\alpha)\mu_0 + 2L \frac{\mu_0}{\mu_0 + \mu} \right] \tag{3.27}$$

where L describes the degree of limb darkening (as k in Minnaerts law) and A_{LL} is the Lunar-Lambert's albedo.

Lumme and Bowell's

Lumme and Bowell have used, as Hapke, a physical model to parametrize most of the evident effects in light scattering process by regoliths. The mathematical formalism is somewhat different from that of Hapke, but they introduce similar assumptions. The major difference is that in Lumme and Bowell's model the roughness affects only the single-scattering term (Bowell et al. 1989).

Shkuratov

Shkuratov provided also a physically-based model of the light scattering process but he ignored all angle dependence of reflectance over the disk. Hence the model is not appropriate for disk-resolved photometry (Poulet et al. 2002).

Mishchenko

Mishchenko developed an exact numerical model that solves Maxwell's equations and the radiative transfer equation exactly for discrete media. However, it appears to be not applicable to planetary regoliths (Hapke et al. 2009).

Mie

The Mie theory is used for homogeneous isolated spherical particles. This is highly idealistic and not applicable since regolith particles are irregular in shape and in close contact with each other. However it provides an exact solution for big particles and may be useful in dust coma scattering analysis.

Chapter 4

Photometric Analysis of Asteroid 21-Lutetia

4.1 Instrument and data description

The data analyzed in this chapter have been obtained through the multiband visible camera onboard Rosetta: OSIRIS (see Sec. 2.3.4). It is made of two different telescopes: the Narrow Angle Camera (NAC) and the Wide Angle Camera (WAC), which have identical CCDs and share the same electronics. The main optical characteristics of the two cameras are summarized in Tab. 4.1. Both cameras are equipped with a plane-parallel, anti-reflection coated plate, referred to as Anti-Radiation Plate (ARP), situated on the front of both CCDs for radiation shielding.

	NAC	**WAC**
Optical design	3-mirror off-axis	2-mirror off-axis
Detector type	CCD 2048×2048 px	CCD 2048×2048 px
Pixel dimension [μm]	13.5 × 13.5	13.5 × 13.5
Angular resolution [μrad px^{-1}]	18.6	101
Focal length [mm]	717.4	140 (sag)/131(tan)
Mass [kg]	13.2	9.48
Field of view [°]	2.20 × 2.22	11.35 × 12.11
F-number	8	5.6
Spatial scale from 1 km [cm px^{-1}]	1.86	10.1
Wavelength range [nm]	250–1000	240–720
Number of filters	12	14
Estimated detection threshold [m$_V$]	21–22	18

Table 4.1: Basic parameters of NAC and WAC telescopes.

The NAC camera has been designed to characterize the nucleus of the comet and the two asteroids at high spatial resolution. It has a small field of view of about $2^\circ \times 2^\circ$ and is provided with a set of 11 medium-band filters (Fig. 4.1) that cover the range between 250 nm and 1 μm. In addition, it has a neutral density filter, and four focusing plates: Far Focusing Plates for the UV range (FFP-UV) and visible range (FFP-Vis), Near Focusing Plates for UV (NFP-UV) and visible (NFP-Vis). Filters and focusing plates are mounted in two wheels so that two optics can be used simultaneously, e.g. FFP-Vis and Orange filter. Typically the observations are identified by a "filter combination" indicated by Fxy where x is the number of the filter used in the first wheel, and y is the number of the filter used in the second wheel, for example NAC filter combination F82 refers to observations made using simultaneously Neutral density filter, which is position 8 in the first wheel, and Orange filter, which is position 2 in the second wheel. (see Tab. 4.2 for filters and focusing plates positions and properties).

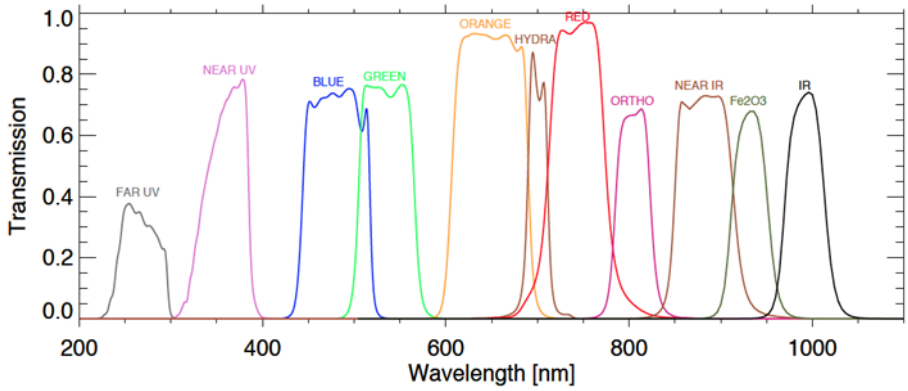

Figure 4.1: NAC bandpass filters.

The WAC camera has been designed to study the coma environment and in particular gas emissions and dust features. For this purpose, the WAC has a rather large field of view, about $12^\circ \times 12^\circ$, and covers a relatively wide spectral range, from 240 nm to 720 nm. Its main 12 narrowband filters (Fig. 4.2) are centered either on molecular emission bands such as CS, OH, NH, CN, NH_2, OI and Na, and on their vicinity for the measure of the relative continuum flux, i.e. UV245, UV295, UV325, UV375, Vis610. In addition, two broadband filters are provided: the Green filter, twin of the NAC one, and the context Red filter. Filters are mounted, as in the NAC telescope, in two filter wheels. Here, however, the first position of each wheel is left

name	**central wavel.** [nm]	**band-width** [nm]	**peak trans.** [%]	**objective**	**wheel**	**N.**
FFP-UV	250-850		> 99	UV focusing plate	1	1
FFP-Vis	250-1000		> 95	Vis focusing plate	1	2
FFP-IR	300-1000		> 99	IR focusing plate	2	1
NFP-Vis	300-1000		> 98	Vis focusing plate	1	3
Neutral	640.0	520.0	5.0	neutral density filter	1	8
Far-UV	269.3	53.6	37.8	surface spectral refl.	2	5
Near-UV	360.0	51.1	78.2	surface spectral refl.	2	6
Blue	480.7	74.9	74.6	surface spectral refl.	2	4
Green	535.7	62.4	75.8	surface spectral refl.	2	3
Orange	649.2	84.5	92.4	surface spectral refl.	2	2
Hydra	701.2	22.1	87.4	water hydration band	2	7
Red	743.7	64.1	96.0	surface spectral refl.	2	8
Ortho	805.3	40.5	69.8	orthopyroxene	1	5
Near-IR	882.1	65.9	78.4	surface spectral refl.	1	4
Fe2O3	931.9	34.9	81.6	iron-bearing minerals	1	6
IR	989.3	38.2	78.1	IR surface reflectance	1	7

Table 4.2: NAC filters and focusing plates properties.

empty and usually single filter "combinations" are used, e.g. F17 refers to the sole OI filter which is in the 7th position of the second wheel (see Tab. 4.3 for filters numbers and properties).

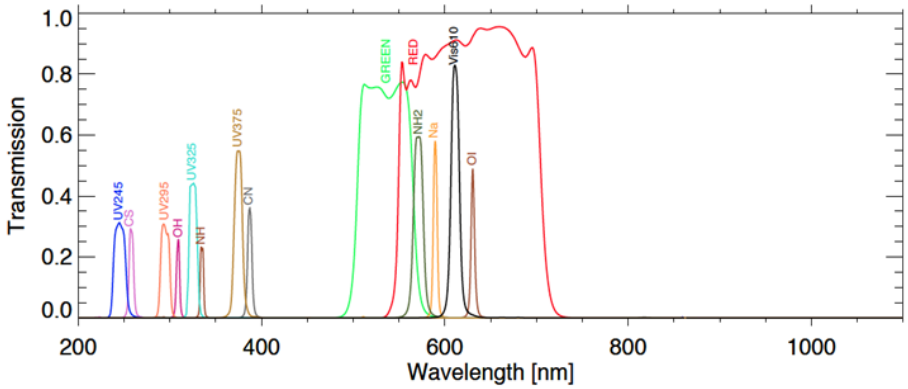

Figure 4.2: WAC bandpass filters.

The Main Belt asteroid 21 Lutetia was pictured by OSIRIS from a distance of about 3 170 km on 10 July 2010 on Rosetta's way to the comet

name	**central wavel.** [nm]	**band-width** [nm]	**peak trans.** [%]	**objective**	**wheel**	**N.**
Empty				empty position	1	1
Empty				empty position	2	1
UV245	246.2	14.1	31.8	continuum	1	3
CS	259.0	5.6	29.8	CS gas emission	1	4
UV295	295.9	10.9	30.4	continuum for OH	1	5
OH-WAC	309.7	4.1	26.0	OH gas emission	1	6
UV325	325.9	10.7	31.6	continuum for OH	1	7
NH	335.9	4.1	23.6	NH gas emission	1	8
UV375	375.6	9.8	57.3	continuum for CN	2	3
CN	388.4	5.2	37.4	CN gas emission	2	4
Green	537.2	63.2	76.8	dust continuum	1	2
NH_2	572.1	11.5	60.9	NH_2 gas emission	2	5
Na	590.7	4.7	59.0	sodium gas emission	2	6
Vis610	612.6	9.8	83.4	continuum for OI	2	8
OI	631.6	4.0	52.4	O gas emission	2	7
R	629.8	156.8	95.7	target detection	2	2

Table 4.3: WAC filters properties.

67P/Churyumov-Gerasimenko. Lutetia, with an equivalent diameter of 98±2 km (Sierks et al., 2011), was the biggest asteroid investigated by a space mission before Dawn's observations of 4 Vesta.

Rosetta's orbit allowed observations of Lutetia from many phase angles (see Fig. 4.3, from Magrin et al., 2012) over a wide wavelength range. The spacecraft approached the asteroid from a phase angle of about 10°, it reached the zero phase angle at a distance of about 16 500 km, about 18 min before the Closest Approach (CA) which was at 3 170 km from the asteroid and a phase angle of about 80°. After the CA the phase angle increased rapidly, and reached about 157°, while the solar elongation decreased down to 23°, so that 16 min after CA, OSIRIS had to stop acquiring images to avoid the direct burning sunlight. This very wide phase angle range is otherwise impossible to reach from Earth observations, where Lutetia's phase angle stays always below about 30°. Hereafter, for clarity, the phase angles before the minimum values, will be referred to as negative.

We concentrated mainly on 3 monochromatic observation sets (PC1-PC3) summarized in Tab. 4.4 and on 8 spectrophotometric observation sets (SP1-SP8), summarized in Tab. 4.5, where Lutetia was imaged rapidly through different filters.

Set ID	**Camera and Filter**	**Acquisition times**	**Phase angles**	**Dist to surface [km]**
PC1	NAC F82	06.18.40 - 13.35.39	[-10.7,-9.5]	509 185 - 116 060
		13.47.40 - 13.47.48	[-9.4, -9.3]	105 245 - 105 121
		13.54.40 - 14.34.38	[-9.3,-8.2]	98 950 - 63 013
		14.45.12	-7.7	53 523
		14.54.40 - 15.04.39	[-7.1,-6.1]	45 027 - 36 080
		15.15.12	-4.3	26 624
		15.22.40 - 15.29.50	[-2.0, 2.3]	19 975 - 13 646
		15.30.49	3.2	12 793
		15.32.31 - 15.36.39	[5.2, 12.8]	11 310 - 7 820
		15.38.15	17.9	6 529
		15.40.00 - 15.40.39	[26.4, 30.7]	5 200 - 4 756
	NAC F22	15.40.47	31.7	4 662
		15.41.35	38.4	4 164
		15.42.41 - 15.42.47	[50.4 - 51.8]	3 604 - 3 560
		15.54.35	63.0	3 293
		15.44.41 - 15.47.09	[80.4, 114.9]	3 169 - 3 915
		15.48.20	125.7	4 628
		15.50.21 - 15.50.39	[137.4, 138.7]	6 072 - 6 304
		15.52.14	144.2	7 573
		15.54.41	149.6	9 615
		16.00.17	156.2	14 470
PC2	WAC F17	06.34.41 - 11.24.40	[-10.7,-10.3]	494 782 - 233 886
		11.44.41 - 12.24.40	[-10.2,-10.1]	215 879 - 179 910
		12.34.41 - 13.44.41	[-10.0,-9.4]	170 898 - 107 933
		13.49.48 - 14.44.40	[-9.3, -7.7]	103 334 - 54 011
		14.45.28 - 15.04.40	[-7.6, -6.0]	53 287 - 36 063
		15.15.30 - 15.30.11	[-4.2,2.6]	26 364 - 13 346
		15.30.53 - 15.37.40	[3.3, 15.8]	12 730 - 6 991
		15.38.11 - 15.40.54	[17.7, 32.6]	6 577 - 4 583
		15.41.38 - 15.43.11	[38.9, 57.2]	4 132 - 3 409
		15.44.02 - 15.47.40	[70.0,120.0]	3 206 - 4 205
		15.48.06 - 15.51.39	[123.8, 142.4]	4 476 - 7 097
		15.52.19 - 15.59.40	[144.4, 155.7]	7 640 - 13 927
PC3	WAC F13	06.25.21	-10.7	503 183
		06.26.09	-10.7	502 457
		06.33.54	-10.7	495 493
		13.47.47 - 13.47.49	-9.4	105 139 - 105 105
		14.45.17	-7.7	53 446
		15.15.20	-4.2	26 510
		15.24.59 - 15.29.35	[-0.9, 2.1]	17 921 - 13 861
		15.30.43	3.1	12 872
		15.31.55 - 15.35.40	[4.4, 10.4]	11 833 - 8 628
		15.38.01	17.0	6 709
		15.41.22	36.5	4 292
		15.43.30	61.8	3 314
		15.47.49	121.4	4 301
		15.52.06	143.8	7 465
		16.00.39	156.5	14 789

Table 4.4: Lutetia monochromatic observations data sets.

Set ID	Camera	Acquisition times	Filters exposed	Phase angles	Dist [km] to surface
SP1	WAC	13.44.39.265 - 13.49.50.109	F17 F31 F51 F71 F13 F15 F16 F18 F17	[-9.4,-8.8]	107 962.9 - 101 799.2
	NAC	13.44.41.233 - 13.51.30.485	F15 F16 F84 F83 F82 F87 F88 F58 F51 F41 F61 F71		
SP2	WAC	14.44.40.178 - 14.45.28.546	F17 F31 F51 F71 F13 F15 F16 F18 F17	[-7.74,-7.66]	54 011.4 - 52 740.5
	NAC	14.44.41.233 - 14.46.05.075	F15 F16 F84 F83 F82 F87 F88 F58 F51 F41 F61 F71		
SP3	WAC	15.14.41.474 - 15.15.30.398	F17 F31 F51 F71 F13 F15 F16 F18 F17	[-4.4,-4.1]	27 096.4 - 25 852.2
	NAC	15.14.41.224 - 15.16.04.794	F15 F16 F84 F83 F82 F87 F88 F58 F51 F41 F61 F71		
SP4	WAC	15.30.11.201 - 15.30.53.510	F17 F31 F51 F71 F13 F15 F16 F18 F17	[2.6,4.2]	13 346.4 - 11 978.4
	NAC	15.30.13.208 - 15.31.45.434	F15 F16 F84 F83 F82 F87 F88 F41 F61 F71		
SP5	WAC	15.37.40.166 - 15.38.11.418	F17 F31 F51 F71 F13 F15 F16 F18 F17	[15.8,21.4]	6 991.4 - 5 893.2
	NAC	15.37.41.223 - 15.39.04.399	F15 F16 F84 F83 F82 F87 F88 F51 F41 F61 F71		
SP6	WAC	15.40.54.950 - 15.41.38.925	F17 F31 F51 F71 F13 F15 F16 F18 F17	[32.6,42.5]	4 582.8 - 3 933.8
	NAC	15.41.11.312 - 15.42.00.263	F16 F24 F23 F22 F27 F41 F71		
SP7	WAC	15.43.11.917 - 15.44.02.793	F17 F71 F13 F15 F16 F18 F17	[57.1,70.0]	3 412.2 - 3 212.3
	NAC	15.43.11.261 - 15.44.00.348	F16 F24 F23 F22 F28 F41 F71		
SP8	WAC	15.47.40.232 - 15.48.06.688	F17 F71 F13 F15 F16 F18 F17	[120.0,131.3]	4 205.3 - 5 189.5
	NAC	15.47.41.251 - 15.49.09.907	F15 F16 F24 F22 F27 F28 F51 F41 F61 F71		

Table 4.5: Lutetia spectrophotometric data sets.

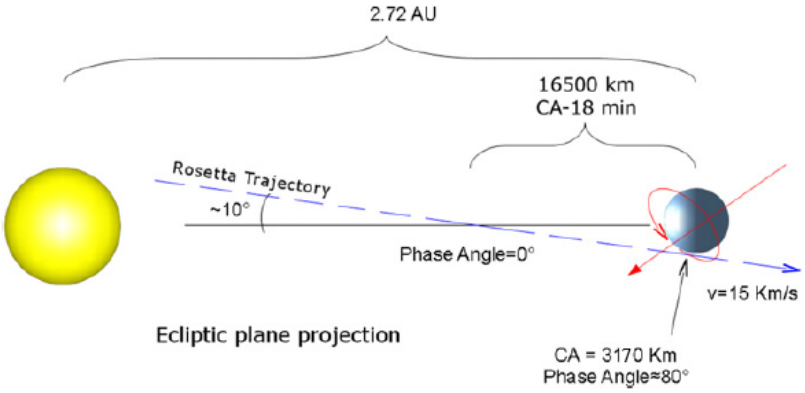

Figure 4.3: Lutetia fly-by geometry (Magrin et al., 2012)

4.2 Photometric Calibration

The raw images from the spacecraft are provided in DN s^{-1}, thus an absolute calibration is necessary to convert them into physical flux units, i.e. W m^{-2} nm^{-1} sr^{-1}, which give the total energy emitted by a unit surface of the target, in a unit wavelength and a unit solid angle.

The conversion factor needed to perform this operation is called *absolute calibration factor* and will be ofter referred to as "abscal" factor. The calculation of the abscal factors needs some input: the observations of a well-known reference star, such as Vega, from the same instrument which performed science observations, the calibrated absolute flux of this star, the instrumental response and the resolution of the camera.

The abscal factor A_{xy} of Fxy filter combination is given by (Magrin et al., 2012):

$$A_{x,y} = \frac{K_{x,y} \cdot pxsz \cdot \int_0^{+\infty} S(\lambda)F(\lambda)d\lambda}{\int_0^{+\infty} \varphi_{star}(\lambda)S(\lambda)F(\lambda)d\lambda} \tag{4.1}$$

where K_n is the total count rate measured in the observation of the reference star, $pxsz$ is the mean camera pixel resolution expressed in steradians, $F(\lambda)$ is the transmissivity of the particular filter combination, while $S(\lambda)$ refers to all other instrumental efficiencies (ARP transmissivity, mirrors reflectivity, CCD quantum efficiency), while $\varphi_{star}(\lambda)$ is the spectral irradiance of the reference star outside the instrument.

Mainly two reference stars have been observed by OSIRIS: Vega and 16

Cyg, a solar analog. However this last one is a binary star and contamination errors arose when counting its aperture photometry. Thus Vega has been usually taken as reference star. HST CALSPEC (Calibration Database System, Space Telescope Science Institute - http://www.stsci.edu/hst/observatory/crds/calspec.html) spectrum of Vega has been used for its reference spectral irradiance.

Instrumental response data reported in the official OSIRIS database and acquired before the spacecraft's launch, have been used (see for example Fig. 4.4). Average pixel resolutions over the field of view of the two cameras have been used:

$$pxsz_{WAC} = 9.982 \cdot 10^{-9} \text{ sr} \tag{4.2}$$

$$pxsz_{NAC} = 3.547 \cdot 10^{-10} \text{ sr} \tag{4.3}$$

The calibrated flux of the object in each filter combination is thus obtained by dividing the raw image in DN s^{-1}, corrected for bias, flat field etc., by the abscal factor.

The reflectivity values are then obtained by dividing the flux-calibrated images by the incoming solar flux incident onto the surface of the object.

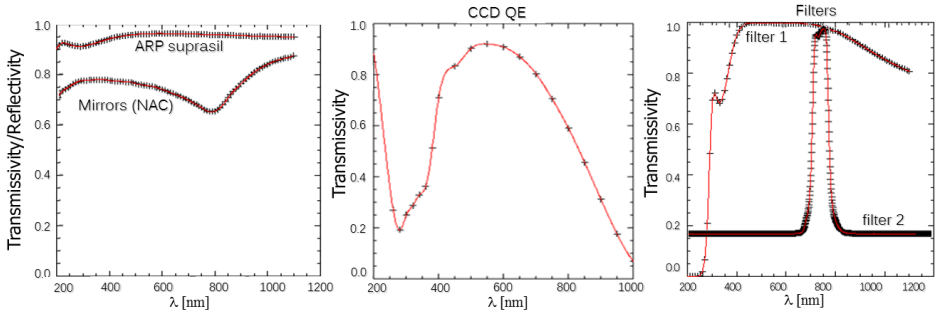

Figure 4.4: OSIRIS instrumental response.

4.3 Integral Phase Curve Analysis

The photometry has been performed using a threshold technique, i.e. considering only the portion of the asteroid above a threshold equivalent to 70% of the maximum signal (yellow contour in Fig. 4.5).

This technique has been adopted after several tests to select the best solution and has been chosen for two main reasons. The first is that simple

aperture photometry would have exhibit a problem in this case for the presence of ghosts. As visible from the red contour in Fig. 4.5, indeed, some filters show ghost images, caused by the optics of the camera, and highlighted by the large difference in luminosity between the asteroid and the background. The subtraction of ghosts of extended sources is definitely a non-straightforward problem, but selecting only the illuminated part of the target, the flux coming from the ghost results negligible and can be ignored.

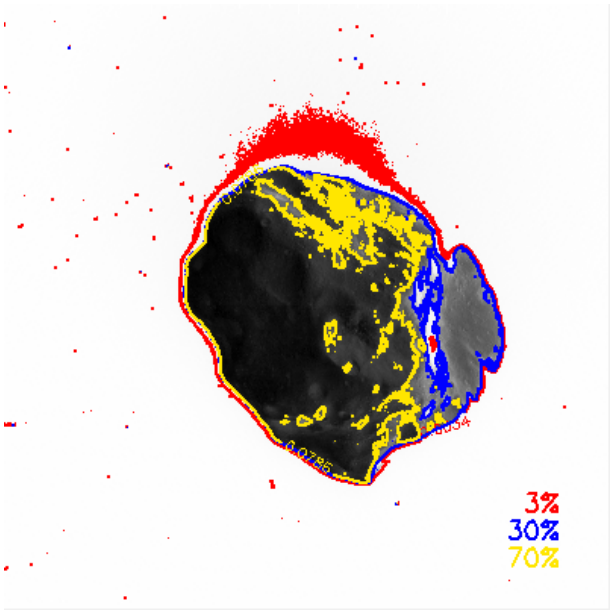

Figure 4.5: NAC F71 image in set SP5 (see Tab. 4.5) with 3%, 30% and 70% threshold contours indicated.

The second reason is that a different threshold value which would define, for example, straight the limb of the asteroid (as the blue contour in Fig. 4.5) has been found to be unsatisfying in comparing images coming from NAC and WAC cameras, since they have different pixel scales. This is mainly due to the limb darkening effect, a diminished intensity of a body from the center of the image to the edge. Including for both cameras the limb of the asteroid means averaging, for the WAC, over a much larger number of limb pixels as respect to NAC images, due to its smaller resolution. Numerous tests showed that the best solution is therefore 70% threshold which compensate the limb darkening effect, considering nearly the sole illuminated pixels.

Reflectances have been computed with this technique, using a reference solar flux from OSIRIS database and correspondent error bars have been

calculated from the Poissonian error on images in counts, propagated for every computation made.

Three main filters have been used to sample Lutetia's phase curve during the fly-by (see Tab. 4.4), the WAC filters OI (WAC F17) and UV375 (WAC F13) and the NAC Orange filter (NAC F82-F22). After 15:40 UT of July 10, 2010, up to the end of the encounter, NAC filter F82 has been substituted by F22, i.e. the FFP-Vis has been preferred to the Neutral filter for Orange observations. F82 and F22 filter combinations share indeed the same bandpass and, if correctly calibrated, can be considered coherent. For each observation we computed the averaged reflectance over the illuminated part of the asteroid obtaining the complete phase curves for those three main filters (Fig. 4.6). They provide a good sampling of the curve, in particular for the peak at very low phase angles due to the opposition effect (see Sec. 3.1.4).

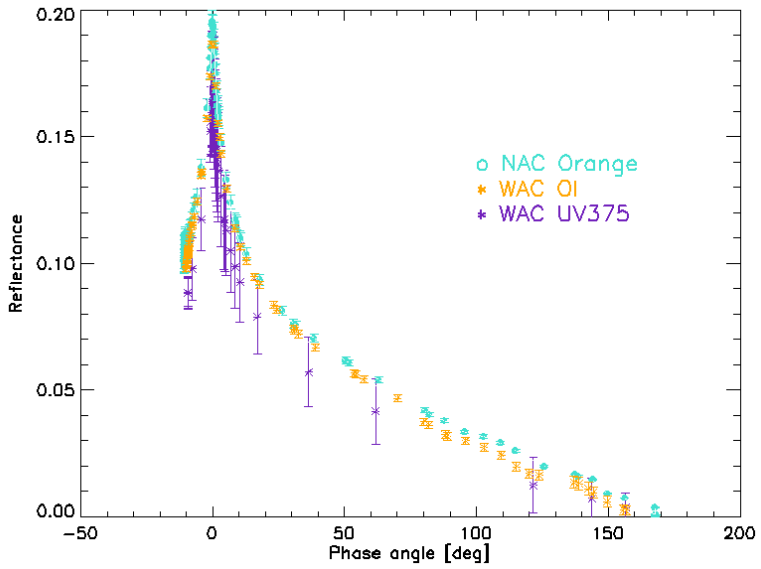

Figure 4.6: Lutetia phase curves observed in filters NAC Orange, WAC OI and WAC UV375.

As the observations in all other filters were not such tight in time (see spectrophotometric observation sets in Tab. 4.5), especially for small phase angles (Fig. 4.7), we used the information from the three well-known phase curves in Fig. 4.6 to obtain the shape and the position of the peak in the other curves.

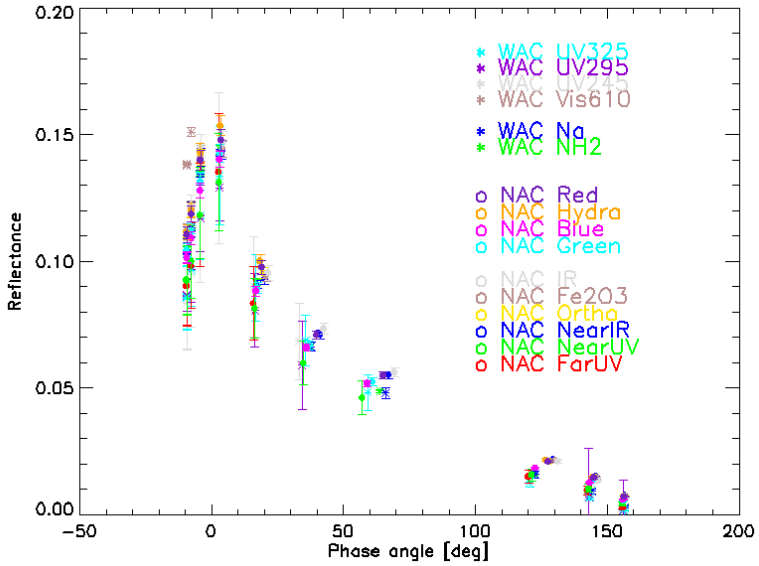

Figure 4.7: Lutetia under-sampled phase curves observed in filters other than NAC Orange, WAC OI and WAC UV375.

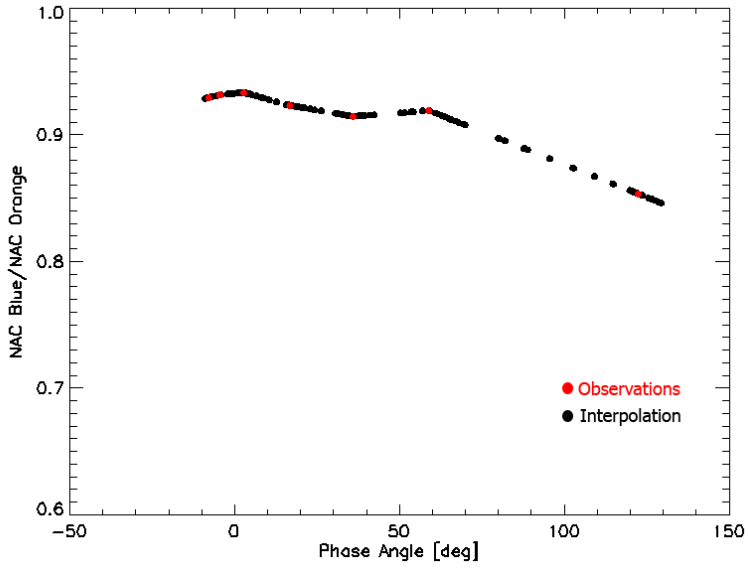

Figure 4.8: Lutetia NAC Blue reflectance divided by the reference NAC Orange reflectance, providing the normalization curve for NAC Blue phase curve "reconstruction".

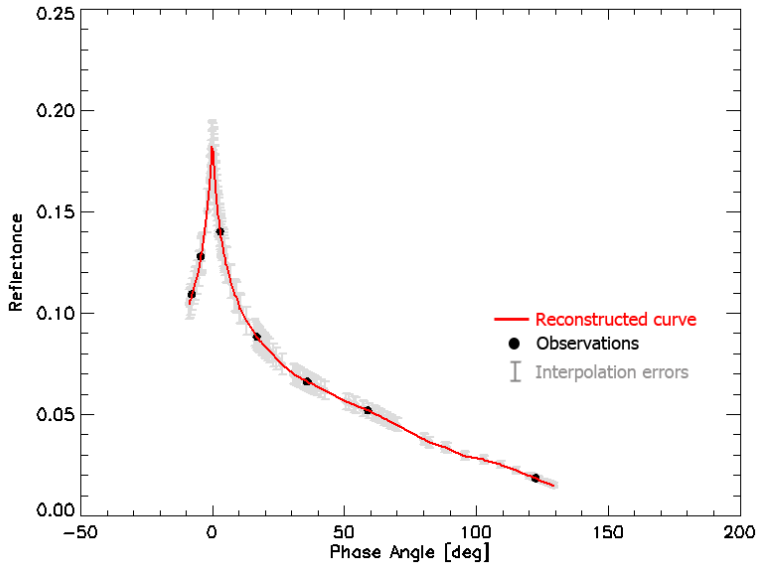

Figure 4.9: Lutetia NAC Blue filter phase curve "reconstructed".

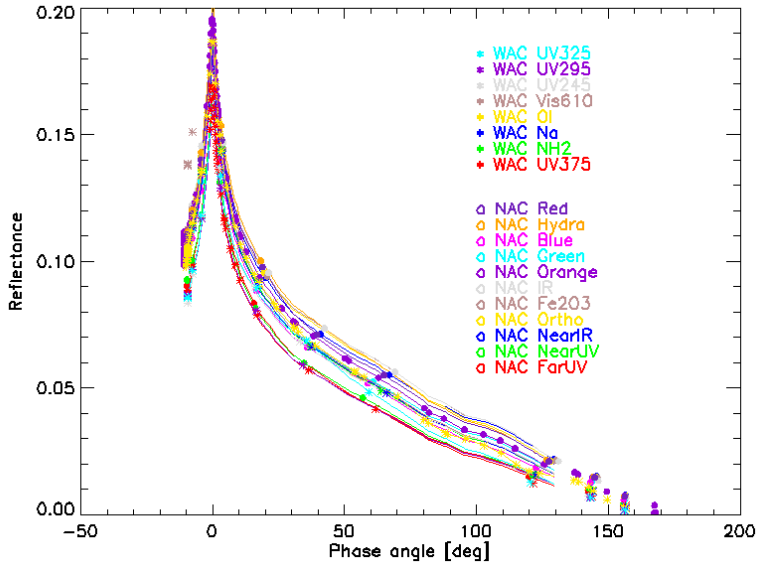

Figure 4.10: Lutetia phase curves "reconstructed" in all available filters.

We interpolated a phase curve for each camera, NAC Orange and WAC OI, preferred to WAC UV375 for the better sampling and the smaller errors, and we used them as reference for the other NAC and WAC curves respectively. We divided each curve for its reference, depending on the camera, obtaining a normalization curve as the one shown in Fig. 4.8.
Therefore we interpolated this curve, obtaining a scaling factor, depending on the phase curve slope, and we scaled the reference curve by this factor, in order to "reconstruct" the under-sampled phase curve. An example of the "reconstructed" phase curve (NAC Blue filter) is shown in Fig. 4.9.

Error estimate takes into account the propagation due to the interpolation steps which cause uncertainties bars to be much higher than those for real measured reflectances. These errors however, overestimate the photometric errors, since the autoconsistency of the phase curves is much better than the interpolated error bars. The resulting curves are plotted in Fig. 4.10 (without error bars for clarity) and show indeed a good consistency.

4.3.1 Hapke's modeling

We modeled the phase curves with the multiparametric integral phase function by Hapke (Eq. 3.19) to obtain the optical properties of the regolith layer covering the asteroid, responsible for the scattering process.
The fitting procedure has revealed a strong degeneracy of the various parameters due also to the limited number of observations and the high number of parameters to fit (see Sec. 3.1.7). In order to solve this problem, various iterations of the Levenberg-Marquardt fitting procedure (Levenberg, 1944; Marquardt, 1963) have been implemented, together with a set of initial parameters varying around the initial guess based on physical considerations.

Fig. 4.11, 4.12 and 4.13 show the resulting fits obtained for the three best sampled phase curves. The derived Hapke's parameters, from the modeling of the phase curves in all NAC and WAC filters are summarized in Tab. 4.6, in wavelength order. Hapke's modeling allows also to retrieve the geometric albedo A_p and the Bond albedo A_B for each filter, which are summarized in Tab. 4.7.

The resulting Hapke's parameters (Tab. 4.6) show that Lutetia particles are very highly reflecting, having a high single scattering albedo in the range 0.507-0.638, This is consistent with the overall geometric albedo of the surface, ∼0.170-0.209, that is higher than expected from a primitive object made of very dark carbonaceous materials.
The cosine asymmetry factor is positive, 0.12-0.42, meaning that the regolith particles mainly forward scatter the light, which is indicative of very small

particles, probably with diameter smaller than a micron. This is in agreement with the estimated age of Lutetia, about 3.6 Gyr for the oldest regions (Marchi et al., 2012), which suggests a long exposure to the cosmic ambient and a long-lasting crumbling of the regolith under the action of cosmic rays, solar wind, collisions and so on.

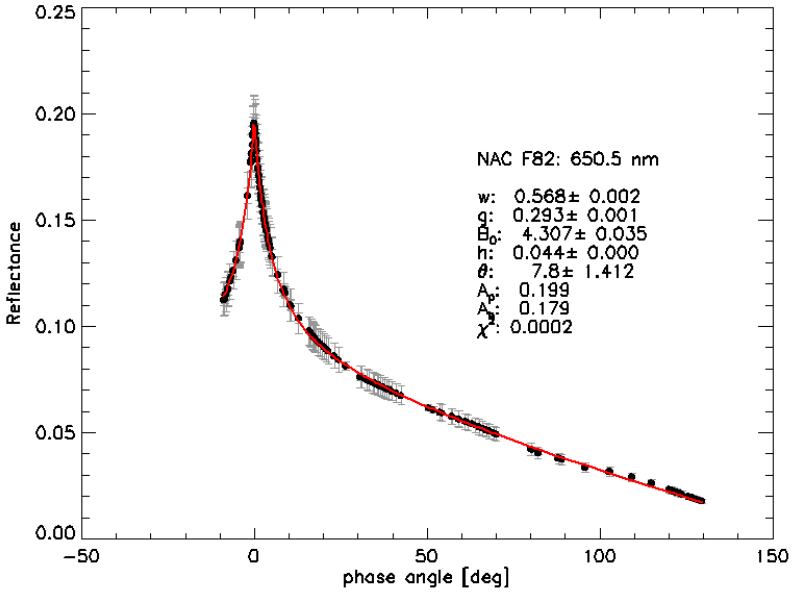

Figure 4.11: Hapke's multiparametric modeling of the NAC Orange phase curve.

The shadow hiding opposition effect is very high in intensity ($B_{0,s} > 1$) and narrow in angular dimension, ($h_s \ll 1$), suggesting that the particles are compact and opaque, as expected from very tiny silicates or carbonaceous grains, and that the body is not very porous, as expected from an old, big and primitive object, and confirmed by the high density value ($3.4 \pm 0.3 \cdot 10^3$ kg, Pätzold et al., 2011).
The mean slope angle is pretty small in the visible range, $0° - 10°$, suggesting an overall smooth surface, as confirmed by the images and expected for such a big object. However, UV filters show instead a quite higher mean slope angle, which may be due to the limit of the method that is probably not a very good representation in the UV region of the spectrum, considering also the under-sampling of the phase curves for these wavelengths.

For a more adequate and resolved modeling of the surface, a shape model is required in order to have a much larger number of points as respect to the

parameters to fit.

The wavelength dependence of h_s has been investigated. Our values show a wavelength-independent behavior within the error bars (Fig. 4.14), suggesting that the observed opposition effect is actually wavelength independent. This is typical for shadow hiding opposition effect, whereas coherent backscattering appears to be wavelength-dependent (Domingue et al., 2002; Li et al., 2004). This result supports our assumption of disregarding the coherent backscattering contribution in modeling the opposition effect (see Sec. 3.1.4).

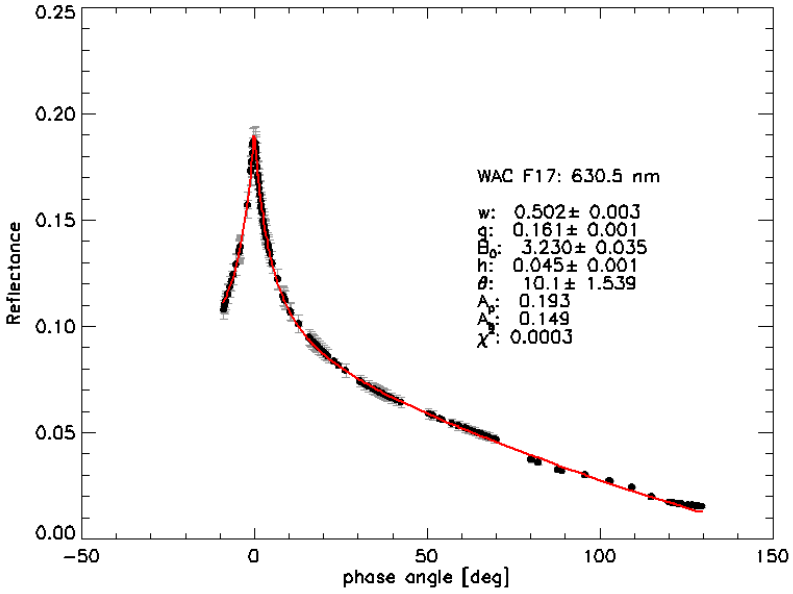

Figure 4.12: Hapke's multiparametric modeling of the WAC OI phase curve.

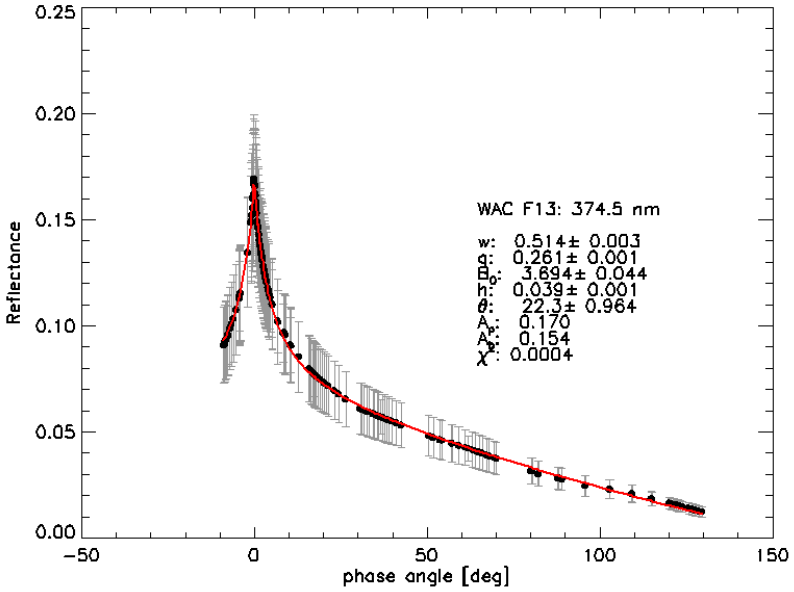

Figure 4.13: Hapke's multiparametric modeling of the WAC UV375 phase curve.

filter	λ	**w**	g	B_0	h	θ
WAC F31	246.2	0.548 ± 0.008	0.277 ± 0.004	3.549 ± 0.103	0.034 ± 0.0020	3.0 ± 9.9
NAC F15	269.3	0.507 ± 0.006	0.235 ± 0.002	3.606 ± 0.074	0.044 ± 0.0010	25.0 ± 1.5
WAC F51	295.9	0.507 ± 0.005	0.265 ± 0.002	3.736 ± 0.063	0.043 ± 0.0010	21.9 ± 1.3
WAC F71	325.9	0.494 ± 0.009	0.116 ± 0.004	2.345 ± 0.084	0.032 ± 0.0020	12.3 ± 4.9
NAC F16	360.0	0.508 ± 0.003	0.253 ± 0.001	3.735 ± 0.033	0.046 ± 0.0000	21.3 ± 0.7
WAC F13	375.6	0.514 ± 0.003	0.261 ± 0.001	3.694 ± 0.044	0.039 ± 0.0010	22.3 ± 1.0
NAC F84	480.7	0.512 ± 0.002	0.227 ± 0.001	3.725 ± 0.029	0.045 ± 0.0000	5.1 ± 1.9
NAC F83	535.7	0.558 ± 0.002	0.328 ± 0.001	4.741 ± 0.032	0.045 ± 0.0000	5.1 ± 1.7
WAC F15	572.1	0.532 ± 0.003	0.263 ± 0.001	4.063 ± 0.034	0.045 ± 0.0000	6.6 ± 1.6
WAC F16	590.7	0.536 ± 0.002	0.267 ± 0.001	4.040 ± 0.031	0.044 ± 0.0000	6.0 ± 1.6
WAC F18	612.6	0.539 ± 0.003	0.261 ± 0.001	4.025 ± 0.035	0.045 ± 0.0010	7.1 ± 1.6
WAC F17	631.6	0.502 ± 0.003	0.161 ± 0.001	3.230 ± 0.035	0.045 ± 0.0010	10.1 ± 1.5
NAC F82	649.2	0.568 ± 0.002	0.293 ± 0.001	4.307 ± 0.035	0.044 ± 0.0000	7.8 ± 1.4
NAC F87	701.2	0.617 ± 0.004	0.343 ± 0.002	4.676 ± 0.058	0.038 ± 0.0010	3.4 ± 4.2
NAC F88	743.7	0.619 ± 0.003	0.391 ± 0.002	5.247 ± 0.054	0.041 ± 0.0010	7.5 ± 1.9
NAC F51	805.3	0.623 ± 0.001	0.381 ± 0.001	5.062 ± 0.020	0.039 ± 0.0000	0.0 ± 0.0
NAC F41	882.1	0.626 ± 0.001	0.424 ± 0.001	5.735 ± 0.020	0.040 ± 0.0000	0.0 ± 0.0
NAC F61	931.9	0.635 ± 0.001	0.406 ± 0.001	5.305 ± 0.021	0.038 ± 0.0000	0.0 ± 0.0
NAC F71	989.3	0.638 ± 0.001	0.410 ± 0.002	5.510 ± 0.026	0.038 ± 0.0000	0.0 ± 0.0

Table 4.6: Hapke's modeling parameters resulting from Lutetia's phase curves analysis.

filter	λ	A_p	A_B
WAC F31	246.2	0.174	0.170
NAC F15	269.3	0.175	0.151
WAC F51	295.9	0.166	0.151
WAC F71	325.9	0.174	0.146
NAC F16	360.0	0.172	0.151
WAC F13	375.6	0.170	0.154
NAC F84	480.7	0.185	0.153
NAC F83	535.7	0.190	0.174
WAC F15	572.1	0.189	0.162
WAC F16	590.7	0.188	0.164
WAC F18	612.6	0.191	0.166
WAC F17	631.6	0.193	0.149
NAC F82	649.2	0.199	0.179
NAC F87	701.2	0.209	0.205
NAC F88	743.7	0.202	0.206
NAC F51	805.3	0.204	0.209
NAC F41	882.1	0.202	0.211
NAC F61	931.9	0.205	0.216
NAC F71	989.3	0.209	0.218

Table 4.7: Lutetia's albedos resulting from Hapke's modeling.

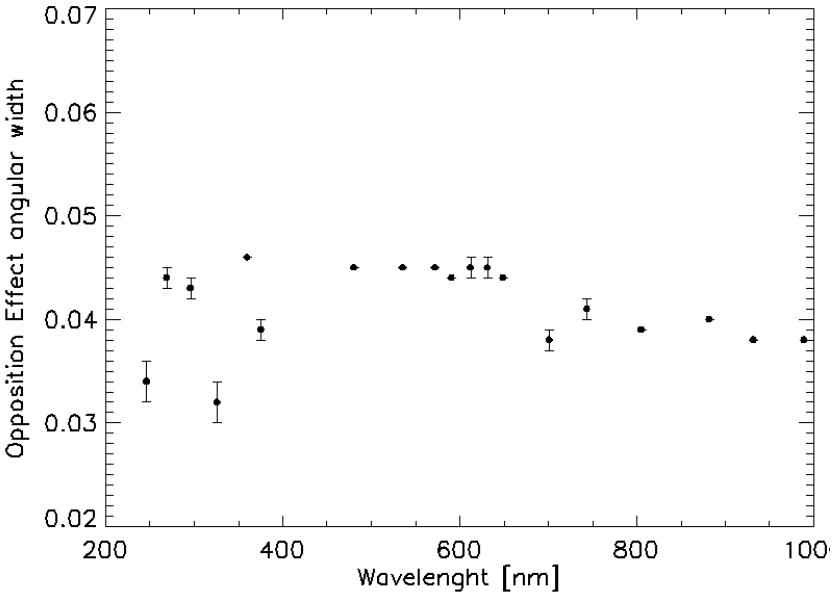

Figure 4.14: Investigation of the wavelength dependence of the opposition effect angular width h_s.

4.4 Spectrophotometry

Combining the integrated reflectances over the selected threshold in all available filters, for all the spectrophotometric observation sets in Tab. 4.5, we obtained a series of low-resolution spectra. Since the observation sets cover quite wide ranges of phase angles (see Fig. 4.15), especially sets SP5, SP6, SP7 and SP8, we corrected the spectra for the phase angle change inside each single set. In fact, different filters were acquired in wavelength order, and, due to the phase angle changing very rapidly, the spectral slope could be affected in a misleading way, influenced by a difference in illuminating condition occurring inside the same observation set.

With the use of the phase curves available in all filters, thanks to the "peak reconstruction", we were thus able to compute the "phase-corrected" spectra, fixed as if all different filters in a set were acquired at the central time and phase angle of the same set, despite the geometry variation inside each single set. This method increases the error bars of the reflectivity values, but, at the same time, it gives a more reliable description of the spectral trend.

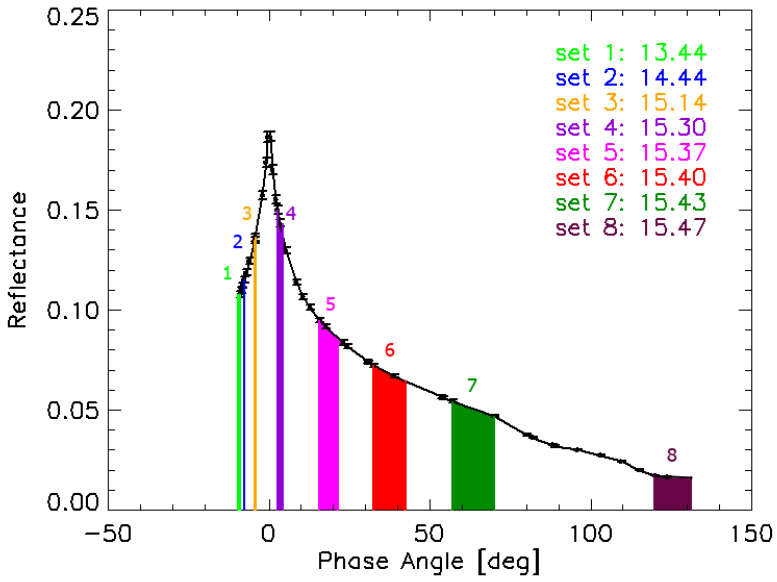

Figure 4.15: Spread in phase angle of each Spectrophotometric set in Tab. 4.5.

Resultant spectra are reported in Fig. 4.16 and 4.17. The vertical error

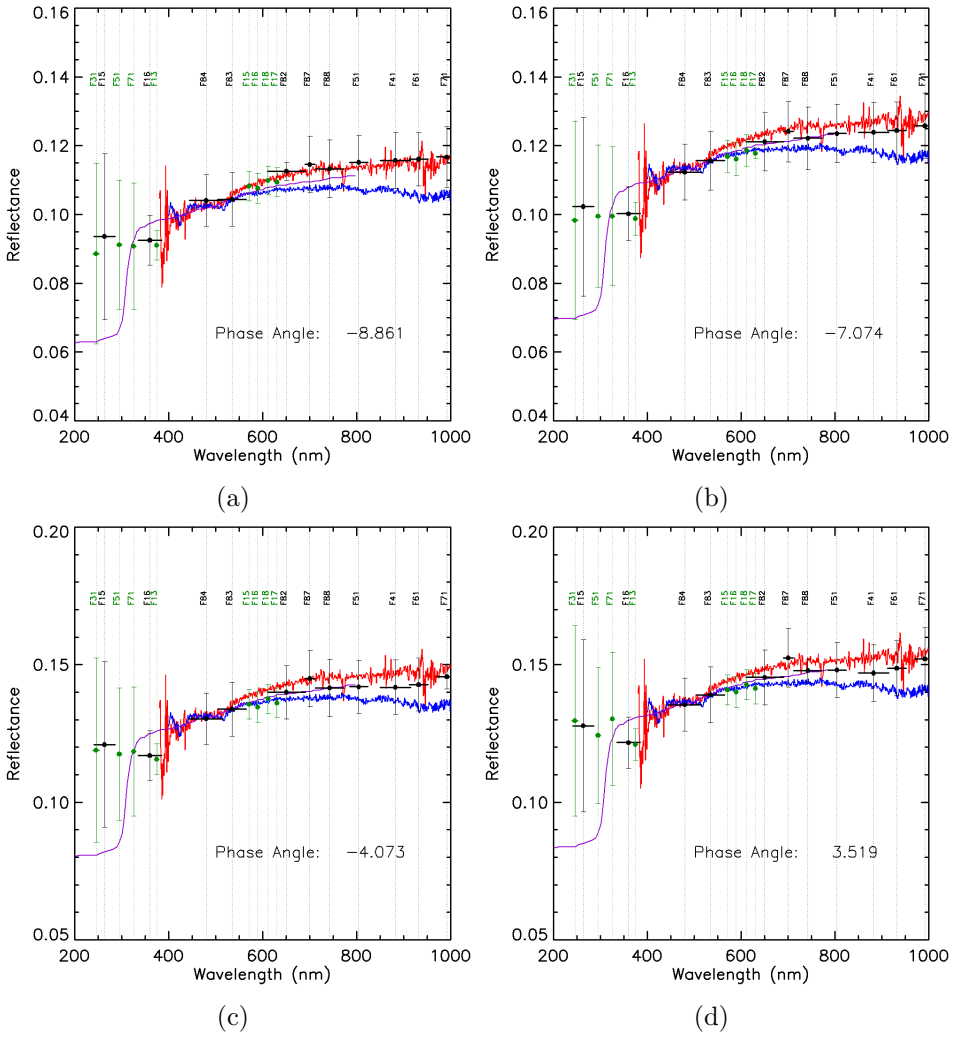

Figure 4.16: Spectrophotometry of Lutetia from sets SP1 to SP4 "phase corrected" and reported to phase angles: (a): -8.861 (b): -7.074 (c): -4.073 (d): 3.519

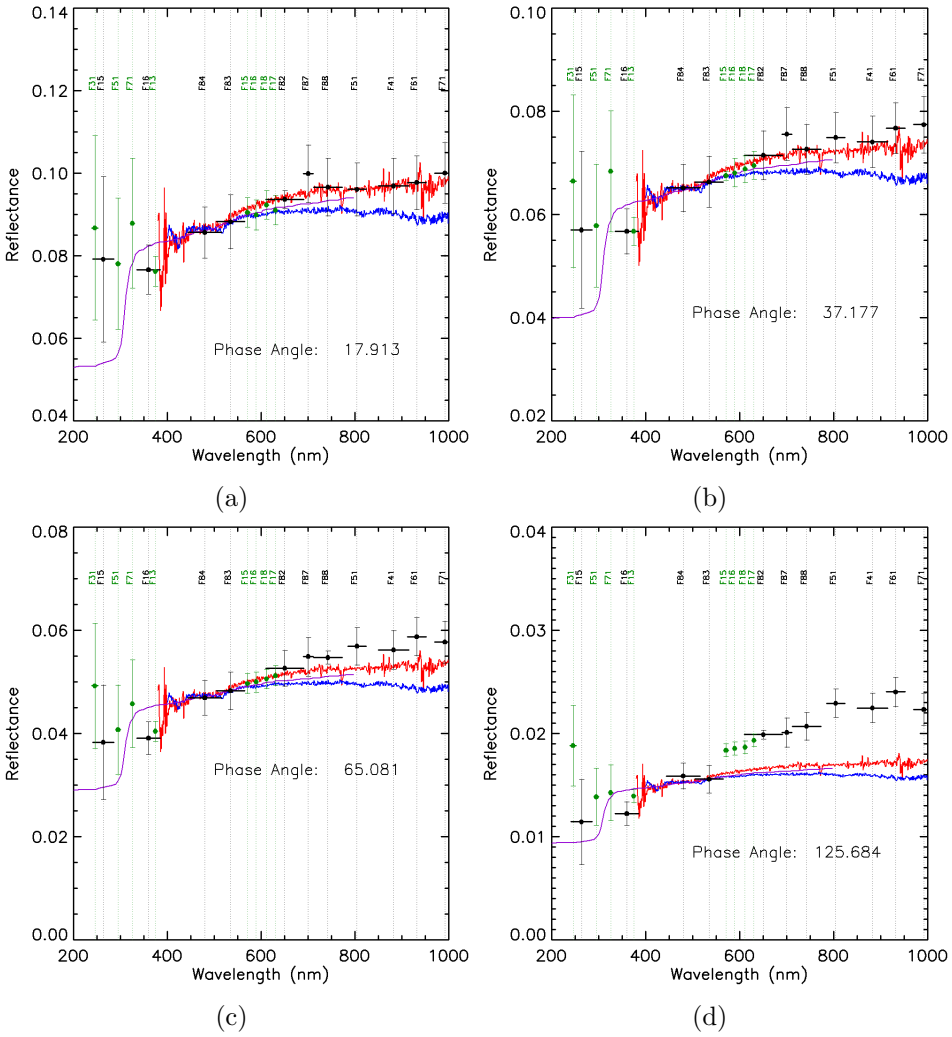

Figure 4.17: Spectrophotometry of Lutetia from sets SP5 to SP8 "phase corrected" and reported to phase angles: (a): 17.913 (b): 37.177 (c): 65.081 (d): 125.684

bars are due to photometric and calibration errors, while the horizontal bars refer to the wavelength width of the filters and do not represent errors.

We compared the spectrophotometry thus obtained with two ground based spectra illustrative of the reddest and bluest spectral visible slopes observed up to date of Lutetia surface, as shown in Lazzarin et al. (2010). The reddest spectrum was observed in May 2003 (Lazzarin et al., 2004) and the bluest in December (Lazzarin et al., 2009). They bound the same region spanned by Perna et al., (2010) data, but have a wider spectral range, hence we decided to use them as a reference. None of those ground-based data covers the UV range, therefore we considered also a spectrum acquired by Weaver et al. (2010) from Hubble Space Telescope (HST) in November 2008 and covering a spectral range from 150 to 700 nm. It shows a quick drop of the albedo by a factor of about 1.5 shortward of 300 nm and it is well confirmed by Rosetta-ALICE UV spectrograph data shortward of 200 nm (Stern et al., 2011).

The agreement with OSIRIS data is good inside error bars longward of 400 nm and the spectral behavior seems to be more consistent with the reddest ground based spectrum, while the UV filters do not seem to reproduce well HST observations. These filters, however, have much larger error bars due to the larger calibration errors in this spectral range.

The data show that Lutetia has a quite flat spectrum, without significant bands, that is compatible with both a carbonaceous chondrite or an enstatite chondrite composition, both quite primitive materials. There has been an high-pitched discussion about the composition of Lutetia because of such a flat spectrum, without a strong feature, but the high density of this body ($3.4 \pm 0.3 \cdot 10^3$ kg, Pätzold et al., 2011), combined with an unusually high albedo for C-type asteroids, tends to suggest more an enstatite chondrite rather than a carbonaceous chondrite composition, and an X-type taxonomic classification rather than a C-type.

An increase of the spectral slope with phase angle is also visible, above the error bars, especially in observation sets from SP5 to SP8. This effect is known as phase reddening and it is investigated in the next section.

4.5 Phase reddening

The phase angle seems to influence the slope of the spectrum so that a spectrum observed at high phase angles appears usually redder than a spectrum of the same object observed at low phase angles. This represents a problem for asteroids with featureless spectra, such as Lutetia, which are

allocated to a taxonomy class on the base of their sole spectral slope.

The phase reddening was first noted by Gehrels et al. (1964) in the lunar surface but ever since the explanation of this evidence has been uncertain. One hypothesis is that the phase reddening is due to the increased contribution of the multiple scattering at large phase angles as the wavelength and albedo increase (Hapke et al., 2012).

OSIRIS data provided the big opportunity to study multi-wavelengths observations of Lutetia at different phase angles allowing the investigation of the phase reddening behavior. Fig. 4.18 shows spectra acquired at different phase angles, all normalized to 1 at 550 nm. There is a clear evidence of increase in spectral slope with the increase of phase angle.

The reddening is usually expressed in %/100 nm between two wavelengths λ_1 and λ_2, and is defined as:

$$R(\lambda_1, \lambda_2) = \frac{r_2 - r_1}{\frac{r_1+r_2}{2}} \cdot \frac{100}{\lambda_2 - \lambda_1} \cdot 100 \qquad \%/100 \text{ nm} \tag{4.4}$$

where r_1 and r_2 are the reflectances of the body at wavelength λ_1 and λ_2, respectively. It simply represents the slope of the spectrum in a certain wavelength range.

Lutetia spectral slope has been measured between $\lambda_1 = 375$ nm and $\lambda_2 = 630$ nm, using as r_1 and r_2 the reflectances of Lutetia in the two best sampled WAC filters: WAC UV375 and WAC OI, respectively (Fig. 4.19a). In this wavelength range the reddening goes from 5%/100 nm at zero phase angle up to 13%/100 nm at 130° of phase angle. At longer wavelengths, between 650 nm and 880 nm, using NAC filters Orange and Near-IR, Lutetia shows a lower reddening (Fig. 4.19b), the slope going from 1%/100 nm at zero phase angle up to almost 6%/100 nm at 130° of phase angle.

This effect may be one of the possible explanation of the continuously variable slope of Lutetia spectrum. In Lazzarin et al. (2010) a comparison of Lutetia spectral slopes, computed in the range from 550 to 800 nm, is reported. The highest slope spectrum is from Barucci et al. (2005) at a phase angle $\alpha \sim 24°$, then there is a spectrum from Lazzarin et al. (2009) at $\alpha = 16°$, and then some of the spectra acquired by Perna et al. (2010), all at angles $\alpha < 1.4°$. While for the first two spectra cited, the redder behavior can be in part explained by the relatively high phase angles, in the Perna et al. (2010) spectra, the slope variation seems to be independent on the phase. Unfortunately all those observations are referred to the shadowed Lutetia South region, not observed by OSIRIS at the time of the fly-by.

This effect causes therefore a problem of the disentanglement between a chondrite and an enstatite composition which are only distinguished by

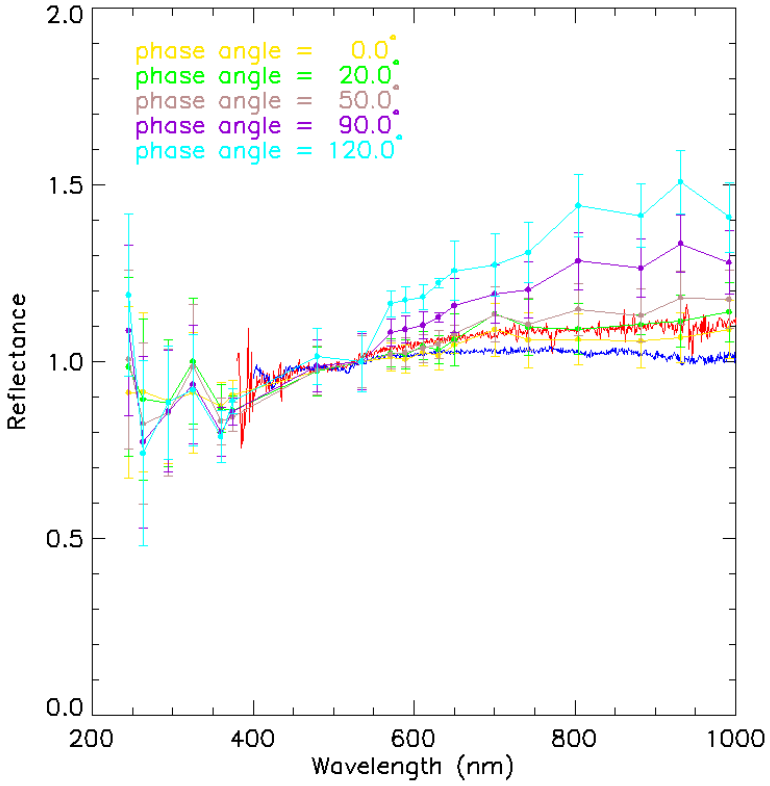

Figure 4.18: Spectral slope of Lutetia increasing with phase angles.

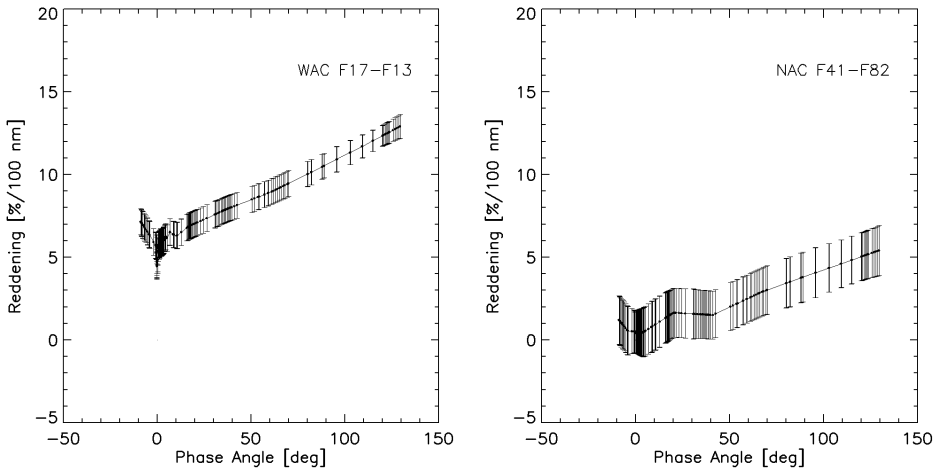

(a) (b)

Figure 4.19: Phase reddening measured (a) from 375 and 630 nm (WAC filters UV375 and OI) and (b) from 650 and 880 nm (NAC filters Orange and Near-IR)

their spectral slope. A further, deeper investigation is needed in order to solve the problem of Lutetia's surface composition and to find an exhaustive explanation of the phase reddening effect.

4.6 Color Variegation

Another photometric tool for the investigation of the compositional and physical properties of the surface of Lutetia is represented by the color maps. Ratios of images in different filters, corresponding to flux ratios, represent the color measurement and may show a possible color variegation of the surface.

A preliminary rescaling, shifting, and morphing of the images, obtained with the help of ITT-ENVI (the Environment for Visualizing Images of the International Telephone and Telegraph Corporation), has been performed in order to match and co-register the images in different filters. Due to the changing observing geometry, the limb portion of the surface was almost always deformed and the registration of the images was imprecise, but in the central portion, far from the edges, the matching resulted reliable.

The analysis has been focused on one particular region, the Baetica Region, which seems to be geologically the most interesting region (see

Massironi et al., 2012), showing indications of fresh material at the crater walls and debris deposits in the bottom regions.

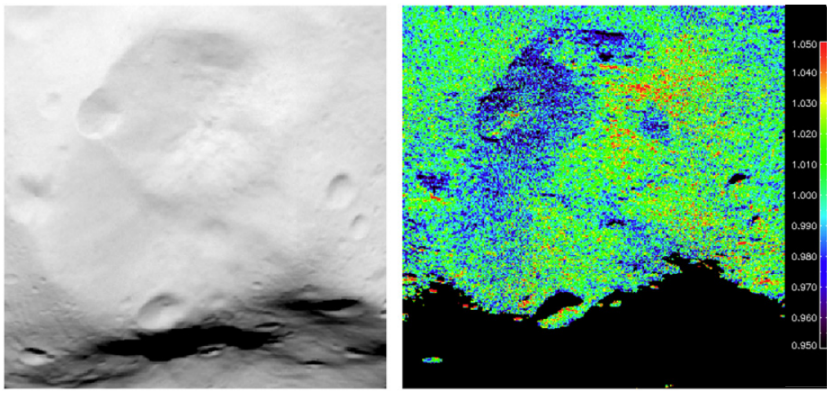

Figure 4.20: Left panel: Baetica region observed in NAC-F16. Right panel: NAC F16/F15 of the same region. Images from observation set SP5.

The Baetica region shows pronounced variegation in the UV bands. In particular, in Fig. 4.20, the Baetica region as pictured through NAC F16 filter acquired on 2010-07-10 at about 15:37UT (obs. set SP5), is shown in the left panel, while in the right panel the colormap resulting from the division NAC-F16/NAC-F15 (about 360 and 264 nm, respectively) is shown. The scale of the colormap is normalized so that we can see differences of $\pm 5\%$ around the mean value. In red we can see regions where the F16/F15 is higher than its average value while in blue we see regions where it is lower than the average value. A total color variegation of about 10% is found in this region.

The visible color differentiation may be due to actual compositional difference or, more likely, to grain size differences. The bluer region is probably indicative of bigger grains, possibly suggesting the presence of fresh material, whereas the redder regions indicate probably smaller grains, more representative of debris deposits. It seems indeed realistic that the crater walls show fresh material while in the flat region debris deposits are visible. Here the topography and the illumination conditions may also cause a misleading color variegation. However these factors are partially corrected by the ratio of reflectances since at first order they do not depend on wavelength.

For a more adequate surface variegation analysis however, the accurate correction for the topography of the surface, and for the illumination conditions is needed.

4.7 Shape Model processing

As mentioned already for the phase curve modeling and for the color variegation analysis, but also in order to obtain a resolved spectrophotometry rather than a simple averaged one, additional information and computations are needed.

An essential tool to interpret the resolved observations is primarily the shape model of the object, but also the information on the geometry of the fly-by and of the illumination conditions at the moment of the fly-by are required. It is not straightforward to handle this information, therefore a series of considerations and pre-reductions are needed.

4.7.1 Geometric data

Solar System constants, space geometry data and reference frames definitions are all stored, for most of the international space missions, in an information system called SPICE. The primary components of SPICE are the kernels, which give also the name to the system:

Spk spacecrafts, planets, satellites, and some comets and asteroids ephemeris;

Pck planetary constants kernels: planets, satellites, comets and asteroids physical and dynamical parameters such as size, shape, orientation of the spin axis, prime meridian, eventually parameters for gravitational model, atmospheric model or rings model;

Ik instrument description kernel, containing descriptive data such as field-of-view size, shape and orientation parameters;

Ck pointing kernel, containing a transformation, the C-matrix, which provides pointing angles for a spacecraft structure upon which science instruments are mounted;

Ek events kernel, summarizing mission activities.

Some additional data products are also important components of the system, even if not contained in the SPICE acronym:

Fk frames kernel, contains specifications for the reference frames typically used by flight projects. This file also includes mounting alignment information for instruments and antennas;

Lsk leap seconds tabulation (for UTC ↔ ET conversion);

Sclk spacecraft clock coefficient (for SCLK ↔ ET conversion).

Besides the kernels SPICE system provides also a toolkit, made of numerous subroutines useful for reading the kernels and calculating observation geometry parameters of interest.

In the case of the Rosetta-Lutetia encounter geometry, the IDL interface "Icy" of SPICE has been used, together with the following kernels:

- DE405.bsp: Spk kernel containing ephemeris data for planet barycenters, and for the Sun, planets and satellites mass centers, until 2050.
- ORHR_____00122.bsp: Spk kernel containing Rosetta spacecraft predicted and reconstructed cruise ephemeris. Spans the cruise phase, from launch to comet rendezvous manoeuvre.
- DE403-MASSES.tpc: Pck kernel containing the masses of the Sun, planets and satellites.
- PCK00010.tpc: Pck kernel containing the size, shape, radii and orientation constants for planets, satellites, Sun and some asteroids.
- ROS_OSIRIS_V11.ti: OSIRIS Ik kernel, containing both NAC and WAC optics, detector, and field-of-view parameters.
- ATNR_P040302093352_00127.bc: Ck kernel containing Rosetta predicted attitude information.
- ROS_V18.tg: Fk kernel containing the complete set of frame definitions for the Rosetta Spacecraft (ROS) including Rosetta fixed and Rosetta science instrument frames.
- NAIF0010.tls: Lsk kernel specifying the relationship between the Barycentric Dynamical Time (TDB, also called Ephemeris Time, ET) and the Coordinated Universal Time (UTC) up to the last modification in the leap seconds: 5 Jan 2012.
- ROS_110405_STEP.tsc: Sclk kernel containing information required for Rosetta spacecraft on-board clock to UTC conversion.

Using these kernels it is possible to reconstruct the spacecraft trajectory, and calculate many of the geometric parameters of interest. In order to create simulated images of what OSIRIS observed and estimate the illumination angles for each pixel of each image, it is necessary to combine those information with the shape model of the target.

4.7.2 Shape model

With "shape model" we generically refer to a mathematical representation of any three-dimensional object in space. These models represent an object using a collection of points, connected by various geometric polygons such as triangles or squares, in a defined reference frame in three dimensional space. This representation is often referred to as a *mesh*.

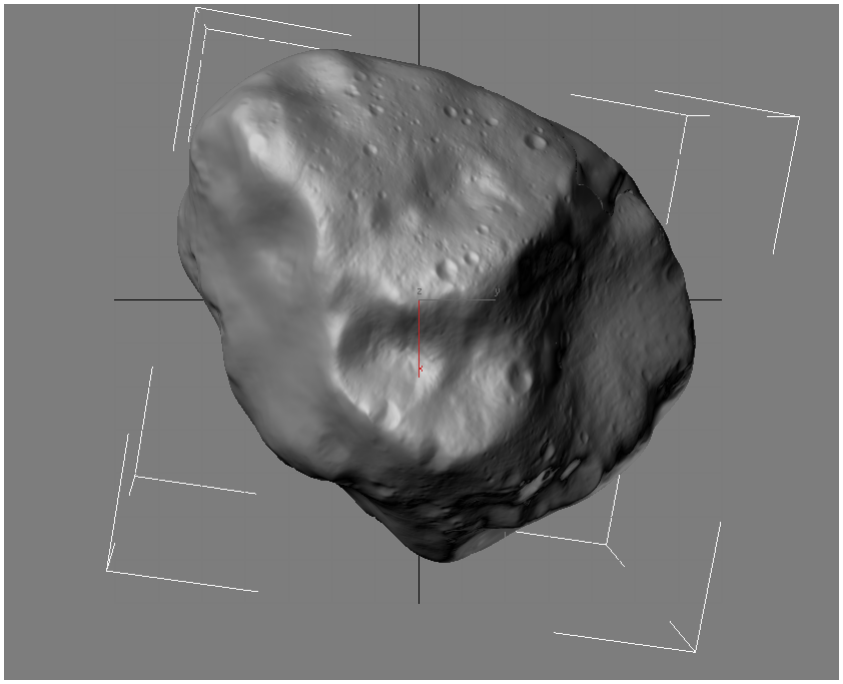

Figure 4.21: 3D visualization of Lutetia shape model

There are many standard computer formats for a mathematical 3D-model. The most commonly used in computer graphics are VRML and Wavefront OBJ but there are many others used in scientific applications. All of them share the same principles: they contain the list of coordinates of each point, which will be called *vertex* in the reference frame, followed by the list of

indices referring to the vertices that form a polygon, which will be called *plate*. The differences between formats may be in the indexation of vertices or in the plate definitions.

Although OSIRIS has no stereo capability, the motion of Rosetta relative to the nucleus and the many different viewing geometry have been used by OSIRIS team to build the 3D shape model of Lutetia. Two techniques have been used: stereophotoclinometry for the regions observed by OSIRIS, complemented by the inversion of photometric light curves and adaptive optics profiles for the rest of the surface. Lutetia model (Jorda et al., 2011), shown in Fig. 4.21, is a very high definition shape model made up of 1 572 866 vertices and 3 205 731 triangular plates connecting the vertices.

Lutetia reference frame is defined by the position of the north rotational pole in the equatorial J2000 frame given by right ascension and declinations: $\alpha = 51.8°$, $\delta = 10.8°$. Lutetia north pole is therefore tilted with respect to its orbital plane by 96° (Sierks et al. 2011) which makes Lutetia a retrograde rotator with a period of 8.19 hours.

4.7.3 Synthetic images

From the shape model of the asteroid, knowing the geometry of the encounter and the properties of the camera, it is possible to generate synthetic images correspondent to the actual observations. This is an important step in matching the mathematical model with the actual observations performed during the fly-by, and a useful method to find possible errors in both the model and the geometry or pointing data.

The production of synthetic images has been accomplished by projecting the shape model in the plane of the image using the *polyshade* method in IDL.

The projection requires information on the time of the actual image to simulate and on the geometry of the fly-by, in particular the observer vector in the body-fixed frame. It also necessitates the dimension of the actual image in pixels and the pixel resolution of the camera, the orientation of the camera and the offset of the boresight from the image center.

The time of the image to simulate as well as its dimensions are stored in the image header, while the observer vector in Lutetia's frame has been extracted from the Spk SPICE kernel.
The pixel resolution of the camera is stored in the OSIRIS Ik kernel.
The orientation of the camera at the time of the observation has been derived from Ik and Ck kernels. The transformation matrix from Lutetia frame to NAC camera frame (ROS_NAC) has been applied to the north vector in

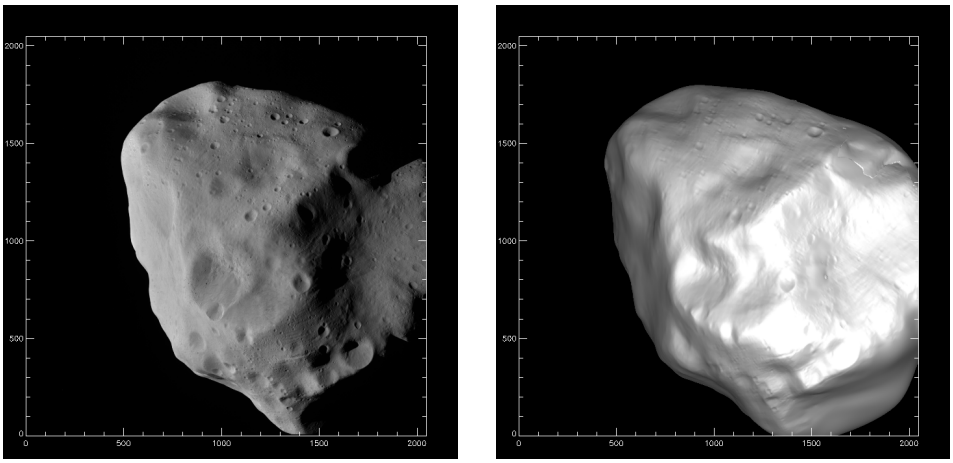

(a) (b)

Figure 4.22: An example of the actual observation (a) acquired on 10 July 2010 at 15:43 UT and its synthetic equivalent image (b).

Lutetia frame. The angle between the projection of this vector in the XY plane of the image and the Y axis of the image itself is the searched camera orientation.
The boresight offset instead can not be derived from SPICE kernels because the pointing kernel is not accurate enough. A cross-correlation between the actual images and the synthetic images has been performed. This technique allowed also to perform an analysis of the camera boresight offsets during Lutetia approach (Fig. 4.23), showing a significant error in the predicted pointing kernels as respect to the occurred pointing.

A good agreement is found between actual and synthetic images (an example is shown in Fig. 4.22) for all the encounter images but one, acquired on 10 July 2010 at 15.42 UT. This problem does not seem to be related neither with the spacecraft flip, that occurred just before the CA, because it was already done by 15.12 UT, nor with the CA itself, that occurred at 15.44, because image acquired at 15.43 is already in much more agreement with its synthetic equivalent.

The projection of the shape model produces also a side result that is called the *plate map* (Fig. 4.24). This is a 2-D array mapping the indices of the triangular plates of the shape model over the visible part of the asteroid in the image. This provides a connection point by point between each image and the shape model plates, indicating the portion of the shape which is

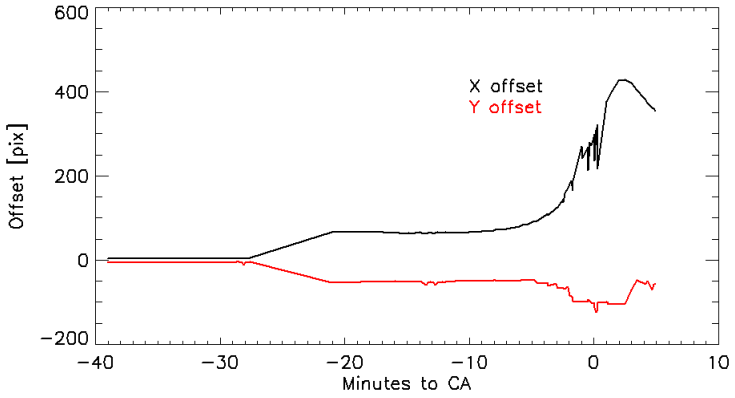

Figure 4.23: Analysis of the camera boresight offsets during Lutetia approach.

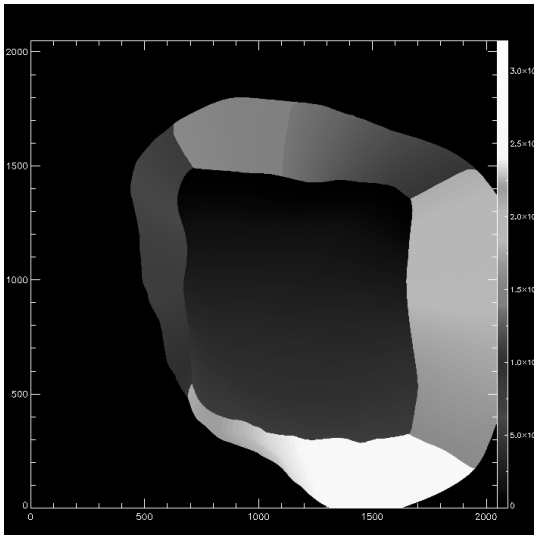

Figure 4.24: Plate map for image acquired on 10 July 2010 at 15:43 UT.

imaged at that time. The distribution of the plates suggests that they are not numbered continuously over the surface but in sectors and possibly reflect the order of creation of the shape model itself

4.7.4 Incident and emission angles maps

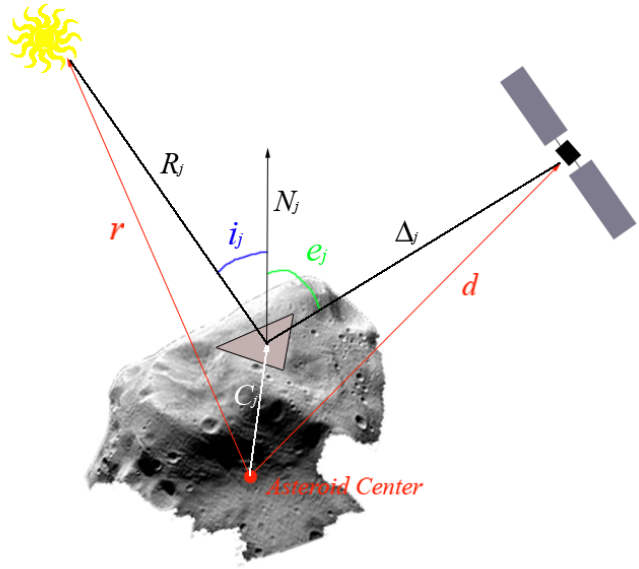

Figure 4.25: Representation of the main vectors definitions used.

The shape model is then used, for photometric purposes, to derive the maps of the incident, emission and phase angles (e, i, α) over the surface of the asteroid for each image acquired.

We give here some definitions of the key vectors (see Fig. 4.25). Two vectors are univocally defined for the whole asteroid:

- range r: vector from nucleus center to Sun;
- distance d: vector from nucleus center to spacecraft;

where the nucleus center is the origin of the Lutetia inertial frame. Four other vectors are instead defined per each plate j of the shape model:

- plate center vector C_j: vector from the nucleus center to the j-th plate center, defined as the average of the coordinates of the vertices forming the j-th plate;
- plate normal versor N_j: versor normal to the j-th plate pointing out of the object;
- plate-to-Sun vector R_j: vector from j-th plate center to Sun;
- plate-to-spacecraft vector Δ_j: vector from j-th plate center to spacecraft;

The angle between R_j and N_j is the incident angle i_j of the j-th plate, while the angle between Δ_j and N_j is the emission angle e_j of the j-th plate.

If E_{j1} and E_{j2} are two consecutive edges of the j-th plate, N_j is calculated as

$$N_j = \frac{E_{j1} \times E_{j2}}{|E_{j1} \times E_{j2}|} \tag{4.5}$$

while R_j is defined as $R_j = r - C_j$, and Δ_j is defined as $\Delta_j = d - C_j$.

All these vectors and angles are continuously changing with time during the observations since the relative positions of light source, asteroid and spacecraft are rapidly changing with time.

The acquisition times of the actual images have been used as reference times to derive the vectors using the SPICE kernels, in order to obtain as many illumination angles maps as the images acquired.

For each acquisition time, that is for each image, the incident angle and the emission angle 3-D models are derived, all over the asteroid.

It is then necessary to project the incident and emission angles 3-D models on the plane of the image in order to refer them to the actual imaged region on the surface of the asteroid.

Using again the *polyshade* method of IDL and the SPICE kernels it is then possible to produce projected 2D i-maps and e-maps (Fig. 4.26) for each image.

These maps would allow to perform the disk-resolved bidirectional reflectance modeling with Hapke's function (Eq. 3.1) for each plate individually in order to characterize, in principle, the regolith properties of the area covered by each single pixel in the asteroid image. However usually the values are averaged over regions that look homogeneous. The resulting values may also be averaged over the entire illuminated and visible surface of the asteroid in order to make comparison with the integral phase curve analysis.

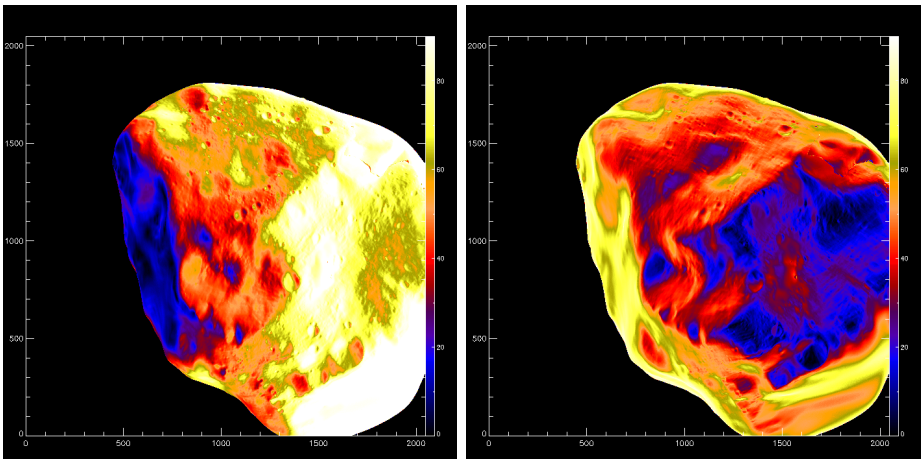

(a) i-map (b) e-map

Figure 4.26: Incident and emission angle maps for Lutetia image acquired on 10 July 2010 at 15:43 UT.

The e-map and i-map have been also iteratively used to improve the stacking between synthetic and actual images. Using these maps indeed it has been possible to consider, in the cross-correlation, only the visible and illuminated regions ($e < 90°$, $i < 90°$).

4.7.5 Latitude-longitude map

Another interesting application of the shape model is the production of a latitude-longitude projection of the surface.

Once the rectangular XYZ body-fixed reference frame has been defined for a celestial body, the equator is defined as the XY plane, the north pole is the point where the Z positive axis intercepts the shape model and the prime meridian is defined as the meridian passing through the pole and the intercept of the X positive axis with the shape model.

Given these definitions, the conversion of the vertices coordinates from a rectangular frame to a spherical frame is straithforward and will yield for each vertex of the shape model a value of latitude, longitude and elevation, i.e. the radius from the center of the body to the vertex.

This gives the Digital Elevation Model (DEM) of a surface (Fig. 4.27).

However, to see the actual visual aspect of the surface, such as features and craters, on a latitude-longitude grid, it is necessary to use a *shading* method such as *polyshade* that reproduces how our eyes would see that

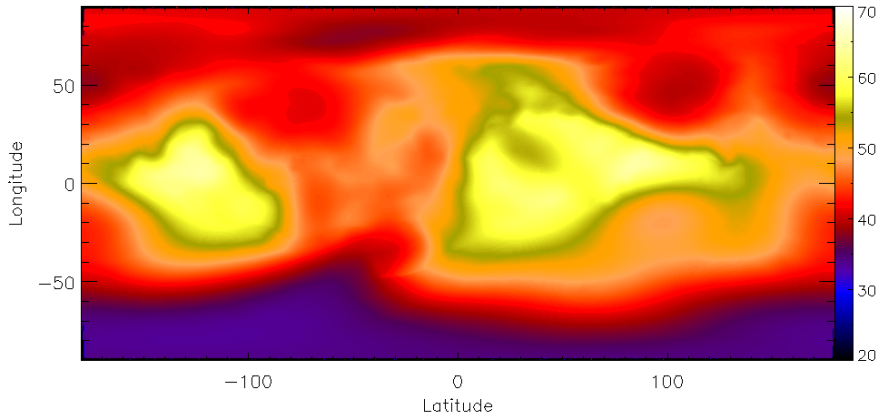

Figure 4.27: Lutetia DEM. The color index describes the elevation in meters.

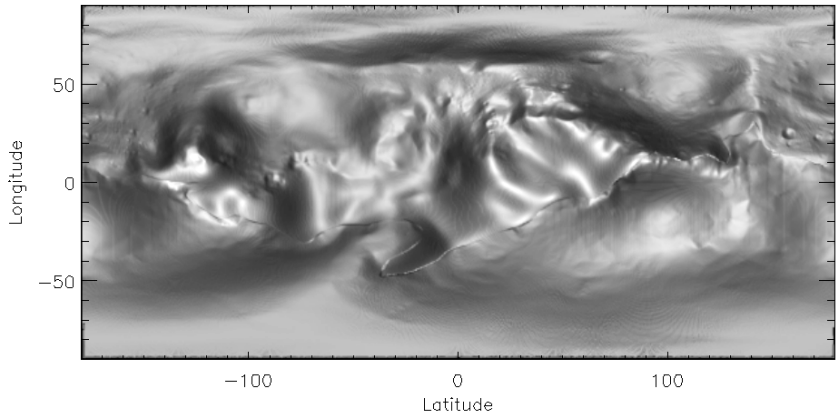

Figure 4.28: Latitude-Longitude map of Lutetia surface.

surface elevation for usual incident and emission angles.

Since the shape model vertices are not evenly spaced in the latitude-longitude space, there are many missing data in the latitude-longitude map, mainly in the poles regions. To solve this problem a nearest neighborhood interpolation has been performed all over the grid.

In the resulting map (Fig. 4.28), some vertical stripes are visible, that seem to follow the elevation of the surface but at the same time in the region close to the poles seem to have a 45° regular pattern. This is possibly due to an interpolation numerical problem.

Once each vertex of the shape model has been converted into a point in lat-long space it is also possible to project a lat-long grid on each image plane. Thanks to the plate map (Fig. 4.24), obtained during the production of synthetic images, each pixel in the image is related to a plate index. The plate index in turn is directly connected with the three vertices that form the plate and with their rectangular coordinates. It is sufficient to average them and convert the result into spherical coordinates to obtain the latitude and longitude values for each pixel of the image (Fig. 4.29) and overplot the relative grid on the image (Fig. 4.30) in order to relate the coordinates to surface features.

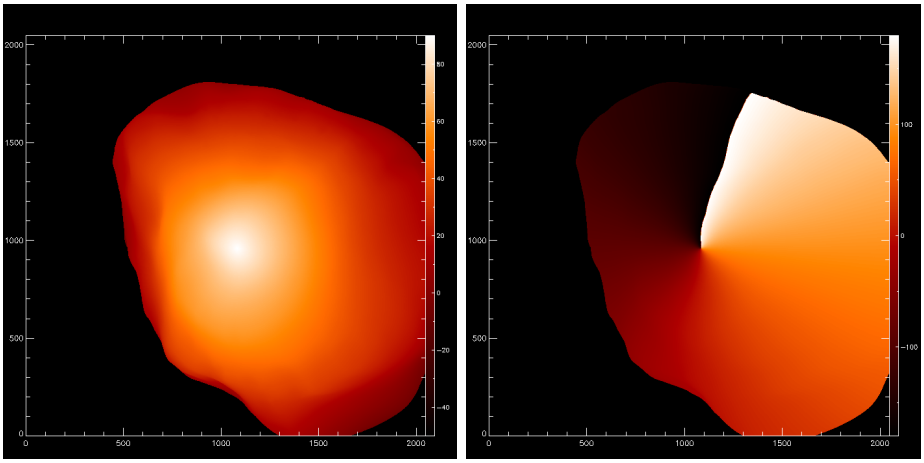

(a) Latitude map. (b) Longitude map.

Figure 4.29: Latitude and longitude projection on the image plane for image acquired on 10 July 2010 at 15:43 UT.

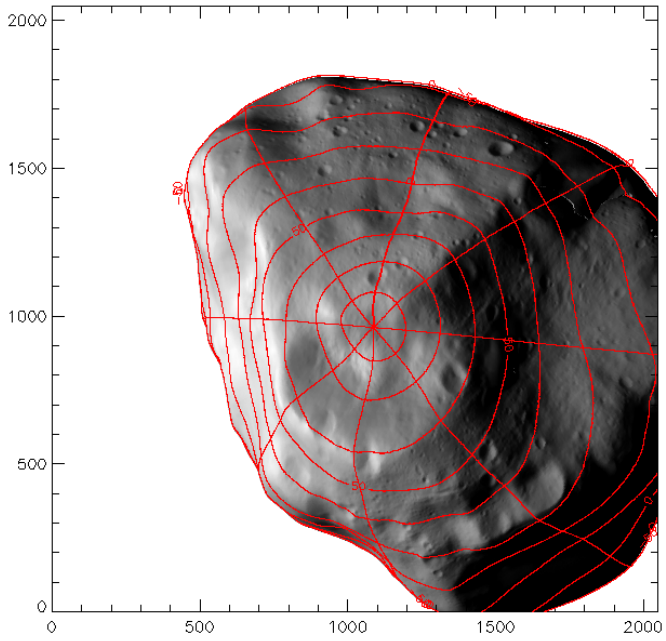

Figure 4.30: Longitude and latitude grid overlapped on the actual image acquired at time 15:43 UT. The north pole appears to be in the Baetica region.

4.8 Future Improvements

The purpose of the application of the shape model analysis is the improvement of all the analysis described in this chapter that will be applied to different resolved areas over the surface of the asteroid, allowing therefore the study of local surface properties rather than global ones.

The disk-resolved photometric analysis using Hapke's bidirectional reflectance model, has been performed already for all the asteroids and comets nuclei visited by spacecrafts so far (e.g. Li et al., 2004; Li et al., 2006; Li et al., 2007 and others), therefore it will be important to perform it on Lutetia as well, providing another term of comparison. This will give detailed information on the regolith surface and will also help in understanding the limits of the Hapke model in representing a non-semiinfinite body surface.

Another application would be the topographic correction of the surface

of the asteroid and the following analysis of the color variegation over the surface.

Applying the shape model analysis to a cometary nucleus will be very useful in defining and following the active regions over the surface of the nucleus and making connection with the possible coma features.

Chapter 5

Coma Gas Emissions

The photometric analysis of a cometary atmosphere requires also some further considerations on the gas emission process and its effects.

The physical and chemical conditions existing at comets, changing as function of the heliocentric distance and of the solar activity, are responsible for the ices and volatiles sublimation and determine, together with the property of the nucleus, the way the coma gas is formed, the quantity of gas released, and eventually the total intensity of the flux observed. The issue is thus to deal with the observed flux incoming from comets and, using appropriate models and theories, trace back the properties of nucleus. Hence it is necessary to understand the physics involved in order to retrieve information about the nucleus composition and to understand how the cometary activity develops and evolves in time.

In the optical wavelength region, apart from the continuum flux coming from the dust, only daughter species emission bands are usually observable and the interpretation of these measurements requires complex production and kinematics models, beyond a knowledge of the emission mechanisms and an overview of the possible chemical reactions occurring.

5.1 Gas production models

The original quantitative model of a cometary coma was developed by Eddington in 1910 and was called *fountain model*. In this very simplified model, the comet is assumed as uniform and isotropic point source of emitters of light whose density falls as the inverse square distance law. The light emitters are considered uniformly accelerated by a force coming from the Sun's direction.

It is defined *column density*, N, the density of gas molecules integrated in the line-of-sight column of an optically thin coma, expressed in mol cm^{-2}.

Following the fountain model, the column density would be related to the global gas molecule *production rate* Q expressed in mol s^{-2} by:

$$N = \frac{Q}{4v\rho} \tag{5.1}$$

where ρ is the projected distance on the sky-plane from the source and v is the initial uniform outflow speed of the emitting particles. This model, although obsolete, is still applied more adequately to the dust particles in the coma, rather than to the gas molecules.

In the following decades, observations showed that the gas species identified in the spectra were unstable radicals produced through photodissociation of more stable parent molecules by solar UV radiation. Haser (1957) developed a more complex gas production model in order to describe the expected distribution of daughter species created from parent molecules.

5.1.1 Haser's model

Haser's model adopts several simplifying assumptions: a spherical symmetric collisionless coma, a direct production of the parent molecule isotropically from the nucleus, a steady-state gas production, and in particular, a constant radial outflow velocity of both parents and daughters.

The assumption of a spherical coma, even though highly restrictive, is partially justified considering that the nucleus rotation, the molecules collisions and the dust particles scattering of the solar light, tend to reduce the effects of anisotropies and inhomogeneities and make the gas distribution more isotropic.

Haser considers the distribution of a secondary species being produced by the photodissociation of a parent molecule and in turn being destroyed by some photo-destruction processes. The coma is considered a spherically symmetric point source of uniformly outflowing parent molecules, where an exponential lifetime describes their destruction. The density, n_p, of the parent molecule at distance r from the source is then given by:

$$n_p(r) = \frac{Q_p}{4\pi r^2 v} e^{-r/\gamma_p} \tag{5.2}$$

and the density, n_d, of the daughter species is given by:

$$n_d(r) = \frac{Q_p}{4\pi r^2 v} \frac{\gamma_d}{\gamma_p - \gamma_d} (e^{-r/\gamma_p} - e^{-r/\gamma_d}) \tag{5.3}$$

where Q_p is the production rate of the parent molecule, v is the radial outflow speed, and γ_p and γ_d are the parent and daughter *scale lengths*, i.e. the average distance traveled by the molecules in their lifetimes:

$$\gamma_p = v\tau_p \qquad \gamma_d = v\tau_d \tag{5.4}$$

where τ_p and τ_d are respectively the parent's and of the daughter's exponential lifetimes.

Eq. 5.3 is numerically integrated along the line of sight to obtain a column density profile to compare with the observed spatial profiles of the gaseous daughter species. Comparing the model with the observations allows thus to determine some important parameters such as the scale-lengths and, assuming the outflow velocity, the lifetimes of parent and daughter. This would allow for example to determine the plausible parent molecule of an observed daughter by comparing the derived lifetime with the photochemical measured lifetimes of possible parents of the observed radical.

Haser's model is a very simplified one, however it takes into account the basic physics occurring in the coma and thus it is sill widely used today for its simplicity.

5.1.2 Festou's Vectorial model

Festou (1981a) introduced more complexity to Haser's model in order to take into account physical processes that Haser's instead neglected. He considers the existence of a collision sphere around the nucleus, where collisions are significant, and assumes that the parent molecule outflow is constant and radial only outside this sphere of radius $r_c \sim 10^2 - 10^4$ km. However, the most important originality of Festou's model consists in allowing the daughter species to be emitted with an arbitrary orientation as respect to the source parent molecule, considering that during the photodissociation process some energy is released, which can be converted in kinetic energy of the daughter species. The daughter is thus produced with a velocity distribution rather than a constant outflow velocity.

Fig. 5.1 shows the representation of the typical quantities used in the vectorial model. The parent molecule P is moving radially from the nucleus with constant velocity $\vec{\mathbf{v_p}}$; the daughter molecule, emitted in D, has velocity $\vec{\mathbf{v}}_\mathbf{e}$ in the parent-fixed reference frame, but it has velocity $\vec{\mathbf{v}}_\mathbf{d}$ in the cometocentric reference frame:

$$\vec{\mathbf{v}}_\mathbf{d} = \vec{\mathbf{v}}_\mathbf{p} + \vec{\mathbf{v}}_\mathbf{e} \qquad v_d = \sqrt{v_p^2 + v_e^2} \tag{5.5}$$

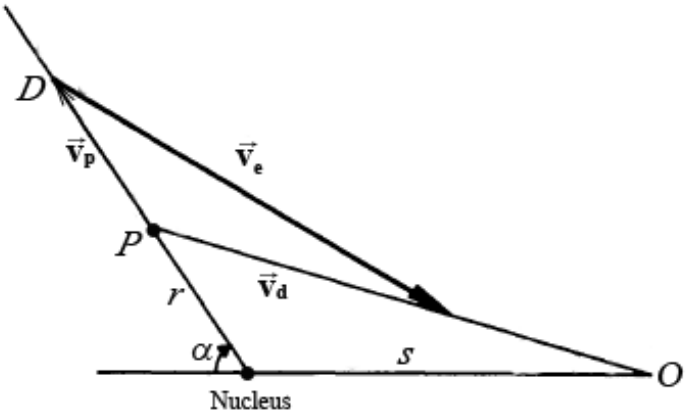

Figure 5.1: Representation of Festou's vectorial model of gas production(Festou, 1981a).

Festou assumes that the parent molecule density $n_p(r)$ is still given by Haser's model (Eq. 5.2) and finds that, with the new conditions, the density of the daughter molecule at any point O at distance s from the nucleus is instead described by equation:

$$n_d(s) = \int_r \int_\alpha \int_{v_d} 2\pi r^2 \sin\alpha \frac{n_p(r)}{4\pi\tau_p} f(v_e) \left(\frac{v_d}{v_e}\right)^2 \frac{e^{-p/\gamma_d}}{p^2 v_d} d\alpha dr dv_d \qquad (5.6)$$

where $f(v_e)$ is the velocity distribution function of the daughter molecule, and p is the distance between P and O in Fig. 5.1.

The limits of this models are still the assumptions of spherical symmetry and isotropic emission of parent molecules, beyond the disregard of the radiation pressure effects.

With respect to Haser's model, however, it is characterized by a fundamental property: thanks to the excess velocity, a daughter molecule produced at a certain distance may go back towards the nucleus and contribute to the density in the inner coma, which was impossible in a pure radial outflow model.

It is thus predictable that densities estimated with vectorial model in the vicinity of the nucleus will be higher than Haser's estimates. In other words, this means that Haser's model tends to overestimate the lifetime of the daughter molecules. It is therefore possible to represent the density through the Haser model if an artificially reduced lifetime is considered.

Hence it is possible to use the Haser formula to obtain an "Haser-vectorial equivalent model" if a set of re-definitions (Combi et al., 2004) are made, in particular for the Haser equivalent scalelengths $\gamma_{p,H}$ and $\gamma_{d,H}$:

$$\tan\delta \equiv \frac{v_p}{v_e} \qquad \mu \equiv \frac{\gamma_p}{\gamma_d} \qquad \mu_H \equiv \frac{\gamma_{p,H}}{\gamma_{d,H}} \tag{5.7}$$

The equivalent model will be given by Haser's formulas (Eq. 5.2 and 5.3) but substituting $\gamma_{p,H}$ and $\gamma_{d,H}$ to γ_p and γ_d respectively, and $v_{d,H}$ to v_d, obtained by using the following equations (Combi et al., 2004):

$$\gamma_d^2 - \gamma_p^2 = \gamma_{p,H}^2 - \gamma_{d,H}^2 \tag{5.8}$$

$$\mu_H = \left(\frac{\mu + \sin\delta}{1 + \mu\sin\delta}\right)\mu \tag{5.9}$$

$$\mu = (\mu_H - 1)\frac{\sin\delta}{2}\left[(\mu_H - 1)^2\frac{\sin^2\delta}{4} + \mu_H\right]^{1/2} \tag{5.10}$$

$$v_{d,H} = v_d\frac{\gamma_d, H}{\gamma_d} \tag{5.11}$$

Comparing vectorial (or Haser-vectorial equivalent) model's column density estimates of daughter molecules to the observed column densities is extremely useful in order to determine the production rates of the parent molecules, in particular of water. Therefore it will be used in Chapter 6 to determine the water production rate of comet 103P/Hartley 2.

5.2 Photochemistry of Water

The parent molecules are usually the ices that sublimate directly from the nucleus while the daughters are the products of the photodissociation of parents.

Water ice is the source of the primary parent molecule: water vapor. It indeed dominates the volatiles species that outflow from cometary nucleus at heliocentric distances smaller than 3-4 AU. During the outflow, the H_2O molecule is destroyed initially and primarily through photodissociation, and then also through photoionization, and interactions with solar wind ions and electrons.

The destruction of H_2O molecule produces a series of daughter molecules such as OH and H_2, atomic products, such as O and H, and various ions. The

photodestruction rate of H_2O and of its products depends on the heliocentric distance of the comet, and on the solar activity. The inverse of the total photodestruction rate is the lifetime of the molecule.

The photochemistry and kinetics of water have been studied in great detail and thanks to the improvements in studying the solar spectrum and the molecules cross sections, a good level of knowledge has been reached today. A summary of the most relevant water photodestruction reactions, their rates and branching ratios and exothermic velocities of the products is given in Tab. 5.1 (Combi et al., 2004 and references therein).

Wavelength range [Å]	**Reaction** $H_2O+h\nu \rightarrow$	**Exothermic velocity [km s^{-1}]** prod. 1	prod. 2	**Branching ratios** quiet	active	**Photod. rates [10^{-6} s^{-1}]** quiet	active
1357-1860	$\rightarrow$H+OH($X^2\Pi$)	18.5 (H)	1.09 (OH)	0.465	0.380	4.84	5.36
	$\rightarrow H_2+O^*(^1D)$	<13.7 (H_2)	<1.71 (O)	0.005	0.004	0.05	0.05
1216 (Ly-α)	$\rightarrow$H+OH($X^2\Pi$)	17.2 (H)	1.01 (OH)	0.291	0.321	3.02	4.53
	$\rightarrow$H+OH*($A^2\Sigma^+$)	5 (H)	0.3 (OH)	0.033	0.037	0.35	0.52
	$\rightarrow H_2+O^*(^1D)$	<15 (H_2)	<1.8 (O)	0.042	0.046	0.43	0.65
	$\rightarrow$H+O+H	<7.4 (2H)	<0.87 (O)	0.050	0.055	0.52	0.78
984-1357	$\rightarrow$H+OH($X^2\Pi$)	<37-27 (H)	<2.2-1.6 (OH)	0.028	0.032	0.30	0.45
excl. Ly-α	$\rightarrow$H+OH*($A^2\Sigma^+$)	<25-0 (H)	<1.5-0 (OH)	0.003	0.004	0.03	0.05
	$\rightarrow H_2+O^*(^1D)$	<22-14 (H_2)	<2.7-1.7 (O)	0.004	0.005	0.04	0.07
	$\rightarrow$H+O+H	<17-0 (2H)	<2.0-0 (O)	0.005	0.005	0.05	0.08
<984	$\rightarrow$neutral products	–	–	0.024	0.029	0.25	0.41
	$\rightarrow$ionized products	–	–	0.050	0.082	0.52	1.16
			TOTAL:	**1.0**	**1.0**	**10.40**	**14.11**

Table 5.1: Summary of the most relevant water photodestruction reactions (Combi et al., 2004). Note that "quiet" and "active" in the last four columns refer to "quiet Sun"and "active Sun".

From Tab. 5.1 it is clear that the Ly-α solar spectrum peak contributes for about $\sim 41.6-45.9\%$ of the total water photodestruction rate (depending on the solar activity). The total photodestruction rate of H_2O for quiet Sun is thus $1.04 \pm 0.123 \cdot 10^{-5}$ s^{-1} which leads to a total water lifetime $\tau_{H_2O} \sim 0.96 \cdot 10^5$ s. For active Sun the photodestruction rate is rather higher, $1.411 \pm 0.175 \cdot 10^{-5}$ s^{-1} and the lifetime shorter $\tau_{H_2O} \sim 0.71 \cdot 10^5$ s.

Each product of the photodestruction of water will produce a series of emission bands, at different specific wavelengths, and of distinct intensities depending on the branching ratio, which determines the fraction of water molecules which dissociate to give that product, on its final exothermic velocity, which influence the populations of its vibrational and rotational excited levels, and obviously depending on its energy levels and selection

rules applicable.

OH($X^2\Pi$) is the most observed water radical emitting in the optical wavelength region where it shows a strong band at $\sim$ 308.5 nm.

Similarly to water, a deep photochemistry analysis is required for all the parent molecules, to know the possible daughters and all their physical and chemical properties, in order to identify and analyze their emission bands observable in the optical spectral range.

5.3 Molecular Spectroscopy

Detailed analysis of high-resolution cometary spectra demonstrated that the observed emissions are produced for the most part by resonant fluorescence of solar radiation, i.e. the daughter molecules are excited by solar radiation and jump to higher rotational, vibrational and electronic energetic levels to later decay to the original ground state and provoke an emission band at the same exciting wavelength.

Although the process is in principle very simple, the emission spectrum of even the simplest diatomic molecule shows complicated behavior comprising different bands made up of many lines. This is due to the fact that the two atoms in the molecule can vibrate individually along the common axis as well as rotate along the axis perpendicular to the common axis. The energy of each of these motions is quantized, hence the total number of energy levels is usually very high. Furthermore many of these motions usually interact and couple together in various ways, forming an even more complicated structure of energy levels.

The total energy of the molecule is the sum of the kinetic and potential energies of the electrons and the nuclei, which is very complex. It is however usually approximated by the product of three independent factors: the electronic, vibrational and rotational energies:

$$E = E_e + E_v + E_r \quad \text{where} \qquad E_e > E_v > E_r \tag{5.12}$$

It results that each electronic level is subdivided into vibrational levels characterized by the quantum number v, which can take values 0, 1, 2, ... Each vibrational level is further split up into rotational levels characterized by the rotational quantum number J which can also take values 0, 1, 2, ...

The classification of the electronic states of a molecule is based on a scheme similar to that employed for atoms. $L = L_1 + L_2$ and $S = S_1 + S_2$ are the total orbital and spin angular momenta, respectively. L and S projections

along the axis of the molecule are denoted respectively as Λ and Σ. The total angular momentum Ω is given by:

$$\Omega = \Lambda + \Sigma \tag{5.13}$$

Λ can take values 0, 1, 2,...,L and the correspondent electronic states are designed as in the atomic case, but in greek letters:

$\Lambda =$	0	1	2	3	...	
	Σ	Π	Δ	Φ	...	for molecules
	S	P	D	F	...	for atoms

The final designation of an electronic state is a term like:

$$X^1\Pi^+_{1/2,g}$$

here X identifies the state as ground state, other states with the same symmetry and angular momentum properties are labeled as A, B, C, etc in order of increasing energy; the superscript 1 identifies it as a singlet state, it can be 2, 3 etc.; the Π indicates that its orbital angular momentum is 1, it may have values $\Sigma, \Pi, \Delta, \Phi$ etc.; 1/2 is the value of the total angular momentum Ω; g indicates the parity of the wavefunction, which can be u or g; and + indicates the reflection symmetry along an arbitrary plane containing the internuclear axis, it may be + or −.

A transition may occur among any rotational, vibrational and electronic energy levels, compatibly with the selection rules applicable. In a transition the quantum numbers of the upper level are denoted as prime, like v' and J' while that of the lower level as double prime, like v'' and J''.
The selection rules for the electronic transitions are:

$$\begin{aligned} \Delta\Lambda &= 0, \quad \pm 1 \\ \Delta\Sigma &= 0 \\ \Delta\Omega &= 0, \quad \pm 1 \end{aligned}$$

There are no rigorous selection rules for the vibrational quantum number and so the transition can take place between any two vibrational levels of the two electronic states involved. A pure vibrational transition between the two electronic states, called a *band* is denoted as (v', v''), i.e., the quantum number of the upper level is written first. Pure vibrational transitions in a given electronic state are not allowed for homonuclear molecules like C_2, N_2, etc.

Each of the vibrational bands is further split up into a large number of rotational lines. The selection rule for the rotational quantum number J is given by:

$$\begin{array}{ll} \Delta J = 0, \pm 1 & \text{if} \quad \Lambda \neq 0 \\ \Delta J = -1 & \text{if} \quad \Lambda = 0 \end{array}$$

Therefore, the rotational transitions give rise to three series of lines called P, Q and R branches corresponding to $\Delta J = -1, 0, +1$. The rotational lines of a given vibrational band cannot in general be distinguished in low resolution spectra and result in a blended feature, a band, unless a very high spectral resolution is available.

The electronic transitions in a molecule give rise to various intensity patterns depending on the type of the molecule. For example, for some molecules the (0, 0) transition is the strongest, while for others the strongest line may be due to a different (v', v'') transition. The observed intensities of the lines can be understood in terms of the *Franck-Condon principle*: the electron jump takes place from one electronic state to another preferentially at the turning points of any vibrational level. This is due to the fact that the time of passage between two turning points is much shorter than the time spent at the turning points. Therefore the probabilities of an electronic transition to occur depend on the potential curves of the two electronic states.

The intensity of an emission line from state 2 to state 1 is generally given by:

$$I_{21} = N_2 A_{21} h\nu_{21} \tag{5.14}$$

where N_2 is the population of level 2, ν_{21} is the frequency of the emitted radiation from state 2 to state 1, and A_{21} is the Einstein coefficient. It gives the probability for a spontaneous transition from state 2 to state 1 to happen, even without any external influence, and is the inverse of the mean lifetime of state 2 as respect to $2 - 1$ transition:

$$\tau_2 = \frac{1}{A_{21}} \tag{5.15}$$

A_{21} can be expressed as:

$$A_{21} = \frac{64\pi^4 \nu_{21}^3}{3hc^3 g_2} S_{21} \tag{5.16}$$

where g_2 is called the *statistical weight* or the degeneracy of the upper level and S_{21} is the *total line strength* of the molecular line and can be expressed as the product of electronic, vibrational and rotational components:

$$S_{21} = S_{el} S_{vib} S_{rot} \tag{5.17}$$

Usually S_{el} and S_{vib} are combined together:

$$S_{el} S_{vib} \equiv S_{el}^{vib} = \left| \int \psi_{v'} R_e \psi_{v''} dr \right|^2 \tag{5.18}$$

where $\psi_{v'}$ and $\psi_{v''}$ are the eigenfunctions for the vibrational states v' and v'', and R_e is called the *electronic transition moment* and is proportional to the probability of a transition between two electronic states to occur. It is defined by the expression:

$$R_e = \int \psi'_e \mu_e \psi''_e d\tau_e \tag{5.19}$$

where ψ'_e and ψ''_e are instead the electronic wavefunctions and μ_e is the electric dipole moment for the electrons. In general ψ_e depends on the internuclear distance r, therefore R_e should also depend on the internuclear distance, however, since its variation with r is slow, it is often neglected and it is replaced by an average value:

$$R_e \simeq \bar{R}_e(r_{v'v''}) \tag{5.20}$$

where $r_{v'v''}$ is called the *r-centroid* and it is a characteristic internuclear separation which can be associated with a given (v', v'') band:

$$r_{v'v''} = \frac{\int \psi_{v'} r \psi_{v''} dr}{\int \psi_{v'} \psi_{v''} dr} \tag{5.21}$$

With this approximation Eq. 5.18 becomes:

$$S_{el}^{vib} \simeq R_e^2(r_{v'v''}) \left| \int \psi_{v'} \psi_{v''} dr \right|^2 \tag{5.22}$$

and the integral over the products of the vibrational wavefunctions in Eq. 5.22 is known as the *overlap integral* and is generally called the Franck-Condon factor $q_{v'v''}$ of the (v', v'') band. Therefore, Eq. 5.17 can be written as:

$$S_{21} = R_e^2(r_{v'v''}) q_{v'v''} S_{rot} \tag{5.23}$$

The total strength of a molecular line is essentially given by the product of the three-strength factors, namely $R_e^2(r_{v'v''})$ which describes the electronic strength, the Franck-Condon factor, $q_{v'v''}$, which gives a measure of the relative band intensities for a vibrational transition, and S_{rot} usually called the Höln-London factor, related to the rotational strength.

The values of the electronic transition moment for any band has to come from the laboratory measurements of the intensity of the lines, as theoretical calculations are very difficult.

The Franck-Condon factors can be calculated from the knowledge of the wavefunction of the vibrational levels, which comes out of the solution of the Schrödinger equation. For many molecules of astrophysical interest, the values of $q_{v'v''}$ have been published in the literature.

On the other hand, the Höln-London factors have to be calculated from the theory. They depend upon the structure of the molecule, the type of coupling, the type of transition involved, etc.

The calculation of the intensities of lines involves, beyond those factors, the knowledge of the relative population of different excited states, as expressed by N_2 in Eq. 5.14.

In a thermal equilibrium, in which every process is balanced by its inverse, the population distribution among various levels is described according to Boltzmann formula. While in a cometary atmosphere, where collisions are not such frequent due to the small density, Boltzmann approximation is not adequate. Thus it becomes indispensable to determine the population distribution from the solution of the statistical equilibrium equations which considers the absorbing and emission processes. The populations depend on the exciting process involved. The total number of equations involved depends on the total number of energy levels considered and may be very tricky.

Schleicher and A'Hearn (1982), for example, carried out accurate calculations of the relative populations of OH molecule due to fluorescence mechanism, for a total of 93 levels and 93 simultaneous equations and were able to reproduce very well the observed, ultraviolet cometary spectra of OH. Similar calculations have been performed for other daughter molecules such as CN (Schleicher, 2010), CH (Sohn et al., 2012) etc. and many other still need to be completed.

5.4 Gas Fluorescence

Detailed analysis of high-resolution spectra demonstrated that cometary emissions are produced mainly by fluorescence of the solar radiation.

It is defined *fluorescence* the mechanism by which a radical product of photodissociation of parent molecule is left in the ground electronic state, absorbs a specific solar photon and is excited to a higher electronic state from where it decays and emits light. It is called *resonant fluorescence* if the emitted photon has the same wavelength of the excitation photon absorbed.

The main goal of studying the spectral emission of molecular gas in the coma is to retrieve the abundance of the parent gas. The total number of molecule of the emitting gas, M, is given by:

$$M = Q\tau r_h \tag{5.24}$$

where Q is the production rate in mol s^{-1}, τ is the lifetime of the molecule at 1 AU and r_h is the heliocentric distance of the comet. The luminosity, in photons cm^{-2} s^{-1}, of a molecular band at wavelength λ is thus proportional to M:

$$L(\lambda) = Mg(\lambda, r_h) \tag{5.25}$$

where $g(\lambda, r_h)$ is called *fluorescence efficiency* factor and is defined by Chamberlain and Hunten (1987) in cgs units as:

$$g(\lambda, r_h) = \frac{\frac{\pi e^2}{mc^2}\lambda^2 f_\lambda \pi F_\odot \tilde{\omega}}{r_h^2} \qquad \text{ph s}^{-1}\ \text{atom}^{-1} \tag{5.26}$$

where e, m and c have their usual atomic meaning, f_λ is the absorption oscillator strength, $\pi F_\odot$ is the solar flux per unit wavelength at 1 AU and $\tilde{\omega}$ is the albedo for single scattering (with has nothing to do with the single-scattering albedo w in Chapter 3) but is instead defined as the relative Einstein coefficient for the given transition.

The fluorescence efficiency factor depends not only on the heliocentric distance of the comet but also on the heliocentric velocity. Swings (1941) pointed out indeed that, because of the presence of Fraunhofer absorption lines in the visible region of the solar spectrum, which may suffer Doppler shift, the absorption of solar photons in a given molecular band varies with the comet's heliocentric velocity. This effect leads to observable differences in the structure of the bands and is now commonly known as *Swings effect*. It is particularly important for OH, CN and NH emission bands. Schleicher and A'Hearn (1982, 1988) carried out detailed calculations of the fluorescence

efficiencies for OH emission bands as function of the heliocentric velocities, taking into account the Swings effect, and found that OH fluorescence varies up to a factor of 5 due to this effect.

In the visible and near-UV often the excitation and de-excitation of the electrons may occur many times in the radicals lifetime, causing a cyclic process which leads to a "fluorescence equilibrium" of the rotational levels within the ground vibrational level.

Fluorescence mechanism is responsible for many emission bands from radicals not only in the optical but also in other spectral ranges (Feldman et al., 2004).

The OH radical is the easiest dissociation product of water to observe and is often use to determine the production rate of water. In the near-UV the strongest OH emission band is $A^2\Sigma^+ - X^2\Pi(0,0)$ band at ~ 308.5 nm. In Fig. 5.2 (Schleicher and A'Hearn, 1982) the molecular structure of OH is shown and the possible transitions are indicated. OH has also observable emissions in the radio, at 18 cm, and in high-resolution IR spectra near 3 μm.

H_2 Lyman series are usually visible near 160.0 nm and have been observed through IUE observatory.

There are two principal observed band systems of C_2 molecule: the optical Swan system, consisting of a series of bands extending in the green from 430 nm up to 630 nm, and the infrared Phillips system but another, called Mulliken system has also been detected in the UV. The Swam system allowed to identify for the very first time a molecule in cometary spectra.

There are two CN electronic band systems in the optical: the violet system $B^2\Sigma^+ - X^2\Sigma^+$ and the red system $A^2\Pi - X^2\Sigma^+$. The violet system is one of the most prominent features seen in spectra of comets with heliocentric distances less than 3 AU.

C_3 molecule, although its parent is unknown, has strong features between 390 and 414 nm with a maximum at 430 nm. The density of the lines is so high that the band results a pseudo-continuum.

CH radical shows the (0,0) $A^2\Delta - X^2\Pi$ band with its peack at 421.4 nm. Its probable parent is methane CH_4.

NH radical also shows its (0,0) band $A^3\Pi_i - X^3\Sigma^-$ between 334.5 nm and 337.5 nm which is generally the only one observed.

Emission bands from NH_2 have been also detected throughout a region from 398 m, to more than 1μm. NH_3 is the plausible parent of NH_2 which in turn decays into NH.

Ultraviolet emission from CS from $A^1\Pi - X^1\Sigma^+$ band at 257.6 nm is the strongest of four bands between 250 and 270 nm. The CS parent is also quite

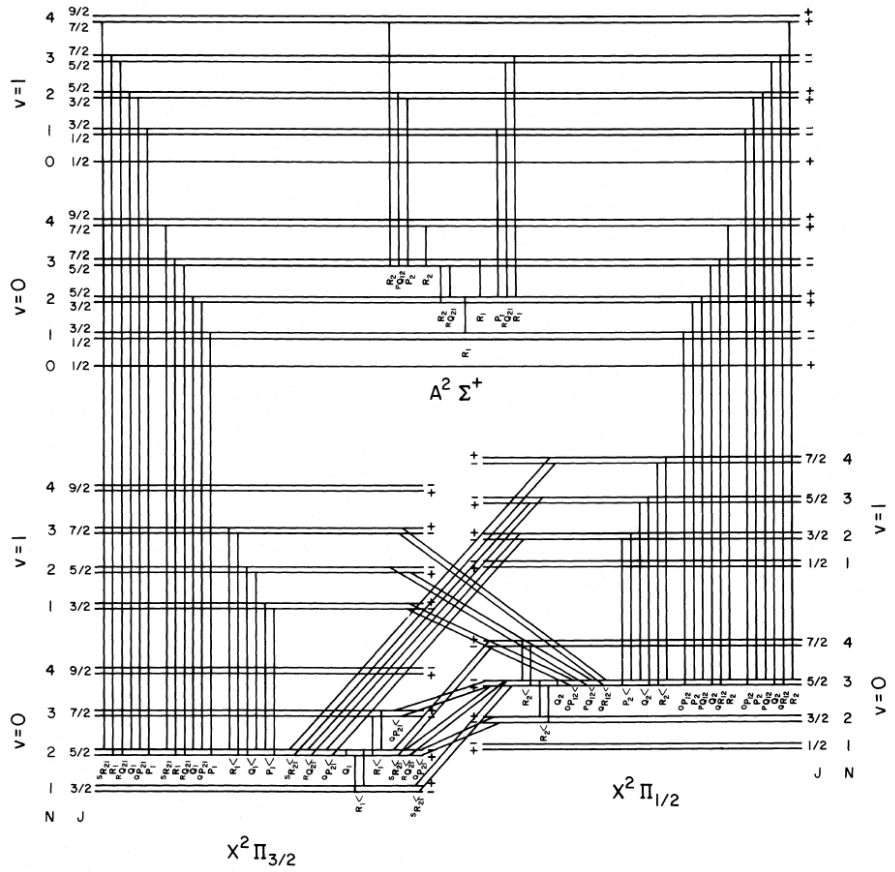

Figure 5.2: Energy level diagram of OH molecule. The two lowest electronic states ($X^2\Pi_{1/2}$ and $A^2\Sigma^+$) are shown, which are split up into two vibrational states each ($v = 0, v = 1$), in turn split up into four rotational states each ($N = 0, 1, 2, 3$) (Schleicher and A'Hearn, 1982).

uncertain, it may be CS_2, however a more probable source of S is actually considered H_2S while another possible source of CS is OCS, recently detected in the radio spectrum of some comets.

5.5 Prompt Emission

Photodissociation of parent molecules may leave a fraction of daughter molecules in an excited state (see for example reactions that produce OH* in Tab. 5.1). These already excited radical products promptly decay and

spontaneously emit a photon. This process is called *emissive photodissociation* but it is often referred to as "prompt emission".

The fundamental difference in the excitation mechanism is that the radical products are left in highly vibrationally and rotationally excited states that cannot be excited instead by fluorescence.
Carrington (1964) carried out a detailed calculation of the rotational population distribution of OH*($A^2\Sigma^+$) formed by dissociation of water and found a significant population up to J=24 rotational level while population of high rotational levels (J>5) in OH excited by fluorescence are exceedingly small, as calculated by Schleicher and A'Hearn (1982, 1988).

Since these states are very unstable, the process is much faster than fluorescence and the radical emits a photon right in the place it has been produced. Therefore prompt emissions provide a means for mapping directly the spatial distribution of the parent molecules.

Prompt emission is usually much weaker than resonance fluorescence because it occurs only once at the creation of each excited molecule, while ground-state molecule undergoes many subsequent fluorescence cycles before being dissociated.

OH prompt emission was observed in the infrared region near 3 μm band in comets C/1999 H1 LEE and C/2001 A2 LINEAR and was quantitatively measured and interpreted by Bonev et al. (2004).

OH prompt emission in the near-UV band at 308.5 nm due to $A^2\Sigma^+ - X^2\Pi$ transition was studied by Bertaux (1986) who described a bright spot of $\sim$ 33 km in the inner coma where this mechanism is dominant as respect to fluorescence. Evidences of this emission were later detected in comet IRAS-Araki-Alcock by Budzien and Feldman (1991) and in comet Hyakutake by A'Hearn et al. (2007).

The radiative lifetime of the OH*($A^2\Sigma^+$) state is $0.83 \cdot 10^{-6}$ s (Bertaux, 1986), much shorter then the collisional de-excitation lifetime, because of the very small density of molecules in the coma, so its de-excitation by collisions (quenching) is negligible and the photon is emitted within a centimeter from the place of photodissociation of water. Therefore OH prompt emission is reflecting exactly the distribution of its parent H_2O in the coma.

Since the electronic states involved in the prompt emission are the same involved in the fluorescence emission, but the rotational levels are different, the spectroscopic pattern of OH prompt emission would be slightly different than OH fluorescence, as reported in laboratory data by Becker and Haaks (1973), and modeled by Budzien and Feldman (1991), as shown in Fig. 5.3. A very high spectral or spatial resolution is therefore necessary to distinguish the two emission mechanisms.

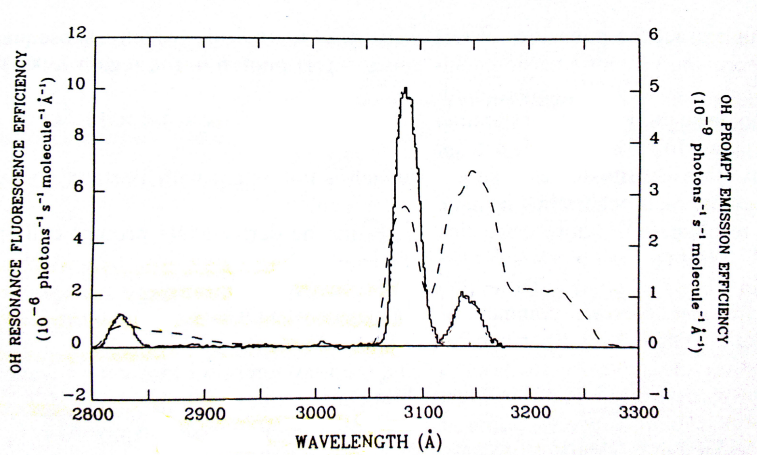

Figure 5.3: Spectral comparison of OH fluorescence efficiency (solid line) and OH prompt emission efficiency (dashed line)(Budzien and Feldman, 1991).

Atomic Oxygen shows also some prompt emissions in cometary spectra. Three forbidden transitions in the optical region are observed: the red doublet at 630-636 nm ($^1D - ^3P$) and the green line ($^1S - ^1D$) at 557.7 nm, which are the result of prompt emission. However O in excited state may have different parents: H_2O, CO, CO_2, OH. It is believed that water is dominant out to distances of 10^5 km beyond which OH becomes dominant.

However, a limitation of using O prompt emission as a tracer of water distribution is that the branching ratios of reactions that dissociate water are still quite uncertain: while OH is produced ∼90% of the times, O is produced only ∼10% of the times, thus errors in the branching ratio would reflects in much bigger errors in water production rate estimate from O than from OH prompt emissions. Furthermore all $OH^*(A^2\Sigma^+)$ is a daughter of water and no other mechanisms for OH prompt emission are known, whereas only a small part of the $O^*(^1D)$ is daughter of the dissociation of water, but the rest is a product of subsequent dissociation of OH and other parents. In addition, because $[O(^1D)]$ is a forbidden transitions, it has a comparatively a long lifetime (∼ 120 s), so collisional quenching may be important in high-density regions near the nucleus.

Chapter 6

Photometric Analysis of Comet 103P/Hartley 2

6.1 Instrument and data description

The data analyzed in this Chapter have been acquired by the MRI instrument onboard EPOXI spacecraft.

MRI camera has been designed for coma observations and is based on a 2.1 m focal length Cassegrain telescope, with 12 cm aperture, a field of view of approximately 35 × 35 arcminutes, and a per pixel resolution of 2 arcsec (A'Hearn et al., 2005).

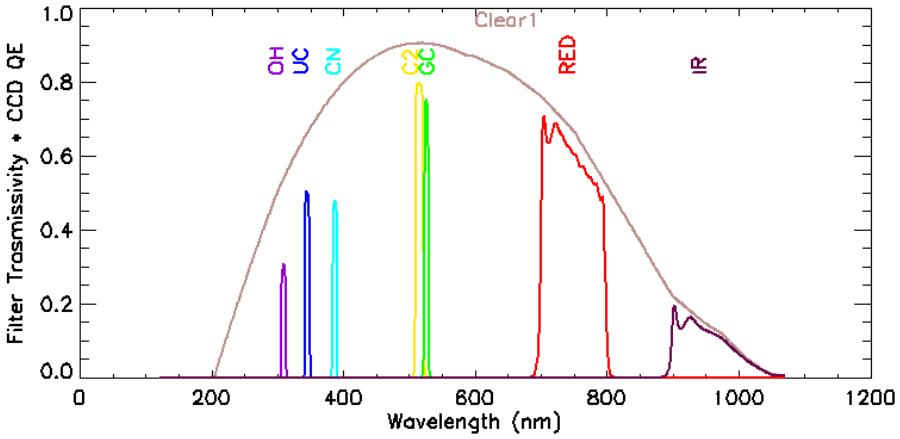

Figure 6.1: MRI filters transmission convolved with the CCD quantum efficiency.

name	**effective wavel. [nm]**	**band-width [nm]**	**peak trans. [%]**	**objective**	**N.**
OH	309.48	6.2	53	OH gas emission	9
Violet	345.41	6.8	72	violet continuum	8
CN	388.80	6.2	58	CN gas emission	7
C_2	515.31	11.8	82	C_2 gas emission	2
Green	525.95	5.6	78	green continuum	3
Clear1	626.07	>700	93	dust flux	1
Clear6	626.08	>700	93	dust flux	6
Red	746.00	100	88	red continuum	4
IR	957.35	100	84	IR continuum	5

Table 6.1: MRI filters properties.

MRI camera is equipped with a total of nine filters (Fig. 6.1, Tab. 6.1), five of them are based on the Hale-Bopp narrowband filter set (Farnham et al., 2000), with three filters designed to measure different gas species (CN, OH, and C_2) and two to measure the continuum at 345 (Violet) and 526 (Green) nm; two other filters are medium-width for measuring colors at 750 (Red) and 950 (IR) nm, and two are nearly identical broadband filters (Clear1 and Clear6) sensitive to the whole 200 - 1100 nm wavelength range.

The effective wavelengths in Tab. 6.1 have been evaluated using the formula:

$$\lambda_{eff} = \frac{\int_0^\infty \lambda \cdot T(\lambda) M(\lambda) QE(\lambda) d\lambda}{\int_0^\infty T(\lambda) M(\lambda) QE(\lambda) d\lambda} \tag{6.1}$$

where λ is the wavelength, $T(\lambda)$ is the filter transmission, $M(\lambda)$ is the mirrors reflectivity and $QE(\lambda)$ is the CCD quantum efficiency.

The EPOXI spacecraft had its closest approach (CA) to the hyperactive comet 103P/Hartley 2 on 4 November 2010 at 13:59:47.31 UTC, when they encountered at the very low distance of $\sim$ 694 km. At that time the comet was at 1.064 AU from the Sun, just one week after its perihelion passage. The spacecraft flew under the comet at a speed of 12.3 km s^{-1} with a northward trajectory in a Solar System reference frame. Observations of the comet were carried out for a total of two months and three weeks (from 5 September to 26 November), during which more than 10^5 images and spectra were obtained (A'Hearn et al., 2011).

Since MRI narrowband filters require a relatively long exposure time to

get a good signal to noise, during most the encounter Clear1 filter has been preferred in order to get an optimal sampling of the comet's lightcurve. Some OH, CN and C_2 observations have been also performed between 28 October and 16 November (Bodewits et al., 2012). We concentrated on continuum observations obtained the same date of the CA, occurred on day of year (DOY) 308 of 2010 (see Tab. 6.2) in order to study the dust structures in the innermost coma. Moreover we investigated OH and CN observations obtained from some days before the CA, i.e. the day of the perihelion, to a few days afterward (see Tab. 6.3, 6.4, 6.5) for the study of the coma gas structures and production rates.

6.2 Data processing

A series of complementary reductions have been performed on the data which have been useful for the photometric analysis. Among others, some important processing carried out are the staking of the images, the cosmic rays removal, the conversion in polar coordinates, the use of enhancement techniques, and the stripes removal. Even though not mandatory, those steps have been applied when necessary and helpful and avoiding to increase excessively the error bars. Those reductions are briefly described in the next sections.

6.2.1 Images Stacking

The images stacking is a very helpful tool for photometric analysis and it has been used in different cases: to combine many images in the same filter in order to increase the signal to noise ratio; to check and clean the images from cosmic rays; to stack the continuum images to the gas images.

By definition, different images can not be acquired at exactly the same time, and the spacecraft is moving fast respect to the comet, so that the distance spacecraft-target is changing rapidly. Therefore the images have been rescaled, aligned and subject to a final cross correlation in order to be stacked.

In the header of the image the pixel scale is recorded, i.e. the resolution of a pixel over the surface of the target at the instantaneous distance spacecraft-target, expressed in cm pix^{-1}. Using the ratio of the pixel scales of two images, the most resolved is rescaled respect to the least resolved, down to the sub-pixel level. In the case of a gas filter image to be stacked to a continuum filter image, the first one is rescaled to the second one because the continuum has a steeper profile.

Index	**Image name**	**Filt.**	**DOY**	**time**	**range** [km]	**exp.** [s]	**size** [pix]	**resol.** [m/pix]
d1	mv10110413_5000143_001_r.fit	CLEAR1	308	13.38.39	15 628	500	1024	156.280
d2	mv10110413_5000156_001_r.fit	CLEAR1	308	13.41.26	13 583	500	1024	135.830
d3	mv10110413_5002001_001_r.fit	CLEAR1	308	13.43.55	11 748	500	1024	117.480
d4	mv10110413_5002015_001_r.fit	CLEAR1	308	13.46.14	10 030	500	1024	100.300
d5	mv10110413_5002025_001_r.fit	CLEAR1	308	13.48.12	8 582	500	1024	85.820
d6	mv10110413_5002029_001_r.fit	VIOLET	308	13.48.55	7 882	30 000	1024	78.820
d7	mv10110413_5002034_001_r.fit	RED	308	13.50.06	7 185	450	1024	71.850
d8	mv10110413_5002035_001_r.fit	GREEN	308	13.50.10	7 102	7 000	1024	71.020
d9	mv10110413_5002039_001_r.fit	CLEAR1	308	13.50.30	6 893	500	1024	68.930
d10	mv10110413_5002051_001_r.fit	CLEAR1	308	13.52.53	5 148	500	1024	51.480
d11	mv10110413_5002055_001_r.fit	IR	308	13.53.31	4 668	1 700	1024	46.680
d12	mv10110413_5002056_001_r.fit	RED	308	13.53.36	4 618	450	1024	46.180
d13	mv10110413_5002061_001_r.fit	CLEAR1	308	13.54.20	4 082	500	1024	40.820
d14	mv10110413_5002069_001_r.fit	CLEAR1	308	13.55.32	3 210	500	1024	32.100
d15	mv10110413_5004001_001_r.fit	CLEAR1	308	13.56.30	2 523	500	1024	25.230
d16	mv10110413_5004005_001_r.fit	CLEAR1	308	13.57.00	2 171	500	1024	21.710
d17	mv10110413_5004009_001_r.fit	CLEAR1	308	13.57.27	1 857	500	1024	18.570
d18	mv10110413_5004014_001_r.fit	CLEAR1	308	13.57.58	1 513	120	1024	15.130
d19	mv10110413_5004021_001_r.fit	CLEAR1	308	13.58.17	1 303	120	1024	13.030
d20	mv10110413_5004025_001_r.fit	CLEAR1	308	13.58.37	1 106	120	1024	11.060
d21	mv10110413_5004029_001_r.fit	CLEAR1	308	13.58.53	963	120	1024	9.630
d22	mv10110413_5004031_001_r.fit	CLEAR1	308	13.59.02	884	120	1024	8.840
d23	mv10110413_6000001_001_r.fit	CLEAR1	308	13.59.12	815	120	1024	8.150
d24	mv10110413_5004041_001_r.fit	CLEAR1	308	13.59.22	759	120	1024	7.590
d25	mv10110413_5004044_001_r.fit	CLEAR1	308	13.59.31	719	120	1024	7.190
d26	mv10110413_5004046_001_r.fit	CLEAR1	308	13.59.41	697	120	1024	6.970
d27	mv10110413_5004051_001_r.fit	CLEAR1	308	13.59.51	696	120	1024	6.960
d28	mv10110414_5004053_001_r.fit	CLEAR1	308	14.00.01	715	120	1024	7.150
d29	mv10110414_5004056_001_r.fit	CLEAR1	308	14.00.10	753	120	1024	7.530
d30	mv10110414_5004058_001_r.fit	CLEAR1	308	14.00.20	807	120	1024	8.070
d31	mv10110414_5004061_001_r.fit	CLEAR1	308	14.00.31	882	120	1024	8.820
d32	mv10110414_5004063_001_r.fit	CLEAR1	308	14.00.41	962	120	1024	9.620
d33	mv10110414_5004066_001_r.fit	CLEAR1	308	14.00.56	1 096	120	1024	10.960
d34	mv10110414_5006001_001_r.fit	CLEAR1	308	14.01.15	1 294	120	1024	12.940
d35	mv10110414_5006011_001_r.fit	CLEAR1	308	14.01.36	1 517	120	1024	15.170
d36	mv10110414_5006016_001_r.fit	CLEAR1	308	14.02.09	1 886	500	1024	18.860
d37	mv10110414_5006020_001_r.fit	CLEAR1	308	14.02.38	2 219	500	1024	22.190
d38	mv10110414_5006024_001_r.fit	CLEAR1	308	14.03.14	2 644	500	1024	26.440
d39	mv10110414_5006030_001_r.fit	CLEAR1	308	14.04.12	3 346	500	1024	33.460
d40	mv10110414_5006037_001_r.fit	CLEAR1	308	14.05.22	4 187	500	1024	41.870
d41	mv10110414_5006046_001_r.fit	CLEAR1	308	14.06.30	5 024	500	1024	50.240
d42	mv10110414_5006058_001_r.fit	CLEAR1	308	14.08.57	6 815	500	1024	68.150
d43	mv10110414_5006060_001_r.fit	GREEN	308	14.09.07	6 982	8 000	1024	69.820
d44	mv10110414_5006061_001_r.fit	RED	308	14.09.18	7 071	500	1024	70.710
d45	mv10110414_5006062_001_r.fit	IR	308	14.09.21	7 123	1 900	1024	71.230
d46	mv10110414_5006064_001_r.fit	VIOLET	308	14.09.54	7 699	30 000	1024	76.990
d47	mv10110414_5006067_001_r.fit	CLEAR1	308	14.11.35	8 754	600	1024	87.540

Table 6.2: Continuum images analyzed for dust structures.

Index	**Image name**	**Filt.**	**DOY**	**time**	**range** [km]	**exp.** [s]	**size** [pix]	**resol.** [m/pix]
g1	mv1010280_6000001	OH	301	00:38:26	8023810	400	512	80238.1
g2	mv1010280_6000003	OH	301	03:38:26	7891621	400	512	78916.2
g3	mv1010282_6000007	OH	301	22:38:25	7053770	400	512	70537.7
g4	mv1010290_6000009	OH	302	01:38:25	6921382	400	512	69213.8
g5	mv1010291_6000001	OH	302	13:38:26	6391557	400	512	63915.6
g6	mv1010291_6000003	OH	302	16:38:25	6259045	400	512	62590.5
g7	mv1010292_6000007	OH	302	22:38:25	5993954	400	512	59939.5
g8	mv1010300_6000009	OH	303	01:38:25	5861375	400	512	58613.8
g9	mv1010301_6000001	OH	303	13:38:25	5330825	400	512	53308.3
g10	mv1010301_6000003	OH	303	16:38:25	5198141	400	512	51981.4
g11	mv1010302_6000007	OH	303	22:38:25	4932717	400	512	49327.2
g12	mv1010310_6000009	OH	304	01:38:25	4799977	400	512	47999.8
g13	mv1010311_6000001	OH	304	13:38:25	4268824	400	512	42688.2
g14	mv1010311_6000003	OH	304	16:38:25	4135998	400	512	41360.0
g15	mv1010312_6000007	OH	304	22:38:25	3870303	400	512	38703.0
g16	mv1011010_6000009	OH	305	01:38:24	3737433	400	512	37374.3
g17	mv1011011_6000001	OH	305	13:38:25	3205798	400	512	32058.0
g18	mv1011011_6000003	OH	305	16:38:25	3072862	400	512	30728.6
g19	mv1011012_6000007	OH	305	22:38:25	2806958	400	512	28069.6
g20	mv1011020_6000009	OH	306	01:38:24	2673990	400	512	26739.9
g21	mv1011021_6000001	OH	306	19:38:25	1875983	400	512	18759.8
g22	mv1011022_6000003	OH	306	22:38:25	1742968	400	512	17429.7
g23	mv1011030_6000007	OH	307	04:38:24	1476920	400	512	14769.2
g24	mv1011032_4000104	OH	307	20:19:15	781507	400	256	7815.1
g25	mv1011032_4000105	OH	307	20:25:56	776571	400	256	7765.7
g26	mv1011032_4000114	OH	307	21:19:14	737168	400	256	7371.7
g27	mv1011032_4000115	OH	307	21:25:55	732232	400	256	7322.3
g28	mv1011032_4000124	OH	307	22:19:13	692828	400	256	6928.3
g29	mv1011032_4000125	OH	307	22:25:54	687892	400	256	6878.9
g30	mv1011032_4000134	OH	307	23:19:12	648489	400	256	6484.9
g31	mv1011032_4000135	OH	307	23:25:53	643552	400	256	6435.5
g32	mv1011040_4000306	OH	308	00:25:14	599918	360	256	5999.2
g33	mv1011040_4000315	OH	308	01:17:32	561015	400	256	5610.2
g34	mv1011040_4000316	OH	308	01:24:13	556079	400	256	5560.8
g35	mv1011040_4000327	OH	308	02:23:34	512197	400	256	5122.0
g36	mv1011040_4000328	OH	308	02:30:15	507261	400	256	5072.6
g37	mv1011040_4000337	OH	308	03:17:30	472333	400	256	4723.3
g38	mv1011040_4000338	OH	308	03:24:11	467397	400	256	4674.0
g39	mv1011040_4000504	OH	308	04:16:45	428535	400	256	4285.4
g40	mv1011040_4000505	OH	308	04:23:26	423598	400	256	4236.0
g41	mv1011040_4000514	OH	308	05:16:44	384193	400	256	3841.9
g42	mv1011040_4000515	OH	308	05:23:25	379256	400	256	3792.6
g43	mv1011040_4000524	OH	308	06:17:07	339556	400	256	3395.6
g44	mv1011040_4000525	OH	308	06:23:48	334619	400	256	3346.2
g45	mv1011040_4000534	OH	308	07:16:56	295337	400	256	2953.4
g46	mv1011040_4000535	OH	308	07:23:37	290400	400	256	2904.0
g47	mv1011040_4000604	OH	308	08:16:09	251562	400	256	2515.6
g48	mv1011040_4000605	OH	308	08:22:50	246626	400	256	2466.3
g49	mv1011040_4000614	OH	308	09:16:03	207277	400	256	2072.8
g50	mv1011040_4000615	OH	308	09:22:44	202340	400	256	2023.4
g51	mv1011041_4000626	OH	308	10:24:19	156814	400	256	1568.1
g52	mv1011041_4000635	OH	308	11:16:56	117919	400	256	1179.2

Table 6.3: Gas images analyzed for coma structures (1).

Index	**Image name**	**Filt.**	**DOY**	**time**	**range** [km]	**exp.** [s]	**size** [pix]	**resol.** [m/pix]
g53	mv1011041_4000636	OH	308	11:23:37	112983	400	256	1129.8
g54	mv1011041_5000006	OH	308	12:16:46	73687	400	256	736.9
g55	mv1011041_5000007	OH	308	12:23:27	68751	400	256	687.5
g56	mv1011041_5002027	OH	308	13:48:25	8303	20	1024	83.0
g56cn	mv1011041_5002031	CN	308	13:49:32	7463	24	1024	74.6
g57cn	mv1011041_5006063	CN	308	14:09:27	7330	24	1024	73.3
g57	mv1011041_5006065	OH	308	14:10:27	8256	55	1024	82.6
g58	mv1011041_4000902	OH	308	16:31:52	116717	700	256	1167.2
g59	mv1011041_4000903	OH	308	16:43:32	125348	700	256	1253.5
g60	mv1011041_4001102	OH	308	17:32:45	161722	700	256	1617.2
g61	mv1011041_4001103	OH	308	17:44:26	170353	700	256	1703.5
g62	mv1011041_4001202	OH	308	18:01:13	180751	375	256	1807.5
g63	mv1011041_4001502	OH	308	19:31:21	249381	700	256	2493.8
g64	mv1011041_4001503	OH	308	19:43:02	258012	700	256	2580.1
g65	mv1011042_4001702	OH	308	20:31:35	293893	700	256	2938.9
g66	mv1011042_4001703	OH	308	20:43:16	302525	700	256	3025.3
g67	mv1011042_4001902	OH	308	21:31:55	338481	700	256	3384.8
g68	mv1011042_4001903	OH	308	21:43:35	347112	700	256	3471.1
g69	mv1011042_4002102	OH	308	22:32:24	383189	700	256	3831.9
g70	mv1011042_4002103	OH	308	22:44:05	391820	700	256	3918.2
g71	mv1011042_4002302	OH	308	23:32:44	427780	700	256	4277.8
g72	mv1011042_4002303	OH	308	23:44:25	436411	700	256	4364.1
g73	mv1011050_4002502	OH	309	00:32:55	472255	700	256	4722.6
g74	mv1011050_4002503	OH	309	00:44:35	480886	700	256	4808.9
g75	mv1011050_4002702	OH	309	01:33:15	514752	360	256	5147.5
g76	mv1011050_4002801	OH	309	01:41:57	521400	395	256	5214.0
g77	mv1011050_4002901	OH	309	01:51:14	528108	370	256	5281.1
g78	mv1011050_4003102	OH	309	02:33:35	561438	700	256	5614.4
g79	mv1011050_4003103	OH	309	02:45:15	570069	700	256	5700.7
g80	mv1011050_4003302	OH	309	03:33:28	605695	700	256	6057.0
g81	mv1011050_4003303	OH	309	03:45:08	614326	700	256	6143.3
g82	mv1011050_4003402	OH	309	04:04:21	626190	320	256	6261.9
g83	mv1011050_4003702	OH	309	05:34:16	694975	700	256	6949.8
g84	mv1011050_4003703	OH	309	05:45:56	703605	700	256	7036.1
g85	mv1011050_4003902	OH	309	06:34:17	739330	700	256	7393.3
g86	mv1011050_4003903	OH	309	06:45:57	747961	700	256	7479.6
g87	mv1011050_4004102	OH	309	07:34:18	783686	700	256	7836.9
g88	mv1011050_4004103	OH	309	07:45:58	792317	700	256	7923.2
g89	mv1011050_4004302	OH	309	08:34:19	828041	700	256	8280.4
g90	mv1011050_4004303	OH	309	08:45:59	836672	700	256	8366.7
g91	mv1011050_4004502	OH	309	09:34:20	872397	700	256	8724.0
g92	mv1011050_4004503	OH	309	09:46:00	881027	700	256	8810.3
g93	mv1011051_4004702	OH	309	10:34:21	916751	700	256	9167.5
g94	mv1011051_4004703	OH	309	10:46:01	925381	700	256	9253.8
g95	mv1011051_4004902	OH	309	11:34:21	961093	700	256	9610.9
g96	mv1011051_4004903	OH	309	11:46:01	969723	700	256	9697.2
g97	mv1011051_4005102	OH	309	12:34:21	1005434	700	256	10054.3
g98	mv1011051_4005103	OH	309	12:46:01	1014064	700	256	10140.6
g99	mv1011051_4005302	OH	309	13:34:21	1049775	700	256	10497.8
g100	mv1011051_4005303	OH	309	13:46:01	1058405	700	256	10584.1
g101	mv1011051_4005502	OH	309	14:34:21	1094118	700	256	10941.2
g102	mv1011051_4005503	OH	309	14:46:01	1102749	700	256	11027.5

Table 6.4: Gas images analyzed for coma structures (2).

Index	**Image name**	**Filt.**	**DOY**	**time**	**range** [km]	**exp.** [s]	**size** [pix]	**resol.** [m/pix]
g103	mv1011051_4005702	OH	309	15:34:21	1138458	700	256	11384.6
g104	mv1011051_4005703	OH	309	15:46:01	1147088	700	256	11470.9
g105	mv1011051_4005902	OH	309	16:34:21	1182798	700	256	11828.0
g106	mv1011051_4006102	OH	309	17:34:21	1227137	700	256	12271.4
g107	mv1011051_4006103	OH	309	17:46:01	1235767	700	256	12357.7
g108	mv1011051_4006302	OH	309	18:34:21	1271477	700	256	12714.8
g109	mv1011051_4006303	OH	309	18:46:01	1280106	700	256	12801.1
g110	mv1011051_4006502	OH	309	19:34:21	1315814	700	256	13158.1
g111	mv1011051_4006503	OH	309	19:46:01	1324444	700	256	13244.4
g112	mv1011052_4006702	OH	309	20:34:21	1360151	700	256	13601.5
g113	mv1011052_4006703	OH	309	20:46:01	1368781	700	256	13687.8
g114	mv1011052_4006902	OH	309	21:34:21	1404489	700	256	14044.9
g115	mv1011052_4006903	OH	309	21:46:01	1413118	700	256	14131.2
g116	mv1011052_4007102	OH	309	22:34:21	1448825	700	256	14488.3
g117	mv1011052_4007103	OH	309	22:46:01	1457454	700	256	14574.5
g118	mv1011052_4007302	OH	309	23:34:21	1493161	700	256	14931.6
g119	mv1011052_4007303	OH	309	23:46:01	1501790	700	256	15017.9
g120	mv1011060_4007502	OH	310	00:34:21	1537496	700	256	15375.0
g121	mv1011060_4007503	OH	310	00:46:01	1546125	700	256	15461.3
g122	mv1011060_4007702	OH	310	01:34:21	1581831	700	256	15818.3
g123	mv1011060_4007703	OH	310	01:46:01	1590460	700	256	15904.6
g124	mv1011060_4007902	OH	310	02:34:21	1626165	700	256	16261.7
g125	mv1011060_4007903	OH	310	02:46:01	1634793	700	256	16347.9
g126	mv1011060_4008102	OH	310	03:34:20	1670497	700	256	16705.0
g127	mv1011060_4008103	OH	310	03:46:01	1679126	700	256	16791.3
g128	mv1011060_4008302	OH	310	04:34:21	1714830	700	256	17148.3
g129	mv1011060_4008303	OH	310	04:46:01	1723459	700	256	17234.6
g130	mv1011060_4008502	OH	310	05:34:20	1759162	700	256	17591.6
g131	mv1011060_4008503	OH	310	05:46:01	1767790	700	256	17677.9
g132	mv1011060_4008702	OH	310	06:34:21	1803493	700	256	18034.9
g133	mv1011060_4008703	OH	310	06:46:01	1812121	700	256	18121.2
g134	mv1011060_4008902	OH	310	07:34:20	1847823	700	256	18478.2
g135	mv1011060_4008903	OH	310	07:46:01	1856451	700	256	18564.5
g136	mv1011060_4009102	OH	310	08:34:21	1892153	700	256	18921.5
g137	mv1011060_4009103	OH	310	08:46:01	1900781	700	256	19007.8
g138	mv1011060_4009302	OH	310	09:34:21	1936481	700	256	19364.8
g139	mv1011060_4009303	OH	310	09:46:01	1945109	700	256	19451.1
g140	mv1011061_4009502	OH	310	10:34:21	1980810	700	256	19808.1
g141	mv1011061_4009503	OH	310	10:46:01	1989438	700	256	19894.4
g142	mv1011061_4009702	OH	310	11:34:21	2025136	700	256	20251.4
g143	mv1011061_4009902	OH	310	12:34:20	2069462	700	256	20694.6
g144	mv1011061_4009903	OH	310	12:46:01	2078089	700	256	20780.9
g145	mv1011061_4010102	OH	310	13:34:21	2113788	700	256	21137.9
g146	mv1011061_4010103	OH	310	13:46:01	2122415	700	256	21224.2
g147	mv1011061_4100180	OH	310	19:20:36	2367596	380	256	23676.0
g148	mv1011062_4200180	OH	310	22:20:35	2500548	380	256	25005.5
g149	mv1011070_4300180	OH	311	01:20:35	2633491	380	256	26334.9
g150	mv1011070_4400180	OH	311	04:20:35	2766424	380	256	27664.2
g151	mv1011070_4500180	OH	311	07:20:35	2899345	380	256	28993.5
g152	mv1011071_4100180	OH	311	10:25:36	3035958	380	256	30359.6
g153	mv1011071_4200180	OH	311	13:25:35	3168858	380	256	31688.6

Table 6.5: Gas images analyzed for coma structures (3).

Afterward the images are aligned because usually the pointing of the spacecraft is not enough stable and the boresight is moving fairly quickly over the detector.

For the nucleus-unresolved images, the brightest pixel (excluding the cosmic rays) is considered as the center of the nucleus and the images are aligned respect to that pixel. For the nucleus-resolved images instead, the actual nucleus center is defined using a projection of the nucleus shape model in the plane of the image. Values from Farnham, T. (personal communication) have been used for the projection centers.

Since SPICE pointing kernels are usually not enough accurate, as already seen for Lutetia in Sec. 4.7.3, often the alignment to the theoretic nucleus center is not accurate enough, so that a further stacking improvement is performed using an iterative cross correlation process at the precision of a quarter of a pixel.

6.2.2 Cosmic rays removal

The images stacking procedure has been used often on images of the same filter in order to remove the cosmic rays.

A pixel-by-pixel check is performed and if a pixel differs more than a factor 10 in the two images, it is considered a cosmic ray. In this case the cosmic ray pixel is removed from the image and a nearest neighborhood interpolation is performed over the non-cosmic-rays pixels. A further check for the cosmic rays spatial distribution is performed to be sure that it is a random spatial distribution and no artifacts are introduced in the process.

6.2.3 Polar coordinate conversion

Often it is convenient to work with polar images, rather than with rectangular images, especially for spherical symmetric cases. Therefore the images are converted into polar coordinates. This conversion indeed makes some analysis easier, such as the radial and azimuthal profiles derivation and some of the enhancement techniques.

Each pixel of the image, with rectangular coordinate (x, y), is associated to the polar coordinates (r,Θ), i.e. the distance in pixels from the nucleus center, r, and the azimuth angle, Θ, measured counterclockwise from the vertical line going from the center of the object perpendicularly to the bottom of the image. For each coordinate, a 2-D map is produced (Fig. 6.2), describing as the polar coordinates vary over the image.

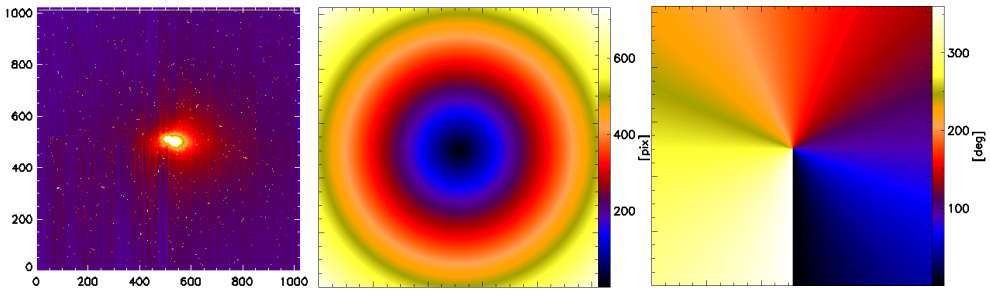

(a) Original image g57 (b) r-map (c) Θ-map

Figure 6.2: Original image g57 (see Tab. 6.4) and its correspondent r and Θ coordinate maps.

If x_i and y_i are the rectangular coordinates of pixel i, the four quadrants are defined as follows:

$$Q_1 : x_i > 0; \quad y_i \leq 0 \tag{6.2}$$
$$Q_2 : x_i \geq 0; \quad y_i > 0 \tag{6.3}$$
$$Q_3 : x_i < 0; \quad y_i \geq 0 \tag{6.4}$$
$$Q_4 : x_i \leq 0; \quad y_i < 0 \tag{6.5}$$

If x_c and y_c are the rectangular coordinates of the nucleus center, the translation of the origin of coordinates to the nucleus center is first applied:

$$x'_i = x_i - x_c \tag{6.6}$$
$$y'_i = y_i - y_c \tag{6.7}$$

then, for each pixel i, r is given by:

$$r = \sqrt{x'^2_i + y'^2_i} \tag{6.8}$$

and an intermediate parameter θ is calculated:

$$\theta = \left| \arcsin\left(\frac{y'_i}{r}\right) \right| \tag{6.9}$$

so that Θ is then given for each quadrant by:

$\Theta[Q_1] = \pi/2 - \theta[Q_1]$
$\Theta[Q_2] = \pi/2 + \theta[Q_2]$
$\Theta[Q_3] = 3\pi/2 - \theta[Q_3]$
$\Theta[Q_4] = 3\pi/2 + \theta[Q_4]$

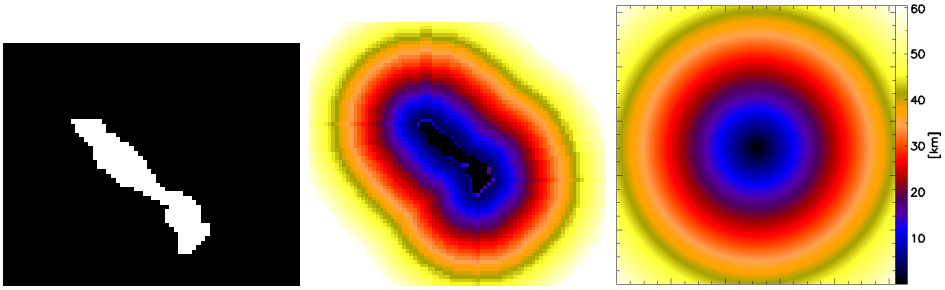

(a) Nucleus shape mask for OH g57

(b) r-map in the near-nucleus region

(c) r-map in km

Figure 6.3: Nucleus shape mask and the r-map in km

A further improvement of r-map is implemented for the nucleus-resolved images (g56-g57 and g56cn-g57cn in Tab. 6.4). Instead of the plane nucleus center, indeed, the nucleus shape mask is used (Fig. 6.3a), obtained from the HRI thermal emission maps (Protopapa, S. personal communication), and r is measured in pixels from the limb, so that r-profiles look as in Fig. 6.3b in the vicinity of the nucleus. Furthermore r-map is usually converted into kilometers (Fig. 6.3c) using the image pixel scale. At large distances the r-profiles look however as circles, as visible in Fig. 6.3c, but in the very innermost regions the nucleus shape mask provides a significant improvement.

6.2.4 Stripes removal

Sometimes the final images present annoying stripes (see Fig. 6.4a) due probably to electrical interferences. Since there are 4 amplifiers for the CCD, the stripes have a four quadrants pattern in full frame images, and may be partially removed using an adequate algorithm. A removing procedure has been developed which checks the first 100 rows samples of each quadrants, counted from the bottom for the two bottom quadrants, and from the top for the two top quadrants. Then those rows are averaged and the pattern of the stripes is fitted with a polynomial function which is then subtracted from the whole quadrant. At the same time the procedure removes also the residual offset among the four quadrants. An example of the application of the procedure is shown in Fig. 6.4.

As it is evident from the color scales changing from Fig. 6.4a to Fig. 6.4b, the procedure causes a relative drop in flux intensity due to the background coma subtracted in the procedure. This has been taken into account in the further photometric analysis.

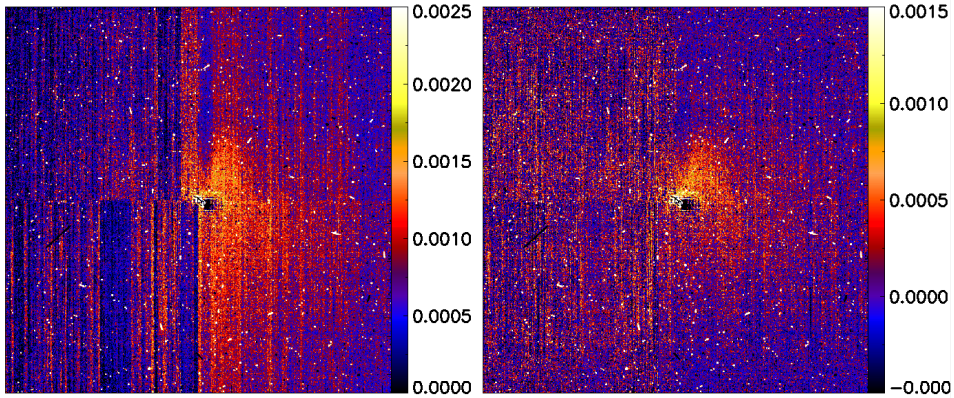

(a) OH gas image before stripes removal procedure

(b) OH gas image after stripes removal procedure

Figure 6.4: Stripes removal procedure application.

6.2.5 Enhancement Techniques

Usually the coma structures are very faint and hidden by the dust and the isotropic components of the coma. Many are the enhancement techniques that can be used to remedy this problem (see Samarasinha et al. 2011).

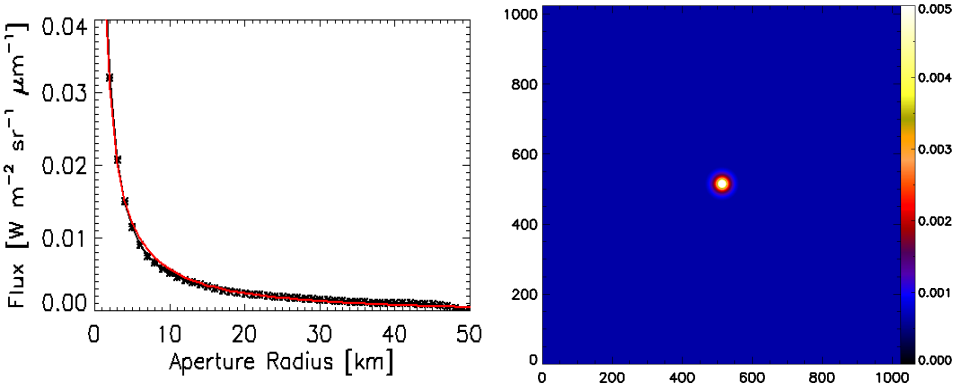

(a) (b)

Figure 6.5: Clear filter radial profile (a) fit and (b) 2D image.

One of the easiest and more used methods, which has been also used in this thesis, is the radial profile subtraction. The radial profile of the comet's coma, averaged over the entire azimuthal range, gives the description of the

isotropic coma brightness.

Subtracting the averaged radial profile from the original images may reveal anisotropic features of the coma that are otherwise hidden under a brighter isotropic coma.

The profile is usually fitted with a polynomial function (Fig. 6.5a) and converted into a 2D image (Fig. 6.5b) which is then subtracted from the original image. This method may highlight interesting jets and structures in the coma which are otherwise concealed.

6.3 Coma Dust analysis

As mentioned in Sec. 1.4, the coma flux is made up of two components: the dust continuum and the gas emissions. The dust brightness and distribution in the coma of Hartley2 is derived from the observations acquired with the Green, Violet, Red, IR and Clear filters, called continuum filters.

The images analyzed are mainly nucleus-resolved, acquired all in DOY 308, approximately from 10 minutes before to 10 minutes after the closest approach. They are summarized in Tab. 6.2.

The dust images in Fig. 6.6-6.7 have been enhanced using the radial profile subtraction. The radial profiles have been fitted with the polynomial function:

$$F = a_0 + a_1/d + a_2/d^2 \tag{6.10}$$

where d is the distance from the nucleus center, while a_0, a_1 and a_2 are three parameters to fit.

6.3.1 Dust structures

Dust structures in the continuum images have been investigated to make comparison with gas structures, to look for a correlation and finally also to check if in the gas profiles the continuum had been well removed.

The dust images in Fig. 6.6-6.7 show different structures. The Clear1 images d1-d5 show a possible rounded structure in the top left side of the nucleus visible also in the violet, red and green images d6, d7 and d8. In Clear1 d10 image a linear structure on the bottom left side of the comet (in the antisolar direction) becomes more evident and stays visible until image d18 when a new small structure coming from the surface becomes evident again on the top left side (antisunward) direction. In d10 image another linear structure becomes visible on the bottom right side, in solar direction, and it seems to separate in many jets in image d16, while the spacecraft

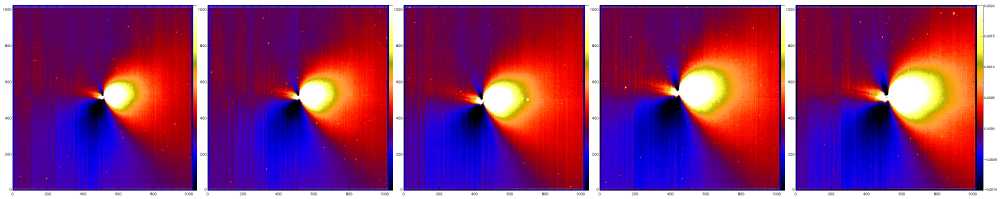

d1. CLEAR1 13.38.39 | d2. CLEAR1 13.41.26 | d3. CLEAR1 13.43.55 | d4. CLEAR1 13.46.14 | d5. CLEAR1 13.48.12

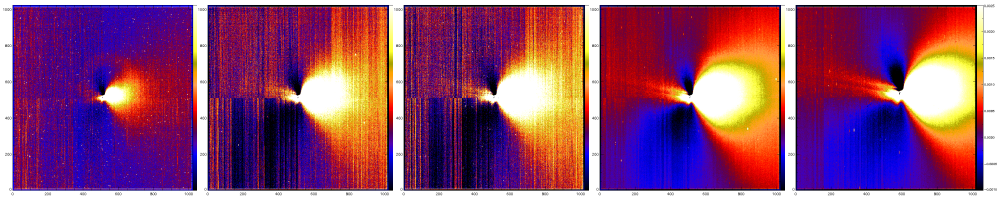

d6. VIOLET 13.48.55 | d7. RED 13.50.06 | d8. GREEN 13.50.10 | d9. CLEAR1 13.50.30 | d10. CLEAR1 13.52.53

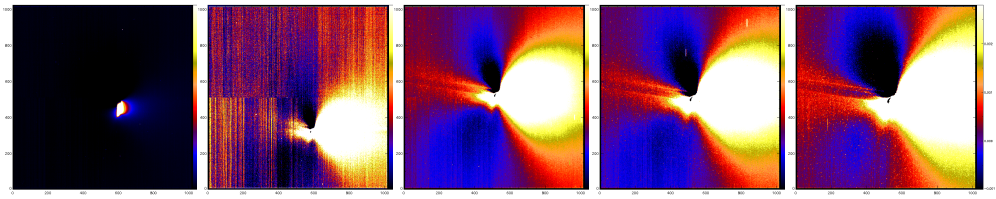

d11. IR 13.53.31 | d12. RED 13.53.36 | d13. CLEAR1 13.54.20 | d14. CLEAR1 13.55.32 | d15. CLEAR1 13.56.30

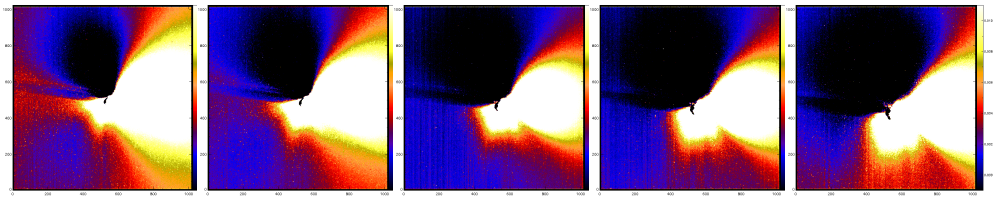

d16. CLEAR1 13.57.00 | d17. CLEAR1 13.57.27 | d18. CLEAR1 13.57.58 | d19. CLEAR1 13.58.17 | d20. CLEAR1 13.58.37

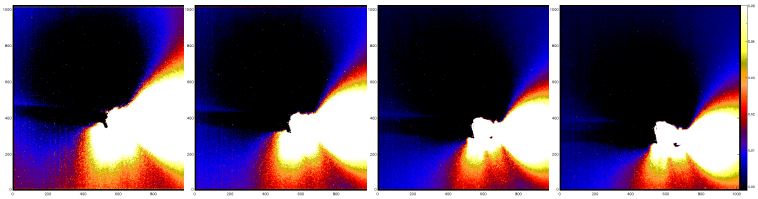

d21. CLEAR1 13.58.53 | d22. CLEAR1 13.59.02 | d23. CLEAR1 13.59.12 | d24. CLEAR1 13.59.22

Figure 6.6: Dust coma observations (1).

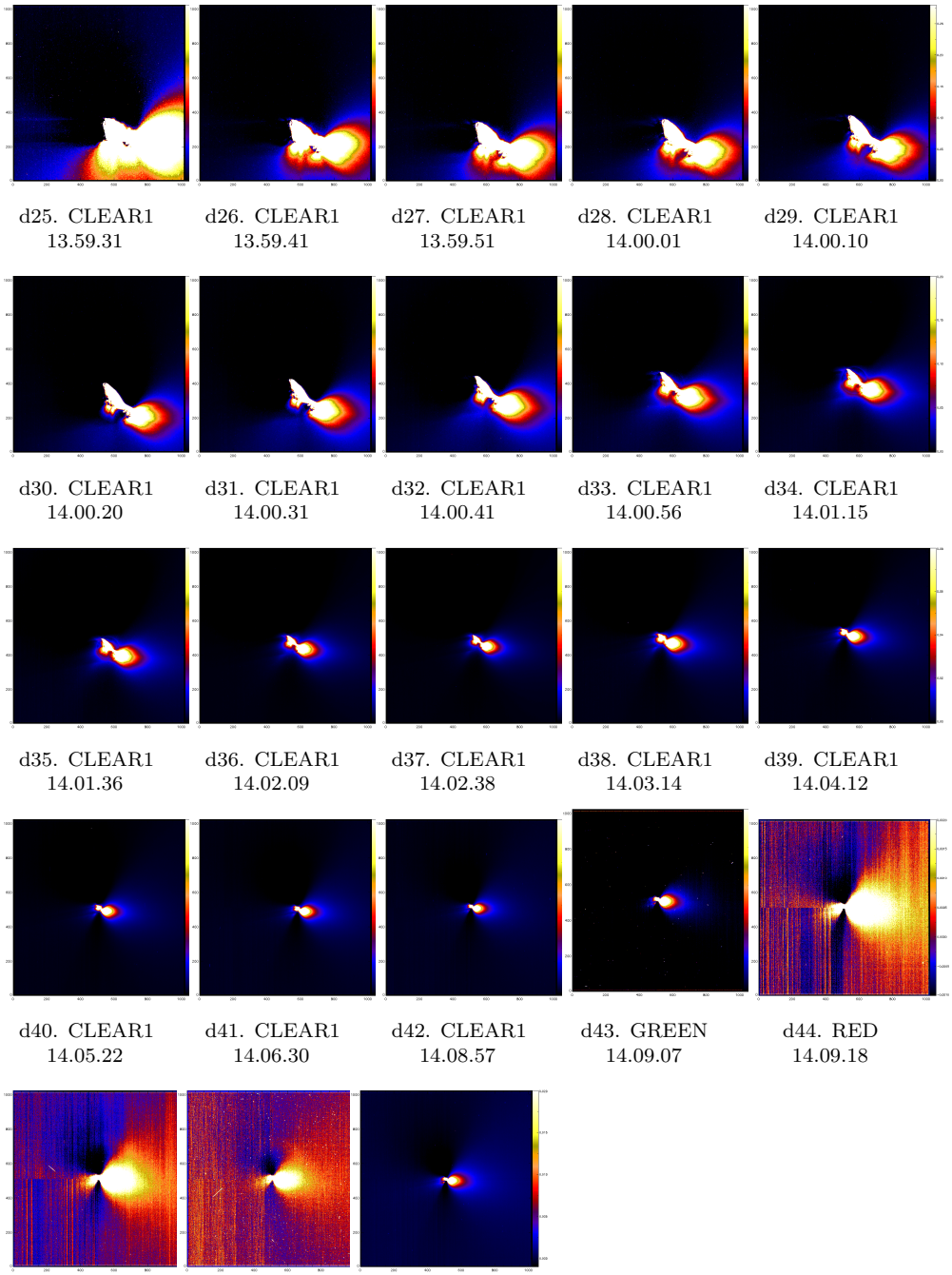

d25. CLEAR1 13.59.31 | d26. CLEAR1 13.59.41 | d27. CLEAR1 13.59.51 | d28. CLEAR1 14.00.01 | d29. CLEAR1 14.00.10

d30. CLEAR1 14.00.20 | d31. CLEAR1 14.00.31 | d32. CLEAR1 14.00.41 | d33. CLEAR1 14.00.56 | d34. CLEAR1 14.01.15

d35. CLEAR1 14.01.36 | d36. CLEAR1 14.02.09 | d37. CLEAR1 14.02.38 | d38. CLEAR1 14.03.14 | d39. CLEAR1 14.04.12

d40. CLEAR1 14.05.22 | d41. CLEAR1 14.06.30 | d42. CLEAR1 14.08.57 | d43. GREEN 14.09.07 | d44. RED 14.09.18

d45. IR 14.09.21 | d46. VIOLET 14.09.21 | d47. CLEAR1 14.11.35

Figure 6.7: Dust coma observations (2).

starts to turn around the comet. From d28 on, smaller and more confined jets are visible from different source regions on the surface of the comet.

6.3.2 Dust colors and reddening

The comet's dust mainly reflects the sunlight so that its spectrum is very similar to the solar spectrum but it has its own characteristics depending on the composition of the dust, the dimension of the particles etc. Usually comets dust reflectance spectra show also a slight reddening respect to the solar spectrum, due probably to the action of the space weathering on the dust particles.

The solar flux incident over the surface of the comet in the filter f is given by:

$$F_{\odot,f} = \frac{\int_0^\infty \frac{F_{\odot,1}(\lambda)}{\pi d^2} T_f(\lambda) M(\lambda) QE(\lambda) d\lambda}{\int_0^\infty T_f(\lambda) M(\lambda) QE(\lambda) d\lambda} \tag{6.11}$$

where $F_{\odot,1}(\lambda)$ is the solar flux expressed in W m^{-2}nm^{-1} at 1 AU, d is the distance Sun-comet in AU, $T_f(\lambda)$ is the transmissivity of the filter f, $M(\lambda)$ is the reflectivity of the mirrors, and $QE(\lambda)$ is the quantum efficiency of the CCD. The flux reflected by the dust in filter f will be then:

$$D_f = r_f \cdot F_{\odot,f} \tag{6.12}$$

where r_f is the reflectance of the dust in the filter f given by:

$$r_f = \frac{\int_0^\infty r(\lambda) T_f(\lambda) M(\lambda) QE(\lambda) d\lambda}{\int_0^\infty T_f(\lambda) M(\lambda) QE(\lambda) d\lambda} \tag{6.13}$$

with $r(\lambda)$ being the reflectance spectrum of the dust. If f_c is a continuum filter, then D_{f_c} will be equivalent to the observed flux in that filter, called I_{f_c}:

$$\text{Continuum filters} : D_{f_c} \equiv I_{f_c} \tag{6.14}$$

so that r_f can be evaluated, only for the continuum filters, using the formula:

$$\text{Continuum filters} : r_f = \frac{I_f}{F_{\odot,f}} \tag{6.15}$$

This is not true for gas filters f_g where the observed flux $I_{f_g} \neq D_{f_g}$ because it is the sum of the dust reflectance and the gas emissions.

If continuum images are available in more than one filter it is possible to estimate the dust colors which are defined as the following:

$$C_{f1,f2} = \frac{D_{f1}}{D_{f2}} \equiv \frac{I_{f1}}{I_{f2}} \tag{6.16}$$

It is also possible to estimate the slope of the dust reflectance spectrum between continuum filter $f1$ and filter $f2$ that is given by:

$$s = \frac{r_{f2} - r_{f1}}{\lambda_{f2} - \lambda_{f1}} \tag{6.17}$$

where λ_{f1} and λ_{f2} are respectively the effective wavelengths of the two filters. The reddening between $f1$ and $f2$ in %/100nm is then defined as (see Eq. 4.4):

$$R_{f1,f2} = \frac{s \cdot 100 \cdot 100}{\frac{r_{f1} + r_{f2}}{2}} \tag{6.18}$$

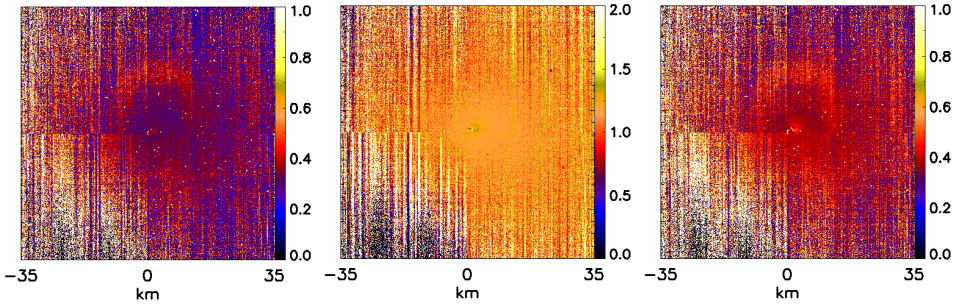

Violet/Green Green/Red Violet/Red

Figure 6.8: Color maps for dust images d6, d7 and d8 in Tab. 6.2.

For the set of narrowband dust images acquired just before CA with the comet (images d6, d7 and d8 of Tab. 6.2), Violet/Green, Green/Red and Violet/Red color maps have been calculated (Fig. 6.8). Furthermore, an azimuthal study of the color maps has been performed. The azimuth-averaged radial profiles are shown in Fig. 6.9. The profiles are quite flat along the aperture, suggesting an homogeneity of the dust at least for these distance ranges. A further analysis has been performed to investigate a possible differentiation in the nature of the dust in the sunward versus antisunward directions. The Sun is on the right side of the images, therefore the profiles have been divided into the sunward direction (azimuth: 0°-180°) and the

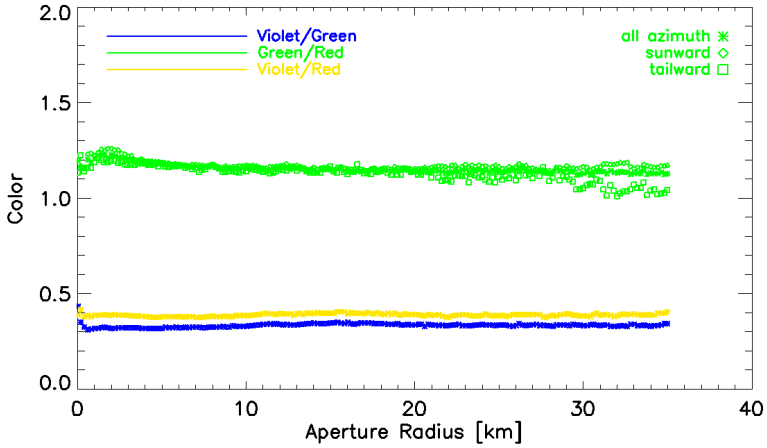

Figure 6.9: Dust colors radial profiles in the sunward (azimuth 0°-180°) and antisunward (azimuth 180°-360°) directions

antisunward direction (azimuth: 180°-360°), the azimuth being Θ in Fig. 6.2c.

The Green/Red color shows a slight decreas of about 10% in the tailward direction for distances higher than 20 km, suggesting that particles are redder in this region. This may be due to a compositional variegation: ices are usually bluer while refractory materials are redder. This is compatible with the standard model of ices and refractories which are emitted in the sunward direction together and then the ices sublimates while the refractories are pushed away by the radiation pressure and form the tail. The slight different may be also due to other physical phenomenon as grain size effect, or fragmentation.

Fig. 6.10 shows instead the reddening maps in the wavelength ranges violet-green, green-red and violet-red.

A radial study of the reddening maps have also been performed and the radial profiles have also been evaluated and shown in Fig. 6.11.

In the Violet-Green wavelength range, the reddening is slightly decreasing over the radial profile going from about 6%/100 nm within 10 km from the nuclesu down to 4.5%/100 nm at about 35 km cometocentric distance. As expected the Green-Red reddening is about 2,5%/100 nm and remains stable from about 10 to 35 km from the nucleus. It is lower than the violet-green reddening since the spectrum is expected to be flatter in this wavelength range. This is consistent with a typical spectrum of a cometary nucleus,

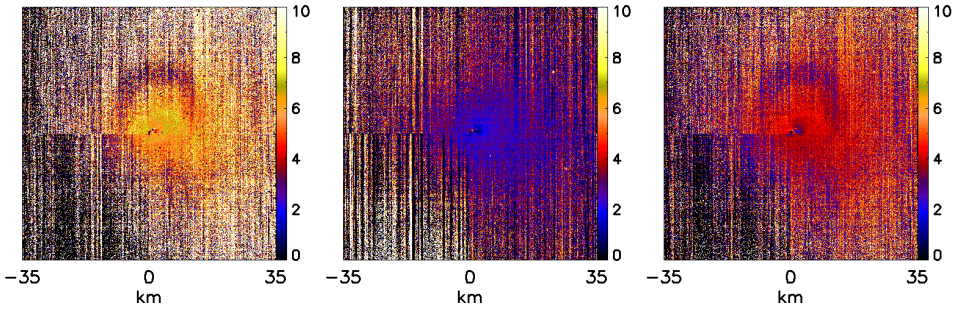

Violet-Green reddening map | Green-Red reddening map | Violet-Red reddening map

Figure 6.10: Reddening maps for the dust images d6, d7 and d8 in Tab. 6.2.

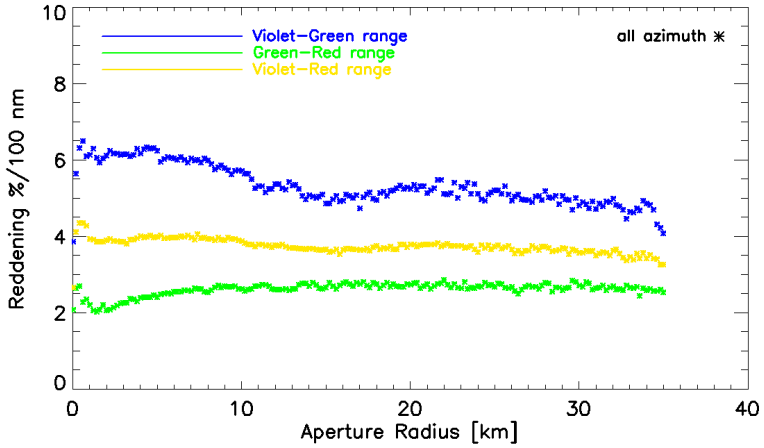

Figure 6.11: Reddening radial profiles in the wavelength range Violet-Green-Red obtained from narrowband dust images d6, d7 and d8 in Tab. 6.2

usually similar to carbonaceous material spectra. The Violet-Red reddening, being a measure over the whole wavelength range, it is obviously in the middle of the two at about 3.5-4%/100 nm.

The Violet-Green and Green-Red reddening maps have been evaluated also for the dust images acquired just after CA (images d43, d44, d46 of Tab. 6.2) and reported in Fig. 6.12, showing a consistency with the reddening obtained from images acquired before the CA.

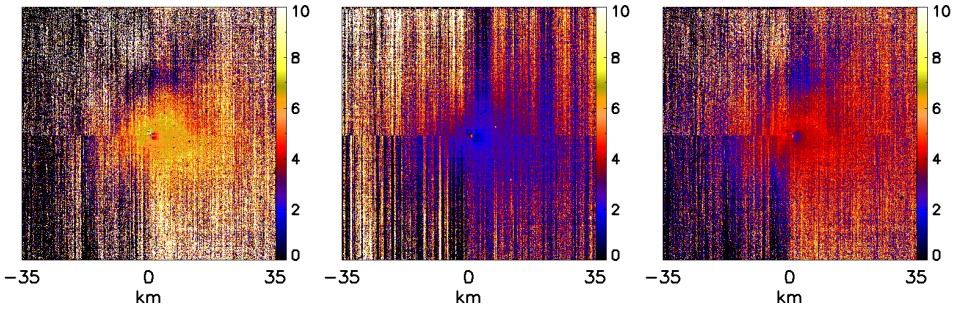

Violet-Green reddening map | Green-Red reddening map | Violet-Red reddening map

Figure 6.12: Reddening maps for the dust images d43, d44, d46 acquired after CA.

6.4 Coma Gas analysis

The gas component of the coma of Hartley 2 has been studied, thanks to the gas filters (OH, CN and C_2) of the MRI camera (see Table 6.1).

We have focused mainly on four nucleus-resolved images in gas filters OH (g56-g57 in Tab. 6.4) and CN (g56cn-g57cn in Tab. 6.4), acquired on DOY 308, approximately from 10 minutes before to 10 minutes after the closest approach. These images are acquired at about 8 000 km of distance from the nucleus center with a pixel scale of 73 to 83 m/pixel and a phase angle ranging from 85° to 92°. The spacecraft flew under the comet so that the orientation of the nucleus in the images before CA and after CA is changed, the Sun is always on the right, while the nucleus itself did not rotate that much in that period since it has a rotation period of 18 hours. These are very important images since they allow the study of the very innermost coma where all the chemical reactions take place and the parent molecules ejected from the nucleus decay into daughter molecules and give rise to the whole comets chemistry. It is still poorly known since this region is totally inaccessible from usual ground-based observations and those kind of information can be retrieved only by space investigations.

Furthermore a total of 153 OH images have been considered, which have been acquired from 7 days before CA to 3 days after CA, i.e. from the day of perihelion (DOY 301) to 10 days after perihelion (DOY 311). They have been analyzed in order to obtain an overview of the evolutions of the structures and of the water production rate computed from OH flux.

6.4.1 Continuum removal

A gas filter observation includes not only the gas emission but also the flux reflected from the dust particles in the coma, so that in order to isolate the gas emission, a careful continuum removal process is necessary to cut out the flux coming from the dust component of the coma.

The continuum images are therefore used as tracers of the dust flux that "contaminates" the gas filters images. However, dust flux incoming in the gas filters is slightly different from the dust flux incoming in the dust filters. Therefore, in order to subtract the right component from the gas emission, it is necessary to know the ratio between the dust flux incoming in the gas filter as respect to the dust flux in the continuum filter, which will be called *continuum removal factors*.

If the reflectance of the dust, $r(\lambda)$, is constant over the wavelength range, which means that the dust has exactly a solar spectrum, then the continuum removal factor for gas filter f_g and continuum filter f_c would be simply given by:

$$CRF_{f_g,f_c} = \frac{D_{f_g}}{D_{f_c}} \tag{6.19}$$

This yields the continuum removal factors in Tab. 6.6.

	OH	CN	C_2
Clear1	0.443	0.727	1.302
Violet	0.668	1.097	1.963
Green	0.337	0.553	0.989
Red	0.497	0.816	1.461

Table 6.6: Continuum removal factors for gas filters assuming a solar spectrum for the dust.

However, this is only a first approximation of the dust flux, since usually the dust does not have a constant albedo but it has its own reflectance spectrum. Anyway if only one continuum observation is available, it is impossible to estimate the slope of the dust reflectance spectrum and assuming a solar spectrum is the only way to proceed.

Usually indeed, due to the long exposure times required by the narrowband continuum filters, only Clear1 filter observations are performed.

Fortunately, for the closest approach, two sets of narrowband continuum filters observations have been acquired, one just before the CA (images d6, d7 and d8 in Tab. 6.2) and another one just after CA (images d43, d44 and

d46 in Tab. 6.2) and the dust colors and spectral slopes have been evaluated in those occasions (see par. 6.3.2).

In this case, the dust reflectance spectrum is not anymore assumed constant but it is instead approximated by two lines, one in the wavelength range violet-green and the second in the wavelength range green-red, each with the slope obtained from Eq. (6.17). The dust reflectance in each gas filters is then evaluated using Eq. (6.13), and the dust flux in the same filter using Eq. (6.12). The previous steps have been performed pixel-by-pixel using the color maps of the coma, to evaluate the dust continuum flux contaminating the OH and CN images g56-g57 (see Tab. 6.4). For example, using the dust Violet, Red and Green images d6, d7 and d8 (see Tab. 6.2), the resulting OH continuum image is shown in Fig. 6.13.

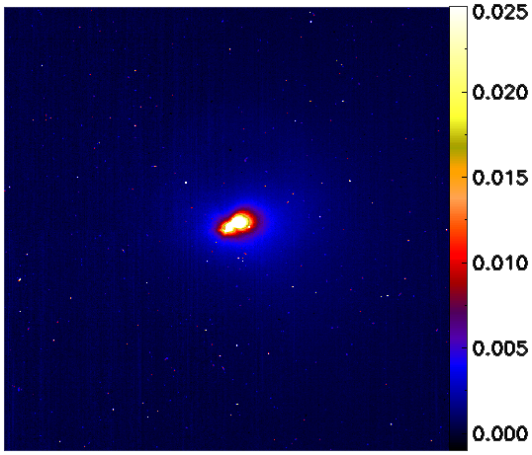

Figure 6.13: Dust flux "contaminating" OH image g56 obtained from Violet, Red and Green images d6, d7 and d8.

If the assumption that the dust spectrum remains somewhat constant is accepted, then, using the slope of the dust spectrum evaluated in this way, it is possible to estimate the "reddened" continuum removal factors, which are a slightly better approximation than simple solar continuum removal factors.

Using the sets of continuum images Violet, Red, and Green images d6, d7 and d8, acquired before CA, the OH and CN continuum removal factors have been evaluated, shown in Fig. 6.14, and summarized in Tab. 6.7.

Often it is not possible to evaluate the continuum in this way since the only continuum observations available are in broad clear filters. In those cases the Clear1 observations have to be used as tracer for the continuum in each gas filters. However it is necessary being careful in using Clear1 filter

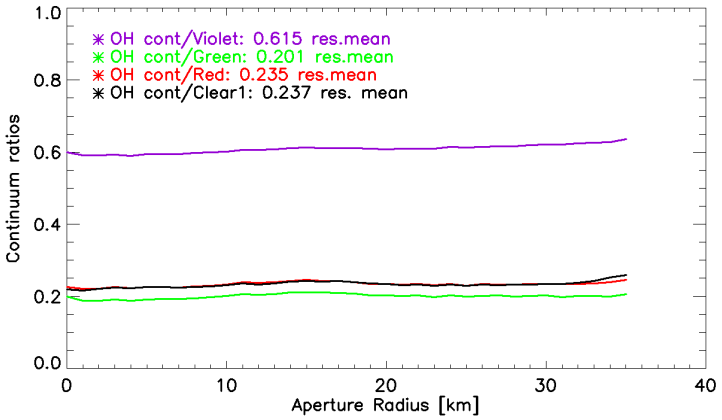

OH/continuum

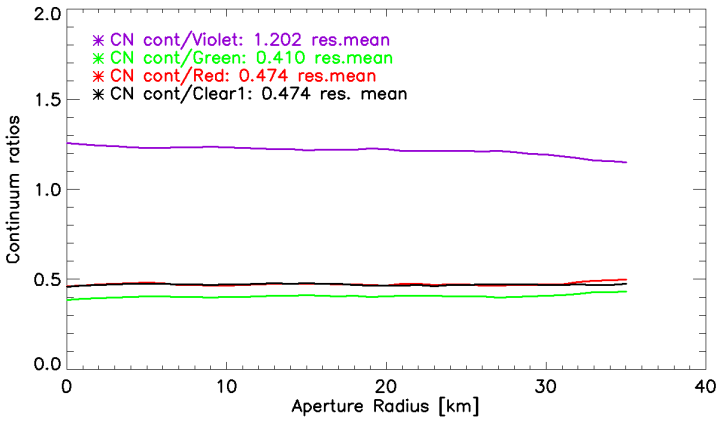

CN/continuum

Figure 6.14: Radial profiles of the ratios of dust flux contaminating OH and CN images over narrowband continuum observations, providing the "reddened" continuum removal factors in Tab. 6.7.

	OH	CN
Clear1	0.237	0.474
Violet	0.615	1.202
Green	0.201	0.410
Red	0.235	0.474

Table 6.7: "Reddened" c ontinuum removal factors assuming a dust reflectance spectrum extrapolated from Violet, Green and Red observations.

for continuum removal since it is well known that, being so wide, it has many strong gas contamination coming probably from C_2, C_3 and other gases like NH, NH_2.

The few narrowband continuum observations performed have been therefore used also as tracer of the gas contamination in the Clear1 filter. Assuming the extrapolated reflectance spectrum, the expected dust flux in the Clear1 filter can be evaluated using Eq. (6.12) pixel by pixel and an an "expected" Clear1 image is generated. In principle, this should correspond to the observed comet's flux in filter Clear1:

$$D_{Clear1} \equiv I_{Clear1} \tag{6.20}$$

but, due to the gas contamination in Clear1 filter, those images differ and the difference provides our estimate of the gas contamination in Clear1 filter (Fig. 6.15a). The relative contamination map is shown in Fig. 6.15b.

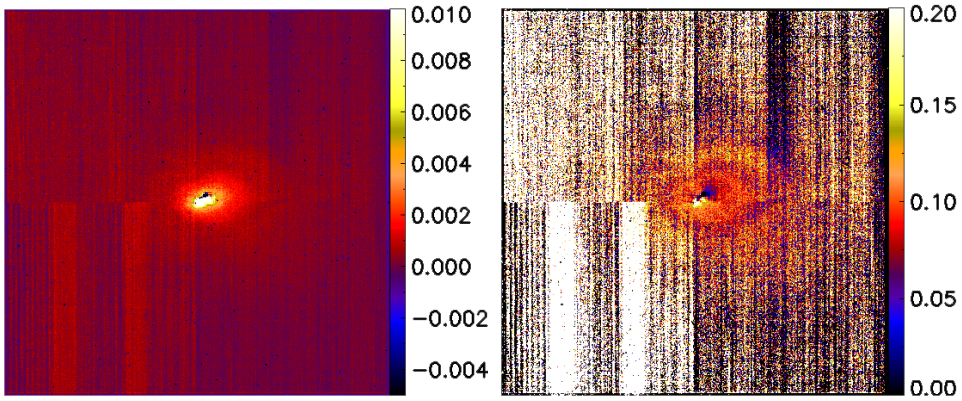

(a) (b)

Figure 6.15: Clear1 filter (a) absolute contamination (difference between observed and expected) and (b) relative contamination.

A radial study of the contamination has been done, resulting in the plot in Fig. 6.16.

If the assumption that the contamination is about constant, which can be considered realistic, since the comet is active during the whole mission timeline, this analysis can be used to correct the Clear1 observations for their contamination in order to be more confident in using them as continuum to be subtracted when none narrowband continuum observation is available.

It results that Clear1 filter is contaminated from 9% to about 12% slightly increasing with cometocentric distance, as expected, since the dust radial

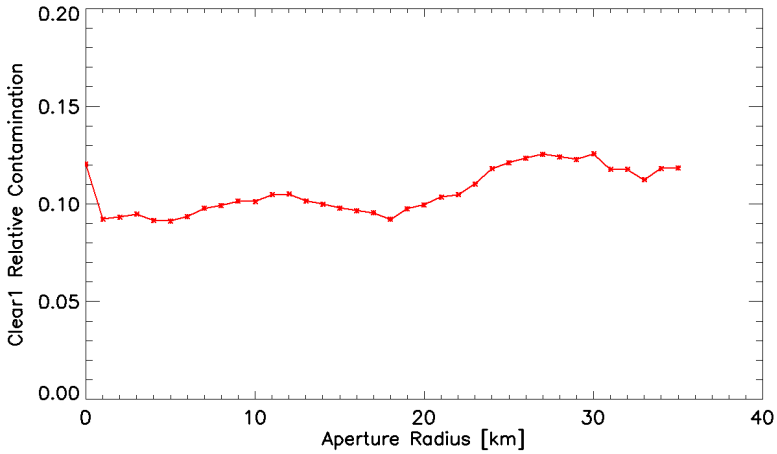

Figure 6.16: Clear1 filter relative contamination radial profile.

profile is usually steeper than the gas, which influences more the outer coma regions.

6.4.2 OH structures

Once the dust contamination has been removed, the resulting image show the pure gas emissions and gas structures in the coma.

Fig. 6.17, 6.18 and 6.19 show the OH gas structures in the coma of Hartley 2 from DOY 301 up to DOY 311 in some of the images reported in Tab. 6.3, 6.4 and 6.5.

Since no narrowband continuum observations were available for most of those images, the continuum removal has been performed using only Clear1 observations, scaled using the "reddened" continuum removal factor in Tab. 6.7 which corrects already for the Clear1 contamination.

In all the images the Sun is on the right side. There is a clear antisolar distribution of OH gas in the coma as seen at large distances. From image g51 a slight radial structure becomes visible in the solar direction which remains visible up to g56 (CA) image. The OH spatial distribution appears almost isotropic from image g54 up to image g58, excluding the two CA images (g56 and g57). Thereafter the OH assumes again an antisolar distribution with no significant jets visible up to image g149 where a strong peak feature appears in the innermost region.

Fig. 6.20a and 6.20b show more in detail the OH emission structure in the vicinity of the nucleus for gas images g56 and g57 of Tab. 6.4, acquired

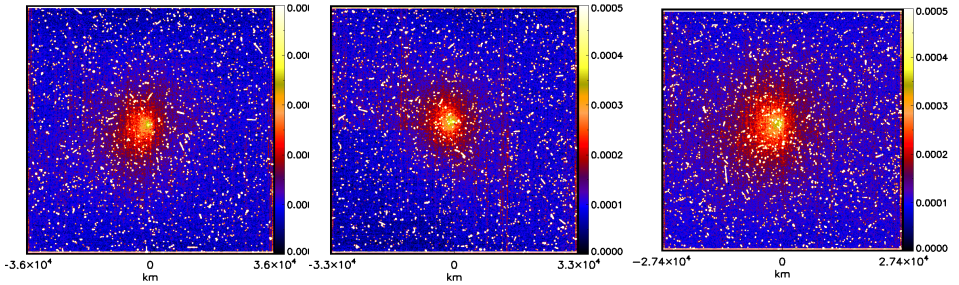

g1. 301 00.38.26 g5. 302 13.38.26 g9. 303 13.38.25

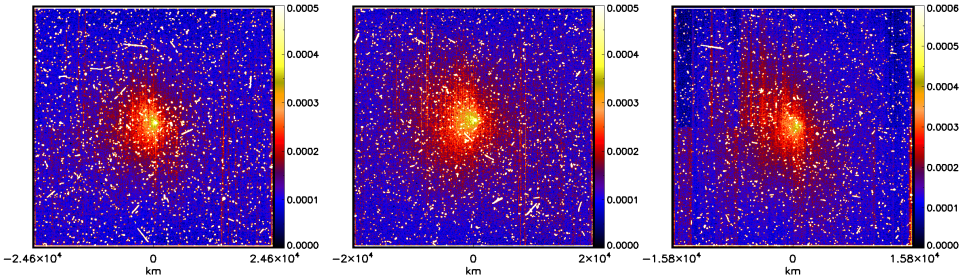

g12. 304 01.38.25 g15. 304 22.38.25 g18. 305 16.38.25

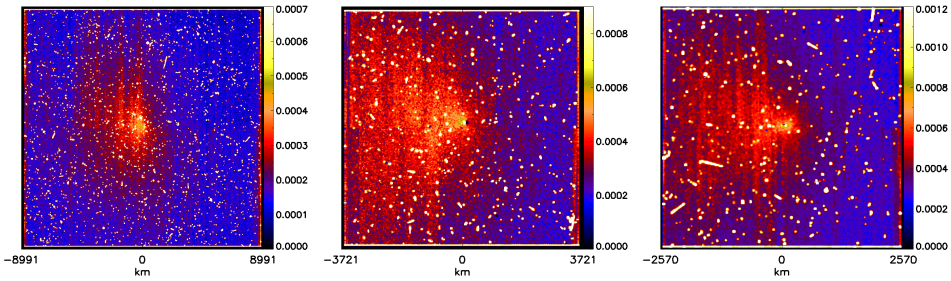

g22. 306 22.38.25 g27. 307 21.25.55 g35. 308 02.23.34

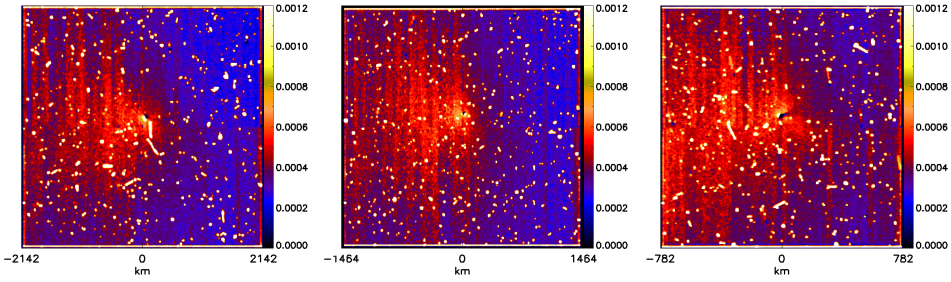

g39. 308 04.16.45 g46. 308 07.23.37 g51. 308 10.24.19

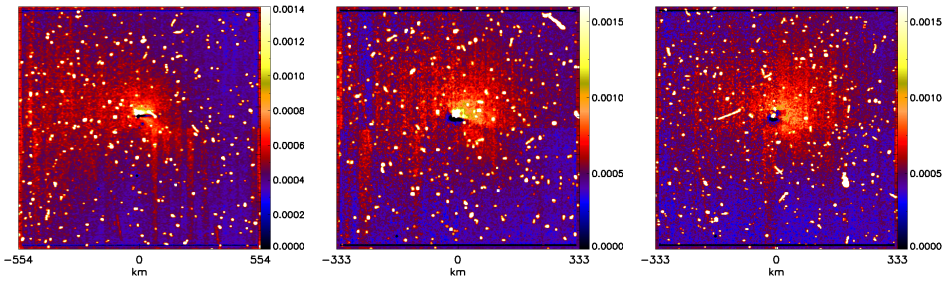

g53. 308 11.23.37 g54. 308 12.16.46 g55. 308 12.23.27

Figure 6.17: OH gas structures (1).

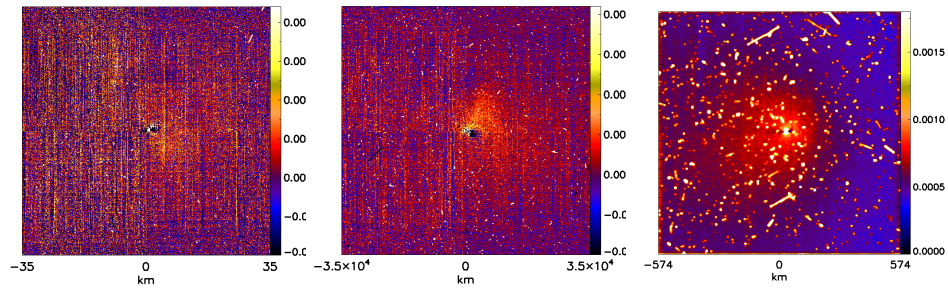

g56. 308 13.48.25 g57. 308 14.10.27 g58. 308 16.31.52

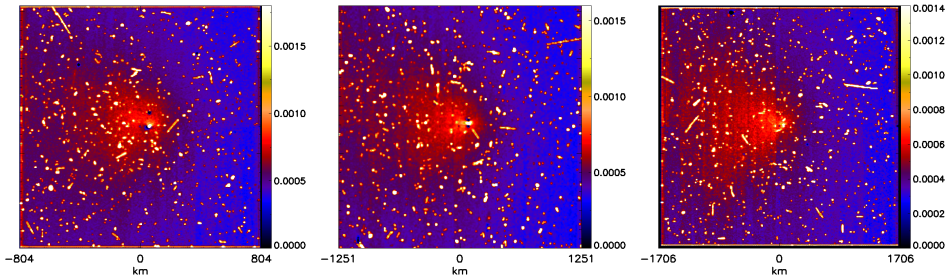

g60. 308 17.32.45 g64. 308 19.43.02 g67. 308 21.31.55

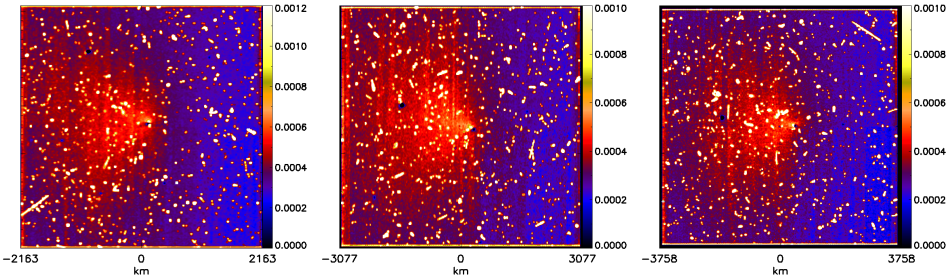

g72. 308 23.44.25 g81. 309 03.45.08 g85. 309 06.34.17

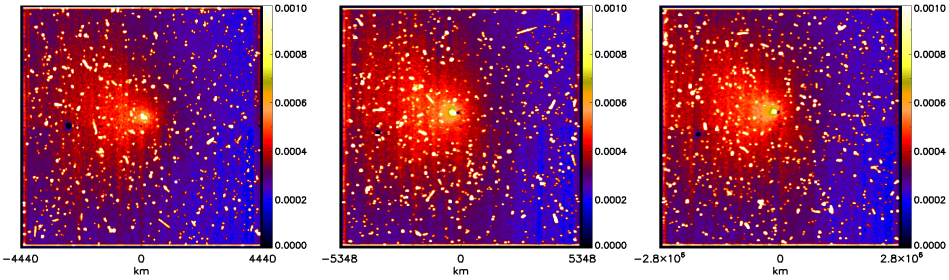

g92. 309 09.46.00 g100. 309 13.46.01 g102. 309 14.46.01

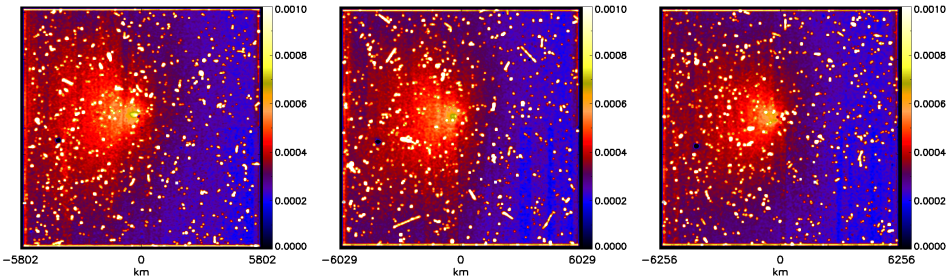

g104. 309 15.46.01 g105. 309 16.34.21 g106. 309 17.34.21

Figure 6.18: OH gas structures (2).

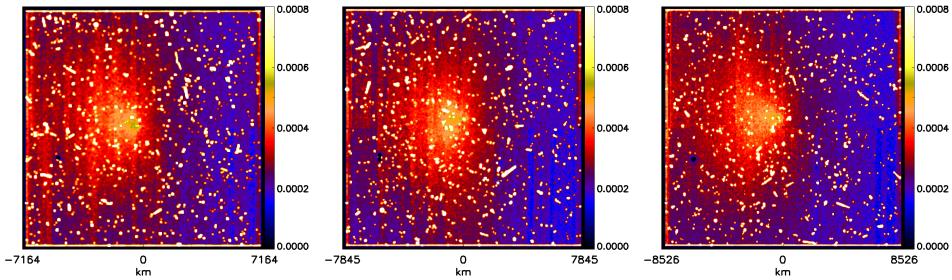

g114. 309 21.34.21 g121. 310 00.46.01 g127. 310 03.46.01

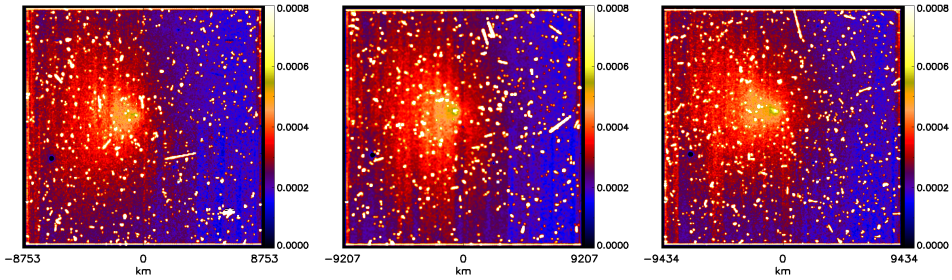

g129. 310 04.46.01 g132. 310 06.34.21 g135. 310 07.46.01

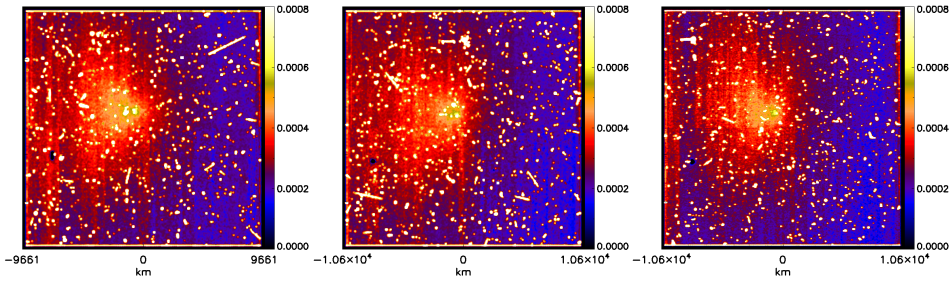

g136. 310 08.34.21 g143. 310 12.34.20 g144. 310 12.46.01

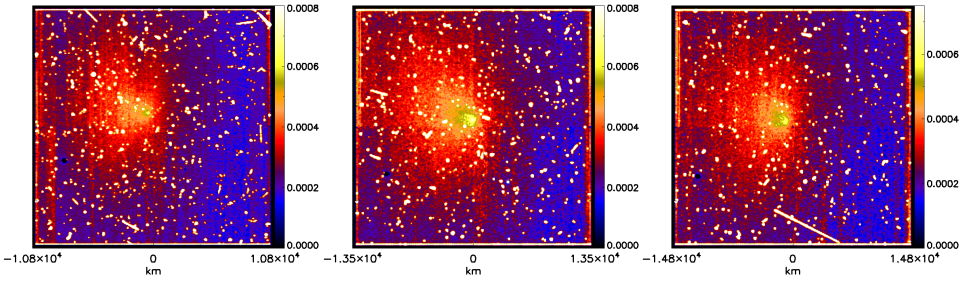

g146. 310 13.46.01 g149. 311 01.20.35 g151. 311 07.20.35

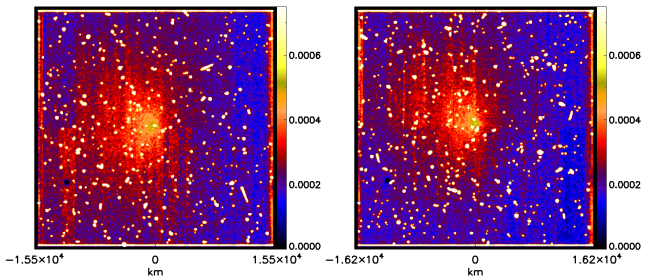

g152. 311 10.25.36 g153. 311 13.25.35

Figure 6.19: OH gas structures (3).

respectively around 10 minutes before CA and 10 minutes after CA.

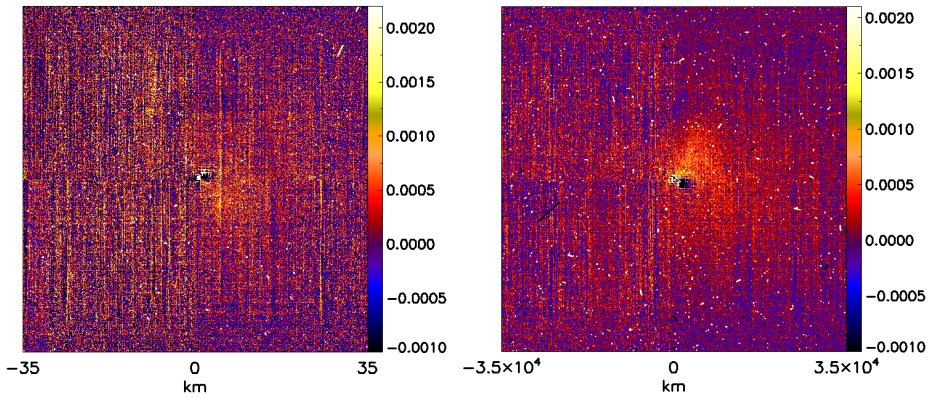

(a) (b)

Figure 6.20: OH gas structures in the inner coma visible in images (a) g56 and (b) g57 of Tab. 6.4.

In both images the Sun is located on the right side while the different orientation of the nucleus is due to the change of viewing point due to the movement of the spacecraft during CA. The geometrical effect of the spacecraft motion is that images after CA are roughly upside down compared to those before the CA.

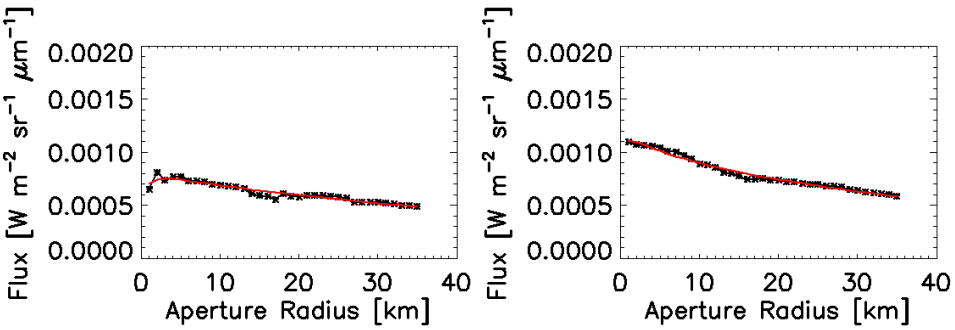

(a) (b)

Figure 6.21: OH radial profiles in images (a) g56 and (b) g57. In red the fit with function in Eq. 6.21 is shown.

It is visible in both images, but more evident in g57, a radial structure coming from the central waist of the nucleus. In g56 it is directed around 30° azimuth while in g57 it is directed around 150° azimuth, which is compatible

with the geometrical change in the point of view, suggesting that it is an actual OH emission feature. To support this hypothesis it should be noted that a compatible radial structure was seen already from image g51 on. The flux intensity looks compatible in the two images which are separated by approximately 20 minutes.

in Fig. 6.21 are reported the resulting azimuthal-averaged radial profiles of the OH emission, fitted with the function:

$$F = a_0 + a_1 d^{a_2} + a_3 * \log(d) \tag{6.21}$$

where d is the distance from the nucleus center and, while a_0, a_1, a_2, and a_3 are parameters to fit.

The profiles look compatible and rather flat as expected for gas profiles. In Fig. 6.21b a weak peak corresponding to the nucleus center is still visible, a probable evidence of a residual continuum.

An azimuthal study of the structures has been performed for both images resulting in Fig. 6.22 and 6.23. For a given distance in kilometers from the nucleus, represented by the circles in the images, the azimuthal profile of the flux is presented. The profiles have been normalized such that the average value, for all azimuth, of each profile is represented by the dashed line in the plots.

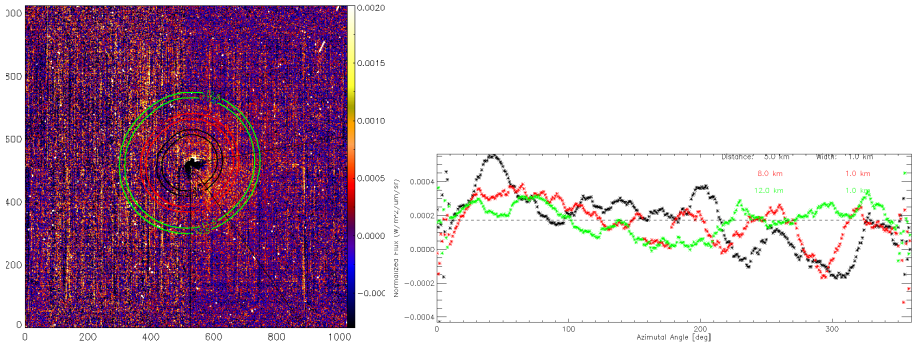

Figure 6.22: OH azimuthal profiles of image g56.

In Fig. 6.22 there is an increase of flux between 25° and 80° in the 5 km profile. The increase is still visible in the further profiles at 8 and 12 km, but the shape becomes broader.

In Fig. 6.23 the peak is clearer between 100° and 170° in the 5 km profile. The 8 km profile shows a similar peak with a broader left wing, while the 12 km curve shows a more similar profile to the 5 km profile.

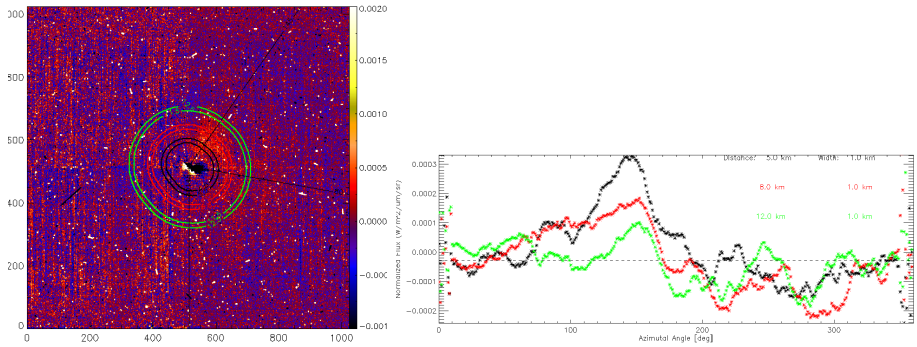

Figure 6.23: OH azimuthal profiles of image g57.

6.4.3 CN structures

The same analysis has been performed for the CN images g55cn and g57cn of Tab. 6.4. Fig. 6.24a and 6.24b show CN emission structures in the vicinity of the nucleus.

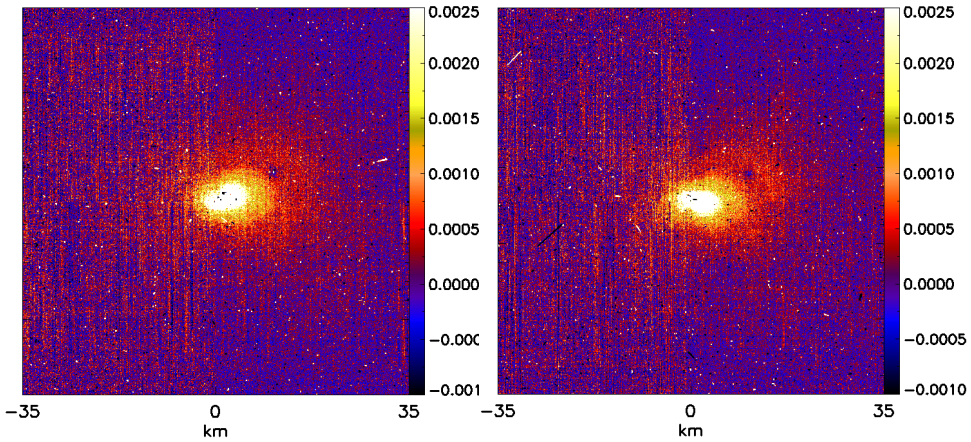

(a) (b)

Figure 6.24: CN gas structures in the inner coma visible in images (a) g56cn and (b) g57cn of Tab. 6.4.

Both images show an halo all around the nucleus which is consistent in the two cases. A bow structure is evident in both images in the upper right region around the nucleus. Moreover in Fig. 6.24b a tentatively radial jet appears directed 45° downwards.

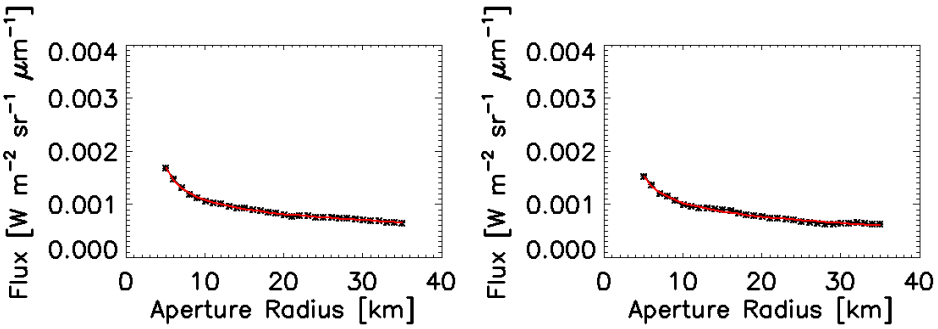

Figure 6.25: CN radial profiles in (a) g56cn image and (b) g57cn image. In red the fit with function in Eq. 6.21 is shown.

The curved path of the structures is explained as an evidence that CN gas is emitted by grains in the coma, rather than by the nucleus directly. The grains indeed are affected by the gravity of the nucleus and its rotation, which is responsible for the curved features. This evidence has been observed already in other comets (see for example A'Hearn et al., 1896; Knight et al., 2013)

The radial profiles of images g56cn and g57cn of Tab. 6.4 have been fit with the function in Eq. 6.21 and are shown in Fig. **??**.

Again an azimuthal profiles study of the structures has been performed for both images resulting in Fig. 6.26 and 6.27.

In Fig. 6.26 it is evident a strong peak of flux between 20° and 170° in the 5 km profile with a narrower higher peak between 70° and 120°. The peak is evident also in the 8 km profile but between 30° and 130° with narrower wings and no further peaks while it is still present but fainter and broader in the 12 km profile. A further smaller peak is present in the 5 km profile between 240° and 290°, suggesting the radial jet mentioned before.

In Fig. 6.27 the 20°-170° peak is still visible and has the same structure as in Fig. 6.26 for all the three profiles. Moreover a smaller peak is again present in the 5 km profile but this time between 300° and 330°.

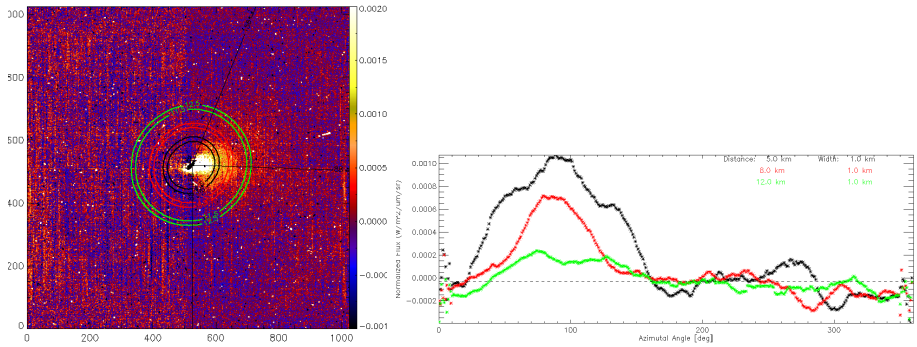

Figure 6.26: CN azimuthal profiles before CA.

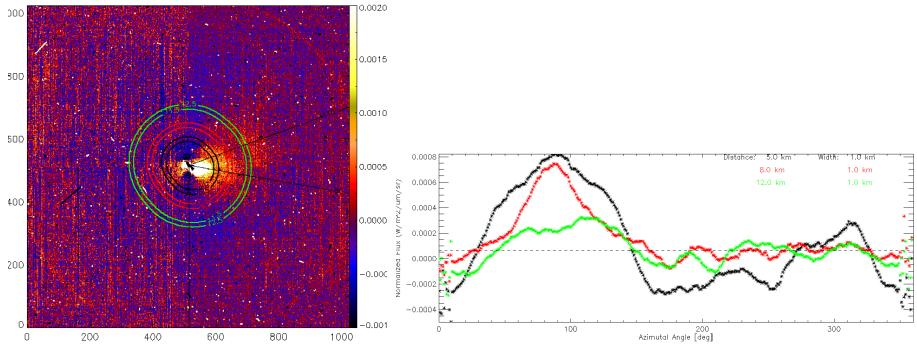

Figure 6.27: CN azimuthal profiles after CA.

6.5 Water Production Investigation

The gas flux intensities have been therefore employed in order to determine the molecules abundances in the coma, and eventually the parent molecules production rates. This has been carried out for the sole OH emission which is the most interesting for the analysis of the distribution of water, its main parent and the most dominant volatile species in cometary atmospheres.

This is possible only knowing in details the processes responsible for the gas emissions. In the case of OH, the main emission mechanism known is the resonance fluorescence. From water photodissociation through solar light in fact, most of the OH molecules are left in the ground base level $X^2\Pi$. Those molecules absorb solar photons and are excited to the first electronic state $A^2\Sigma^+$ (see Sec. 5.2). The excited OH distributes mainly in the first two

vibrational levels $v = 0$ and $v = 1$ in the lowest rotational states. Thus when it decades to the ground state, following the selection rules, it may decay on the $v = 0$, or on the $v = 1$ vibrational levels of the ground electronic state, respectively. Therefore they actually may give rise to two different emission bands, called the (0,0) and the (1,1) band, which constitute the band that is observed through the OH filter at ~ 308.5 nm

6.5.1 OH Column Density

From OH observed flux, the OH molecules abundance in the coma has been estimated, i.e. the OH column density that is the number of molecules per cm^{-2} inside a column along the line of sight.

The column density N has been computed using:

$$N_{[cm^{-2}]} = \frac{4\pi d^2 \Omega d\lambda}{\frac{g}{r_h^2} p^2} F_{OH} \tag{6.22}$$

where d is the distance between the spacecraft and the comet; Ω is the solid angle of a single pixel; $d\lambda$ is the bandwidth; g is the gas fluorescence efficiency at 1 AU; r_h is the heliocentric distance of the comet in AU; p is the pixel scale in cm and F_{OH} is the gas emission flux in the coma measured in W $m^{-2} \mu m^{-1}$ sr^{-1}.

A crucial factor for the column density evaluation is represented by the fluorescence efficiency, also called g-factor, which is the final energy emitted by the gas expressed in photons per second per molecule (see Eq. 5.26). The fluorescence efficiency depends on the temperature of the gas, which in turn depends on the heliocentric distance of the comet and also on its heliocentric velocity because of the Swings effect (Swings, 1941) (see Sec. 5.4).

This is particularly important for OH emission band at 308.5 nm and needs to be taken into account.

The fluorescence rates g_{00} and g_{11} for the two bands (0,0) centered at 308.5 nm and (1,1) centered at 314.3 nm, have been taken from Schleicher and A'Hearn (1988) for the varying heliocentric velocities of about 1-2 km/s and the heliocentric distance of about 1.064 at which Hartley 2 was at the moment of the encounter.

The total g-factor for the overall band is then expressed by:

$$g_{OH} = \frac{g_{00}(\dot{r}_h) f_{00} + g_{11}(\dot{r}_h) f_{11}}{r_h^2} \tag{6.23}$$

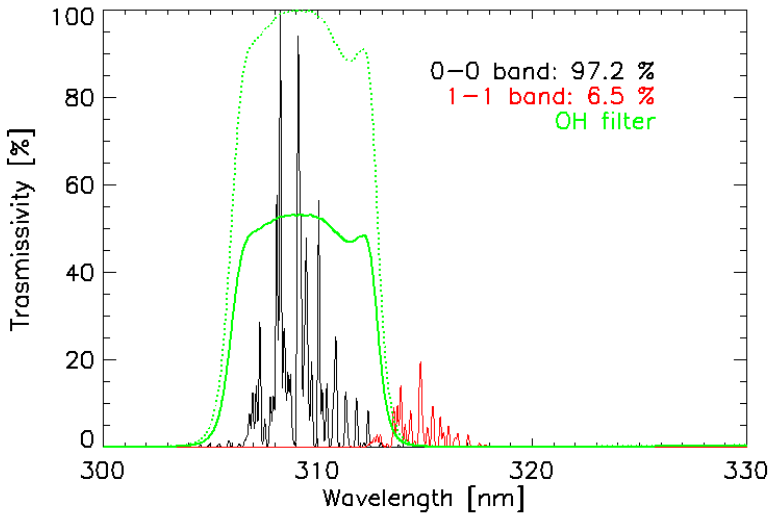

Figure 6.28: OH $A^2\Sigma^+ - X^2\Pi$ (0,0) and (1,1) band fractions observed through OH bandpass filter.

where f_{00} and f_{11} are the fractions of the (0,0) and (1,1) bands respectively which fall inside the filter transmissivity. Those have been evaluated making used of the LIFBASE software (Luque and Crosley, 1999) which has been used to generate a synthetic spectrum of both bands, using the relative populations of the levels, calculated, for fluorescence mechanisms and heliocentric distance and velocity of Hartley 2 at the moment of encounter, by Schleicher (personal communication). The band fractions are normalized to the transmission of OH filter as if the maximum filter transmissivity was 100%.

Using Eq. (6.22) OH gas emission images have been then converted into column density maps. The results are shown in Fig. 6.29 for the two more resolved OH images g56 and g57 of the very innermost coma. The radial profiles of these column densities have been also measured and shown in Fig. 6.30 in a logarithmic plot. As it is visible from the colorbar scales and the radial profiles, the two maps are compatible but a slight offset seems to be present. This was unexpected since the two images are only 20 minutes apart and a large emission variation in not awaited in such short amount of time.

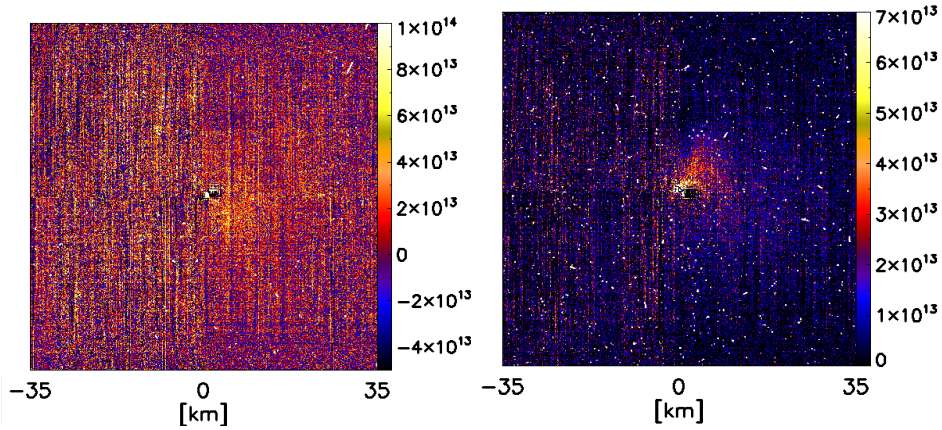

(a) (b)

Figure 6.29: OH column density maps for images (a) g56 and (b) g57.

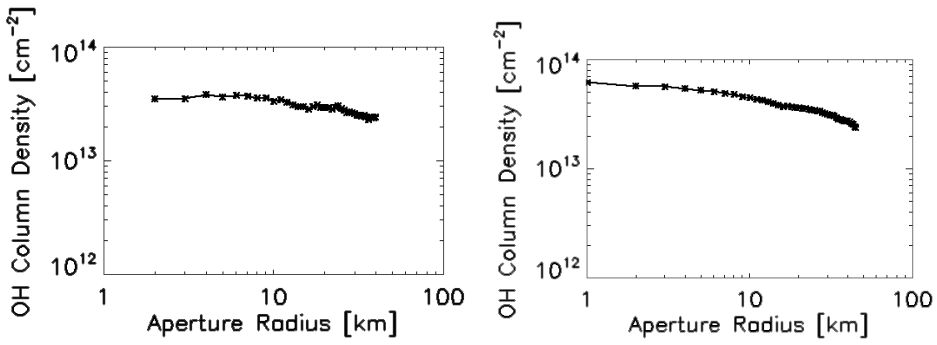

(a) (b)

Figure 6.30: OH column density profiles for images (a) g56 and (b) g57.

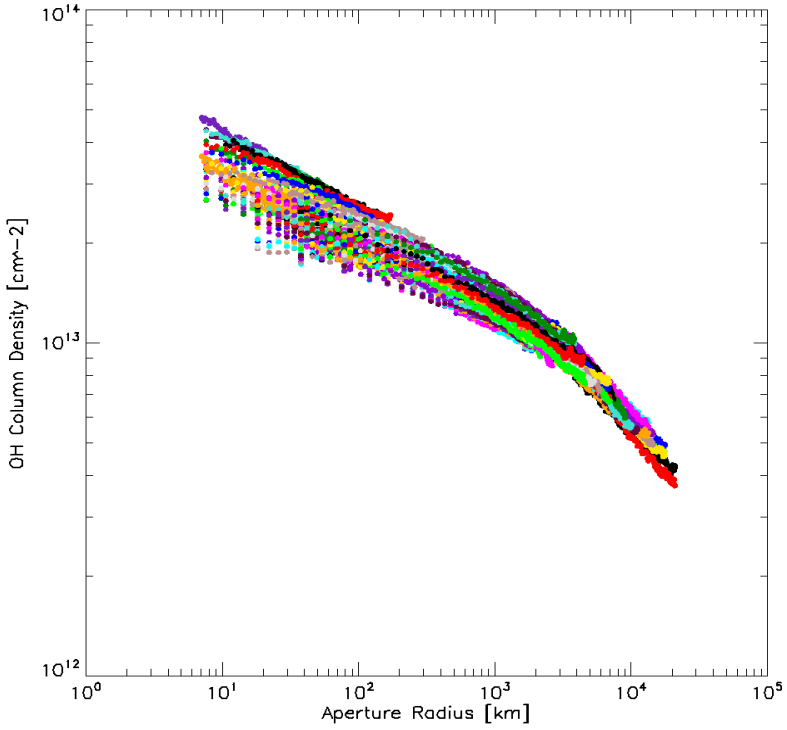

Figure 6.31: OH column density radial profiles computed for observations ranging from DOY 301 to DOY 311.

The column density investigation has been extended to all 153 OH images ranging from perihelion up to 10 days after, i.e. from observations from DOY 301 to DOY 311 as reported in Tab. 6.3, 6.4 and 6.5. The result profiles for all images are shown in Fig. 6.31.

A clear spread in column density is evident but it results that the column densities are overall consistent. The trend is nearly regular with no strong discontinuity detected even in the very innermost regions down to 10 km from the nucleus.

6.5.2 Water production models

The column density profiles have been therefore used in order to derive the water production rate. This step required the use of a coma production model, such as Haser or Festou's vectorial models (see Sec. 5.1) which describe the spatial distribution of the daughter molecules in the coma assuming some parameters on the parent molecules.

Both models have to be integrated along the line of sight in order to compare the resultant column density with the observed column density and derive the correspondent parent production rate. For Festou's model, the Web Vectorial Model (WVM)(http://www.boulder.swri.edu/wvm/) has been used as a reference for this thesis. The vectorial model is however mathematically defined only for the outer coma and it is instead not defined in the inner regions, inside the collision sphere. We used the transformation equations from Combi et al., 2004 (see Sec. 5.1) to convert Haser model into an "equivalent extended vectorial" model. In this way we extended the vectorial model to the innermost coma regions in order to compare it with the column densities observed. A comparison of Haser model, WVM and the newly computer equivalent vectorial model is shown in Fig. 6.32 for a fixed production rate of $Q = 7.9 \cdot 10^{27}$ mol s^{-1}.

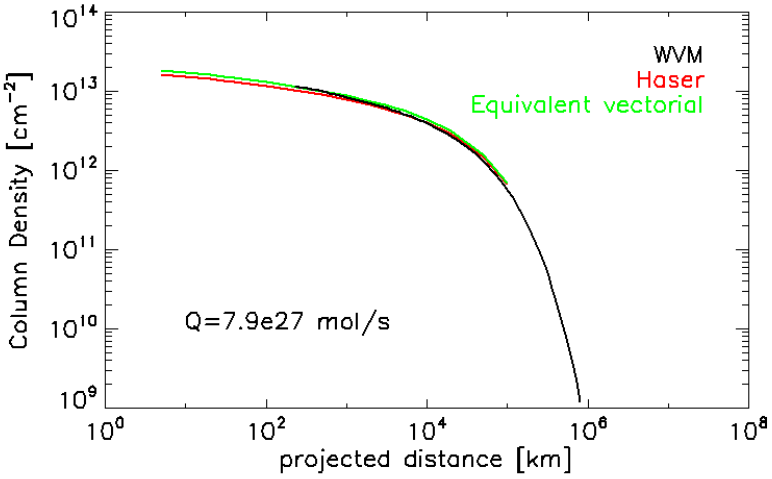

Figure 6.32: Haser, WVM and equivalent extended models comparison.

As visible in Fig 6.32, we verified that the equivalent extended model is correspondent to WVM for the outer part of the coma, extending from 10^2 up to about 10^5 km in the sky plane. The new model stays slightly higher than Haser model as expected since Haser model underestimates the daughter molecules density.

6.5.3 Water production rate

A series of computation of the extended equivalent model have been run, evaluating the column densities profiles for a series of production rates ranging from $Q = 1.0 \cdot 10^{28}$ mol s^{-1} ($\log Q = 28.0$) up to $Q = 1.80012 \cdot 10^{28}$ mol s^{-1} ($\log Q = 28.2553$) with steps of $0.02 - 0.05 \cdot 10^{28}$.

For each observation a best fit model has been searched as the one with minimum residuals. In Fig. 6.33 and 6.34 an example of a production rate fit and residuals respectively are shown for OH image g68 in Tab. 6.4.

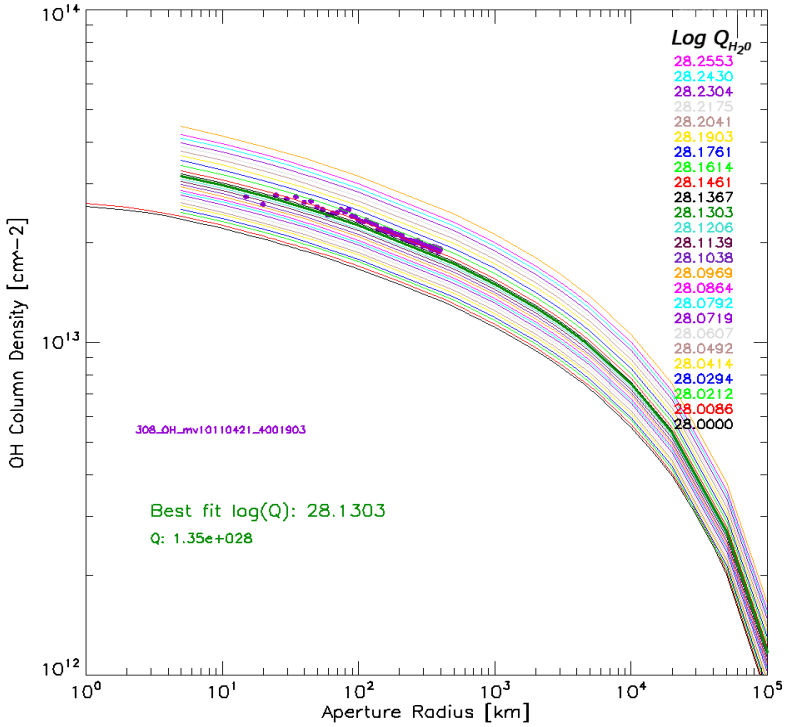

Figure 6.33: Water production rate fit for OH g68 image.

The general plot showing the column densities profiles of all OH images and the correspondent water production rates fitted is shown in Fig. 6.35. The overall the agreement is quite good, showing that the models extension is probably good enough to represent our data, even in the very close region, down to 50 km from the nucleus.

In the innermost regions the data show however higher column densities than expected from the models. This increased OH molecule abundance has

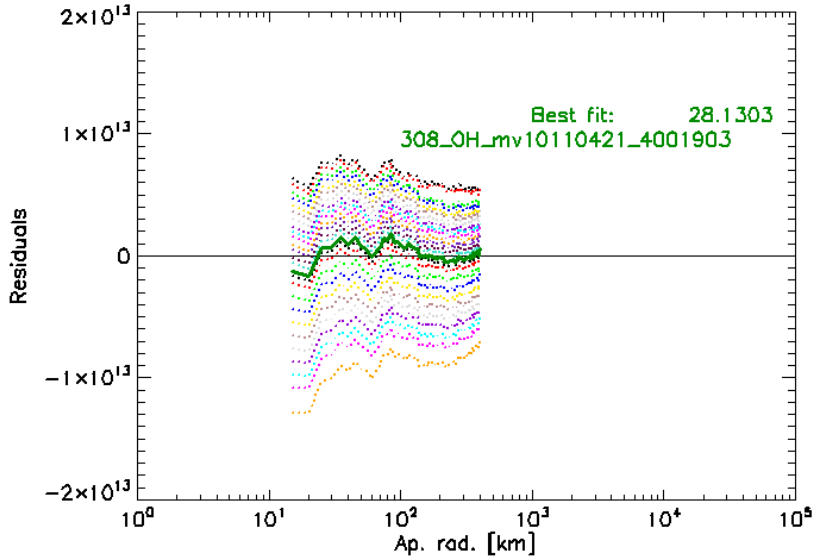

Figure 6.34: Water production rate fit residuals for OH g68 image.

been further investigated invoking the presence of an alternative emission process in addition to fluorescence and will be described in the next section.

The best-fit production rate has been then reported as function of time (in hours) from perihelion in Fig. 6.36. A cosine with period of 18 hours (comet's rotation period) has been reported for reference. Even though the curve is under-sampled due to the scarcity of OH observations far from the CA, it is evident a periodic trend of the water production rate.

This variation can be addressed to a variation in the comet's observed activity, probably caused by the rotation of the comet's nucleus which provokes the active areas to be periodically exposed to the Sun which "activates" .

The highest peak in the curve corresponds to the CA and also to the high jump in the column density profiles between observation g56 and observation g57. It may be only due to the fact that the closest approach occurred about 7 days after perihelion which is a typical time span for the water production rate curve to peak due to an inertia of the heating and emission processes. However such a narrow and confined peak is unlikely. The visible shallow increase in Q with time is quite consistent with this inertia.

The peak in Fig. 6.36 constitutes the second reason that drove us to investigate the prompt emission mechanism, in addition to fluorescence to

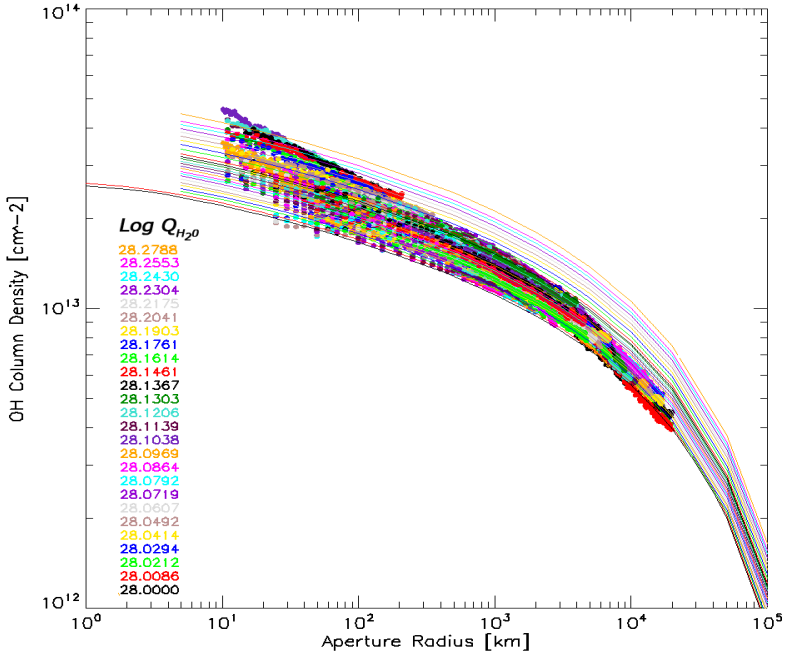

Figure 6.35: OH column density profiles measured for a all 153 images in Tab. 6.3, 6.4 and 6.5, and the correspondent water production rates modeled.

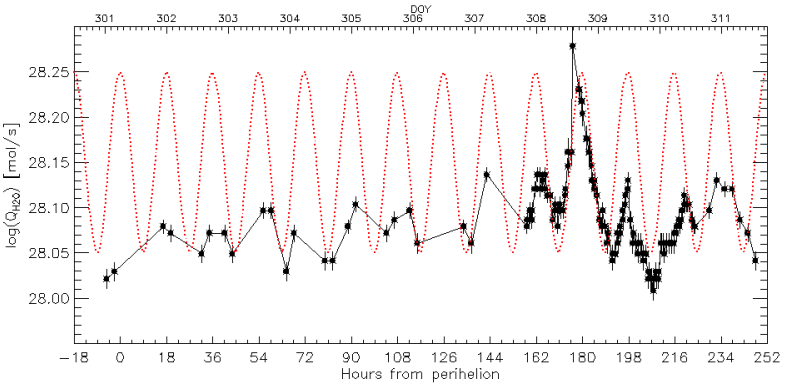

Figure 6.36: Variation of the water production rate as function of time. A cosine with 18 hours period (the comet's rotation period) is also reported for reference.

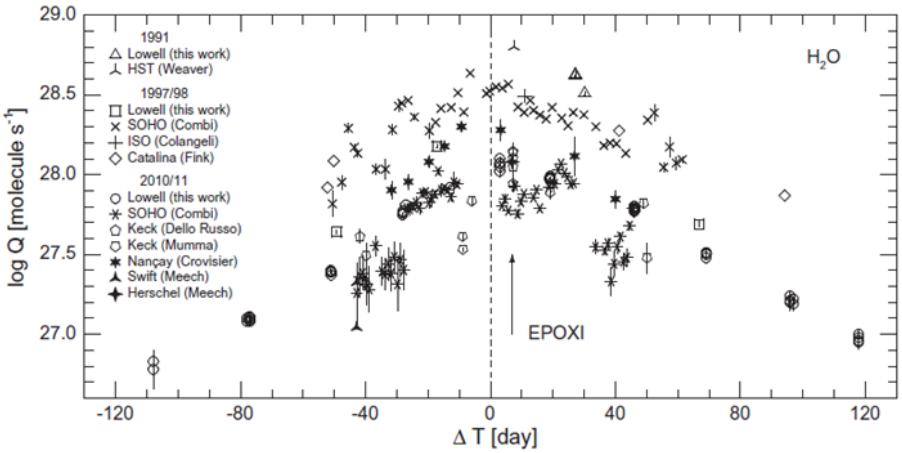

Figure 6.37: Water Production rate measured from other authors (Knight and Schleicher, 2013).

explain this excess brightness.

However a summary plots (from Knight and Schleicher, 2013) is reported (Fig. 6.37) of all other measurements of Hartley 2 water production rate and result to be in great agreement with our average production rate of about $1.17{\cdot}10^{28}$ mol s^{-1} ($\log Q = 28.07$) measured excluding the strong CA peak.

6.6 OH prompt emission investigation

A further investigation has been performed in order to explain the excess OH brightness in the very innermost coma as respect to the model and to the average of the variation curve.

The possibility that the near nucleus structure visible in the OH narrow-band images g56 and g57 is due not only to fluorescence mechanisms but also to OH prompt emission (PE) (see Sec. 5.5) has been considered. A theoretical estimate of the observable OH PE has been therefore carried out.

The total relative strength of the two mechanisms is given by:

$$\frac{S_{PE}}{S_{fl}}(\rho) = \frac{N_{H_2O}(\rho)}{N_{OH}(\rho)} \cdot \frac{D \cdot Br(OH(A^2\Sigma^+))}{g(r_h, \dot{r}_h)} \tag{6.24}$$

where ρ is distance from the comet's nucleus in the sky plane projection; $N_{H_2O}(\rho)$ and $N_{OH}(\rho)$ are respectively the column densities of H_2O molecules and OH molecules at the projected distance ρ; D is the photodissociation rate

of water molecules, i.e. the number of molecule which actually photodissociate per second; $Br(OH*(A^2\Sigma^+))$ is the branching ratio of the photodissociation of water for OH$*(A^2\Sigma^+)$, i.e. the percentage of OH molecules left in the excited $A^2\Sigma^+$ electronic state relative to the total OH molecule produced in the photodissociation; $g(r_h, \dot{r}_h)$ is the fluorescence efficiency.

The ratio $N_{H_2O}/N_{OH}(\rho)$ in Eq. 6.24 has been estimated using Haser model.
The number density of water molecules and OH molecules in the coma are given by Haser (Eq. 5.2 and 5.3) respectively by:

$$N_{H_2O}(r) = \frac{Q}{4\pi r^2 v} e^{-\frac{r}{\gamma_{H_2O}}} \tag{6.25}$$

$$N_{OH}(r) = \frac{Q}{4\pi r^2 v} \frac{\gamma_{OH}}{\gamma_{H_2O} - \gamma_{OH}} (e^{-\frac{r}{\gamma_{H_2O}}} - e^{-\frac{r}{\gamma_{OH}}}) \tag{6.26}$$

where Q is the water production rate of the comet in mol/s; v is the assumed velocity of the gas in the coma; γ_{H_2O} and γ_{OH} are the scalelength of the parent and the daughter respectively:

$$\gamma_{H_2O} = v\tau_{H_2O} \tag{6.27}$$

$$\gamma_{OH} = v\tau_{OH} \tag{6.28}$$

where τ_{H_2O} and τ_{OH} are respectively the lifetimes of H_2O and OH.
In order to compare the Haser model with the observations, it is necessary to integrate the model along the line of sight and derive the density distribution of molecules as function of the projected nucleocentric distance. This is done easily by substituting in Eq. 6.25 and 6.26 the nucleocentric distance r with:

$$r = \sqrt{\rho^2 + x^2} \tag{6.29}$$

where ρ is the projected distance perpendicular to the line of sight and x is the projected distance along the line of sight, and integrating along x (see Fig. 6.38).

The number density of water and OH molecules as function of the projected distance are then given by:

$$N_{H_2O}(\rho) = \int_{-z}^{+z} \frac{Q}{4\pi v(\rho^2 + x^2)} e^{-\frac{\sqrt{\rho^2+x^2}}{\gamma_p}} dx \tag{6.30}$$

$$N_{OH}(\rho) = \int_{-z}^{+z} \frac{Q}{4\pi v(\rho^2 + x^2)} \frac{\gamma_d}{\gamma_p - \gamma_d} (e^{-\frac{\sqrt{\rho^2+x^2}}{\gamma_p}} - e^{-\frac{\sqrt{\rho^2+x^2}}{\gamma_d}}) dx \tag{6.31}$$

Both equations have been numerically integrated, considering a production rate of $Q_{H_2O} = 1 \cdot 10^{28}$ mol s^{-1}, as derived from previous analysis. However N_{H_2O}/N_{OH} ratio is independent on the production rate, since Q is in both formulas and does not depend on x, therefore it can be simplified. A typical gas velocity of $v = 1$ km/s has been considered, a lifetime of water $\tau_{H_2O} = 0.96 \cdot 10^5$ s (Combi et al., 2004), and a lifetime of OH $\tau_{OH} = 1.5 \cdot 10^5$ s (Combi et al., 2004) have been considered for the integration.

The resultant column density profiles for the two species are shown in Fig. 6.39 while $N_{H_2O}/N_{OH}(\rho)$ is shown in Fig. 6.40.

The numerator of the second factor of Eq. 6.24 is composed by two parameters, i.e. the dissociation rate and the branching ratio, which depend mainly on the solar activity and have been computed by many authors. We have considered the values from Combi et al., 2004 (see Sec. 5.2), summarized in Tab. 6.8.

The denominator instead, is the g-factor, which depends on the probability of the absorption and the emission mechanisms and is not straightforward to compute. Values from Schleicher (personal communications) have been

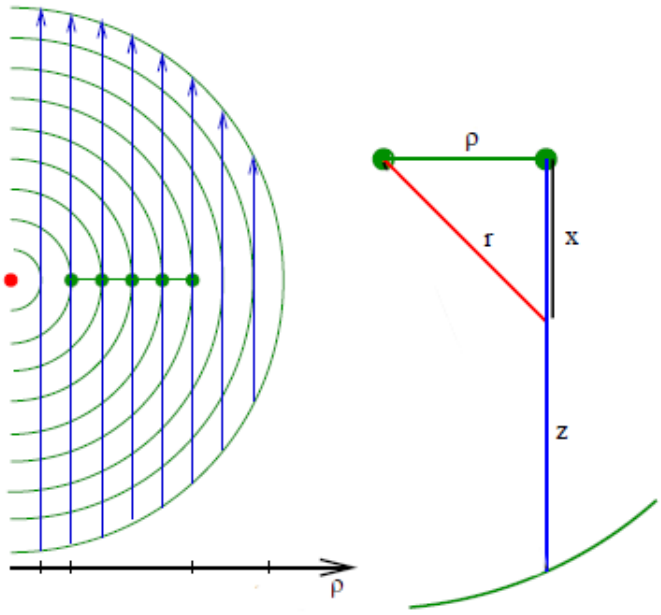

Figure 6.38: Definition of line of sight, nucleocentric distance and projected distance.

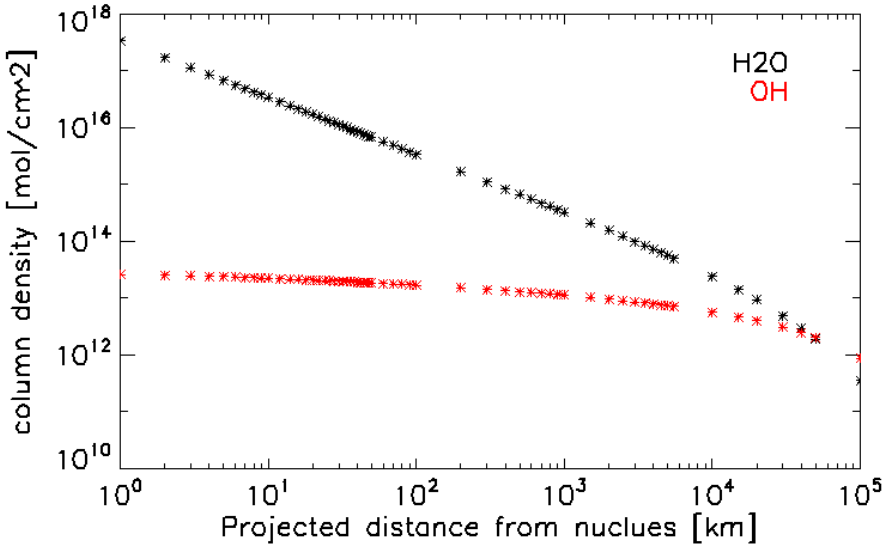

Figure 6.39: Water and OH molecules column density profiles as computed using Haser model with $Q = 1.0 \cdot 10^{28}$ mol s^{-1}.

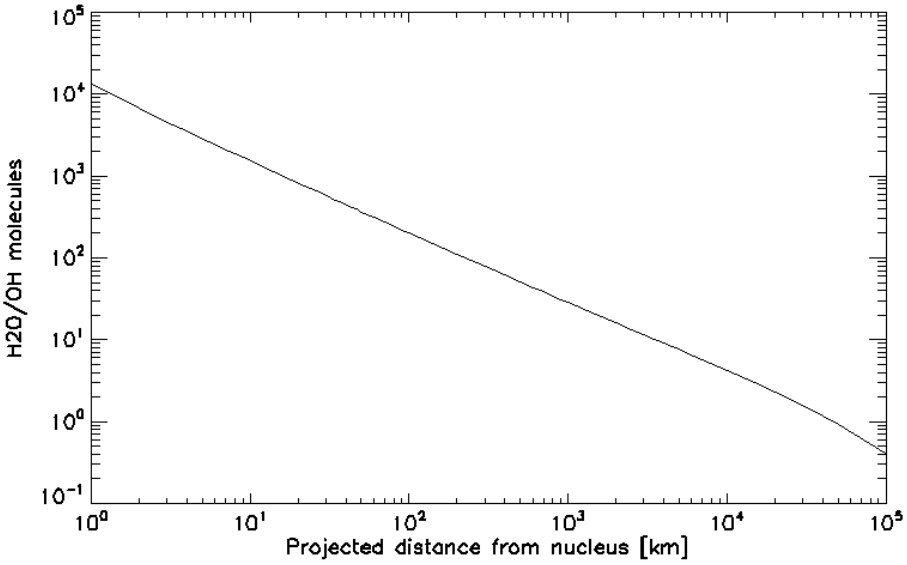

Figure 6.40: $N_{H_2O}/N_{OH}(\rho)$ obtained using Haser model.

	τ_{H_2O} [s]	D [mol/s]	$Br(OH*(A^2\Sigma^+))$ [%]
Quite Sun	$0.96{\cdot}10^5$	$1.04{\cdot}10^{-5}$	3.6
Active Sun	$0.71{\cdot}10^5$	$1.411{\cdot}10^{-5}$	4.1

Table 6.8: Lifetime, photodissociation rate of H_2O and branching ratios for OH*($A^2\Sigma^+$) from Combi et al. (2004) as in Tab. 5.1

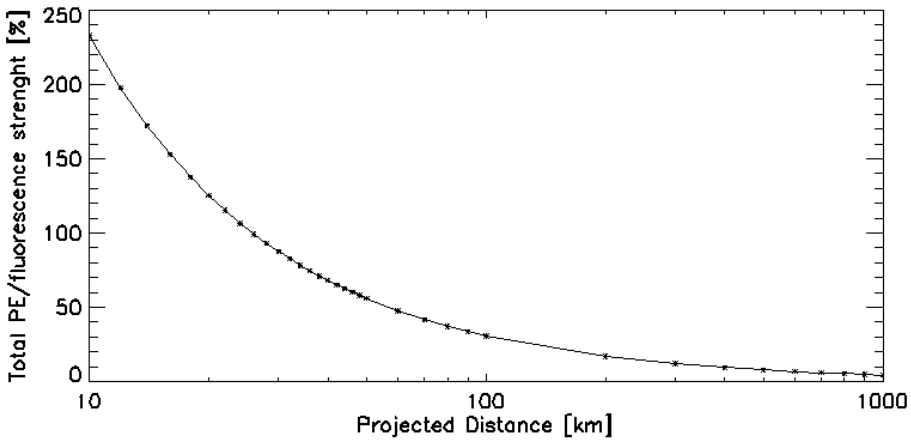

Figure 6.41: Prompt emission to fluorescence relative strength as function of the projected distance from the nucleus of the comet. using Haser model.

used, computed for the heliocentric velocity of Hartley 2 comet (about 1-2 km/s) and scaled for the square of the heliocentric distance of the comet at the moment of the fly-by (1.064 AU).

The total theoretical ratio S_{PE}/S_{fl} in Eq. 6.24 has been therefore computed for projected distance from 10 up to 1000 km and the result is shown in Fig. 6.41. It is clear that very close to the nucleus the prompt emission is much more efficient than fluorescence but it decreases very fast with the distance and soon the fluorescence becomes dominant.

However for the OH inner coma structures interpretation, another factor has been considered: the actual spectral distribution of fluorescence and PE emissions and their relative strengths as seen through MRI-OH filter.

The excited OH*($A^2\Sigma^+$) released from H_2O photodissociation is left with a population distribution totally different from the fluorescence one, such that the high rotational levels are highly populated and give rise to transition at higher wavelengths and different intensities as respect to the fluorescence

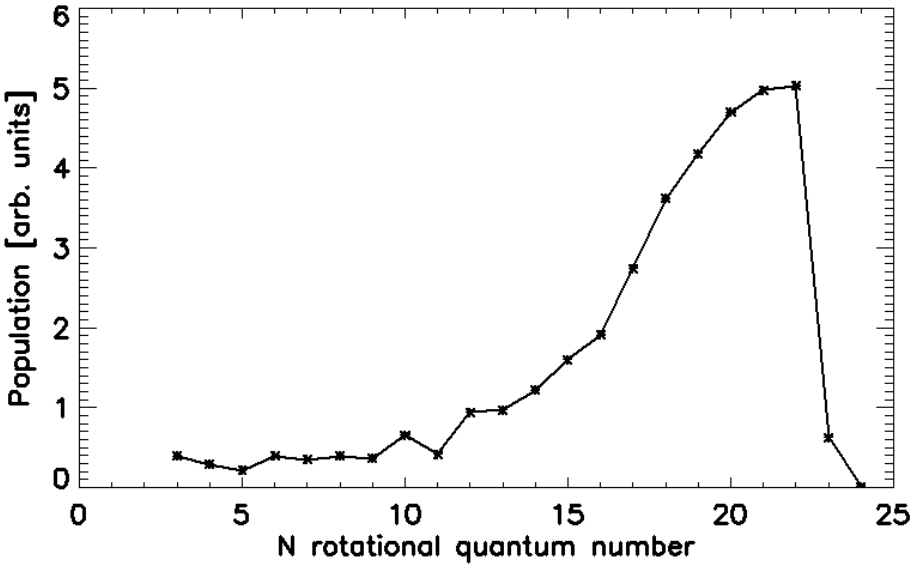

Figure 6.42: Rotational levels population distribution (Carrington et al., 1964).

emission (see Sec. 5.5). This means that the fluorescence spectrum and the prompt emission spectrum are slightly different not only for absolute efficiency but also for their spectral distribution (see Fig. 5.3).

The rotational distribution of OH*($A^2\Sigma^+$) coming from photodissociation of water has been studied by many authors. We considered the result by Carrington (1964) shown in Fig. 6.42. As it is clear the rotational levels from 18 to 23 are the most populated ones.

The spectral distribution of OH emission for both emission mechanisms have been computed using the software LIFBASE (Luque and Crosley, 1999). The prompt emission spectral distribution and its convolution through OH filter are shown in Fig. 6.43 and, if compared with Fig. 6.28 where fluorescence (0,0) and (1,1) bands are shown, it is evident that is different from fluorescence emission spectral distribution. Only a small fraction of OH PE is actually visible through MRI-OH filter, in particular the 38.75%.

In Fig. 6.44 both spectral distributions are shown, where the prompt emission spectrum has been computed at a distance of 50 km from the nucleus. The relative total intensity of the two emissions have been normalized so that the ratio of the two is given by Eq. 6.24 for a projected distance of 50 km and is represented in Fig. 6.41. The OH filter transmissivity has been reported for reference. As it is clear, the intensity is different but also

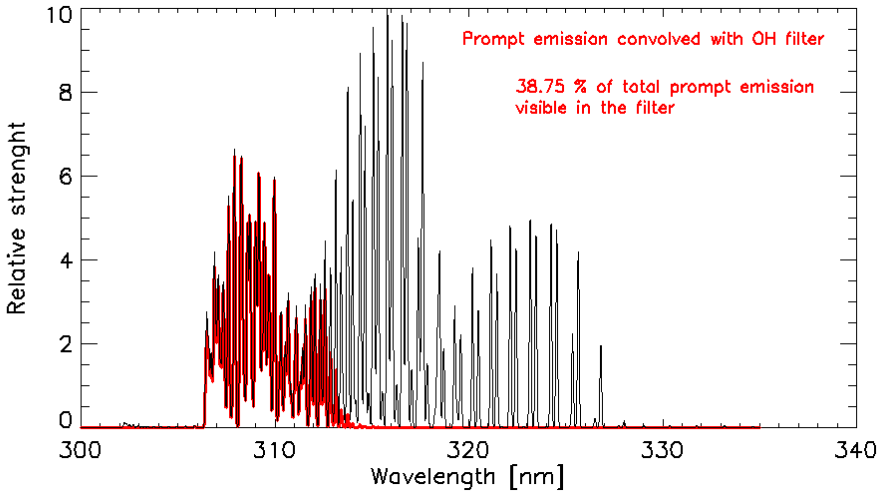

Figure 6.43: Fraction of prompt emission spectrum visible in the OH filter.

the spectral distribution is different in wavelength extension and in relative strength of the lines.

Unfortunately not the whole wavelength extension of the prompt emission passes through the OH filter. Thus the fraction of the theoretic OH prompt emission which should be visible in the OH filter (f_{PE}), is reduced by the convolution with OH filter both for a wavelength cut and for an intensity decreasing.

The fraction has been taken into account in the evaluation of the observable relative strength so that Eq. 6.24 becomes:

$$\frac{S'_{PE}}{S'_{fl}}(\rho) = \frac{N_{H_2O}(r)}{N_{OH}(\rho)} \cdot \frac{D \cdot Br(OH(A^2\Sigma^+))}{g(r_H, v_H)} \cdot f_{PE} \tag{6.32}$$

where S'_{PE}/S'_{fl} represents now the actual theoretic relative strength of the emissions observable trough MRI OH narrowband filter. At 50 km from the nucleus $f_{PE} \sim 0.26$ as shown in Fig. 6.44.

Since the relative strength of PE/fluorescence is varying with the projected distance, also f_{PE} would be variable. Therefore it has been computed again as function of the projected distance from comet's nucleus and the resultant $S'_{PE}/S'_{fl}(\rho)$ is shown in Fig. 6.45 in a logarithmic scale.

It exponentially decreases and, for example, at the cometocentric distance of 50 km, $S'_{PE}/S'_{fl} \simeq 0.26$, i.e. the PE strength is about one fourth of the

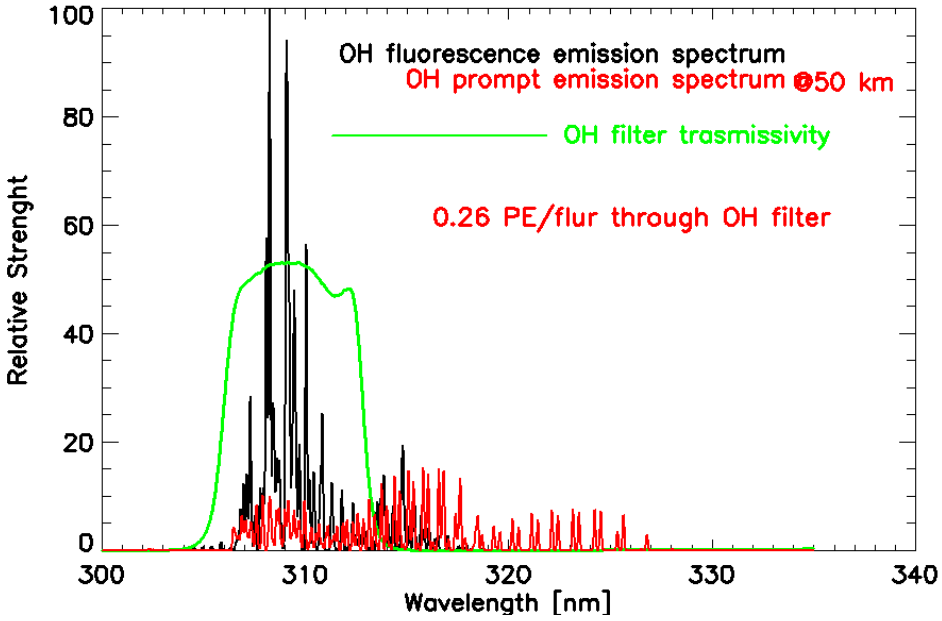

Figure 6.44: Relative strength of theoretical fluorescence and prompt emission spectra as computed at 50 km of nucleocentric projected distance. OH filter transmissivity is reported for reference.

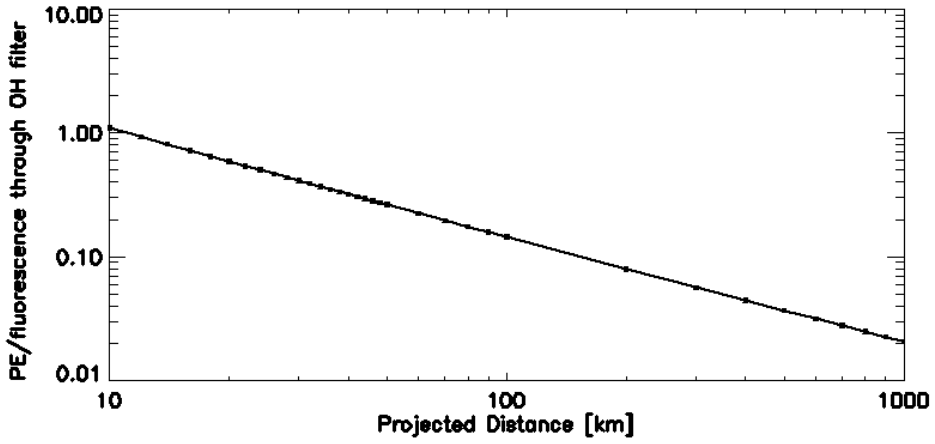

Figure 6.45: PE/fluorescence relative strength through OH narrowband filter as function of nucleocentric projected distance.

fluorescence emission. Thus it seems to be a non negligible fraction of the flux which may be due to prompt emission at these nucleocentric distances.

This result allows to infer that the prompt emission may be actually the mechanism responsible for the OH inner coma structures observed in MRI closest approach images.

This prompt emission theoretical calculation has been tested on the observed column density profiles and it is proposed also as the mechanism responsible for the peak intensity in the very close up observations of the inner most coma, where it would only be observable. If the entire theoretic value is believed and this quantity is subtracted from the observed flux in computing the OH column density profiles, since these are referred only to OH in the ground state which emits for fluorescence, the profiles blend excessively in the region below 50 km (Fig. 6.46) and could not be described by coma model adopted.

Whereas, if we assume that the 40% of the theoretical prompt emission occurs, meaning that, for example, at 50 km from the nucleus, the PE is actually about 10% of fluorescence, and we subtract this portion, then the column density curves corrected (Fig. 6.47) appear to be even more consistent with the production rate models, as respect to the case of pure fluorescence mechanism assumed (Fig. 6.35).

This result may suggest that the equivalent extended vectorial model can be actually a good representative of the data also in the innermost coma regions if a prompt emission mechanism of 40% of the theoretical value is considered to explain the innermost coma OH structures observed and their excess brightness.

The production rate variation curve has been also corrected assuming a 40% of the theoretical prompt emission (Fig. 6.48). The strongest peak visible is remarkably reduced and more close to the trend of the periodicity variation, even if it is still visible at CA but less pronounced than in the case of no prompt emission correction (Fig. 6.36). This residual peak of brightness corresponding to the closest approach may be due to an effect of increased resolution inside the coma or to a real peak of the comet's activity .

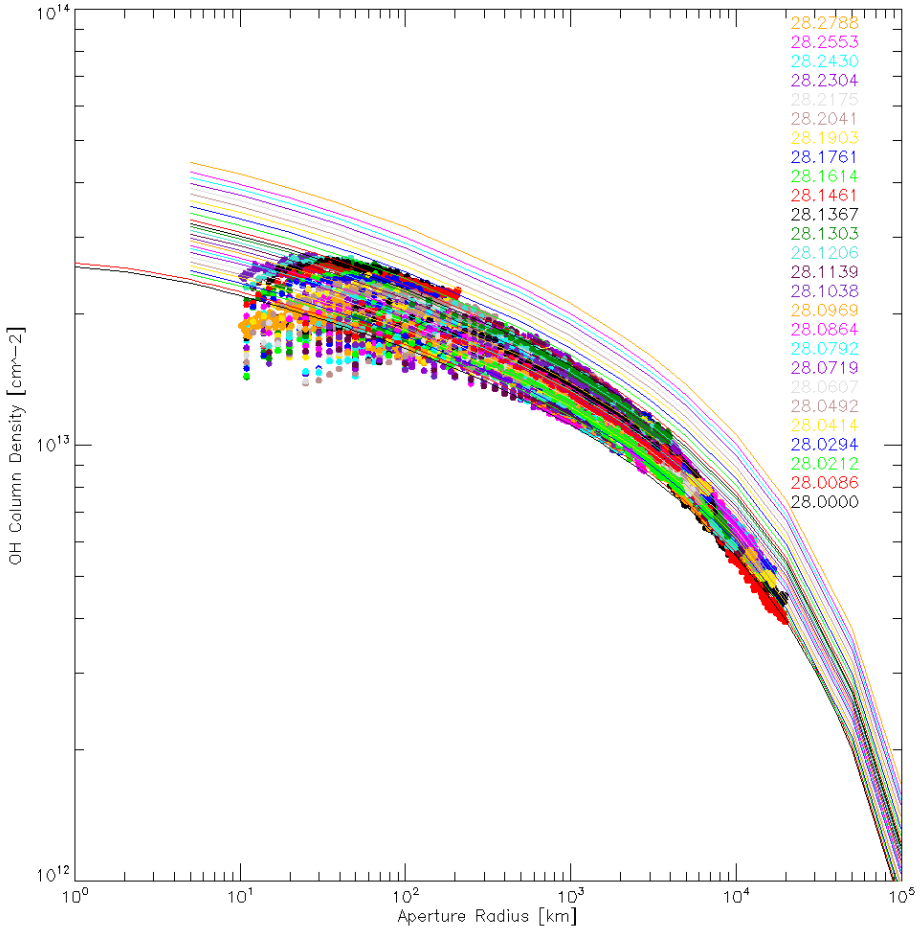

Figure 6.46: Column Densities profiles corrected for the total theoretical estimated prompt emission.

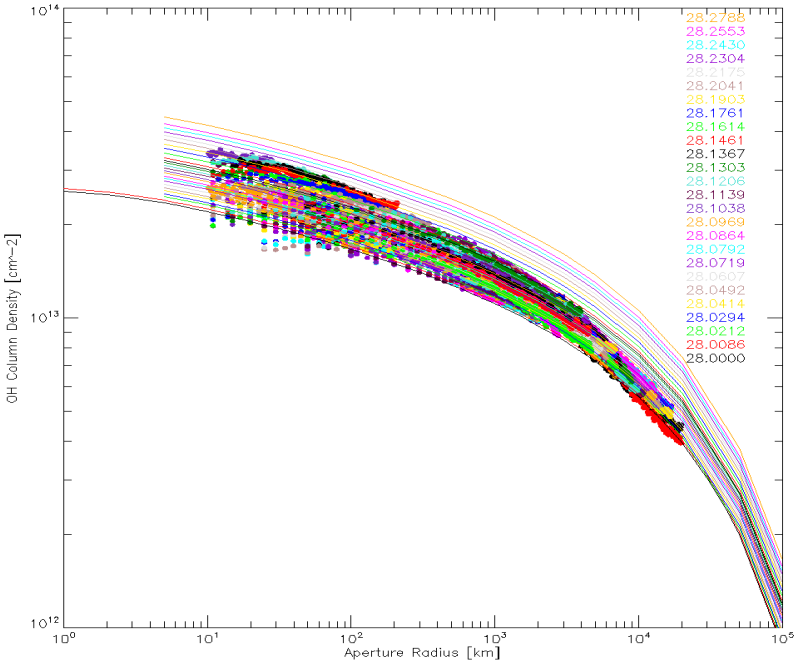

Figure 6.47: Column Densities profiles corrected for 40% of the theoretical estimated prompt emission.

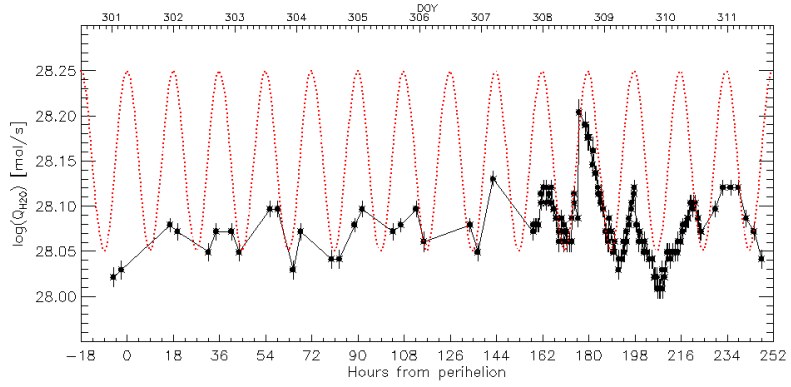

Figure 6.48: Production rate variation curve corrected for 40% of the theoretical estimated prompt emission.

Conclusions

In conclusion we could say that the close encounters performed by Rosetta and EPOXI missions provided a wealth of data and a consistent improvement for the small bodies science investigations.

The photometric analysis of asteroid 21 Lutetia, visited by Rosetta spacecraft on 10 July 2010, has been focused mainly on its surface physical properties. The various photometric methods adopted allowed to conclude a series of considerations about the nature, composition and variegation of the surface of this primitive Main Belt asteroid.

The integral phase curve analysis showed that the particles constituting Lutetia's surface are highly reflecting, very small, probably less than 1 micron, compact and opaque, indicative of tiny silicates or carbonaceous grains which form a low-porosity and high-density regolith layer with an overall smooth surface. This is consistent with Lutetia being a very big (98 ± 2 km of equivalent diameter, Sierks et al., 2011) and high-density ($3.4 \pm 0.3 \cdot 10^3$ kg m^{-3}, Pätzold et al., 2011) primitive space body.

The quite flat and featureless spectra obtained from various sets of spectrophotometric observations acquired at different phase angles, suggests, combined with the high density of the body, a spectral taxonomy as an X-type and a possible enstatite chondrite composition. The spectral behavior of different sets is consistent with the ground based spectra observed until now in the visible wavelength range, but some discrepancies are found between OSIRIS and HST data (Weaver et al., 2010) in the ultraviolet regions.

The spectral slope is found to be very dependent on the phase angle showing a pronounced reddening with the increasing phase angle. We found a spectral slope increasing from 5%/100 nm at zero phase angle up to 13%/100 nm at 130° phase angle, in the spectral range between 375 nm and 630 nm. A flatter reddening is found at higher wavelengths, between 650 nm and 880 nm where it increases from about 1%/100 at zero phase angle up to 6%/100 nm at 130° phase angle. This evidence, still to be completely explained, may be one possible explanation of the continuously changing spectral slope of

Lutetia spectrum observed from Earth.

We found strong evidences of a compositional and/or grain size diversity on the Baetica Region, since the NearUV-UV color-map shows a variegation of about 10%, suggesting the presence of bluer material on the crater walls and of redder material at the bottom of the slant. The bluer region is probably indicative of bigger grains, possibly revealing fresh material, whereas the redder regions indicate perhaps smaller grains, more representative of debris deposits. It seems indeed realistic that the crater walls show fresh material, while in the flat region debris deposits are visible, causing the measured color differentiation.

Most of the mentioned analysis would require a detailed topographic model of the terrain in order to obtain a local characterization rather than a global description. For this purpose a high-resolution shape model and a series of complementary processing tools have been implemented. We undertake the shape model analysis and application even though the full implementation of the resolved photometric analysis is postponed to a future but upcoming work. The shape model has been projected in order to generate synthetic images to be compared with actual observations, incident and emission angle maps have been produced, giving the complete information about the physical illumination condition of the body at each moment during the encounter, a latitude-longitude grid map of the observed surface has been projected on each image. This side tools will be therefore soon applied for topographic surface correction, resolved phase curve modeling, spectrophotometry and color variegation.

The photometric analysis of comet 103P/Hartley 2, visited by EPOXI spacecraft on 4 November 2010, has been focused instead on the cometary atmosphere and its dust and gas structures and emission processes. The analysis allowed to conclude a series of considerations about OH and CN structures observed in the innermost coma and to suggest a secondary mechanism as a possible contributor to OH emission in the inner coma.

A series of technical data processing have been performed such as images stacking, which required geometrical warping and a cross-correlation algorithm, cosmic rays removal, polar coordinate transformation, stripes removal, and radial profile subtraction enhancement, in order to clean images, make some analysis easier and retrieve coma structures which were otherwise hidden under different components.

Dust observations have been analyzed and varying structures have been observed. The study of the colors and reddening of the dust using the Violet,

Green and Red narrowband continuum observations allowed to conclude that dust in Hartley 2 coma substantially homogeneous even if a slightly redder trend in the tailward direction has been found. This is explained probably considering that ices and refractories are both emitted in the sunward direction together, but, while ices sublimate, the refractories are pushed away by the radiation pressure and form a slightly redder tail. The subtle difference may be due also to different phenomenon such as grain size effect or fragmentation. The dust in the coma also present a spectral slope higher than solar's, resulting in a reddening about 6% in the wavelength range Violet-Green, and 2.5% in the wavelength range between Green and Red filters.

Gas observations have been analyzed with particular consideration for OH and CN nucleus-resolved images of the inner coma. The narrowband continuum observations allowed to evaluate and subtract the dust contamination in the gas filters and extract the sole gas flux. At the same time an estimate of the contamination of the Clear1 filter has been carried out resulting in a value about 9% in the vicinity of the nucleus and raising up to 12% at around 35 km from the nucleus. This allowed to use Clear1 filter for the dust contamination subtraction for the unresolved OH observations and to obtain a detailed study of OH structures spanning from the day of perihelion up to 10 days afterward. OH shows an overall radial antisunward distribution in all images apart the CA where a radial sunward jet coming from the central waist of the nucleus becomes evident. This OH emission very close to the nucleus provided the first indication of a possible secondary emission mechanisms due to prompt emission from photodissociation of water.

CN inner coma structures analysis show instead a strong halo all around the nucleus, a bow structure in the solar direction and a fainter jet coming from the small lobe of the nucleus in the antisunward direction. The evidence of gaseous emission in rounded structure are interpreted as indications that the gas is emitted in the coma by grains or particles that are affected by the nucleus rotation. CN has been observed to produce those types of features already in other comets (see for example A'Hearn et al., 1896; Knight et al., 2013).

OH observations have been further analyzed in order to derive the production rate of water, its main parent and the dominant volatile in the cometary atmosphere. Thanks to the implementation of an equivalent extended model, correspondent to vectorial model but extending inside the coma down to the nucleus, the average water production rate has been found to be about $1.17{\cdot}10^{28}$ mol s^{-1} ($\log Q = 28.07$), compatible with other authors measures (see Knight et al., 2013). Moreover it is found to be varying as function of

time with a periodicity that suggests a correlation with the nucleus rotation. However a strong peak in the production rate variation curve, correspondent to Hartley 2 closest approach, provided a second indication that the prompt emission mechanism may be a contributor to the observed OH flux.

Therefore the prompt emission mechanism for OH molecules production has been investigated and a theoretical evaluation of the observable OH prompt emission flux through MRI-OH narrowband filter has been performed, providing an efficiency of 26% of fluorescence efficiency at 50 km from the nucleus. Observations, however, indicate that if PE efficiency is assumed to be about 40% of its theoretical value (about 10% of fluoresce at 50 km), the column density profiles would be described well by the coma models adopted even in the regions close to the nucleus.

Future Perspectives

The first development of this work will be the application of the shape model information, tools and implementation to the resolved analysis of 21 Lutetia surface regolith. The topographic correction will be performed and the subsequent spectrophotometry, surface variegation analysis and resolved phase curve model will be carried out.

However, the main and most substantial extension of this work will be the application of all the techniques studied, implemented and used in this thesis to the analysis of space observations that will be acquired during the upcoming encounter of Rosetta with the comet 67P/Churyumov-Gerasimenko.

Rosetta mission, presently traveling towards the comet and just awakened after more than 2 years of hibernation, will allow the detailed study of the onset of activity and of the chemical and physical processes that take place in a cometary environment. Rosetta will approach the comet on August 2014, will deliver a lander to the comet's surface on November 2014 providing the first in-situ analysis of a cometary nucleus. Then it will escort the comet along its orbit for more than a year to testimony the onset of its activity close to perihelion. Thousands of high spatial resolution multi-band images, acquired with high time frequency, will be obtained by OSIRIS, the imaging instrument onboard Rosetta, providing a unique data set. This encounter will revolutionize the present understanding of comets supplying important and unknown enlightenment also to the knowledge of the history of our Solar System.

The future perspective is thus to analyze and interpret the massive quantity of photometric data acquired by OSIRIS camera during the whole duration of the prime mission. The dynamical and rotational state, the topographic and mineralogical properties, the spectroscopic and photometric characteristics, the physical and chemical aspects of gas and dust emissions in the coma and of spatial and temporal activity variation will be investigated. Therefore the analysis and the techniques implemented in this work will be essential all will be combined together to understand the interconnections

and the exchanges existing between the coma and the nucleus and to identify the features characteristics of those connections, with the final aim to better understand the comets in all their aspects.

References

A'Hearn, M. F.; Schleicher, D. G.; Millis, R. L.; Feldman, P. D.; Thompson, D. T., **1984**. Comet Bowell 1980b. *Astronomical Journal*, 89, 579-591.

A'Hearn, M. F.; Hoban, S.; Birch, P. V.; Bowers, C.; Martin, R.; Klinglesmith, D. A. III, **1986**. Cyanogen jets in comet Halley. *Nature*, 324, 649-651.

A'Hearn, M. F.; Belton, M. J. S.; Delamere, W. A.; Kissel, J.; Klaasen, K. P.; McFadden, L. A.; Meech, K. J.; Melosh, H. J.; Schultz, P. H.; Sunshine, J. M.; Thomas, P. C.; Veverka, J.; Yeomans, D. K.; Baca, M. W.; Busko, I.; Crockett, C. J.; Collins, S. M.; Desnoyer, M.; Eberhardy, C. A.; Ernst, C. M.; Farnham, T. L.; Feaga, L.; Groussin, O.; Hampton, D.; Ipatov, S. I.; Li, J.-Y.; Lindler, D.; Lisse, C. M.; Mastrodemos, N.; Owen, W. M.; Richardson, J. E.; Wellnitz, D. D.; White, R. L., **2005**. Deep Impact: Excavating Comet Tempel 1. *Science*, 310, 5746, 258-264.

A'Hearn, M. F.; Krishna Swamy, K. S.; Wellnitz, D. D., **2007**. Prompt Ultraviolet Emission by OH in Comet Hyakutake. *American Astronomical Society, DPS meeting 39*, 48.02; Bulletin of the American Astronomical Society, 39, 507.

A'Hearn, M. F.; Feaga, L. M.; Bertaux, J.-L.; Feldman, P. D.; Parker, J. Wm.; Slater, D. C.; Steffl, A. J.; Stern, A. S.; Throop, H.; Versteeg, M.; Weaver, H. A.; K., U. H., **2010**. The far-ultraviolet albedo of Steins measured with Rosetta-ALICE. *Planetary and Space Science*, 58, 9, 1088-1096.

A'Hearn, M. F.; Belton, M. J. S.; Delamere, W. A.; Feaga, L. M.; Hampton, D.; Kissel, J.; Klaasen, K. P.; McFadden, L. A.; Meech, K. J.; Melosh, H. J.; Schultz, P. H.; Sunshine, J. M.; Thomas, P. C.; Veverka, J.; Wellnitz, D. D.; Yeomans, D. K.; Besse, S.; Bodewits, D.; Bowling, T. J.; Carcich, B. T.; Collins, S. M.; Farnham, T. L.; Groussin, O.; Hermalyn, B.; Kelley, M. S.; Kelley, M. S.; Li, J-Y.; Lindler, D. J.; Lisse, C. M.; McLaughlin, S. A.; Merlin, F.; Protopapa, S.; Richardson, J. E.; Williams, J. L., **2011**. EPOXI at Comet Hartley 2. *Science* 332, 6036, 1396.

Allen, C., **1946**. The spectrum of the corona at the eclipse of 1940 October 1. *Proc. Roy. Astron. Soc. London*, 106, 137-50.

Bailey M. E.; Clube S. V. M.; Napier W. M., **1990**. The Origin of Comets. *Pergamon*, Oxford, 599 pp.

Barucci, M. A.; Fulchignoni, M.; Fornasier, S.; Dotto, E.; Vernazza, P.; Birlan, M.; Binzel, R. P.; Carvano, J.; Merlin, F.; Barbieri, C.; Belskaya, I., **2005**. Asteroid target selection for the new Rosetta mission baseline. 21 Lutetia and 2867 Steins. *Astronomy and Astrophysics*, 430, 313-317.

Becker, K.H.; Haaks, D.; **1973**. Measurement of the natural lifetimes and quenching rate constants of OH($^2\Sigma^+$, $v = 0, 1$) and OD($^2\Sigma^+, v = 0, 1$) radicals. *Z. Naturforsch. A*, 28, 249.

Bertaux, J. L., **1986**. The UV bright SPOT of water vapor in comets. *Astronomy and Astrophysics*, 160, 2, L7-L10.

Bertini, I., **2011**. Main Belt Comets: A new class of small bodies in the Solar System. *Planetary and Space Science*, 59, 365-377.

Bodewits, D.; Farnham, T. L.; Li, J. Y.; Kelley, M. S.; Williams, J. L.; McFadden, L. A.; Sunshine, J. M.; A'Hearn, M. F.; Meech, K. J.; Lisse, C. M.; DIXI Team, **2012**. Gas and Dust in the Coma Around Hartley-2. *ACM*, 16-20 May 2012, Niigata, Japan. 1667, 6081.

Bonev, B. P.; Mumma, M. J.; Dello Russo, N.; Gibb, E. L.; DiSanti, M. A.; Magee-Sauer, K., **2004**. Infrared OH Prompt Emission as a Proxy of Water Production in Comets: Quantitative Analysis of the Multiplet Near 3046 cm$^-$1 in Comets C/1999 H1 (Lee) and C/2001 A2 (LINEAR). *The Astrophysical Journal*, 615, 2, 1048-1053.

Bowell, E.; Hapke, B.; Domingue, D.; Lumme, K.; Peltoniemi, J.; Harris, A. W.; **1989**, Application of photometric models to asteroids. *Asteroids II*. R. P. Binzel, T. Gehrels, M. S. Matthews, (eds.), 524-556.

Budzien, S. A.; Feldman, P. D., **1991**. OH prompt emission in Comet IRAS-Araki-Alcock (1983 VII). *Icarus*, 90, 308-318.

Bus, S. J.; R. P. Binzel, **2002a**. Phase II of the Small Main-Belt Asteroid Spectroscopic Survey. A Feature-Based Taxonomy. *Icarus*, 158, 146-177.

Bus, S. J.; R. P. Binzel, **2002b**. Phase II of the Small Main-Belt Asteroid Spectroscopic Survey. The Observations. *Icarus*, 158, 106145.

Carrington, T., **1964**. Angular Momentum Distribution and Emission Spectrum of OH ($^2\Sigma^+$) in the Photodissociation of H_2O. *Journal of Chemical Physics*, 41, 2012.

Combi, M. R.; Harris, W. M.; Smyth, W. H., **2004**. Gas Dynamics and Kinetics in the Cometary Coma: Theory and Observations. *Comets II*, M. C. Festou,

H. U. Keller, and H. A. Weaver (eds.), University of Arizona Press, Tucson, 745 pp., 523-552.

Chamberlain, J. W.; Hunten, D. M., **1987**. Theory of planetary atmospheres: an introduction to their physics and chemistry. 2nd revised and enlarged edition. *Academic Press* ,Orlando, FL. International Geophysics Series, 36, 493 p.

Cheng, A. F.; Domingue, D. L., **2000**. Radiative transfer models for light scattering from planetary surfaces. *Journal of Geophysical Research*, 105, E4, 9477-9482.

Clark, B. E.; Veverka, J.; Helfenstein, P.; Thomas, P. C.; Bell, J. F.; Harch, A.; Robinson, M. S.; Murchie, S. L.; McFadden, L. A.; Chapman, C. R., **1999**, NEAR Photometry of Asteroid 253 Mathilde. *Icarus*, 140, 53-65.

Clark, B. E.; Helfenstein, P.; Bell III, J. F.; Peterson, C.; Veverka, J., **2002**. NEAR infrared spectrometer photometry of asteroid 433 Eros. *Icarus*, 155, 189-204.

Coradini, A.; Capaccioni, F.; Erard, S.; Arnold, G.; De Sanctis, M. C.; Filacchione, G.; Tosi, F.; Barucci, M. A.; Capria, M. T.; Ammannito, E.; Grassi, D.; Piccioni, G.; Giuppi, S.; Bellucci, G.; Benkhoff, J.; Bibring, J. P.; Blanco, A.; Blecka, M.; Bockelee-Morvan, D.; Carraro, F.; Carlson, R.; Carsenty, U.; Cerroni, P.; Colangeli, L.; Combes, M.; Combi, M.; Crovisier, J.; Drossart, P.; Encrenaz, E. T.; Federico, C.; Fink, U.; Fonti, S.; Giacomini, L.; Ip, W. H.; Jaumann, R.; Kuehrt, E.; Langevin, Y.; Magni, G.; McCord, T.; Mennella, V.; Mottola, S.; Neukum, G.; Orofino, V.; Palumbo, P.; Schade, U.; Schmitt, B.; Taylor, F.; Tiphene, D.; Tozzi, G., **2011**. The Surface Composition and Temperature of Asteroid 21 Lutetia As Observed by Rosetta/VIRTIS. *Science*, 334, 6055, 492.

Cremonese, G.; Boehnhardt, H.; Crovisier, J.; Rauer, H.; Fitzsimmons, A.; Fulle, M.; Licandro, J.; Pollacco, D.; Tozzi, G. P.; West, R. M, **1997**. Neutral Sodium from Comet Hale-Bopp: A Third Type of Tail. *Astrophysical Journal Letters*, 490, L199.

Crifo, J. F.; Fulle, M.; Kmle, N. I.; Szego, K., **2004**. Nucleus-coma structural relationships: lessons from physical models. *Comets II*, M. C. Festou, H. U. Keller, and H. A. Weaver (eds.), University of Arizona Press, Tucson, 745 pp., 471-503.

DeMeo, F. E.; Binzel, R. P.; Slivan, S. M.; Bus, S. J., **2009**. An extension of the Bus asteroid taxonomy into the near-infrared. *Icarus*, 202, 1, 160-180.

DeMeo, F. E.; Binzel, R. P.; Lockhart, M., **2013**. Mars Encounters cause fresh surfaces on some near-Earth asteroids. *arXiv:* 1309.4839 [astro-ph.EP]

Domingue, D. L.; Robinson, M.; Carcich, B.; Joseph, J.; Thomas, P.; Clark, B. E., **2002**. Disk-Integrated photometry of 433 Eros. *Icarus*, 155, 205-219.

Dones, L., Weissman, P. R., Levison, H. F., Duncan, M. J., **2004**. Oort cloud formation and dynamics, *Comets II*, M. C. Festou, H. U. Keller, and H. A. Weaver (eds), University of Arizona Press, Tucson, 745 pp, 153-174.

Farnham, T. L.; Schleicher, D. G.; A'Hearn, M. F., **2000**. The HB Narrowband Comet Filters: Standard Stars and Calibrations. *Icarus* 147, 1, 180-204.

Farnham, Tony; Bodewits, D.; Feaga, L. M.; A'Hearn, M. F.; Sunshine, J. M.; Wellnitz, D. D.; Klaasen, K. P.; Himes, T. W. **2013**. Imaging Comets ISON and Garradd With the Deep Impact Flyby Spacecraft. *American Astronomical Society*, DPS meeting 45, 407.08.

Feaga, L. M.; Protopapa, S.; Besse, S.; Sunshine, J. M.; Groussin, O.; Merlin, F.; A'Hearn, M. F.; DIXI Team, **2012**. Volatile Distribution, Heterogeneities, and Extended Source of Water for 103P/Hartley 2 as Observed by the Deep Impact HRI-IR. *ACM*, 16-20 May 2012, Niigata, Japan, 1667, 6441.

Feldman, P. D.; Brune, W. H., **1976**. Carbon production in comet West 1975n. *Astroph. J. Lett.*, 209, L45-L48.

Feldman, P. D.; Cochran, A. L.; Combi, M. R., **2004**. Spectroscopic investigations of fragment species in the coma. *Comets II*. M. C. Festou, H. U. Keller, and H. A. Weaver (eds.), University of Arizona Press, Tucson, 745 pp., 425-447.

Festou, M. C., **1981**. The density distribution of neutral compounds in cometary atmospheres. I - Models and equations. *Astronomy and Astrophysics*, 95, 1, 69-79.

Fornasier, S.; Lazzarin, M., **2001**. E-Type asteroids: spectroscopic investigation on the 0.5 μm absorption band. *Icarus*, 152, 127-133.

Fornasier, S.; Migliorini, A.; Dotto, E.; Barucci, M. A., **2008**. Visible and near infrared spectroscopic investigation of E-type asteroids, including 2867 Steins, a target of the Rosetta mission. *Icarus*, 196, 1, 119-134.

Gehrels, T.; Coffeen, D.; Owings, D., **1964**. Wavelength dependence of polarization. III. The lunar surface. *The Astronomical Journal*, 69, 826-852.

Greenberg J. M., **1998**. Making a comet nucleus. *Astron. Astrophys.*, 330, 375-380.

Gulkis, S.; Keihm, S.; Kamp, L.; Lee, S.; Hartogh, P.; Crovisier, J.; Lellouch, E.; Encrenaz, P.; Bockelee-Morvan, D.; Hofstadter, M.; Beaudin, G.; Janssen, M.; Weissman, P.; von Allmen, P. A.; Encrenaz, T.; Backus, C. R.; Ip, W.-H.; Schloerb, P. F.; Biver, N.; Spilker, T.; Mann, I., **2012**. Continuum and spectroscopic observations of asteroid (21) Lutetia at millimeter and submillimeter wavelengths with the MIRO instrument on the Rosetta spacecraft. *Planetary and Space Science*, 66, 1, 31-42.

Hapke, B., **1981a**. Bidirectional reflectance spectroscopy. I - Theory. *Journal of Geophysical Research*, 86, 3039-3054.

Hapke, B.; Wells, E., **1981b**. Bidirectional reflectance spectroscopy. II - Experiments and observations. *Journal of Geophysical Research*, 86, 3055-3060.

Hapke, B., **1984**. Bidirectional reflectance spectroscopy. III - Correction for macroscopic roughness. *Icarus*, 59, 41-59.

Hapke, B., **1986**. Bidirectional reflectance spectroscopy. IV - The extinction coefficient and the opposition effect. *Icarus*, 67, 264-280.

Hapke, B., **1993**. Theory of Reflectance and Emittance Spectroscopy. *Cambridge University Press.* Cambridge, UK.

Hapke, B., **2002**. Bidirectional reflectance spectroscopy. 5. The coherent backscatter opposition effect and anisotropic scattering. *Icarus* 157, 523-534.

Hapke, B.; **2008**. Bidirectional reflectance spectroscopy. 6. Effects of porosity. *Icarus*, 195, 918-926.

Hapke, B. W.; Shepard, M. K.; Nelson, R. M.; Smythe, W. D.; Piatek, J. L., **2009**. A quantitative test of the ability of models based on the equation of radiative transfer to predict the bidirectional reflectance of a well-characterized medium. *Icarus*, 199, 210-218.

Hapke, B.; Denevi, B.; Sato, H.; Braden, S.; Robinson, M., **2012**. The wavelength dependence of the lunar phase curve as seen by the Lunar Reconnaissance Orbiter wide-angle camera. *Journal of Geophysical Research*, 117.

Haser, L., **1957**. Distribution d'intensite dans la tete d'une comete. *Bull. Acad. R. Sci. Liege*, 43, 740-750.

Hayashi, C., **1981**. Structure of the solar Nebula, growth and decay of magnetic fields and effects of magnetic and turbulent viscosities on the Nebula. *Progress of Theoretical Physics Supplement* 70, 35-53.

Helfenstein, P.; Veverka, J., **1989**, Physical characterization of asteroid surfaces from photometric analysis. *Asteroids II.* R. P. Binzel, T. Gehrels, M. S. Matthews (eds.), 557-593.

Helfenstein, P.; Veverka, J.; Thomas, P. C.; Simonelli, D. P.; Lee, P.; Klaasen, K.; Johnson, T. V.; Breneman, H.; Head, J. W.; Murchie, S., **1994**. Galileo photometry of Asteroid 951 Gaspra. *Icarus*, 107, 37.

Helfenstein, P.; Ververka, J.; Thomas, P. C.; Simonelli, D. P., **1996**. Galileo photometry of asteroid 243 Ida. *Icarus*, 120, 1, 48-65.

Henyey, C.; Greenstein, J., **1941**. Diffuse radiation in the galaxy. *Astrophys. J.*, 93, 70-83.

Jewitt, D.; Luu, J., **1993**. Discovery of the candidate Kuiper belt object 1992 QB1. *Nature*, 362, 6422, 730-732.

Jorda, L.; Gaskell, R.; Lamy, P.; Kaasalainen, M.; Groussin, O.; Faury, G.; Gutierrez, P.; Sabolo, W.; Hviid, S., **2011**. Shape and Physical Properties of Asteroid (21) Lutetia from OSIRIS Images. *EPSC-DPS Joint Meeting 2011, 2-7 October 2011, Nantes, France*, 776.

Keil, K., **2002**. Geological History of Asteroid 4 Vesta: The "Smallest Terrestrial Planet "*Asteroids III*, W. F. Bottke Jr., A. Cellino, P. Paolicchi, and R. P. Binzel (eds), University of Arizona Press, Tucson, 573-584.

Keller, H. U.; Barbieri, C.; Koschny, D.; Lamy, P.; Rickman, H.; Rodrigo, R.; Sierks, H.; A'Hearn, M. F.; Angrilli, F.; Barucci, M. A.; Bertaux, J.-L.; Cremonese, G.; Da Deppo, V.; Davidsson, B.; De Cecco, M.; Debei, S.; Fornasier, S.; Fulle, M.; Groussin, O.; Gutierrez, P. J.; Hviid, S. F.; Ip, W.-H.; Jorda, L.; Knollenberg, J.; Kramm, J. R.; Khrt, E.; Kppers, M.; Lara, L.-M.; Lazzarin, M.; Moreno, J. Lopez; Marzari, F.; Michalik, H.; Naletto, G.; Sabau, L.; Thomas, N.; Wenzel, K.-P.; Bertini, I.; Besse, S.; Ferri, F.; Kaasalainen, M.; Lowry, S.; Marchi, S.; Mottola, S.; Sabolo, W.; Schrder, S. E.; Spjuth, S.; Vernazza, P., **2010**. E-Type Asteroid (2867) Steins as Imaged by OSIRIS on Board Rosetta. *Science*, 327, 5962, 190.

Kelley, M. S.; Lindler, D. J.; Bodewits, D.; Lisse, C. M.; A'Hearn, M. F.; Kolokolova, L.; Farnham, T.; Kissel, J.; Hermalyn, B.; DIXI Science Team, **2012**. New Constraints on the Large Particles of Comet 103P/Hartley 2. *ACM*, 16-20 May 2012, Niigata, Japan, 1667, 6379.

Kitazato, K.; Clark, B. E.; Abe, M.; Abe, S.; Takagi, Y.; Hiroi, T.; Barnouin-Jha, O. S.; Abell, P. A.; Lederer, S. M.; Vilas, F., **2008**. Near-infrared spectrophotometry of Asteroid 25143 Itokawa from NIRS on the Hayabusa spacecraft, *Icarus*, 194, 137145.

Knight, M. M.; Schleicher, D. G., **2013**. The highly unusual outgassing of Comet 103P/Hartley 2 from narrowband photometry and imaging of the coma. *Icarus*, 222, 2, 691-706.

Lambert, J.H., 1760. Photometria sive de mensura et gradibus luminis, colorum et umbrae. Germany, Eberhardt Klett.

Lazzarin, M.; Marchi, S.; Magrin, S.; Barbieri, C., **2004**. Visible spectral properties of asteroid 21 Lutetia, target of Rosetta Mission. *Astronomy and Astrophysics*, 425, L25-L28.

Lazzarin, M.; Marchi, S.; Moroz, L. V.; Brunetto, R.; Magrin, S.; Paolicchi, P.; Strazzulla, G., **2006**. Space Weathering in the Main Asteroid Belt: The Big Picture. *The Astroph. J.*, 647, 2, L179-L182.

Lazzarin, M.; Marchi, S.; Moroz, L. V.; Magrin, S., **2009**. New visible spectra and mineralogical assessment of (21) Lutetia, a target of the Rosetta mission. *Astronomy and Astrophysics*, 498, 1, 307-311.

Lazzarin, M.; Magrin, S.; Marchi, S.; Dotto, E.; Perna, D.; Barbieri, C.; Barucci, M. A.; Fulchignoni, M., **2010**. Rotational variation of the spectral slope of (21) Lutetia, the second asteroid target of ESA Rosetta mission. *Monthly Notices of the Royal Astronomical Society*, 408, 3, 1433-1437.

Levenberg, K., **1944**. A method for the solution of certain non-linear problems in least squares. *The quarterly of applied mathematics, 2*, 164-168.

Levin B. Y., **1943**. The emission of gases by the nucleus of a comet and the variation of its absolute brightness. *Soviet Astron. J.*, 20, 37-48.

Levison, H. F., **1996**. Comet Taxonomy. *Completing the Inventory of the Solar System*, Astronomical Society of the Pacific Conference Proceedings, 107, T.W. Rettig and J.M. Hahn (eds.), 173-191.

Levison, H. F.; Duncan, M. J., **1997**. From the Kuiper Belt to Jupiter-family comets: the spatial distribution of ecliptic comets. *Icarus*, 127, 13-32.

Li, J-Y.; A'Hearn, M. F. and McFadden, L. A.,**2004**. Photometric analysis of Eros from NEAR data. *Icarus* 172, 415-431.

Li, J-Y.; McFadden, L. A.; Parker, J. Wm.; Young, E. F.; Stern, S. A.; Thomas, P. C.; Russell, C. T. and Sykes, M. V., **2006**. Photometric analysis of 1 Ceres and surface mapping from HST observations. *Icarus*, 182, 143-160.

Li, J-Y.; A'Hearn, M. F.; McFadden, L. A. and Belton, M. J.S., **2007a**. Photometric analysis and disk-resolved thermal modeling of Comet 19P/Borrelly from Deep Space 1 data. *Icarus*, 188, 195-211.

Li, J.-Y.; A'Hearn, M. F.; Belton, M. J. S.; Crockett, C. J.; Farnham, T. L.; Lisse, C. M.; McFadden, L. A.; Meech, K. J.; Sunshine, J. M.; Thomas, P. C.; Veverka, J., **2007b**. Deep Impact photometry of Comet 9P/Tempel 1, *Icarus*, 187, 41-55.

Li, J.-Y.; A'Hearn, M. F.; Farnham, T. L.; McFadden, L. A., **2008**. Photometric Analysis of the Nucleus of Comet 81P/Wild 2 from Stardust NAVCAM Data, *LPI Contributions*, 1405, 8290.

Lumme, K.; Bowell, E., **1981**, Radiative transfer in the surfaces of atmosphereless bodies. I - Theory. II - Interpretation of phase curves *Astronomical Journal*, 86, 1694-1721.

Luque, J.; Crosley, D.R., **1999**. LIFBASE: Database and Spectral Simulation Program (Version 1.5). *SRI International Report*, MP 99-009.

Lyttleton R. A., **1948**. On the origin of comets. *Mon. Not. R. Astron. Soc.*, 108, 465-475.

Magrin, S., **2006**. SINEO: Spectroscopic Investigation of Near Earth Objects. *PhD Dissertation*.

Magrin, S.; La Forgia, F.; Pajola, M.; Lazzarin, M.; Massironi, M.; Ferri, F.; da Deppo, V.; Barbieri, C.; Sierks, H. and the Osiris Team. **2012**. (21) Lutetia spectrophotometry from Rosetta-OSIRIS images and comparison to ground-based observations. *Planetary and Space Science*, 66, 1, 43-53.

Marchi, S.; Massironi, M.; Vincent, J.-B.; Morbidelli, A.; Mottola, S.; Marzari, F.; Kppers, M.; Besse, S.; Thomas, N.; Barbieri, C.; Naletto, G.; Sierks, H., **2012**. The cratering history of asteroid (21) Lutetia. *Planetary and Space Science*, 66, 1, 87-95.

Marquardt, D., **1963**. An algorithm for least-squares estimation of nonlinear parameters. *SIAM Journal on Applied Mathematics*, 11, 431-441.

Massironi, M.; Marchi, S.; Pajola, M.; Snodgrass, C.; Thomas, N.; Tubiana, C.; Vincent J. B.; Cremonese, G.; da Deppo, V.; Ferri, F.; Magrin, S.; Sierks, H.; Barbieri, C.; Lamy, P.; Rickman, H.; Rodrigo, R.; Koschny, D. and the Osiris Team, **2012**. Geological map and stratigraphy of asteroid 21 Lutetia. *Planetary and Space Science*, 66, 1, 125-136.

McCord, T. B.; Sotin, C., **2005**. Ceres: Evolution and current state. *Journal of Geophysical Research*, 110, E5.

McGuire, A., **1993**. Experimental Investigations of Light Scattering by Large, Irregular Particles. *Ph.D. Dissertation*, University of Pittsburgh.

Mekler, Y.; Podolak, M., **1994**. Formation of amorphous ice in the protoplanetary nebula. *Planetary and Space Science*, 42, 10, 865-870.

Mie, G., **1908**. Beitrage zur Optik trüber Medienspeziell kolloidaler Metallösungen. *Ann. Phys.*, 25, 377-445.

Minnaert, M., **1941**, The reciprocity principle in lunar photometry. *Astrophysical Journal*, 93, 403-410.

Morbidelli, A., **2008**. Comets and their reservoirs: current dynamics and primordial evolution. *Saas-Fee Advanced Course 35: Trans-Neptunian Objects and Comets*, 79-164, Springer Ed.

Nesvorný, D.; Jedicke, R.; Whiteley, R. J.; Ivezić, Ž., **2005**. Evidence for asteroid space weathering from the Sloan Digital Sky Survey. *Icarus* 173, 132152.

Öpik E. J., **1966**. Sun-grazing comets and tidal disruption. *Irish Astron. J.*, 7, 141-161.

Pajola, M.; Lazzarin, M.; Bertini, I.; Marzari, F.; Turrini, D.; Magrin, S.; La Forgia, F.; Thomas, N.; Kppers, M.; Moissl, R.; Ferri, F.; Barbieri, C.; Rickman, H.; Sierks, H., **2012**. Spectrophotometric investigation of Phobos with the Rosetta OSIRIS-NAC camera and implications for its collisional capture. *Monthly Notices of the Royal Astronomical Society*, 427, 4, 3230-3243.

Pajola, M.; Lazzarin, M.; Dalle Ore, C. M.; Cruikshank, D. P.; Roush, T. L.; Magrin, S.; Bertini, I.; La Forgia, F.; Barbieri, C., **2013**. Phobos as a D-type Captured Asteroid, Spectral Modeling from 0.25 to 4.0 ?m. *The Astrophysical Journal*, 777, 2, 127.

Ptzold, M.; Andert, T. P.; Asmar, S. W.; Anderson, J. D.; Barriot, J.-P.; Bird, M. K.; Husler, B.; Hahn, M.; Tellmann, S.; Sierks, H.; Lamy, P.; Weiss, B. P., **2012**. Asteroid 21 Lutetia: Low Mass, High Density. *Science*, 334, 6055, 491.

Petit, J.-M.; Morbidelli, A.; Chambers, J., **2001**. The Primordial Excitation and Clearing of the Asteroid Belt. *Icarus*, 153, 2, 338-347.

Perna, D.; Dotto, E.; Lazzarin, M.; Magrin, S.; Fulchignoni, M.; Barucci, M. A.; Fornasier, S.; Marchi, S.; Barbieri, C., **2010**. Inhomogeneities on the surface of 21 Lutetia, the asteroid target of the Rosetta mission. Ground-based results before the Rosetta fly-by. *Astronomy and Astrophysics*, 513, id L4.

Pieters, C. M.; Englert, P. A. J., **1993**. *Remote Geochemical analysis: elemental and mineralogical composition*. Cambridge University Press.

Poulet, F.; Cuzzi, J. N.; Cruikshank, D. P.; Roush, T.; Dalle Ore, C. M.; **2002**. Comparison between the Shkuratov and Hapke Scattering Theories for Solid Planetary Surfaces: Application to the Surface Composition of Two Centaurs. *Icarus*, 160, 313-324.

Preston, G. W., **1967**. The spectrum of Ikeya-Seki (1965f). *Astroph. J.*, 147, 718-742.

Protopapa, S.; Sunshine, J. M.; Feaga, L. M.; Besse, S.; Groussin, O.; Merlin, F.; Kelley, M. S.; Li, J.-Y.; Farnham, T. L.; A'Hearn, M. F.; DIXI Team, **2012**. Ice and Refractories in the Ambient Coma of 103P/Hartley 2. *ACM*, 16-20 May 2012, Niigata, Japan, 1667, 6360.

Prialnik, D.; Benkhoff, J.; Podolak, M., **2004**. Modeling the structure and activity of comet nuclei. in *Comets II*, M. C. Festou, H. U. Keller, and H. A. Weaver (eds.), University of Arizona Press, Tucson, 745 pp., 359-387.

Samarasinha N. H., **1999**. A model for the breakup of comet LINEAR (C/1999 S4). *Icarus*, 154, 540-544.

Samarasinha, N. H.; Larson, S. M., **2011**. Comparison of image enhancement techniques for cometary comae. *EPSC-DPS Joint Meeting 2011, 2-7 October 2011, Nantes, France*, 1400.

Sanchez, J. A.; Reddy, V.; Nathues, A.; Cloutis, E. A.; Mann, P.; Hiesinger, H., **2012**. Phase reddening on near-Earth asteroids: Implications for mineralogical analysis, space weathering and taxonomic classification. *Icarus*, 220, 1, 36-50.

Schleicher, D. G.; A'Hearn, M. F., **1982**. OH fluorescence in comets - Fluorescence efficiency of the ultraviolet bands. *Astrophysical Journal*, 258, 864-877.

Schleicher, D. G.; A'Hearn, M. F., **1988**. The fluorescence of cometary OH. *Astrophysical Journal*, 331, 1058-1077.

Schleicher, D. G.; Farnham, T. L., **2004**. Photometry and imaging of the coma with narrowband filters. *Comets II*, M. C. Festou, H. U. Keller, and H. A. Weaver (eds.), University of Arizona Press, Tucson, 745 pp., 449-469.

Schleicher, D. G., **2010**. The Fluorescence Efficiencies of the CN Violet Bands in Comets *The Astronomical Journal*, 140, 4, 973-984.

Schönberg, E., **1929**. Theoretische Photometrie. *Handbuch der Astrophysik*, 2, G. Eberhard, A. Kohlschutter and H. Ludendorff, (eds.), pp. 1-280. Berlin. Julius Springer.

Shepard, M. K.; Helfenstein, P., **2007**. A test of the Hapke photometric model. *Journal of Geophysical Research*, 112, E3.

Sierks, H.; Lamy, P.; Barbieri, C.; Koschny, D.; Rickman, H.; Rodrigo, R.; A'Hearn, M. F. et al., Angrilli, F.; Barucci, M. A.; Bertaux, J.-L.; Bertini, I.; Besse, S.; Carry, B.; Cremonese, G.; Da Deppo, V.; Davidsson, B.; Debei, S.; De Cecco, M.; De Leon, J.; Ferri, F.; Fornasier, S.; Fulle, M.; Hviid, S. F.; Gaskell, R. W.; Groussin, O.; Gutierrez, P.; Ip, W.; Jorda, L.; Kaasalainen, M.; Keller, H. U.; Knollenberg, J.; Kramm, R.; Khrt, E.; Kppers, M.; Lara, L.; Lazzarin, M.; Leyrat, C.; Moreno, J. J. Lopez; Magrin, S.; Marchi, S.; Marzari, F.; Massironi, M.; Michalik, H.; Moissl, R.; Naletto, G.; Preusker, F.; Sabau, L.; Sabolo, W.; Scholten, F.; Snodgrass, C.; Thomas, N.; Tubiana, C.; Vernazza, P., **2011**. Images of Asteroid 21 Lutetia: A Remnant Planetesimal from the Early Solar System. *Science* 334, 6055, 487.

Sohn, M.; Kim, S. J.; Sim, C. K.; Lee, C. U.; Lee, D. J., **2012**. CH Fluorescence in Comets. *Asteroids, Comets, Meteors 2012*, Proceedings of the conference held May 16-20, 2012 in Niigata, Japan. LPI Contribution No. 1667, 6221.

Spjuth, S., **2009**. Disk-Resolved Photometry of Small Bodies. *PhD dissertation*. Copernicus Publications

Stern, S. A.; Parker, J. Wm.; Feldman, P. D.; Weaver, H. A.; Steffl, A.; A'Hearn, M. F.; Feaga, L.; Birath, E.; Graps, A.; Bertaux, J.-L.; Slater, D. C.; Cunningham, N.; Versteeg, M.; Scherrer, J. R., **2011**. Ultraviolet Discoveries at Asteroid (21) Lutetia by the Rosetta Alice Ultraviolet Spectrograph. *The Astronomical Journal*, 141, 6, 199.

Sunshine, J. M.; Farnham, T. L.; Feaga, L. M.; Groussin, O.; Merlin, F.; Milliken, R. E.; A'Hearn, M. F., **2009**. Temporal and Spatial Variability of Lunar Hydration As Observed by the Deep Impact Spacecraft. *Science*, 326, 5952, 565.

Swings, P., **1941**. Complex structure of cometary bands tentatively ascribed to the contour of the solar spectrum. *Lick Obs. Bull.* 508, 131-136.

Tholen, D. J., **1989**. Asteroid taxonomic classifications. *Asteroids II*, 11391150.

Thomas, P. C.; Parker, J. Wm.: McFadden, L. A.; Russell, C. T.; Stern, S. A.; Sykes, M. V.; Young, E. F., **2005**. Differentiation of the asteroid Ceres as revealed by its shape. *Nature* 437, 7056, 224-226.

Tosi, F.; Coradini, A.; Capaccioni, F.; Filacchione, G.; Grassi, D.; de Sanctis, M. C.; Capria, M. T.; Barucci, M. A.; Fulchignoni, M.; Mottola, S.; Erard, S.; Dotto, E.; Baldetti, C. and the Virtis Team. **2010**. The light curve of asteroid 2867 Steins measured by VIRTIS-M during the Rosetta fly-by. *Planetary and Space Science*, 58, 9, 1066-1076.

Tosi, F.; Capaccioni, F.; Coradini, A.; Erard, S.; Filacchione, G.; de Sanctis, M. C.; Capria, M. T.; Giuppi, S.; Carraro, F. and the Virtis Team. **2012**. The light curve of asteroid 21 Lutetia measured by VIRTIS-M during the Rosetta fly-by. *Planetary and Space Science*, 66, 1, 9-22.

Weaver H. A.; Sekanina Z.; Toth I.; Delahodde C. E.; Hainaut O. R.; Lamy P. L.; Bauer J. M.; AHearn M. F.; Arpigny C.; Combi M. R.; Davies J. K.; Feldman P. D.; Festou M. C.; Hook R.; Jorda L.; Keesey M. S. W.; Lisse C. M.; Marsden B. G.; Meech K. J.; Tozzi G. P.; West R., **2001**. HST and VLT investigations of the fragments of comet C/1999 S4 (LINEAR). *Science*, 292, 1329-1334.

Weissman, P. R.; Bottke, W. F., Jr.; Levison, H. F., **2002**. Evolution of Comets into Asteroids. *Asteroids III*, W. F. Bottke Jr., A. Cellino, P. Paolicchi, R. P. Binzel (eds), University of Arizona Press, Tucson, 669-686.

Weissman P. R.; Richardson D. C.; Bottke W. F., **2003**. Random disruption of cometary nuclei by rotational spin-up. *Bull. Am. Astron. Soc.*, 35, 1012.

Weissman, P. R.; Asphaug, E.; Lowry, S. C., **2004**. Structure and Density of Cometary Nuclei. *Comets II*, M. Festou, H. U. Keller, H. A. Weaver (eds), University of Arizona Press, Tucson, 337-357.

Whipple, F. L., **1950**. A coma model. I. The acceleration of Comet Encke. *Astrophys. J.*, 111, 375-394.

Wiegert, P.; Tremaine, S., **1999**. The evolution of long-period comets. *Icarus*, 137, 84-121.

Woods, T. N.; Feldman, P. D.; Dymond, K. F.; Sahnow, D. J., **1986**. Rocket ultraviolet spectroscopy of comet Halley and abundance of carbon monoxide and carbon. *Nature*, 324, 436-438.

Yau K.; Yeomans D.; Weissman P., **1994**. The past and future motion of Comet P/Swift-Tuttle. *Mon. Not. R. Astron. Soc.*, 266, 305-316.

Yeomans D. K., **1991**. Comets. A Chronological History of Observation, Science, Myth, and Folklore. *Wiley*, New York, 485 pp.